Title
Digital Microfluidic Lab-on-a-Chip Platform for Tissue Engineering

Author
Bender, Brian Francis

Publication Date
2015

Peer reviewed|Thesis/dissertation

UNIVERSITY OF CALIFORNIA

Los Angeles

Digital Microfluidic Lab-on-a-Chip Platform

For Tissue Engineering

A dissertation submitted in partial satisfaction of the

requirements for the degree Doctor of Philosophy

in Bioengineering

By

Brian Francis Bender

2015

ABSTRACT OF THE DISSERTATION

Digital Microfluidic Lab-on-a-Chip Platform

For Tissue Engineering

by

Brian Francis Bender

Doctor of Philosophy in Bioengineering

University of California, Los Angeles, 2015

Professor Robin L. Garrell, Chair

Stem cell technology and tissue engineering offer exciting opportunities for improving medical therapies. Success in these endeavors will depend on advances in our basic understanding of tissue culture and the development of supporting technologies. Digital microfluidics (DμF) is one technology that could offer important and unique advantages for automating stem cell culture and cell-based assays to support tissue culture, drug discovery and basic biomedical research.

Digital microfluidics refers to a miniaturized lab-on-a-chip platform that enables the automation of a wide array of laboratory procedures by handling liquids

as droplets rather than streams. It has been applied to many chemical and biochemical protocols and assays. Advantages include reduced reaction times and reduced reagent volumes, and the ability to process multiple samples in an automated way: in series or in parallel, identically or uniquely.

This dissertation describes technological advances and applications of DμF for tissue engineering. Vertical dimensionality was developed by stacking multiple layers and incorporating a protocol for transferring droplets between layers. This added functionality enables new applications, exemplified by the demonstration of three previously un-achievable applications: creating a calcium alginate hydrogel with a radial crosslink density; creating a hydrogel based particle sieve; and the ability to retrieve 3D embryoid bodies on-chip. Protocols for growing three-dimensional tissue structures were established by encapsulating cells within hydrogel matrices. This protocol was used to demonstrate invasion assays for modeling tumor growth. Stem cell microenvironments were investigated by developing a protocol for the long-term growth and differentiation of embryoid bodies for cardiac tissue engineering. Non-invasive impedance assays were demonstrated for observing phenotypic behavior, maturation, and responses to chronotropic and inotropic agents. Finally, preliminary experiments were carried out to explore the feasibility of integrating piezoelectric PZT-based materials into DμF devices for added functionality. The voltage change generated via the pyroelectric effect was measured for exothermic chemical reactions, and strain induced in the substrate produced from contracting cardiomyocytes was monitored via piezoelectric effect.

The innovations presented here will provide the DμF and tissue engineering communities with design parameters and processing protocols necessary for manipulating collagen, producing 3D cell-ECM constructs, and creating a stem cell microenvironment for cardiomyogenesis.

The dissertation of Brian Francis Bender is approved.

Benjamin Wu

Andrea Kasko

Atsushi Nakano

Robin L. Garrell, Committee Chair

University of California, Los Angeles

2015

I would like to dedicate this dissertation to my fiancé, who has patiently supported me through this journey from start to finish.

TABLE OF CONTENTS

List of Figures

Acknowledgments

Chapter 1 introduces the motivation for the research performed in this dissertation frames the ensuing chapters. Chapters 2 and 3 provide background information to aid understanding of the research presented.

Chapter 4, "Digital Microfluidics for Spheroid-Based Invasion Assays," describes research performed in conjunction with Dr. Andrew Aijian. This chapter appears as a chapter in Dr. Aijian's dissertation and is in preparation for publication. Dr. Aijian's primary contributions to this work were to develop the protocol for creating spheroids and replacing the media, and the cancer-associated fibroblast invasion assay. My contributions to this work were to conceive, develop and characterize spheroid encapsulation in collagen matrices and the BMP2/PGE2 invasion assay. This work was published in the 2014 *μTAS* Conference Proceedings, p. 633-635, in an abbreviated form. This chapter is in preparation for publication as a full research article. It is included here with Dr. Aijian's permission.

Chapter 5, "Digital Microfluidic System with Vertical Functionality," has been submitted for publication in the journal *Micromachines* in their special issue entitled "Droplet Microfluidics – Techniques and Technologies."

Chapter 6, "Lab-on-a-Chip Platform for Culturing and Assaying Cardiomyocyte Tissue Derived from Human Embryonic Stem Cells" is in preparation for publication. This work is also described in a U.S. Provisional Patent Application Serial No. 62/150,708 entitled "Device and Method for Culturing and Assaying 3D Embryonic Stem Cells," filed 4/21/2015.

Chapter 7 "Digital Microfluidic Platform with Integrated Piezoelectric/Pyroelectric Sensing," presents emerging research, and is in

preparation for publication as a short communication article. This work is also described in a U.S. Provisional Patent Application Serial No. 62/204,909 entitled "Digital Microfluidic Platform with Piezoelectric/Pyroelectric Sensor Integration," filed 8/13/2015.

Chapter 8 presents possible future directions for research based on the work presented in this dissertation. Chapter 9 concludes the dissertation by summarizing key findings and framing the novelty and contribution this dissertation provides to the field of digital microfluidics.

Appendix A presents research performed within the Garrell Lab prior to starting any coursework, and was presented at UCLA's MCTP 2011 Symposium. This work is not in preparation for publication, but is included to provide broader context to the work performed on cell spheroid development. Appendix B presents research on adipogenesis. This work is not in preparation for publication.

VITA

EDUCATION

M.S., Biomedical Engineering, University of California, Los Angeles 2012
B.S., Materials Science & Engineering, North Carolina State University 2009

HONORS & AWARDS

Dissertation Year Fellowship, UCLA 2014-2015
Conference Fellowship, 16th UC Bioengineering Symposium 2015
Poster Competition – 2nd Prize, 9th International Meeting on Electrowetting and Related Micro/Electrofluidic Science and Technology 2014
ITA Student Entrepreneur Venture Competition – 1st Prize, UCLA 2014
Tony B. Academic Conference Travel Award, Society for Laboratory Automation & Screening 2014
Dr. Ursula Mandel Fellowship, UCLA 2013-2014
Malcolm R. Stacey Fellowship, UCLA 2013-2014
MCTP Bridge Fellowship, UCLA 2011

PUBLICATIONS (* - authors contributed equally)

Bender, B.F., Garrell, R.L. "Digital Microfluidic Platform with a Piezoelectric Substrate." *Micromachines. (In preparation)*

Bender, B.F., Garrell, R.L. "Digital Microfluidic Stem Cell Niche for the Long-Term Culture, Differentiation, and Assaying of Embryoid Bodies." *(In preparation)*

Bender, B.F., Garrell, R.L. "Digital Microfluidic System with Vertical Functionality." *Micromachines. (Submitted for publication)*

Bender, B.F.,* Aijian, A.P.,* Garrell, R.L. "Digital Microfluidic Platform for Cell Spheroid-Based Migration/Invasion Assays." *Lab Chip. (Submitted for publication)*

Bender, B.F.,* Aijian, A.P.,* Garrell, R.L., "Digital Microfluidic Platform for Cell Spheroid-Based Migration/Invasion Assays." *μTAS*, **2014**. p. 633-635.

PROVISIONAL PATENTS

Bender, B.F., "Device and Method for Culturing and Assaying 3D Embryonic Stem Cells," U.S. Provisional Application Serial No. 62/150,708, Filed 4/21/2015.

Bender, B.F., "Digital Microfluidic Platform with Piezoelectric/Pyroelectric Sensor Integration," U.S. Provisional Application Serial No. 62/204,909, Filed 8/13/2015.

CONFERENCE PRESENTATIONS (* - presenting author)

"Lab-on-a-Chip Platform for Culturing and Assaying Cardiomyocyte Tissue Derived from Embryonic Stem Cells." **Bender, B.F.,*** Garrell, R.L. 16th UC Bioengineering Symposium, Santa Cruz, CA, 2015 - poster presentation.

"Digital Microfluidic Platform for Cell Spheroid-Based Migration/Invasion Assays." **Bender, B.F.,*** Aijian, A.P., Garrell, R.L. 18th International Conference on Miniaturized Systems for Chemistry and Life Sciences, San Antonio, TX, 2014 - poster presentation.

"Digital Microfluidic Platform for Cell Spheroid-Based Migration/Invasion Assays." **Bender, B.F.,*** Aijian, A.P., Garrell, R.L. Biomedical Engineering Society 2014 Annual Meeting, San Antonio, TX, 2014 - poster presentation.

"Vertical Functionality in Digital Microfluidic Devices for Tissue Engineering." **Bender, B.F.,*** Aijian, A.P., Garrell, R.L. 9th International Meeting on Electrowetting and Related Micro/Electrofluidic Science and Technology, Cincinnati, OH, 2014 - poster presentation.

"Digital Microfluidic Device with Vertical Functionality." **Bender, B.F.,*** Aijian, A.P., Garrell, R.L. UCLA HSSEAS 2014 Tech Forum, Los Angeles, CA, 2014 - poster presentation.

"Digital Microfluidic Device with Vertical Functionality." **Bender, B.F.,*** Aijian, A.P., Garrell, R.L. Society for Laboratory Automation and Screening 3rd Annual Conference and Exhibition, San Diego, CA, 2014 - poster presentation.

"Cell Spheroid Development via Non-Adherent Conditions." **Bender, B.F.,*** Garrell, R.L. UCLA MCTP Symposium, Los Angeles, CA, 2011 - poster presentation.

RESEARCH & PROFESSIONAL EXPERIENCE

Garrell Lab, UCLA, Ph.D. Candidate, Bioengineering	2011-2015
Teaching Assistant, UCLA, Organic Chemistry	2011
UCLA OIP-ISR, Los Angeles, CA, Senior Technology Transfer Fellow	2013-2015
NAVAIR, Cherry Point, NC, Materials Engineer	2009-2011
Corning, Wilmington, NC, Product and Process Development Engineer	2009
Corning, Wilmington, NC, Manufacturing Engineering Intern	2008
Dielectric Devices, LLC, Raleigh, NC, Research Assistant	2006-2008
Kingon Lab, NCSU, Raleigh, NC, Research Assistant	2006

EXTRACURRICULAR ACTIVITIES

StartupUCLA Summer Accelerator, UCLA	2013
SonoSpecs, Co-Founder	2013-2014
BSC Certificate, UCLA Business of Science Center	2012-2014
BSC Venture Competition Finalist, UCLA BSC	2014
Ideation Lab 1st Prize, UCLA Technical Entrepreneurs Community	2013

OUTREACH

Chancellor's OIP-ISR Oversight Committee, UCLA	2014-2015
Graduate Student Instructor, UCLA High School NanoScience Program	2013-2014
Graduate Student Instructor, UCLA NanoScience Lab Summer Institute	2013-2015
Engineering Liaison, UCLA Veteran's Resource Office	2013-2014

UCLA OIP-ISR Conference Volunteer, OIP's 3rd Annual UCLA Medical Device Partnering Conference, UCLA Advanced Materials Partnering Conference, 2nd Annual UCLA Medical Device Partnering Conference, and UCLA Cleantech & Advanced Materials Industry Partnering Conference 2013-2015

Venice Family Clinic, UCLA BSC Social Entrepreneurship Initiative 2014

THE DISSERTATION

1 MOTIVATION

Cardiovascular disease remains the number 1 global cause of death, affecting over 85 million Americans, resulting in over 17.3 million global deaths each year, and carrying an estimated economic burden of over $320 billion annually [1]. Ischemic heart disease is the largest cause of death in the western world, congenital heart defects are the leading cause of death in the first year of life [2], and cardiotoxicity is a leading cause for drugs to be withdrawn from the market [3]. There are many approaches to attacking these problems, but one revolves around cardiac tissue engineering. Cardiac tissue engineering has demonstrated the potential for heart repair as well as the ability to better recapitulate native tissue for screening early stage drug candidates. But while innovations in tissue engineering garner optimism for the future of treating cardiovascular disease, many challenges persist.

The process for developing new drugs is expensive and lengthy. A recent study by DiMasi et al. [4] at the Tufts Center for the Study of Drug Development estimates the cost of getting a single new drug to market at nearly $2.6 billion. This study also highlights that the average time for clinical drug approval takes over 15 years, after an additional synthesis and candidate approval phase of over 10 years. To make matters worse, this study, updated from a similar 2003 study by the same authors [5] indicates that the growth rate in costs is roughly 8.5% on an annualized basis. Although new drugs still manage to find their way to market, the increasing

costs of R&D required to develop these new therapeutics seem unsustainable. This trend, if unchanged, will likely result in fewer new drugs getting to market and higher costs to the consumer and to the health care system as a whole.

Failure can occur at many points along the drug development pathway, which is to be expected. The later drugs fail in the development pipeline, the greater the costs: for example, a drug that fails in Phase III clinical trials is much more expensive than a drug candidate that fails in vitro toxicology tests. The availability of better predictive assays early in the development process could reduce the number of costly failures down the road. According to a 2014 market research report by BCC Research, "the key parameters for improving [cell-based assays for the] early phase of the drug discovery process depend on predictability, automation, miniaturization, cost-effectiveness, high speed and multiplexing" [6]. To continue to provide new therapeutics economically, a dramatic change to the drug development process needs to occur. Sophisticated lab-on-a-chip platforms offer advantages for improving cell and tissue-based assays that can potentially bring down the costs of drug development by addressing these key parameters for early phase testing.

Microelectromechanical systems (MEMS) offer the potential to address several challenges in tissue engineering while providing automated, high-throughput capabilities [7]. Automated 3D tissue culture platforms that incorporate non-invasive assay capabilities have the potential to advance basic research in cardiomyogenesis and support non-invasive cardiotoxicity assays. Digital microfluidics (DμF) has been steadily growing as a platform for both academic research and as a commercial platform (Figure 1). Although it shows promise for

applications that include stem cell culture, it has not been optimized for this purpose, nor developed for the specific application of cardiac tissue engineering.

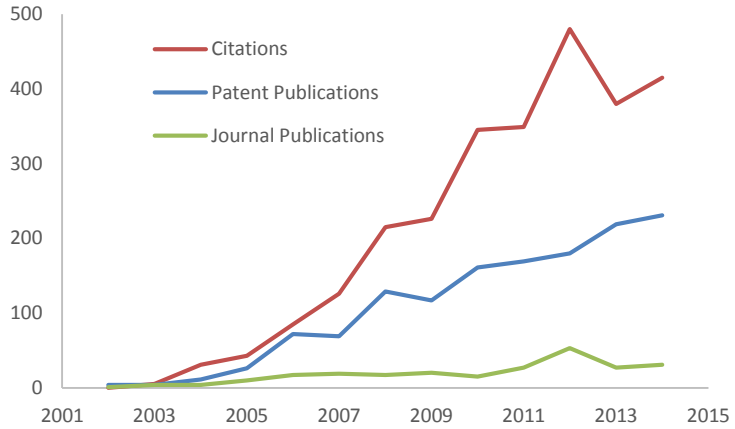

Figure 1. Number of hits by year for a Web of Science and PatSnap search for ["Digital Microfluidics" OR "EWOD"] shows the steady growth in journal publications, citations, and patent publications.

An in vitro DμF culture platform would not be limited to cardiomyogenesis. It would enable the culture of a broad range of 3D tissue samples, including the delivery of external chemical and/or electrical stimulation, and the ability to perform non-invasive assays of phenotypic behavior. This could be particularly significant as a tool to support in vitro drug screening.

2 THEORY OF DIGITAL MICROFLUIDICS

2.1 BACKGROUND IN MICROFLUIDICS

Microfluidics is a rather broad term that encompasses all systems that manipulate liquids in the microliter (or lower volume) regime. The development of microfluidic devices was driven by the desire to create miniature "lab-on-a-chip" systems [8]. These systems aim to reduce the size of standard laboratory procedures to improve processing power and throughput while reducing reagent consumption [9, 10].

Many microfluidic devices are designed to flow continuous liquid volumes through microchannels (Figure 2a). These channel-based microfluidic systems have found myriad applications and work well for miniaturizing assays, increasing throughput, and reducing costs [10, 11]. One of the notable drawbacks of these early systems was the requirement that samples be transported in continuous liquid flows, so it was difficult to create or manipulate discrete samples on-chip. This limitation led to the development of a subset of microfluidics called droplet microfluidics. In one permutation of droplet microfluidics, a large number of distinct droplets are formed and encapsulated within the continuous flow of a surrounding liquid medium (Figure 2b). This technique has led to many interesting opportunities and applications for high-throughput sampling [11].

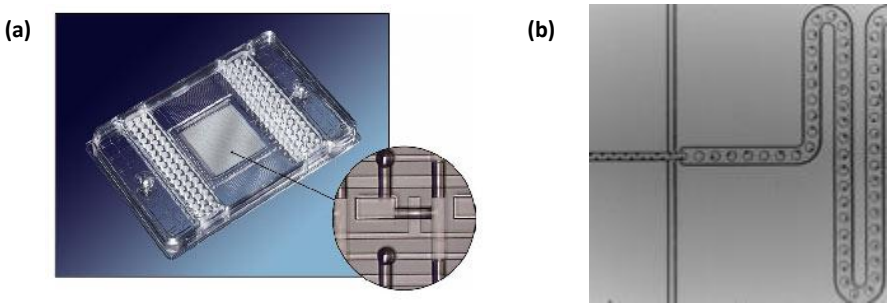

Figure 2. Channel microfluidic devices. (a) Commercial channel-based microfluidic system developed by Fluidigm Inc. [12] and (b) a channel-based droplet microfluidic design from Prof. Dino Di Carlo's lab at UCLA [13].

DμF systems operate on an entirely different platform, in which discrete liquid droplets (tens of pL to several hundred μL in volume) are deposited on a surface or sandwiched between parallel plates and are actuated by applying electric fields (Figure 3). For such small liquid volumes, the surface-to-volume ratio is relatively large and capillary forces dominate [14]. Through the application of these electric fields, electrowetting and dielectrophoretic forces [15] act to perform such actions as the dispensing, splitting, merging, and translation of liquid droplets [9, 16]. While DμF systems confer advantages similar to other microfluidic platforms, such as low reagent consumption and fast reaction times, there are several interesting and unique advantages. For example, because these systems do not employ continuous flow regimes, they do not require external pumps or valves [17]. This reduces the overall system complexity and eliminates the need for external mechanical systems to drive these pumps. Channel-based systems must also be designed and fabricated with the channels in one particular configuration. Therefore the desired liquid manipulations cannot be changed once the device has

been built because these pre-configured, “hardwired” paths cannot be changed [14]. In contrast, DμF systems are fabricated using an array of individually addressable electrodes. This allows reconfigurable procedures and the ability to alter flow paths in real-time [14]. The manipulations that can be accomplished are defined by the electrode size and shape [17]. For example, interdigitated electrodes have been used for dielectrophoretic particle sorting [18], and refined microelectromechanical (MEMS) processing techniques have allowed liquid volumes to reach the subnanoliter regime [19].

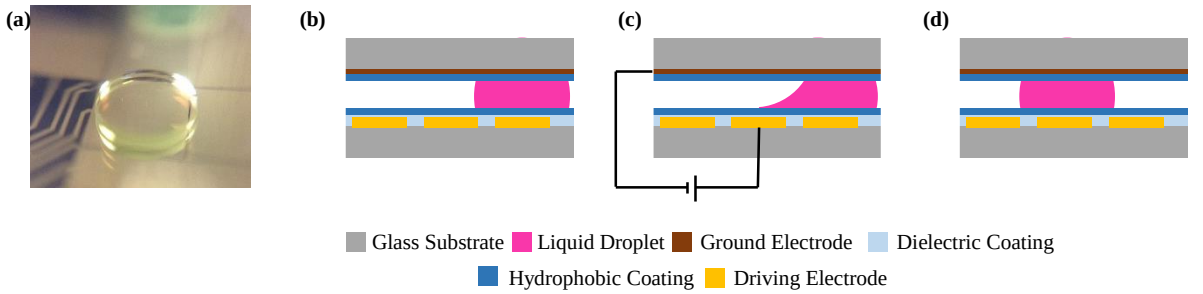

Figure 3. Image and schematic of two-plate DμF system. (a) Oblique image of a 1-μL droplet sandwiched between a gold driving electrode and a transparent top plate. (b) Side schematic of a droplet in a standard DμF configuration with layers indicated by color. (c) By applying a voltage across an adjacent electrode, electrowetting and dielectrophoretic forces drive droplet translation and (d) position the droplet over the actuated electrode.

2.2 ELECTROWETTING THEORY

Electrocapillarity was discovered by Gabriel Lippmann in 1875, when he found that the capillary depression between mercury and an electrolytic solution could be changed by applying a voltage between the two [20]. Dahms subsequently performed electrocapillarity measurements with an insulator separating the solid conductor and the conductive liquid media in 1969 [21]. In 1990, Colgate and Matsumoto performed investigations of micropumping by electrically controlling interfacial tension and proposed microdevices for electrowetting and electrowetting-on-dielectric [22]. In 1993, Berge built on this work by incorporating an insulating layer between a water droplet and an actuating electrode to prevent electrolysis while inducing a voltage-derived change in the contact angle of a sessile drop [23]. This work led to the introduction of the term electrowetting-on-dielectric (EWOD) to describe these systems and enabled the use of much larger voltages to actuate droplet movement. Over the 25 years since its discovery, much work has since gone into modeling and characterizing EWOD-based droplet movement.

The surface wettability of a DμF device is an important parameter. A liquid droplet that comes in contact with a solid surface will wet the surface to varying degrees, depending on the material properties of the liquid, the solid, and the ambient medium. The droplet quickly reaches an equilibrium contact angle (θ) described by the Young equation (Equation 1).

$$\gamma_{SG} = \gamma_{SL} + \gamma_{LG} cos\theta \qquad \text{Equation 1}$$

Here, γ is the surface tension between the solid (S), liquid (L), or gas (G) phases. Qualitative descriptions of wetting behavior usually follow the convention that a material is hydrophobic, or non-wetting, when the contact angle is greater than 90° (Figure 4a), and hydrophilic, or wetting, when the contact angle is below 90° (Figure 4b). For DμF manipulation of droplets, hydrophobic surfaces are preferable due to a smaller contact angle hysteresis effect [14]. Indeed, experiments have shown that a larger static contact angle leads to a decrease in the actuation voltage required to initiate droplet movement, and a larger contact angle change is correlated with facile translation [24].

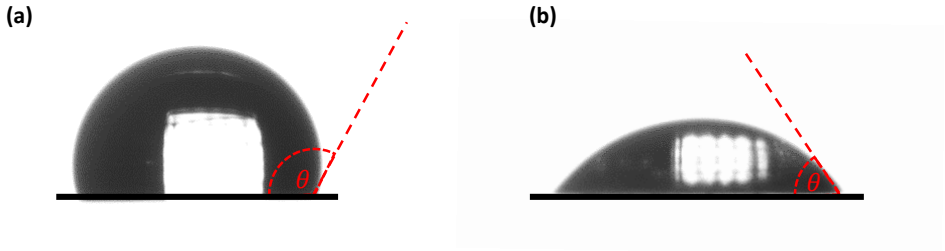

Figure 4. Sessile water droplets will adopt a contact angle, θ, when placed on surface according to the interplay between surface tensions of the solid, the fluid, and the surrounding medium. (a) The surface of Cytop® is hydrophobic and renders a water droplet with $\theta > 90°$. (b) Coating the Cytop® with collagen makes the surface hydrophilic and renders a water droplet with $\theta < 90°$.

Berge's work on EWOD configurations led to the development of the Young-Lippmann equation (Equation 2), a central equation for DμF systems [23].

$$cos\theta(V) = cos\theta_o + \frac{\varepsilon_o \varepsilon V^2}{2\gamma_{LV} d} \qquad \text{Equation 2}$$

The second term in Equation 2 is known as the electrowetting number ($\mathrm{E_W}$). This number represents the relationship between the capacitance of the dielectric layer relative to the interfacial energy at the liquid-vapor interface [14]. This term is fundamental for describing many DμF operations, such as modeling the conditions necessary for droplet splitting and dispensing [25]. This equation models droplet behavior in DμF systems quite well under low voltage conditions [26]. However, contact angle saturation occurs at high voltages; a phenomena whose mechanistic origins are still debated [27]. Contact angle saturation is a condition whereby droplet spreading by electrowetting reaches a maximum decrease in contact angle despite being subjected to an increase in voltage. While this energy minimization approach was derived from early experimental electrowetting observations, electromechanical modeling has helped refine our understanding of the forces involved in EWOD-based droplet manipulation.

2.3 Mechanism of Droplet Actuation

Several models have been developed to describe dynamic wetting and moving contact lines [14, 28, 29]. The methods used to derive these models with respect to electric field-induced actuation include energy minimization, electromechanical, hydrodynamic, molecular kinetic theory, and "hybrid" models

that combine components of multiple approaches [9, 29]. The forces that drive droplet translation include an electrostatic force, a surface tension force, and a pressure force [14]. The various models for droplet behavior and forces are consistent, but because they focus on different aspects of the phenomenon, they vary in their applicability to particular experimental conditions [9, 14]. For example, the equation used to describe the dielectrophoretic (DEP) wetting force in the electrohydrodynamic model can simplify to the equation used to describe the electrowetting (EW) wetting force as the electric field moves from AC to DC [16].

The electrostatic force has been modeled using the Maxwell stress tensor solved at incremental points along the liquid-fluid interface [16, 30, 31]. When a field is applied, a normal electrostatic force is created due to a net charge on the liquid-solid interface. This force is exerted downwards towards the electrode. Additionally, the fringe field near the liquid-fluid-solid boundary creates a net force parallel to the solid and causes the droplet to spread [14]. When only part of the droplet exists within the field, only the part of the droplet that is within the field will spread. This leaves the droplet in an asymmetric condition, with part of the droplet appearing to wet the surface to a greater extent. It is important to note that droplet spreading is not a requirement for droplet translation [9, 16, 32]. Rather, it is a consequence of the electrostatic pressure imposed during the application of an electric field; the droplet subjected to these electrostatic forces would move even if the droplet could not deform and undergo an apparent change in the contact angle [16]. This fact is exemplified by work of Chatterjee et al. [15, 24], who modeled electromechanical actuation of both conductive and insulating liquids. At high frequencies, the DEP forces can dominate over the EW force and drive droplet

translation with little to no change in the contact angle. Furthermore, it has been demonstrated that even during droplet spreading, the microscopic contact angle does not change at the length scale comparable to the dielectric layer thickness.

As mentioned previously, the surface tension force and the pressure force are two other methods for describing the conditions the drive droplet translation. The surface tension force can be used to describe the unbalanced condition of partial droplet spreading (Equation 3). This force that arises from an imbalance in the surface tension, γ, will drive the droplet towards the actuated end of the droplet.

$$F(V) = \gamma cos\theta_a(V) \qquad \text{Equation 3}$$

Similarly, the Laplace pressure can be considered when describing droplet translation due to asymmetric droplet spreading. This change to the radius of curvature creates a pressure differential across the droplet, described by the Young-Laplace equation (Equation 4), were r_1 and r_2 are the two principle radii of curvature.

$$\Delta P = \gamma_{LV}\left(\frac{1}{r_1} + \frac{1}{r_2}\right) \qquad \text{Equation 4}$$

The pressure force can therefore be described by Equation 5. During actuation, $\mathrm{P_r}$ is always larger than $\mathrm{P_a}$, causing a driving force towards the actuated side of the droplet. This equation highlights the increase in the driving force that results from an increase in the pressure differential, which derives from a change in

the contact angle. These different models should not be viewed as contradictory; taken together they provide a more complete understanding.

$$F(V) = (P_r - P_a(V)) \cdot h \qquad \text{Equation 5}$$

2.4 Lumped Circuit Model of Electric Field

An electrical circuit model can be used to describe an EWOD system, and has the advantages of simplicity and the ability to incorporate the dependence of the electromechanical force on the frequency of the applied AC electric field [32] A lumped circuit model of a DμF system will be described to model the electric field distribution across the liquid and its relevance to manipulating cell suspensions.

The voltage drop across a liquid suspension of cells on an EWOD configuration in an AC field depends on the signal frequency, the relative permittivity of the dielectric layer and liquid medium, and the thickness of the dielectric layer and the liquid medium [33]. The frequency-dependent ratio of V_L/V is expressed in Equation 6 [33].

$$\frac{V_L}{V} = Re\left(\frac{j2\pi f C_D R_L}{1 + j2\pi f (C_D + C_L) R_L}\right) \qquad \text{Equation 6}$$

Here, the DμF arrangement is modeled as an equivalent circuit of capacitors and resistors (Figure 5) [33]. V_L represents the voltage drop across the liquid, V represents the applied voltage, and, f represents the applied frequency.

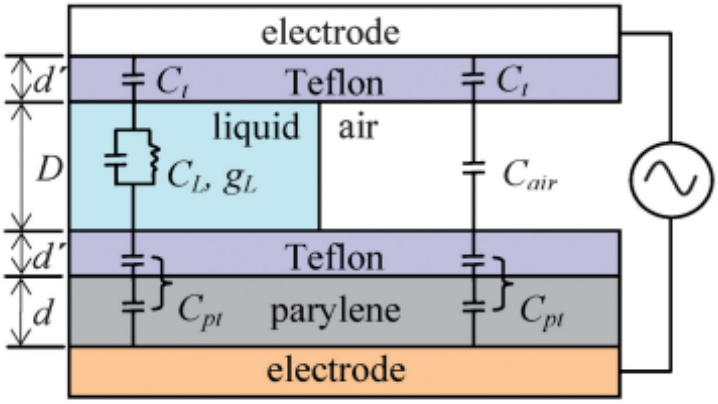

Figure 5. Lumped circuit model of an EWOD configuration (adapted from [15]).

The capacitance and resistance, as expressed in relative permittivity and capacitor geometry, are described in Equation 7 - Equation 9.

$$C_L = \varepsilon_L \varepsilon_o \frac{A}{d} \qquad \text{Equation 7}$$

$$C_D = \varepsilon_D \varepsilon_o \frac{A}{t} \qquad \text{Equation 8}$$

$$R_L = \frac{d}{\sigma_L A} \qquad \text{Equation 9}$$

Using Equation 7 - Equation 9 and simplifying for the real part of Equation 6 takes on the more useful form shown in Equation 10.

$$\frac{V_L}{V} = \frac{\left(\frac{4\pi^2 f^2 \varepsilon_o^2 \varepsilon_D \frac{d}{t}\left(\varepsilon_L + \varepsilon_D \frac{d}{t}\right)}{\sigma_L^2}\right)}{1 + \left(\frac{2\pi f \varepsilon_o \left(\varepsilon_L + \varepsilon_D \frac{d}{t}\right)}{\sigma_L}\right)^2}$$

Equation 10

Here, ε_o represents the permittivity of free space, ε_D represents the relative permittivity of the dielectric layer, ε_L represents the relative permittivity of the liquid layer, *d* represents the dielectric layer thickness, *t* represents the liquid thickness, and σ_L represents the conductivity of the liquid. Solving Equation 10 yields the voltage drop and electric field across the liquid. Plotted in Figure 6 is the voltage drop across the liquid as a function of frequency.

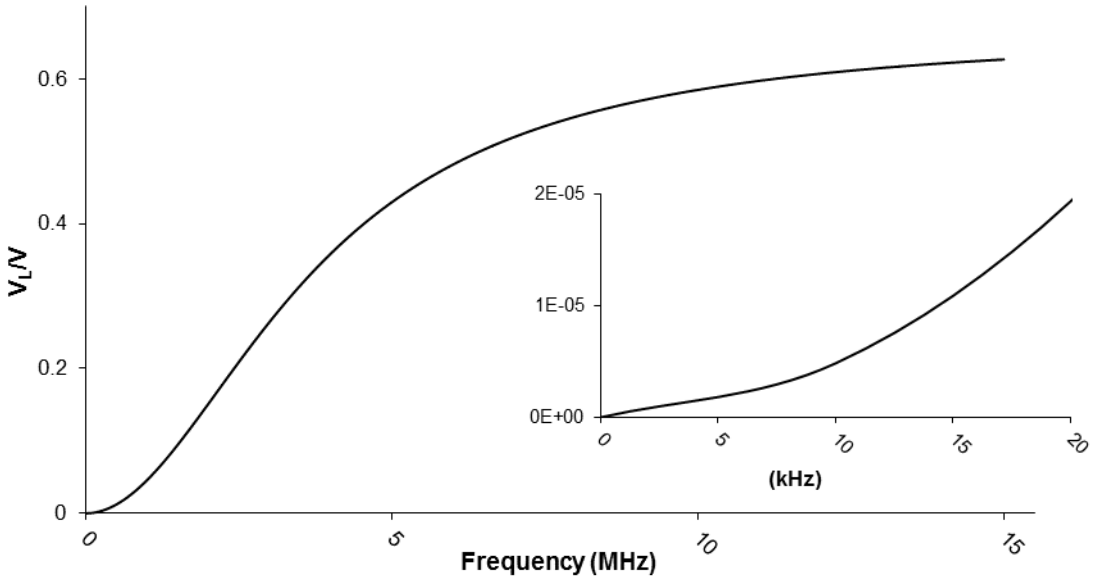

Figure 6. Voltage drop across the liquid as a function of frequency. Inset magnifies the low frequency domain typically associated with common DµF parameters.

2.5 DIELECTROPHORESIS (DEP)

2.5.1 DEP Droplet Actuation

DEP refers to "the force exerted on the induced dipole moment of an uncharged dielectric and/or conductive particle by a nonuniform electric field" [34]. The DEP force, along with the EW force, are associated with liquid droplet movement in AC fields [34-37]. The electrohydrodynamic force density, $f^{EHD}$is described by Equation 11.

$$f^{EHD} = \rho_e E - \sum_{i=1}^{m} \alpha_i \nabla \left(\frac{\partial W}{\partial \alpha_i}\right) \qquad \text{Equation 11}$$

The first term in Equation 11 is the Coulombic force density, while the second term is the DEP force density. The DEP force is due to polarization in the liquid droplet that arises from non-uniform fields that develop in both the liquid and the ambient fluid. DEP forces at the two-fluid interface, at the tri-phase contact line, and in the bulk of the fluids are all simultaneously present [16].

The intensification of the electric field within a droplet at higher frequencies was modeled by Lee et al. [38] in a sessile drop. The field lines show both the increase in electric field within the liquid as well as a decrease in the field intensification at the contact line. This description is useful as a qualitative understanding of the field distribution throughout the droplet as a function of frequency, because the composition of both the liquid droplet and the ambient fluid dictate this phenomena [15]. Understanding the field distribution in and around a

droplet is important for many reasons, such as understanding failure mechanisms like electrolysis or dielectric breakdown. It is also necessary to understand any potential field effects when manipulating biological cells, such as electroporation, particle sorting, or dielectrophoretic cell stretching.

2.5.2 DEP Particle Positioning

An applied AC electric field may produce a DEP force on a suspended dielectric particle, such as a biological cell, according to the well-established expression below (Equation 12).

$$\langle F_{DEP} \rangle = 2\pi r_m^3 \varepsilon_L Re\left(\underline{K}\right) \nabla E_L^2 \qquad \text{Equation 12}$$

However, another interesting reason to consider the DEP force is when investigating its effect on biological cells present in EWOD systems. According to Equation 12, the DEP force is dependent on the particle radius, r_m, the relative permittivity of the suspension medium, ε_L, the real part of the complex Clausius-Mossotti function, $\underline{K}$, and the electric field gradient, ∇E_L. The Clausius-Mossotti function relates the complex effective relative permittivity of the cell, ε_c', to the permittivity of the suspension medium, ε_L (Equation 13). The complex relative permittivity is a function of the absolute permittivity of free space, ε_o, and is a complex function of the medium conductivity, σ_m, and the field frequency, *f*, where $j = \sqrt{-1}$ (Equation 14).

$$\underline{K} = \frac{\underline{\varepsilon_c'} - \underline{\varepsilon_L}}{\underline{\varepsilon_c'} + 2\underline{\varepsilon_L}} \qquad \text{Equation 13}$$

$$\underline{\varepsilon_m} = \varepsilon_o \varepsilon_m - j\frac{\sigma_m}{2\pi f} \qquad \text{Equation 14}$$

The complex effective relative permittivity described in Equation 14 is then used in Equation 15 when calculating the Clausius-Mossotti function.

$$\underline{\varepsilon_c'} = \underline{\varepsilon_m}\left\{\frac{\left(\frac{r_m}{r_c}\right)^3 + 2\left(\frac{\underline{\varepsilon_c} - \underline{\varepsilon_m}}{\underline{\varepsilon_c} + 2\underline{\varepsilon_m}}\right)}{\left(\frac{r_m}{r_c}\right)^3 - \left(\frac{\underline{\varepsilon_c} - \underline{\varepsilon_m}}{\underline{\varepsilon_c} + 2\underline{\varepsilon_m}}\right)}\right\} \qquad \text{Equation 15}$$

The magnitude and sign of the DEP force is dependent on the electric field gradient, the field frequency, and the relationship between the cell and medium permittivities. In typical microfluidic configurations, the magnitude of the DEP force is on the scale of piconewtons to micronewtons [18, 39, 40]. Following the work done by MacQueen et al. [41], the following approximations were made for the local electric field (Equation 16) and electric field gradient (Equation 17) to estimate the imposed DEP forces (Figure 7).

$$\langle |E_{rms}(x)| \rangle = 0.7E_o \qquad \text{Equation 16}$$

$$\langle \frac{d}{dx} |E_{rms}(x)| \rangle = n \frac{E_o}{r_m} \qquad \text{Equation 17}$$

Here, n represents a geometry and material property dependent factor and approximately equal to ~1.5 [41], and, r_m represents the membrane radius.

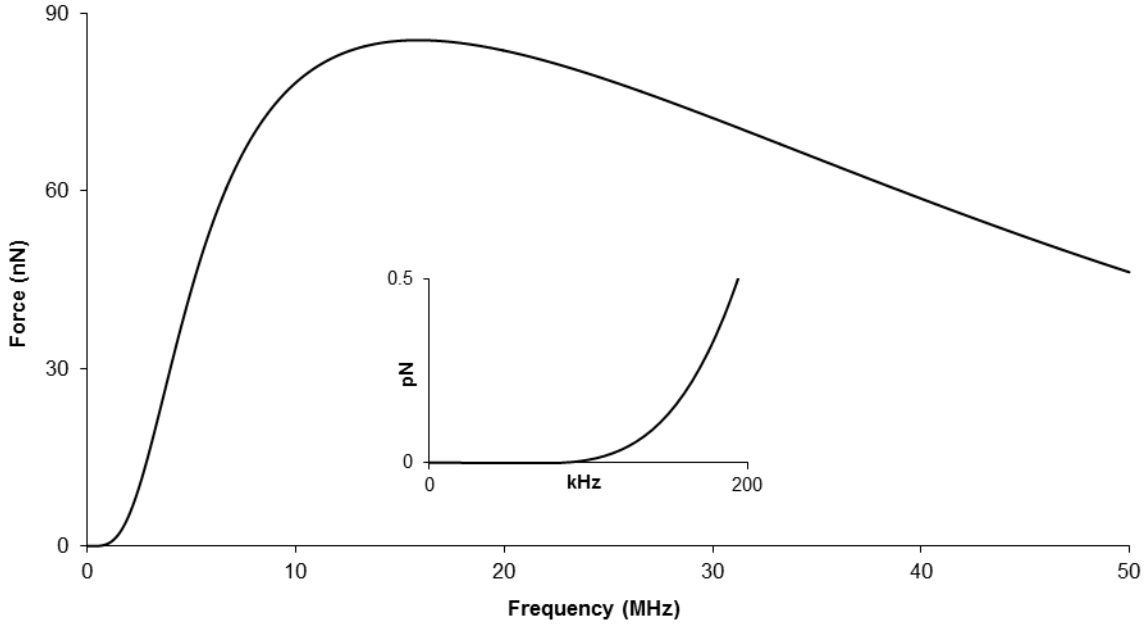

Figure 7. DEP force as a function of signal frequency at 100 V and a 100-μm gap height. In-set magnifies the low frequency domain.

The electric field gradient within a microfluidic environment has been modeled analytically, experimentally, and through finite element analysis, and shows field gradients strongest near the electrode edges (Figure 8) [39, 40, 42-47].

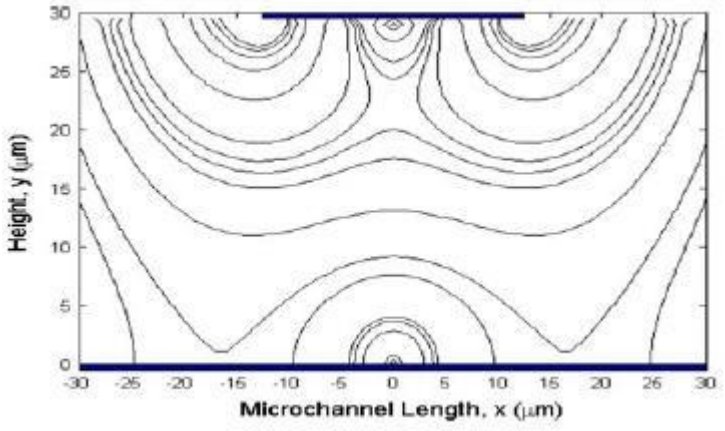

Figure 8. Analytical solution to the magnitude of the electric field around an electrode exemplifies the gradients where DEP forces are the strongest (reprinted from [42]).

Electrode size and spacing become an important design parameter when considering DEP, as the magnitude of the DEP force increases as electrode size and spacing are decreased (Figure 9) [34, 47]. These studies mirror the scaling proportion of DEP force to the characteristic length of the electrodes, L, as $F_{DEP} \propto V^2/L^3$ [34, 45].

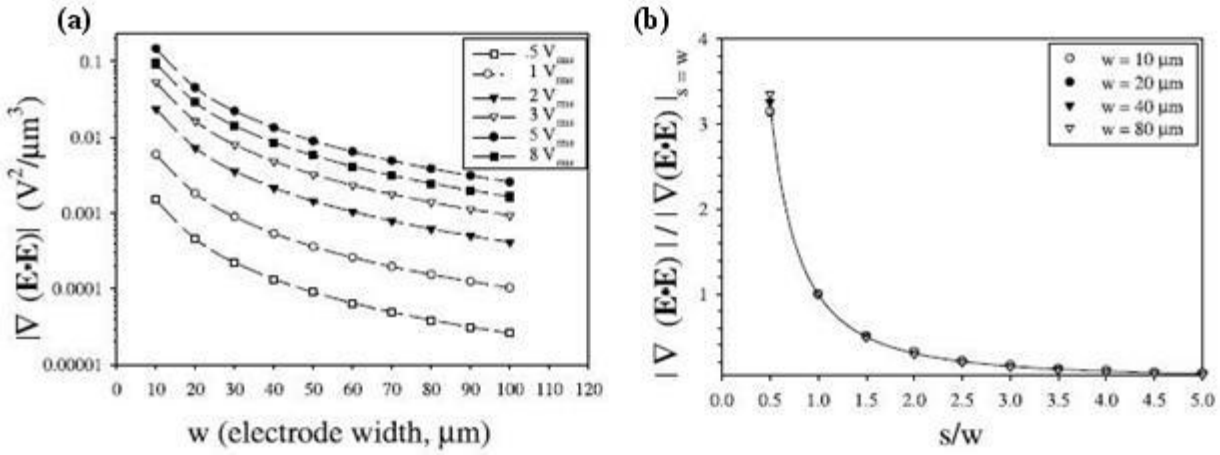

Figure 9. Electric field gradient vs. DµF device dimensions. Analytical solutions by Clague et al. [47] that demonstrate (a) the exponential increase in the magnitude of the electric field gradient upon decreasing electrode width and (b) inter-electrode spacing.

DEP has been used extensively for cell sorting [18, 33, 40, 44, 48-50]. However, another interesting application of DEP cell translation is for positioning cells for specialized tissue culture applications. The positioning of cells can be useful for co-culture systems, migration assays, or when creating complex tissue engineering structures. The following experiment demonstrates the ability to control particle distribution within a hydrogel based on electrode design (Figure 10). Here, the application of a 20 kHz AC field provided a negative DEP force strong enough to move 3 µm non-functionalized silica beads (Bang's Laboratories, Product #SS05N) away from the electrode edges and concentrate within the middle of the electrode. If the field was removed, the particles slowly disbursed (Figure 10a). Instead, a 1-µL droplet of 100 mM calcium chloride was positioned near one side of the 1-µL droplet containing silica beads, while a 1-µL droplet of 2 wt% alginic acid solution

was positioned on the opposite side. A 20 kHz AC field was applied to the suspension containing the silica beads to concentrate the particles using DEP. While the beads were concentrated, the calcium chloride and alginic acid droplets were actuated simultaneously towards the droplet containing the silica beads and mixed. The ensuing ionic reaction between the Ca^{2+} ions and the alginic acid created a crosslinked hydrogel that encapsulated the particles in situ (Figure 10b). The silica beads did not disburse over time.

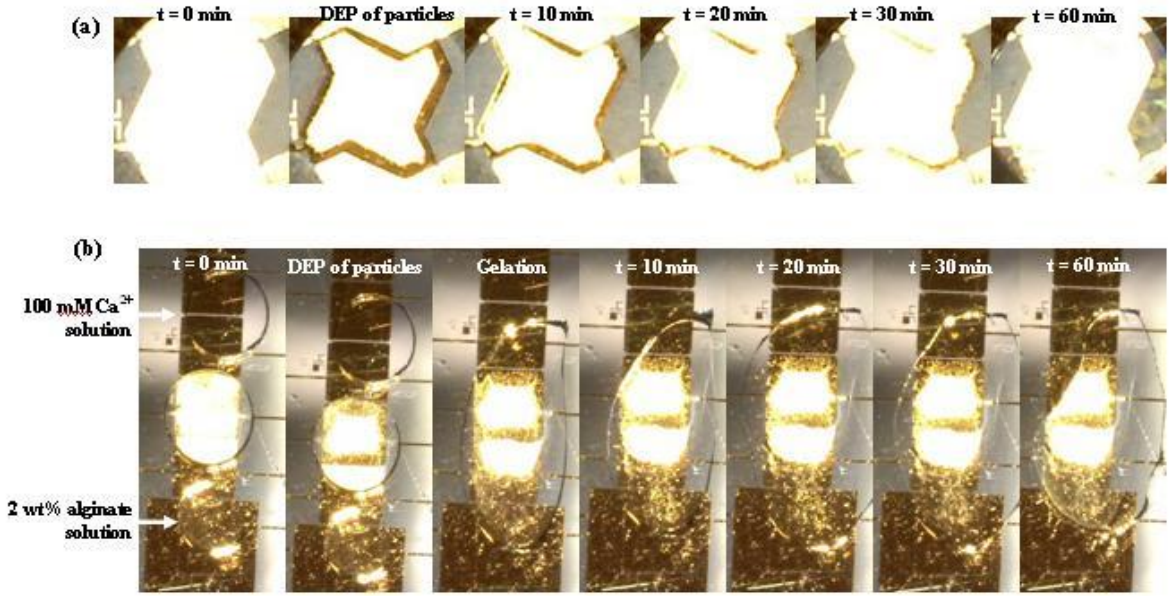

Figure 10. Time-lapse images of silica bead encapsulation after DEP manipulation. (a) DEP forces move silica beads (bright cloud over electrode) inward towards the center of an electrode away from the edges where the electric field gradient is strongest. (b) The calcium and alginate solutions are then merged to form a hydrogel and encapsulate the silica beads. The silica beads do not disperse over time.

Researchers from Taiwan recently performed similar experiments on a DμF platform [51, 52]. By positioning cells using DEP prior to gelation using poly(ethylene glycol) diacrylate and gelatin methacrylate, they were able to encapsulate cells positioned according to the electrode design. As other researchers have shown [53], the ability to position cells prior to gelation could have interesting applications in on-chip tissue design for developing more complex systems.

The ability to manipulate particles using DEP forces can be described by the cutoff frequency, f_c, and is characterized by the medium conductivity, σ_L, the dielectric layer thickness, t, the gap height, d, and the dielectric permittivities of the medium, ε_L, and the cell, ε_D (Equation 18) [18]. The cutoff frequency is a convenient approximation for the minimum frequency required to move cells using DEP forces [18].

$$f_c = \frac{\sigma_L}{2\pi\varepsilon_o(\varepsilon_L + \varepsilon_D \frac{d}{t})} \qquad \text{Equation 18}$$

Using appropriate estimates for medium and cell permittivities, the cutoff frequency becomes approximately 3.7 MHz and is beyond the operating limits of our equipment.

A barrier to this approach is that the DEP force depends on the conductivity and permittivity of the medium. The low conductivity solutions that provide the proper environment for DEP manipulation can usually keep cells viable only for short experimentation times before the cells must be returned to a more traditional media solution containing high ion concentrations and higher conductivities. Studies

have demonstrated the ability to significantly lower the medium conductivity to lower the cutoff frequency required for DEP-induced cell manipulation while preserving cell viability [54], but the need to frequently dilute the culture media can be cumbersome. Nevertheless, improvements to this technique are continually developed and this unique ability provided by DμF offers interesting opportunities for complex tissue engineering tasks.

3 TISSUE CULTURE & ASSAY DEVELOPMENT

3.1 2D VS. 3D TISSUE CULTURE

Advanced culture platforms are needed for drug development assays and tissue engineering [2]. The discrepancy between in vitro studies, animal models, and human in vivo physiological responses means significant difficulties persist in predicting medical outcomes [2]. Drug screening platforms that better recapitulate the native environment predict in vivo cellular responses with greater accuracy [55]. In vitro culture platforms are typically performed in either a 2D, 3D, or suspension-based environment; each has distinct advantages and disadvantages.

Two-dimensional culture platforms have been used for over a century and are still widely used for both fundamental cell research and in commercial drug testing, as they are relatively inexpensive and often easy to develop. The cells are grown in adherent monolayers that are submerged in growth medium. Most mammalian cells will adopt a spread-out morphology as they adhere to the surface of Petri dishes through the production of focal adhesion kinase [56], and they expand to a fully confluent monolayer. Monolayer culture systems, however, fail to resemble native tissue behavior in many important ways [55, 57]. For example, the cells lack the cell-cell and/or cell-ECM junctions that are present in 3D tissue and that ultimately determine cell function (Figure 11). Cells in 2D monolayers also present an unnatural level of homogeneity with unnatural chemical and oxygen diffusion gradients that fail to mimic in vivo conditions [58]. Two-dimensional

platforms continue to provide useful data on a variety of cell behaviors, but these limitations constrain the analysis of their output.

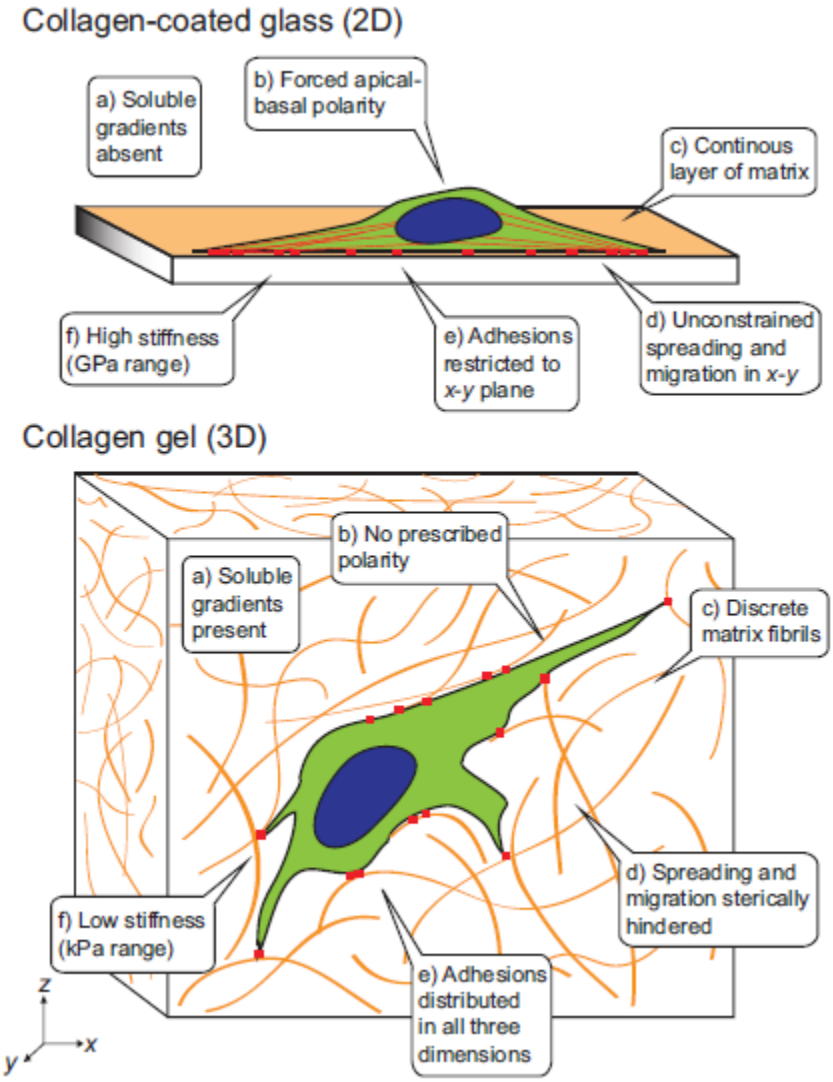

Figure 11. Cartoon showing differences in adhesive, topographical, mechanical, and soluble cues that exist between 2D and 3D cell culture environments (reprinted from [58]).

In contrast, 3D culture systems, including cell encapsulated hydrogels and 3D tissue structures formed in a hanging drop suspensions or via non-adherent conditions (Appendix A), provide a more realistic representation of in vivo conditions compared to 2D culture systems. In 3D, cells develop more natural states with respect to cell-cell adhesions, cell-ECM adhesions, and cell-lumen conditions. These interactions affect gene expression and protein production, so assays in which they are enabled should provide more realistic responses to cell-cell and drug interactions [59]. A disadvantage of 3D culture systems, however, includes the sample-to-sample tissue variability that can develop as tissue growth ensues. For example, cardiomyogenesis performed in 3D tissue structures can result in samples that have differentiated into pacemaker-like, ventricular-like, or atrial-like cardiomyocytes in varying amounts [60, 61]. While the heterogeneity in tissue structure of these systems can be more realistic to in vivo conditions, this can often make data collection and analysis more difficult. Recently, parallel 3D tissue culture platforms have been developed by commercial entities in an attempt to scale these assay models and provide high throughput screening capabilities. Hμrel Corporation has been working on a multiplexed, organ-on-a-chip product designed to test multiple tissue samples at once. Altavex is developing a 3D culture platform for drug testing on tissue models, and Organovo is publicly traded company that has recently been working on 3D printed tissue for drug testing. These technologies are still nascent, and refining these systems will take time and effort.

In suspension-based culture systems cells are grown in non-adherent conditions. In these environments, cells respond by creating cell-cell adhesions

through cadherins, tight junctions, and desmosomes. These conditions also can recapitulate cell-cell and cell-lumen phenotypic responses found in vivo, and are often developed through processes such as mixing bioreactors and hanging drop cultures. These systems have been used as models to study phenomena such as tumorogenesis and organogenesis.

3.2 THE STEM CELL CULTURE NICHE

Stem cells are biological cells that retain properties of self-renewal and the ability to change their structure and function into a different cell line [62]. Embryonic stem cells and induced pluripotent stem cells are pluripotent, and thus retain the ability to differentiate into all three germ lines including the endoderm, ectoderm, and the mesoderm [63]. Once a stem cell has chosen a germ line, it still retains multipotency. A multipotent hematopoietic stem cell, for example, can differentiate into several lines of progenitor cells with more limited differentiation and self-renewal capabilities until reaching terminally differentiated mature hematopoietic cells [64]. Bioengineers have sought to exploit this phenomenon to recreate distinct tissue constructs for drug screening, organ repair, disease modeling, and organ growth [63]. A significant amount of progress has been made in the field of tissue engineering, but different tissue structures and organs present their own unique challenges.

The heart, although once thought to be incapable of self-renewal [65], has been shown to harbor several different stem cell lines [66]. Researchers are attempting to induce cardiac cell line differentiation from several types of stem

cells. Pluripotent stem cells have been differentiated into cardiomyocytes using embryoid bodies, a co-culture with mouse endoderm-like cells, and with specific growth factors in either suspensions or in monolayers (Figure 12) [67].

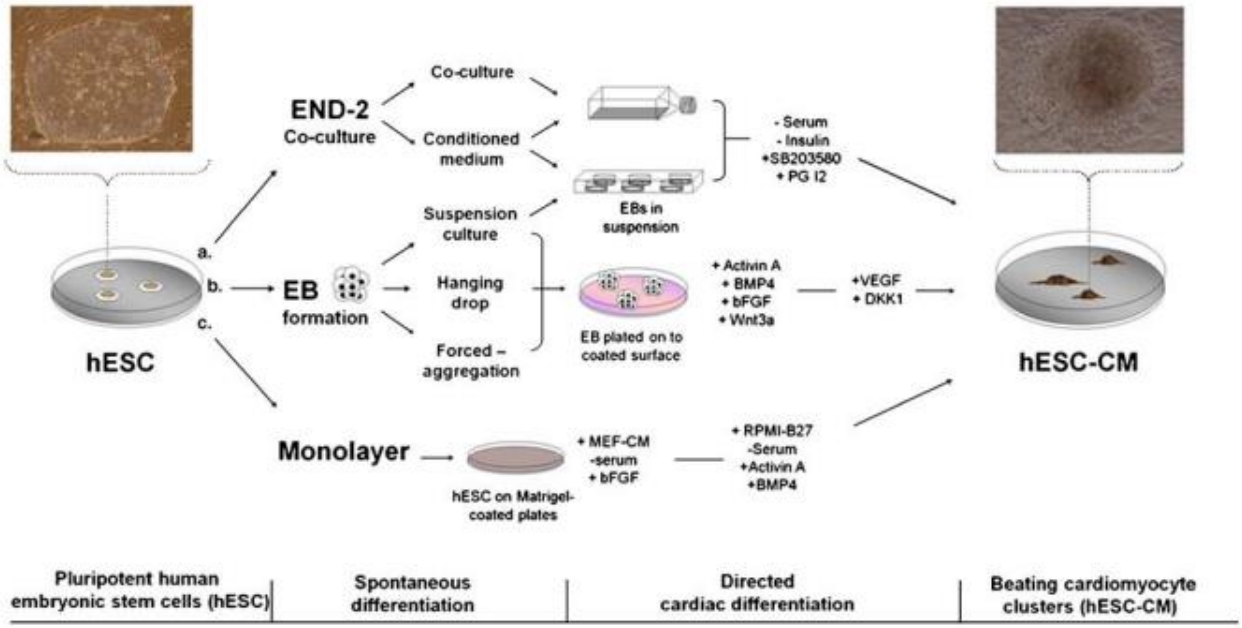

Figure 12. Different methods used for generating cardiomyocytes from pluripotent stem cells (reprinted from [68]).

While early clinical trials aimed at repairing infarcted myocardium show promising results for stem cell based therapies [69], there is still considerable debate over the extent and role that resident stem cells play in cardiac tissue renewal [70]. The small number of resident cardiac progenitor cells presents difficulties for studying cardiomyogenesis and developing new therapies, and therefore renders cardiomyocytes derived from pluripotent stem cells as a potentially efficient source [71]. Research suggests that resident stem cells in the

heart maintain multipotency [65, 72] and have embryonic origins [73]. Because embryonic stem cells are pluripotent they retain the ability to differentiate into all three germ layers – including the heart-derived mesoderm germ layer (Figure 13) [74]. Continued investigations into embryonic stem cell-derived cardiomyocytes will advance our understanding of cardiomyogenesis, better understand the heart's regenerative capacity, develop stem cell based therapies, and progress the field of cardiac tissue engineering [75, 76].

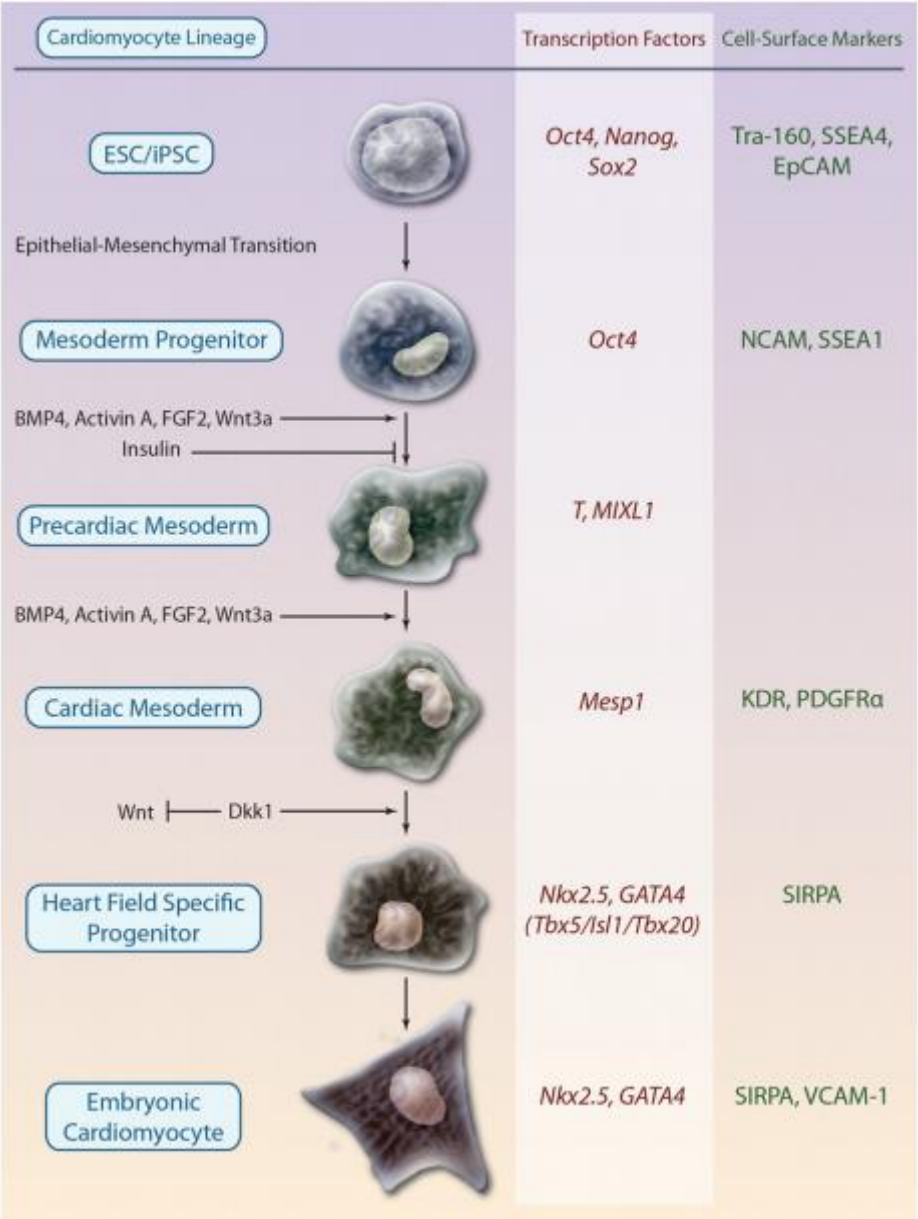

Figure 13. Model of differentiation from pluripotent stem cells through progenitors towards a cardiomyocyte lineage (reprinted from [77]).

Many different stimuli have been shown to effect differentiation and guide fate specification into varying cell lines. These include external stimuli such as chemical and biochemical growth factors [77], mechanical forces, optical signals, and

electromagnetism [62]. For example, the mechanical forces present in the surrounding environment can greatly affect differentiation and other cell behaviors such as adhesion, migration, and cell-cell communication [78]. Many different extracellular matrices of varying stiffness and porosity have been shown to show impact cell behavior [79]. Stretching the substrate during culture and imparting time-varying mechanical forces can also change fate specification [80]. The extracellular matrix composition will affect behavior in significant ways, owing in large part to the surface chemistry and interactions with cell surface proteins [81]. The chemical composition and porosity characteristics affect diffusion rates of soluble chemokines and other proteins, thus altering paracrine signaling [81, 82]. A host of experiments have demonstrated that effects of applied electric fields; the strength, duration of application, frequency of application, and frequency can all impact differentiation and phenotypic behaviors [83].

3.3 HYDROGEL SCAFFOLDING

The extracellular matrix (ECM) plays a vital role in regulating structure and cell behavior within human tissue [84]. The ECM is a complex cellular environment that provides structural support and regulates many cell functions such as organization into tissue, growth, and cell-cell communication [85, 86]. For tissue engineering purposes, it is desired to mimic the native tissue and ECM to replicate native tissue functions in vitro [85-87]. Therefore, the design of an artificial scaffold should support cell growth and maintenance, provide appropriate mechanical, chemical, and biological characteristics of the ECM, allow transport of nutrients and waste,

and provide a means for signal transduction [85-87]. Biomimetic hydrogels have shown great promise in regards to tissue engineering scaffolds because their tunable properties can provide desirable mechanical strength, variable pore size, and the immobilization of cells, drugs, and growth factors [85-88]. However, difficulties in spatiotemporal control over cell seeding and signaling are still a factor [76, 85-87, 89]. An advantage of using hydrogels as tissue engineering scaffolds and drug delivery vehicles is the ability to use the pore structure to control the rate of solute diffusion; this is achieved by controlling the gelation process [85-88, 90]. Gradient hydrogels provide the ability to control chemical delivery through variable diffusion rates [86]. Variable diffusion rates exist extensively in-vivo [85, 86, 89]; closely replicating this feature may be important to mimic the natural environment and replicate normal cell behavior, e.g., for regenerative medicine applications.

To produce acceptable cell scaffolds, tissue engineers have experimented with both natural and synthetic hydrogels. Common synthetic materials used for cardiac tissue engineering include poly(ethylene glycol) (PEG), polylactide (PLA), polylactide-glycolic acid (PLGA), polycaprolactone (PCL), polyacrylamide (PAAm), and polyurethane (PU).[91] Some common natural hydrogels used consist of natural ECM components, such as collagen, fibrin, matrigel, and other decellularized matrices [91]. Because of gelation processes that make collagen and calcium-alginate easily compatible with DμF operation, these materials will be discussed further.

3.3.1 Collagen Scaffolding

Collagen is a broad term used to describe proteins with a characteristic triple helix composed of three polypeptide chains (Figure 14) [92]. Collagen is ubiquitous among mammals and is the primary component of the extracellular matrix [93]. Collagen provides most of the mechanical strength of tissues. It also provides a networked system that regulates tissue growth, cell-cell communication, biochemical diffusion, and mechanotransduction. Because of its excellent biocompatibility, type I collagen has been used extensively in tissue engineering [91]. Collagen is often used as a matrix for observing cell migration and adhesion characteristics [79, 94, 95], and as a scaffold for growing complex 3D tissue structures [85, 87, 91].

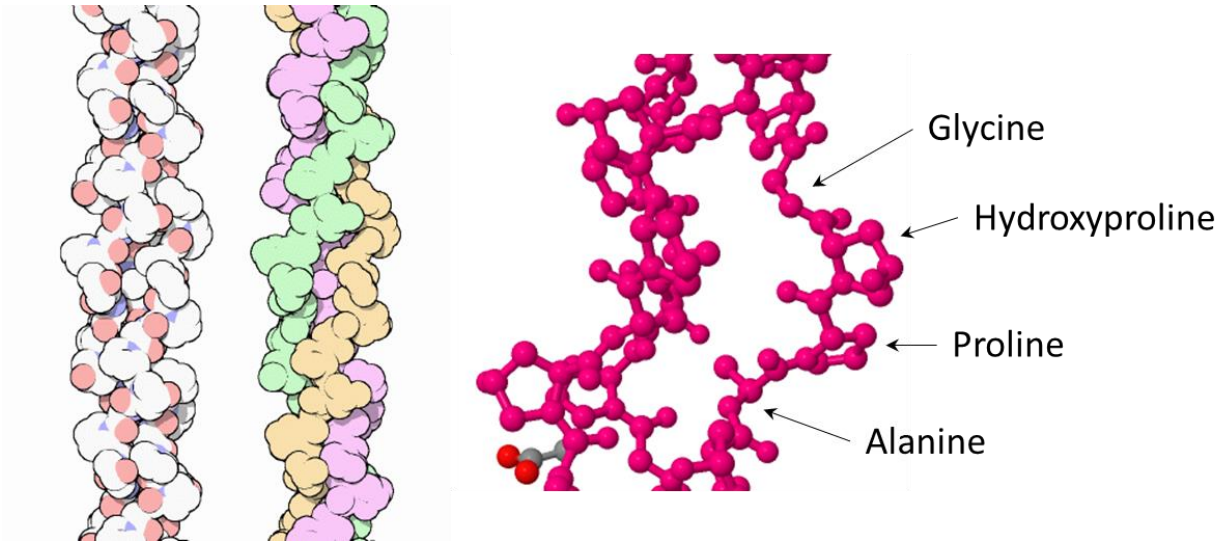

Figure 14. Triple helix structure of collagen (reprinted from [96]) and ball-and-stick model showing amino acid constituents.

Collagen is typically prepared by dissolving the protein in an acidic solution, neutralizing the pH, and storing it at low temperatures [91]. Many characteristics of a collagen matrix can be tailored quite easily by modifying the protein concentration. Higher concentrations lead to stiffer matrices with a higher crosslink density and a smaller pore size [97, 98]. The gelation time is an important consideration when using collagen. Depending on the type of collagen, gelation can occur relatively slowly. This could have implications when, for example, one is trying to create a homogenous, cell-seeded scaffold. Cells in this type of collagen solution might sink to the bottom before gelation has time to solidify them in place. Alternatively, one might find that fast-gelling collagen solutions gel too quickly to encapsulate cells in certain circumstances. Because collagen is so versatile, biocompatible, and has good cell adhesion properties (Figure 15a-b), it is very useful and widely used as a biomaterial for tissue engineering.

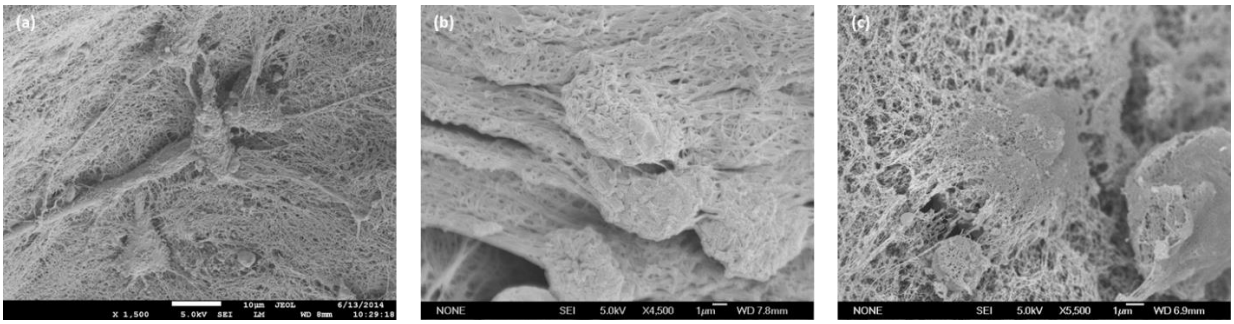

Figure 15. SEM images of difference cells encapsulated in different hydrogel matrices demonstrate that cell adhesion depends on both the cell type and the hydrogel properties. (a) Fibroblastic and (b) epithelial-like cell morphologies both show good adhesion to collagen matrices. (c) However, even fibroblast-like cells tend to adhere very little to calcium alginate hydrogels, and instead become entrapped within them without spreading or interacting with the hydrogel. The scale bar for (a) is 10 μm. The scale bar for (b) and (c) is 1 μm.

3.3.2 Calcium Alginate Hydrogel Scaffolding

Alginate-based hydrogels have been used extensively in tissue engineering as scaffolds for cell encapsulation because they are inexpensive and easy to fabricate with highly tunable properties [99-101]. Alginate is an acidic linear polysaccharide consisting of α-L-guluronic acid (G) and β-D-mannuronic acid (M) [99, 102]. These residues are arranged as either G-block or M-block block copolymers, or as a mixed sequence of MG-blocks [102]. Divalent cations, such as Ca^{2+}, join guluronic acid residues of adjacent chains to form an "egg-box" gel structure (Figure 16) [99].

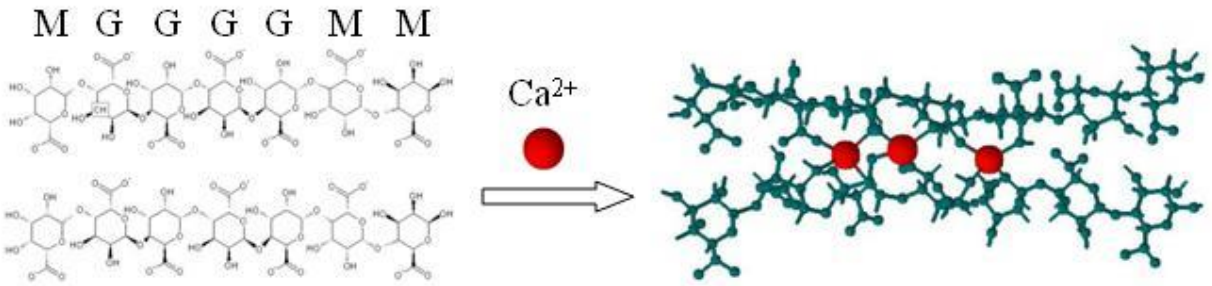

Figure 16. "Egg-box" gelation mechanism of alginate through the addition of divalent cations such as Ca^{2+}.

Alginate hydrogels are biocompatible [99, 103], and their sponge-like structure of large, interconnecting pores promotes cell growth and rearrangement [103]. This quality allows stem cells to aggregate and form spheroidal embryoid bodies that characterize a more sophisticated culture system [104, 105]. Alginate gels also provide a convenient method for encapsulating cells within a 3D environment, which has been shown to evoke a more natural tissue and cellular response to stimuli compared to similar 2D culture systems [85, 87]. The elastic modulus of calcium-alginate gels can vary depending on the nature of cross-linking but has been found to be similar to that of native cardiac tissue [78, 99, 106].

The diffusive properties in alginate hydrogels are tunable [101, 107]. The hydrogels have been shown to deliver growth factors to cells with a diffusion-regulated delayed response [82, 88]. These delayed responses resemble the natural ECM environment closely and promote realistic tissue responses [88]. Changes in diffusion coefficients are prevalent within the body and exist on the micrometer scale [82, 88]. Consequently, the ability to produce hydrogels with a variable diffusion coefficient is desirable [76, 82, 86, 88]. The diffusion of a solute

through a heterogenous hydrogel such as calcium alginate has been modeled to closely fit experimental data based on an equation derived from obstruction theory by Amsden [90, 108] in Equation 19.

$$\frac{D_g}{D_o} = exp\left[-\pi\left(\frac{r_s + r_f}{\bar{r} + r_f}\right)^2\right] \qquad \text{Equation 19}$$

Here, D_g represents the diffusion coefficient in the gel, D_o represents the diffusion coefficient in a liquid at infinite dilution, r_s represents the Stokes-Einstein hydrodynamic radius of the solute described in Equation 20, r_f represents the radius of polymer fiber bundles, and $\bar{r}$ represents the average radius of the openings between the polymer fiber bundles.

$$r_s = \frac{k_B T}{6\pi\eta D_o} \qquad \text{Equation 20}$$

The diffusion coefficient is determined by several factors, one of which is the average radius of the openings between polymer fiber bundles, $\bar{r}$. This is proportional to the polymer mesh size, and is inversely proportional to the crosslink density [101, 107, 109].

The ability to use hydrogels to dictate the rate of diffusion or create chemical concentration gradients is a useful tool for cell-based assays. Hydrogel based tissue models have become recent addition to the DμF platform, so a visual representation of diffusion-controlled chemical delivery was performed on a DμF device to observe this phenomena. A Live/Dead fluorescent staining solution was delivered to a stem

cell-laden calcium alginate hydrogel on a DμF device (Figure 17). The gradient in fluorescence intensity highlights the variation and delayed cell response achievable using on-chip mixing and hydrogel encapsulation.

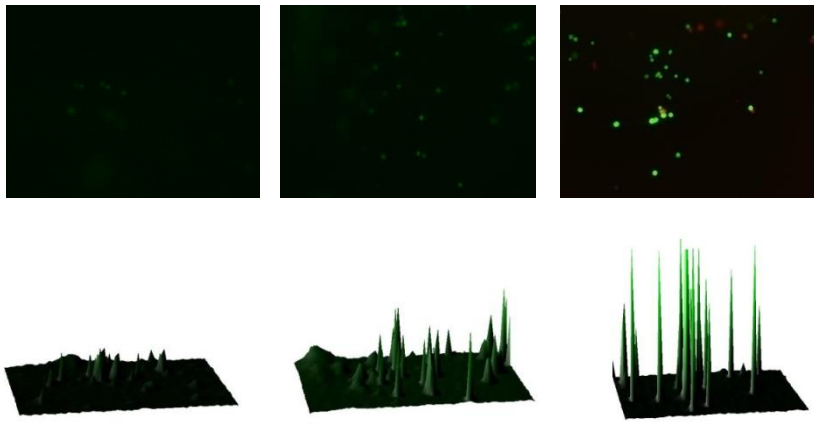

Figure 17. Live/Dead staining of mouse MSC in a calcium alginate hydrogel. The top row of images shows fluorescence imaging of live (green) and dead (red) cells inside the calcium alginate hydrogel, while the bottom row shows a qualitative fluorescence intensity map created using ImageJ image analysis software. The far left image shows cells at ~2 mm from the staining solution mixing site, the middle image shows cells ~1 mm from the staining solution mixing site, and the far right image shows cells at site of mixing.

Although calcium alginate hydrogels are biocompatible, mammalian cells do not adhere to them (Figure 15c) [110, 111]. It can be favorable to exploit the lack of cell-scaffold interactions to elucidate differentiation cues, because stem cells remain in a pluripotent state when cultured in alginate scaffolds [104]. The porous alginate structure also allows embryoid body formation that realistically models

cardiomyogenesis. However, calcium alginate hydrogels can be used to study cell-ECM interactions by conjugating arginylglycylaspartic acid (RGD) containing peptides [110-112]. RGD peptide conjugation has been successfully carried out using standard carbodiimide chemistry, where the carboxylic acid groups are first activated through an aqueous coupled reaction with 1-ethyl-3-(3-dimethylaminopropyl) carbodiimide hydrochloride (EDC) and sulfo-*N*-hydroxysuccinimide (sulfo-NHS) at a pH of around 6.0. The RGD sequence of L-arginine, glycine, and L-aspartic acid has been shown to promote biomacromolecule and cellular adhesion [111], and has been used to characterize the effect of cell seeding density on cell phenotype [110] and encapsulate stem cells for a different approach to cardiac tissue differentiation [112].

3.3.3 Mechanical Properties of Hydrogel Scaffolds

The behavior of cells in matrices is determined in part by the stiffness of the substrate to which they adhere. This has been shown for 2D solid polymer and hydrogel substrates, as well as for 3D scaffolds of varying types [113, 114]. The elastic modulus, also known as the Young's modulus, is a measure of the stiffness of a material. Atomic force microscopy (AFM) is one tool that can be used to probe the mechanical properties of soft polymeric and biological materials with very high spatial precision [115, 116]. It can be performed on hydrated hydrogel structures by immersing the probe tip in a fluid environment. The AFM cantilever probe tip is brought into contact with the material's surface; instead of rastering the surface as is typical in AFM imaging, the force is ramped to press the probe into the sample before relieving the force and pulling the probe away from the surface (Figure 18).

The probe deflection is then correlated to the material stiffness through the elastic modulus of the probe. The Hertz and the Sneddon models can be used to characterize the contact between the AFM cantilever tip and the sample [117].

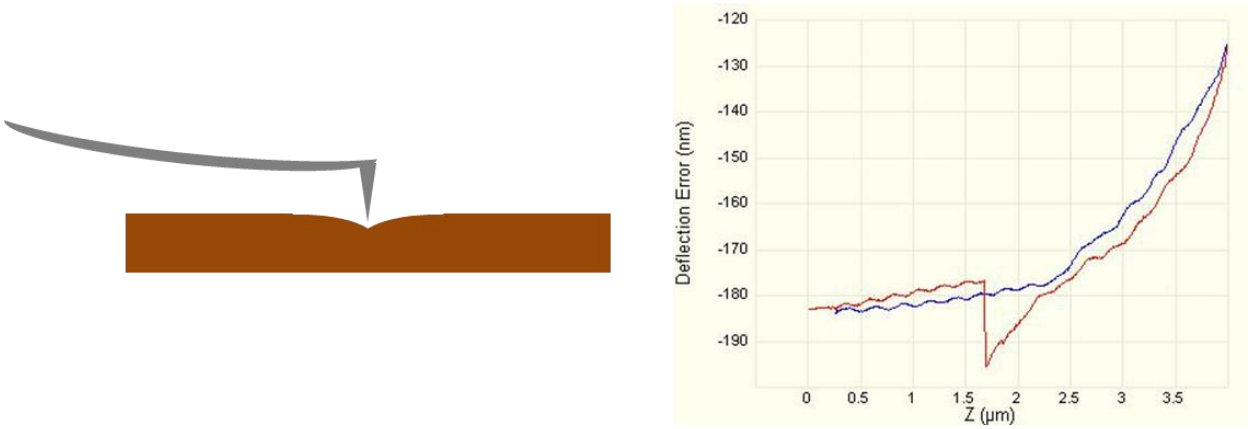

Figure 18. Schematic and deflection curve of AFM being used to measure the Young's modulus of hydrogel. (a) A schematic showing an AFM probe pressed into a sample's surface to measure its Young's modulus. (b) The tip height is monitored as a function of the Z height while the probe is engaged (blue) and retracted (red) in order to measure the degree of probe tip deflection.

Scanning electron microscopy (SEM) is a powerful tool for visualizing nano- to microscale features. An SEM operates by directing a beam of electrons at a sample, and measuring their interactions with the surface in either the secondary ion emission mode or backscattered emission mode. It is essential that the material be comprised of or coated with a conductive material.

Special considerations are required to image hydrogels by SEM. The SEM chamber is operated under vacuum. When a hydrated material such as a hydrogel

is placed directly in the chamber, the water is pulled out and cohesive forces between the strands of the gel cause the structure to collapse. An SEM image of such a collapsed hydrogel structure would be an inaccurate representation of the hydrated gel structure. To maintain the expanded, hydrated structured during and after the drying process, a supercritical drying process can be used [118, 119]. This process takes the sample through an elevated pressure and temperature cycle in a series of aqueous solvent solutions. The final solvent – pure methanol is commonly used – can be removed from the sample without causing the gel structure to collapse from capillary forces. The sponge-like gel can then be sputter coated with a thin metal layer prior to SEM imaging.

3.4 CARDIOMYOGENESIS

Embryonic stem cells begin to spontaneously beat in vitro as they differentiate into cardiomyocytes [68]. This propensity to beat is a fundamental characteristic of the heart and has provided a way for researchers to investigate mechanisms regarding cardiac tissue development. The ability to observe in vitro cardiomyocyte contraction has also improved drug screening models for cardiotoxicity and various arrhythmias [120]. Cardiomyocyte differentiation can be characterized by several different methods. Researchers have assessed cell morphology, proliferation, gene expression, metabolism, sensitivity to damage, inotropic and chronotropic receptors, spontaneous beating rate, synchronous beating propensity, action potentials, ion flux, and structural sarcoplasmic reticulum proteins [61, 121-123]. Label-free detection has shown great promise in assay sensitivity because labeling

can lead to unanticipated and undesirable outcomes [124]. Label-free assaying techniques can eliminate the need for tags, dyes, specialized reagents, and engineered cell lines that can obscure data and deliver false results. While both label and label-free techniques have been used to assay cardiomyocytes, monitoring beating behavior has become a powerful label-free technique for non-invasive characterization.

3.4.1 Electrophysiology

The spontaneous beating of cardiomyocytes is a fundamental and characteristic function of the heart. During the developmental stages, immature cardiomyocytes resemble the pacemaker cells of the postnatal heart [125]. Pacemaker cells are self-excitable cells that rhythmically produce an electrophysiological signal, which triggers cardiomyocyte contraction and electrical signal propagation. This property of pacemaker cells, known as automaticity, means they do not require an external signal to initiate the onset of an action potential (Figure 19a) unlike other cardiomyocytes in the heart [126]. Common ways in which researchers differentiate cardiomyocyte cell lines are through the identification of cell surface receptors, gene profiles, and action potential characteristics.

The action potential of cardiomyocytes is typically defined by a series of repeating depolarization and repolarization processes controlled by voltage-gated ion channels that drive electrical current and stimulate cardiomyocyte contraction. The automaticity of pacemaker cells is due to the slow, leaky “funny” current associated with spontaneous inward flux of sodium ions [126]. As this slow

depolarization process increases the inherently negative transmembrane potential, T-type calcium ion channels are opened and the slow influx of calcium ions continues the depolarization process. At the transmembrane threshold voltage of -40 mV, L-type calcium ion channels are opened and the depolarization crosses 0 mV and overshoots to a positive transmembrane voltage. This triggers the delayed rectifier potassium ion channels to open for a brief plateau phase before repolarizing the transmembrane voltage as calcium ion channels close and the resting potential of the cell returns [127]. This process is similar to atrial and ventricular-like cardiomyocytes, but with a few notable differences worth mentioning. The non-pacemaker cells of the heart do not contain the leaky ion current characteristic of pacemaker cells, and therefore only produce an action potential after they are excited by an external stimulus. This stimulus is provided by the change in ion flux generated by the pacemaker cells and is propagated throughout the heart tissue via gap junctions. As the ion flux generated from spontaneously beating pacemaker cells propagates to the atrial and then ventricular-like cardiomyocytes, the transmembrane potential reaches a threshold that opens fast calcium ion channels to generate a rapid depolarization [127]. Differences lie in the type of number of voltage-gated ion channels that dictate transmembrane threshold voltages and ion flux kinetics, and thus produce varying action potentials with phases of different lengths (Figure 19b).

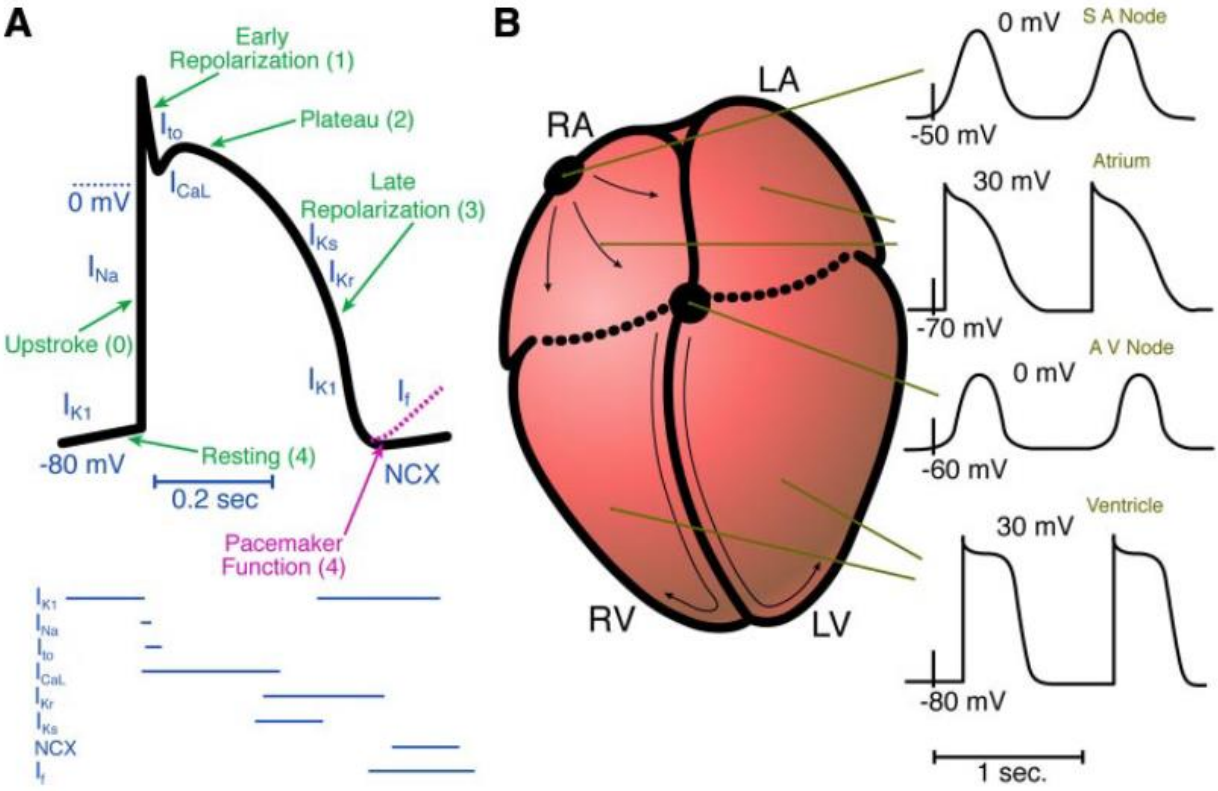

Figure 19. Representations of cardiomyocyte action potentials show the change in voltage over time and varies among different cell types. (a) A description of the 4 phases of an action potential and the corresponding ion flux below. (b) A representation of different action potentials associated with different types of cardiomyocytes located throughout the heart (reprinted from [128]).

Assessing the action potential is used for diagnosing and studying the physiology of the heart and developing new therapeutics [126, 127]. One particularly relevant area is the study of different types of arrhythmias, how they develop, and how they can be treated [129].

The patch-clamp method is a popular technique for measuring cardiomyocyte activity. The patch-clamp method can be performed in a variety of ways, but

typically involves a pipette-like device that comes in contact with the surface of the cell (Figure 20a) [130]. The ion-flux can be measured and action potentials can be acquired using this method. The drawbacks to the patch-clamp method consist of its invasive, transmembrane sampling method and the ability to monitor only one cell at a time. Many other current and voltage measuring devices have been developed in research labs that probe point sources for electrical changes or use microelectrode arrays (Figure 20b) [131]. These systems can also provide very accurate measurements and spatial distribution of electrical activity. However, they also need either invasive electrical probes or non-native adherent monolayers.

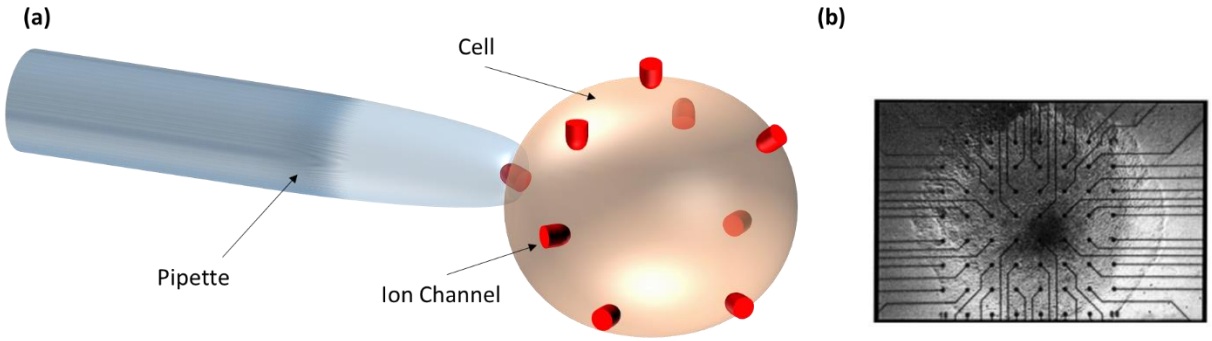

Figure 20. Representations of the patch-clamp method and an image of a microelectrode array used for measuring cardiomyocyte electrophysiology. (a) Schematic of traditional patch-clamp method that measures electrical current by monitoring the ion flux through an ion channel. (b) A cardiomyocyte cluster grown from mouse embryonic stem cells adhered to an array of microelectrodes for measuring electrical activity (reprinted from [132]).

Impedance measurements have recently been used to measure cardiomyocyte contractility, e.g., by using the xCELLigence RTCA Cardio System created by ACEA Biosciences and Roche Applied Science [120]. This system is operated by seeding cells onto an "E-Plate Cardio 96," which is a uniquely designed 96-well plate integrated with gold microelectrodes on the bottom of each well. A low voltage high-frequency AC field is applied and the impedance is measured to noninvasively quantify cardiomyocyte contractility in real-time. Impedance sensing offers the ability to probe beat rate, beat amplitude, and shape of the action potential. These features can help diagnose many types of arrhythmias and investigate cardiotoxicity.

Modulating the frequency of an externally applied AC field is another tool that can assist therapeutic discovery by altering the spontaneous beating behavior. For example, an AC frequency below ~100 Hz can initiate field-evoked activity (FEA) such as entrainment and the ability to control pacing rate. Using an AC frequency of around 1 kHz can induce conduction block, which can then be used to investigate therapeutic approaches to various defibrillation disorders [133, 134]. Much higher frequencies offer the ability to sense beating characteristics without imposing any significant side effects on cell behavior, and offer an approach for effectively assaying drug responses.

A significant disadvantage to commercially available impedance sensing systems is their inability to concurrently act as an automated stem cell niche culture platform. They require culturing and transfer of EBs to the impedance sensing system where further downstream processing takes place. Another disadvantage to these systems is the need to culture 2D monolayers. By using 2D

patterned electrodes, the field is primarily monitored through the change of impedance that occurs via attached cells. Monolayers lose complex 3D tissue properties such as cell morphologies and ion gradients that exist in 3D models, and may therefore exhibit less realistic screening platforms.

3.4.2 Contractile Forces

The contraction of cardiac muscle cells results from converting a chemical signal (associated with the flux of ions during an action potential) into mechanical energy via the work of contractile proteins [135]. This process is initiated after the inward flux of calcium ions causes depolarization of the cell membrane. The inward flux of calcium ions occurs at L-type receptors located on membrane invaginations (Figure 21). These invaginations bring the incoming calcium ions into proximity with ryanodine receptors on the sarcoplasmic reticulum, causing a conformational change that releases an abundance of calcium ions that act on the tropomyosin complex to cause contraction. Briefly, the process begins as calcium binds to troponin C. This causes a conformational change in tropomyosin to expose an active site between actin and myosin. The strength of the cardiomyocyte contraction is proportional to the number of crossbridges that form between myosin heads and the now-active sites along the actin filament. The myosin head pulls itself along the actin filament during what is known as the power stroke. This process will continue, shortening the muscle fibers, as long as there is enough calcium to support the process. Finally, as the action potential repolarizes and calcium ion channels are closed, the process comes to halt when calcium dissociates from troponin C and

tropomyosin's conformational change once again prohibits the myosin actin interaction [135, 136].

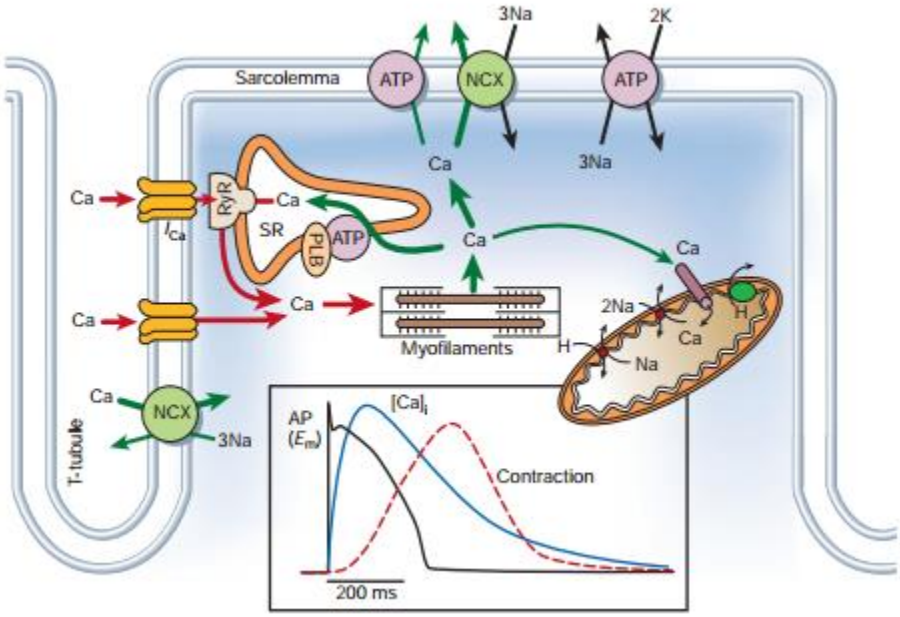

Figure 21. Cartoon of cardiomyocyte membrane proteins involved in contractility. Cardiomyocyte contractility is activated and regulated by the flux of calcium through voltage-gated ion channels located in T-tubules and its interaction with the sarcoplasmic reticulum (reprinted from [135]).

Measuring cardiomyocyte contractility has become an important method for studying cardiomyocyte differentiation and maturation and developing therapeutics [80, 137]. A widely used method for assessing cardiomyocyte tissue involves image analysis. This approach often involves sophisticated algorithms coupled with high sampling rates to extract information such as beating rate, the percentage of cells that are beating, and other spatially relevant information (Figure 22a) [138]. Video data are most useful for 2D monolayers. Occluded internal regions of 3D tissue

structures are difficult to image as the sample thickness increases, and the difficulty of imaging multiple focal planes simultaneously limits the availability of real-time data analysis.

The cardiomyocyte contractile force can also be used for understanding tissue maturation and drug screening. For example, measuring the contractile force with respect to stimulation via inotropic therapeutic agents can investigate drug targets for congestive heart failure. MEMS-based sensors for measuring cellular forces are often based on arrays of micro-posts (Figure 22c). Cells are first allowed to adhere to the tops of micro-post arrays, typically after coating the surfaces with ECM-derived proteins to promote attachment. When the cells contract, they cause the micro-posts to bend, and the contractile forces are calculated based on the amount of deflection. Zhao and Zhang adapted this design for measuring cardiomyocyte contraction forces [139]. It is often difficult to derive force measurements from micro-post array sensors, however, due to the complexity of the system surrounding the micro-post's geometry, viscoelastic properties, and surface characteristics [140]. Atomic force microscopy (AFM) is another tool that has been used to determine the contractility forces in single cardiomyocytes (Figure 22b) [141]. An AFM probe is gently brought into contact with a surface-attached cardiomyocyte, causing the probe to slightly deflect. As the cardiomyocyte beats, the change in probe deflection is measured and a beating force is determined using analytical models and the cantilever's elastic modulus. AFM requires complex equipment and is difficult to integrate into cell culture systems or downstream processing. Both micro-post arrays and AFM are best suited to single cell measurements, as opposed to measurements on 2D and 3D tissue models.

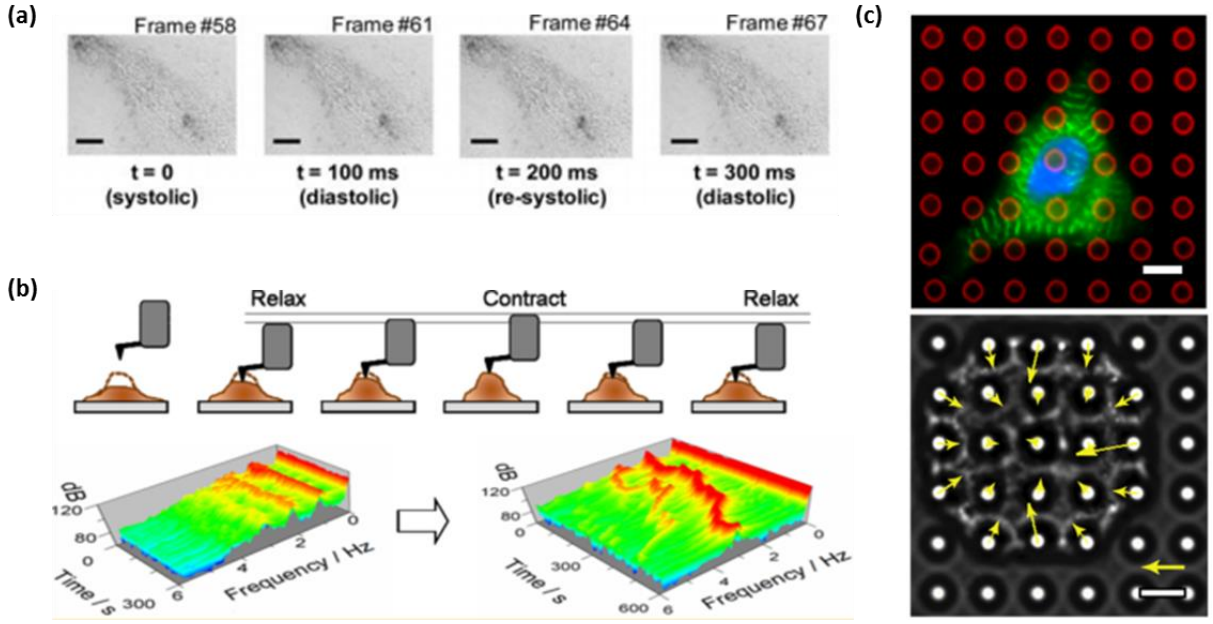

Figure 22. Images depicting different methods used to measure cardiomyocyte contractile forces. (a) Image analysis can analyze beating force and rhythmicity based on pixel movement (adapted from [138]). (b) AFM probe deflection can measure single cell contractility forces (adapted from [141]). (c) Micro-post arrays can measure single cell contractile forces by analyzing post deflection (adapted from [142]).

Tools that measure cardiomyocyte contraction are largely used to study cell behavior or develop therapeutics. Some tools, however, aim to take advantage of cardiomyocyte contractile forces to perform useful work. Two recent studies have used piezoelectric transducers for energy harvesting and power generation based on cardiomyocyte contractility [143, 144]. These systems are elegant in their simplicity. By allowing cardiomyocytes to attach to the surface of piezoelectric materials, these systems take advantage of their inherent capacity to turn

mechanical strain into a useful voltage. Piezoelectricity is a material property that refers to the phenomenological coupling of mechanical and electrical properties. When a stress is applied to a material, the crystal lattice is strained. This distortion in the atomic arrangement displaces the charges associated with ions in the lattice. In piezoelectric materials, this distortion creates a net polarization (Equation 21) [145, 146].

$$P_i = d_{ij}\sigma_i \qquad \text{Equation 21}$$

$$S_i = d_{ij}E_i \qquad \text{Equation 22}$$

Another reason to investigate the use of piezoelectric sensors is the ability to take advantage of their pyroelectric properties. Pyroelectricity is the phenomenological coupling of thermal and electrical properties, and regularly accompanies piezoelectricity [146]. In pyroelectric materials, a temperature change will expand or contract the atomic crystal structure. In a similar manner as piezoelectricity, this distortion of the crystal structure repositions atomic charges and creates a net polarization according to Equation 23. One major benefit to using a piezoelectric and pyroelectric substrate for real-time sensing and actuation is its ability to multiplex these sensing capabilities with one material substrate.

$$p = \frac{dP}{dT} \qquad \text{Equation 23}$$

Piezoelectricity can therefore be used to measure cardiomyocyte contractile forces for studying cell behavior and screening therapeutic targets. In addition to the direct piezoelectric and direct pyroelectric effects described above, piezoelectric materials also behave according to the inverse piezoelectric effect. The inverse piezoelectric effect refers the generation of a mechanical strain in the material subjected to an electric field. Similarly, the inverse pyroelectric effect refers the generation of a mechanical strain in response to a temperature change. The inverse piezoelectric effect if often used as an actuator in applications where extremely fine movements are needed, such as the movement of an AFM probe. This ability to act as both a sensor and an actuator suggests that integrating piezoelectric and pyroelectric materials into DμF platforms may create new applications and simplify existing processes. A disadvantage of this method, however, is that cells must adhere to the surface of the piezoelectric material. This condition creates an unnatural cell state that may alter cellular behavior.

4 DIGITAL MICROFLUIDICS FOR SPHEROID-BASED INVASION ASSAYS

4.1 ABSTRACT

Cell invasion is a key process in tissue growth, wound healing, and tumor progression. Most invasion assays examine cells cultured in adherent monolayers, which fail to recapitulate the three-dimensional nuances of the tissue microenvironment. Multicellular cell spheroids have a three-dimensional morphology and mimic the intercellular interactions found in tissues in vivo, thus providing a more physiologically relevant model for studying the tissue microenvironment and processes such as cell invasion. Spheroid-based invasion assays often require tedious, manually intensive handling protocols, or the use of robotic liquid handling systems, which can be expensive to acquire, operate, and maintain. Here we describe a digital microfluidic (DμF) platform that enables formation of spheroids by the hanging drop method, encapsulation of the spheroids in collagen, and the exposure of spheroids to migration-modulating agents. Collagen sol-gel solutions up to 4 mg/mL, which form gels with elastic moduli up to~50 kPa, can be manipulated on the device. In situ spheroid migration assays show that cells from human fibroblast spheroids exhibit invasion into collagen gels, which can be either enhanced or inhibited by the delivery of exogenous migration modulating agents. Exposing fibroblast spheroids to spheroid secretions from colon cancer spheroids resulted in a >100% increase in fibroblast invasion into the collagen gel, consistent with the cancer-associated fibroblast phenotype. These data show that DμF can be used to automate the liquid handling protocols for spheroid-

based invasion assays and create a cell invasion model that more closely mimics the tissue microenvironment than traditional, two-dimensional techniques. Ultimately, a DμF platform that facilitates the creation and assaying of three-dimensional, in vitro tissue models could make automated 3D cell-based assays more accessible to life sciences researchers.

4.2 INTRODUCTION

The invasion of cells into their surrounding environment is an essential process in wound healing, tissue growth, and tumor metastasis [147, 148]. Cell migration and invasion is dictated by the complex communication and signaling pathways between cells and the extracellular matrix (ECM) of the tissue microenvironment. The nature and extent of this invasion are controlled by multiple parameters, including cell type, matrix type, matrix stiffness, and soluble extracellular signaling cues [148-150]. In vitro assays that can model the complex, three-dimensional cellular microenvironment can yield valuable insights into cellular migration and invasion, and facilitate the discovery and development of treatments and therapeutics for many types of injury and disease.

Most cell migration assays are currently performed using systems that rely on the motility of single or adherent cells. For example, in transwell assays, adherent cells migrate through pores in a membrane in response to a stimulus gradient [151, 152]. Another common migration assay known as a "scratch test" measures the degree to which adherent, monolayer cells migrate into a void created on a substrate by the physical removal of a region of cells, or by otherwise preventing

growth in the void region (Figure 23a) [147]. While these systems provide valuable insight into cell migration, they do not take into account the complex conditions found in three-dimensional tissues in vivo, such as cell signaling associated with intercellular interactions, the epithelial-mesenchymal transition, the cellular heterogeneity that exists within 3D aggregates, or migration mechanisms specific to a 3D microenvironment [147, 153-157].

Spheroid-based cell migration and invasion assays have been developed to provide more physiologically relevant models [147, 152, 158]. These assays typically use 3D cell spheroids encapsulated within a hydrogel matrix (Figure 23b). Cell invasion can be studied by introducing chemical or physical stimuli to modulate cell motility, which can be quantified in situ by microscopy. These assays typically require multiple manual pipetting steps [151], rendering them labor intensive, prone to variability and human error, and difficult to scale. Complex and laborious assay protocols are major factors limiting the adoption of more advanced invasion assays [151].

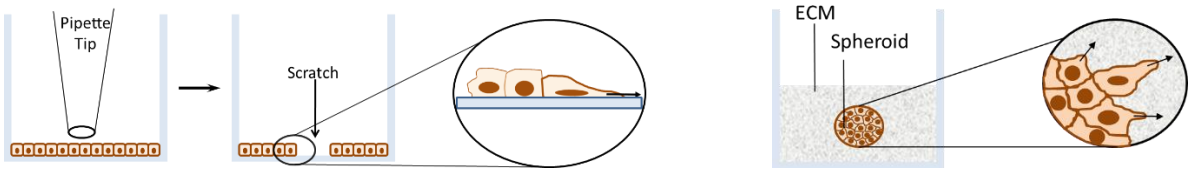

Figure 23. Schematic representations of common invasion assays, including the (a) scratch test and (b) spheroid-based invasion assay.

Here we describe a digital microfluidic (DμF) platform that is capable of automating all the liquid handling steps necessary for performing spheroid-based

invasion assays. Our previous work developed the capability to perform automated hanging drop cell spheroid culture on a DμF device [159]. In this work, we advance upon that technique by developing protocols for the encapsulation and maintenance of spheroids within a collagen hydrogel to study cell migration and invasion.

Digital microfluidics is a liquid handling technique that enables the manipulation (dispensing, translating, splitting, and mixing) of discrete pico- to microliter droplets of liquid on a planar array of electrodes through the controlled application of electric fields [9, 160, 161]. Because DμFs enables automation of complex assay workflows, DμF systems have been used for a variety of biological applications [162] such as on-chip cell culture [163], hydrogel formation [164-167], and cell spheroid culture and analysis [159, 168]. By automating liquid handling, DμF can reduce or eliminate the tedium associated with manual assay protocols. Additionally, DμF can provide lower sample volume requirements, reduced costs, and superior liquid handling flexibility compared to other automated techniques, such as robotic liquid handling [151].

To demonstrate the ability of DμF to enable spheroid-based invasion assays, we used DμF to encapsulate spheroids of human fibroblast cells in hanging-drops of collagen gel. As a key component of the human stroma, fibroblasts play a central role in wound healing and tumor progression and are commonly used to model cell migration and invasion. Through the delivery of migration modulating agents to individual spheroids, we show that gel-encapsulated spheroids can be interrogated and assayed in situ. To demonstrate a physiologically relevant invasion model, we show that DμF can be used to simulate paracrine signaling in the tumor microenvironment, providing a convenient method to model tumor-stromal

communication and the cancer-associated-fibroblast (CAFs) phenotype in vitro. Cancer-associated-fibroblasts are stromal fibroblasts that are 'activated' by chemical and mechanical signaling in the tumor milieu. These activated fibroblasts are crucial to establishing the structural and biochemical properties of the tumor microenvironment, and have been implicated in promoting tumor invasion and metastasis [169, 170]. Thus, an in vitro model for studying the properties and behaviors of CAFs would be a valuable tool in cancer research.

By automating sample handling and reducing the requirement for manual intervention, the DμF platform has the potential to lower the barriers to adoption for more advanced, spheroid-based migration assays. Ultimately, greater adoption of more physiologically relevant, three-dimensional cell-based assays can yield new insights into homeostasis and morphogenesis for both healthy and diseased tissues.

4.3 MATERIALS AND METHODS

4.3.1 Materials and Reagents

HT-29 human colorectal adenocarcinoma cells (ATCC® HTB-38™) and BJ human foreskin fibroblasts (ATCC® CRL-2522™) were purchased from ATCC. Leibovitz L-15 cell culture medium, Dulbecco's Modified Eagle Medium (DMEM), penicillin-streptomycin (P/S) solution (10,000 U/mL Pen., 10 mg/mL Strep.), L-glutamine, fetal bovine serum (FBS), and the LIVE/DEAD® Viability/Cytotoxicity Kit for mammalian cells were obtained from Life Technologies (Carlsbad, CA). Bovine collagen I solutions were purchased from Trevigen, Inc. (Gaithersburg, MD; Cat. #: 3442-005-01) and Corning Life Sciences (Tewksbury, MA; Prod. #: 354231).

Hoechst 33342 solution was purchased from Fisher Scientific (Pittsburgh, PA). Acti-stain 488 phalloidin was purchased from Cytoskeleton Inc. (Denver, CO). Human bone morphogenic protein 2 (BMP-2) and Pluronic® F-68 were purchased from Sigma (St. Louis, MO). Prostaglandin E2 (PGE2) was purchased from Santa Cruz Biotechnology, Inc. (Santa Cruz, CA). Cytop® (CTL-809M) and CT-SOLV 180 were purchased from Bellex International Corporation (Wilmington, DE).

4.3.2 Device Fabrication and Operation

The DμF devices used in this work consisted of two separate plates: a top plate that contained an array of driving electrodes, and a bottom plate that contained a continuous ground electrode and the through-holes necessary for spheroid formation. The devices were fabricated according to previously described protocols in the California NanoSystems Institute (CNSI) Integrated System Nanofabrication Cleanroom at UCLA.[159] Briefly, the top-plate substrates (75 x 50 x 1 mm water white glass slides - LabScientific, Inc., Cat# 7787) were sputter-coated with 110 nm of indium-tin-oxide (ITO) to provide a conductive surface. The ITO was then patterned with the array of driving electrodes using standard photolithography techniques. Through-holes were manually drilled into the footprints of the reservoir electrodes on the top-plates to provide a world-to-chip interface that allowed for the addition of liquid to the devices. The top-plates were subsequently coated with 4-6 μm of Parylene-C via vapor deposition and ~400 nm of Cytop via spin-coating.

The bottom plate of the DμF device consisted of a 1.7 mm thick soda lime glass slide with through-holes, or 'wells,' drilled into specific locations within the

plate. The bottom-plate was similarly coated with a layer of ITO and Cytop to produce a hydrophobic ground electrode. The Cytop was removed from the well walls by physical abrasion in order to expose the underlying glass, rendering the wells hydrophilic.

A schematic of the DμF device setup used in this work is shown in Figure 24. For device operation, the bottom plate was placed on an aluminum holding plate that contained a milled window below the wells to allow hanging drops to form. A glass slide was placed underneath to create an enclosure that would prevent exposure of the hanging drops to the laboratory environment during drop formation and spheroid culture. A small amount of aqueous buffer was placed in the enclosed recess beneath the wells to create a humidified environment. To minimize evaporation, 1.2 μL of 10-cst silicone oil were pre-loaded into each well prior to the formation of hanging drops. The top-plate was secured to another aluminum plate and was interfaced with the bottom-plate such that particular electrodes in the top-plate aligned with the location of the wells in the bottom-plate. The two plates were separated by a custom designed silicone spacers (Grace Biolabs, Bend, OR) to create a gap height of 300 μm and were secured using binder clips. Droplets of cell suspension were added to the reservoir electrodes via through-holes drilled into the top-plate. Droplet actuation was achieved using an AC potential of 100-120 V_{pp} at 18 kHz.

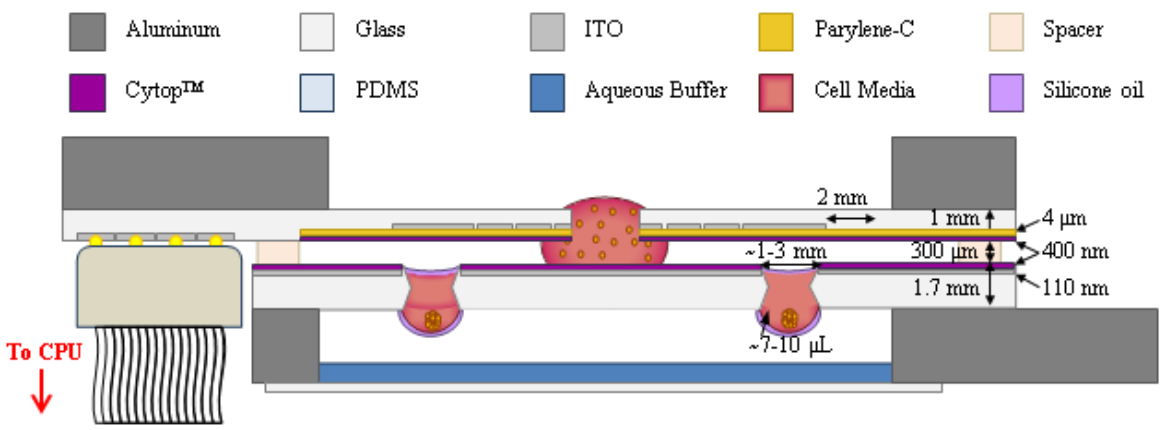

Figure 24. Schematic of DµF device for spheroid culture. To enable spheroid culture, through-holes, or wells, were fabricated into the bottom plate of the DµF device. Droplets of cell-suspension were dispensed and delivered to the location of the wells where they were pulled into the wells spontaneously via capillary forces. Adding multiple drops to a well resulted in the formation of a pendant drop, allowing the cells to settle into an individual, compact spheroid at the bottom of the drop. Aqueous buffer was placed beneath the hanging drops to create a humidified environment for long-term hanging drop culture.

4.3.3 In Situ Spheroid Culture

Cell suspensions of either HT-29 human colorectal adenocarcinoma cells or BJ human fibroblasts were used to form cell spheroids. To prepare the cell suspensions, cryopreserved cell stocks were thawed and seeded in polystyrene dishes in growth medium (DMEM, 4 mM L-glutamine, 10% FBS, 1% P/S solution). Cells were grown to ~80% confluency, trypsinized, and re-suspended in spheroid growth medium (Leibovitz L-15, 4 mM L-glutamine, 7.5% FBS, 1% P/S, 0.04% Pluronic® F-68) at ~1e6 cells/mL for culture on the device. Prior to use, the

devices were sterilized by rinsing them with a 70% aqueous ethanol solution and gently drying with compressed air.

All liquid handling steps were performed using a custom LabView program that enabled the application of the electric potential to any individual or combination of electrodes on the device.

To initiate hanging drop spheroid culture, droplets of cell suspension were dispensed from on-chip reservoirs and delivered to the location of a well, where they were pulled into the well spontaneously via capillary forces. Approximately 5 to 6 dispensed drops of ~1.75 μL each were needed to form a hanging drop with a curved surface that protruded beneath the bottom plate; the curvature at the bottom of the drop is necessary for the aggregation of cells into a spheroid. A thin film polyimide heater was placed in contact with the bottom aluminum holding plate to maintain the device at 37 °C during the handling of cell suspensions. At all other times, the devices were kept in an incubator at 95% relative humidity and 37 °C.

For all spheroid assays, medium exchange was performed every 24 h following hanging drop formation by adding fresh medium and extracting spent medium from the hanging drop according to the following sequence: (1) deliver a drop of fresh medium to the hanging drop; (2) mix the liquid in the drop by repeatedly pulling out and releasing a liquid finger from the well; (3) extract two drops of liquid from the hanging drop; (4) deliver another drop of fresh medium to the hanging drop.

4.3.4 Migration Assays

For migration assays, hanging drops were created from a suspension of human foreskin fibroblasts at ~1e6 cells/mL. Cells were allowed to aggregate for 24 h into compact spheroids prior to encapsulation in collagen gel. The encapsulation process involved extracting the medium from the hanging drop and replacing it with a bovine collagen I solution (0.5-4 mg/mL bovine collagen I, 1% P/S, 4 mM L-glutamine, 0.04% Pluronics F-68, in Leibovitz L-15 medium, PH = 7). The DμF device was then placed in the incubator to allow the collagen drop to gel at 37 °C. To demonstrate the ability to assay spheroids with exogenous migration modulating agents, some spheroids were encapsulated in collagen solutions containing either BMP-2 (100 ng/mL) or PGE2 (5 μg/mL).

Cell migration was quantified 24 h after spheroid encapsulation by staining the hanging drops, per the manufacturer's protocols, with Hoechst 33342 for imaging nuclear DNA and Acti-stain 488 phalloidin for visualizing actin filaments. The stained spheroids were imaged by confocal microscopy. Cell migration was quantified by measuring the radial fluorescence distribution and the total fluorescence intensity for each spheroid using ImageJ. For image analysis, the confocal images were converted into binary images to normalize the fluorescence intensity across multiple experiments and samples. The Radial Profile Plot plugin for Image J was used to measure the radial fluorescence intensity in the region outside the perimeter of the spheroid [171]. Total migration was measured by measuring the integrated fluorescence density of the stained actin everywhere outside the perimeter of the spheroid.

The viability of collagen-encapsulated spheroids was measured using the Life Technologies LIVE/DEAD®Viability/Cytotoxicity Kit according to the manufacturer's protocols. The percentage of viable cells was quantified by counting the number of living and dead cells in multiple z-planes throughout each spheroid.

The physical properties of the collagen gels formed in situ were analyzed using atomic force microscopy (AFM) and scanning electron microscopy (SEM). AFM was used to obtain the Young's modulus of the collagen sample by probing the hydrated gel and calculating the stiffness based on cantilever deflection. Bruker DNP-D and Bruker MSCT-B probes were used in a fluid environment. The spring constants of the probes were calibrated by measuring the thermal noise and fitting the response of a simple harmonic oscillator in fluid. The sample stiffness was measured by fitting probe deflection curves according to the Sneddon model and eliminating close range sample-probe interactions [115, 116]. Scanning electron microscopy was performed in order to visualize and characterize the collagen matrix morphology and cell adhesion. For SEM imaging, gel samples were first fixed in a 10% buffered formalin solution for 2 h. A step-wise dehydration in methanol was then performed by subsequently submerging the samples in 25, 50, 75, 90, and 100% methanol solutions for at least 10 min each. The samples were super-critically dried and sputter coated with gold before SEM imaging.

Figure 25 illustrates the tumor secretion fibroblast stimulation assay protocol. To model tumor-stromal communication and invasion, fibroblast spheroids and HT-29 human colon adenocarcinoma spheroids were formed on the same device. After 24 h of aggregation, the medium from HT-29 spheroid hanging drops was replaced with serum free medium (SFM) to allow for the enrichment of spheroid secretions.

The fibroblast spheroids were maintained in normal growth medium. After an additional 24 h, medium from the fibroblast spheroids was extracted and replaced with drops of medium extracted from the HT-29 spheroids to expose the fibroblasts to the HT-29 spheroid secretions. Drops of 1 mg/mL collagen solution were then added to the wells to create hanging drops with a final collagen concentration of ~0.5 mg/mL. For controls, fibroblast spheroids that were not exposed to HT-29 spheroid secretions were also encapsulated in collagen. After 24 h of encapsulation within collagen, the hanging drops were stained for actin filaments and imaged by confocal microscopy. Migration was quantified by measuring the radial distribution and integrated fluorescence density of stained actin everywhere outside of the body of the spheroid.

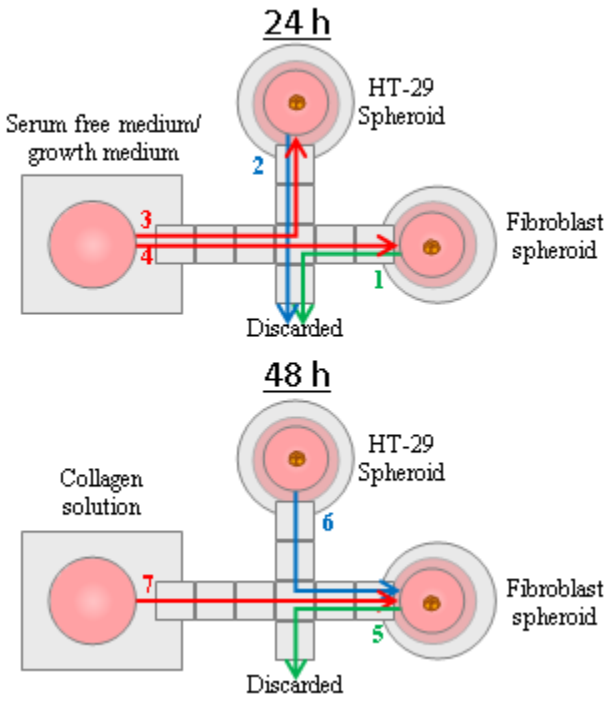

Figure 25. Tumor secretion assay protocol. 24 h after the imitation of hanging drops, both HT-29 and fibroblast cells formed compact spheroids within their respective drops. At the 24 h point, spent medium was extracted from the HT-29 and fibroblast spheroids (steps 1,2) and replaced with serum free medium and normal growth medium, respectively (steps 3,4). After 24 more hours of incubation, medium was extracted from the fibroblast spheroid (step 5) and replaced with medium extracted from the HT-29 spheroid (step 6). Collagen was then added to the fibroblast spheroid (step 7) and the spheroids were allowed to incubate for another 24 h prior to imaging.

4.4 RESULTS

To create a model for three-dimensional cell invasion on the DμF platform, spheroids of human fibroblasts were grown in hanging drops and encapsulated within a collagen hydrogel (Figure 26).

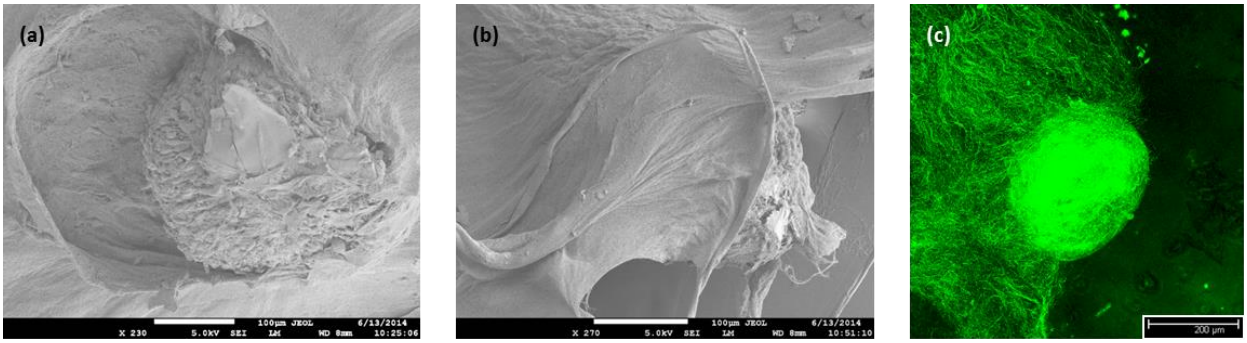

Figure 26. SEM and confocal reflectance microscopy images show cell spheroids encapsulated in collagen matrices. (a) SEM image showing a fibroblast spheroid within a collagen hydrogel, with part of collagen peeled back. (b) Another SEM image of an encapsulated spheroid next to (c) an image acquired using confocal reflection microscopy.

Fibroblasts were used because they are the most abundant cell type in connective tissues and fibroblast motility plays a critical role in both wound healing and cancer invasion [172]. We used collagen gels because collagen is a naturally abundant extracellular matrix protein and is widely used as a matrix in migration and invasion assays [147, 152]. Bovine collagen I was used because the slower gelation rate allowed the collagen solutions to be manipulated longer on the device compared to more rapidly gelling rat tail collagen I solutions. Collagen solutions of

up to 4 mg/mL could be actuated (dispensed, translated back and forth across a 4 electrode path 4 times, and inserted into a well) on our DμF devices. Solutions of higher concentrations of collagen moved too slowly for practical assay protocols. Solutions of up to 4 mg/mL bovine collagen I could be manipulated on the device for ~10 min at room temperature before movement became sluggish due to the onset of gelation of the collagen. Figure 27 shows representative SEM images and the mechanical properties of collagen gels of varying concentrations formed on a DμF device. The SEM images of the gels reveal a highly interconnected network of collagen fibrils. AFM measurements indicate that the Young's Modulus (YM) increases linearly from 1-4 mg/mL up to an average of ~50 kPa. The YM deviates from linearity at concentrations < 1 mg/mL. The Young's moduli measured for the various collagen concentrations used in this work were consistent with values reported in literature [97, 98, 173, 174]. This modulus range spans the elastic moduli of a wide variety of tissue types including lung, breast tumor, kidney, liver, brain, cardiac muscle, skeletal muscle, spinal cord and lymph node tissues [175].

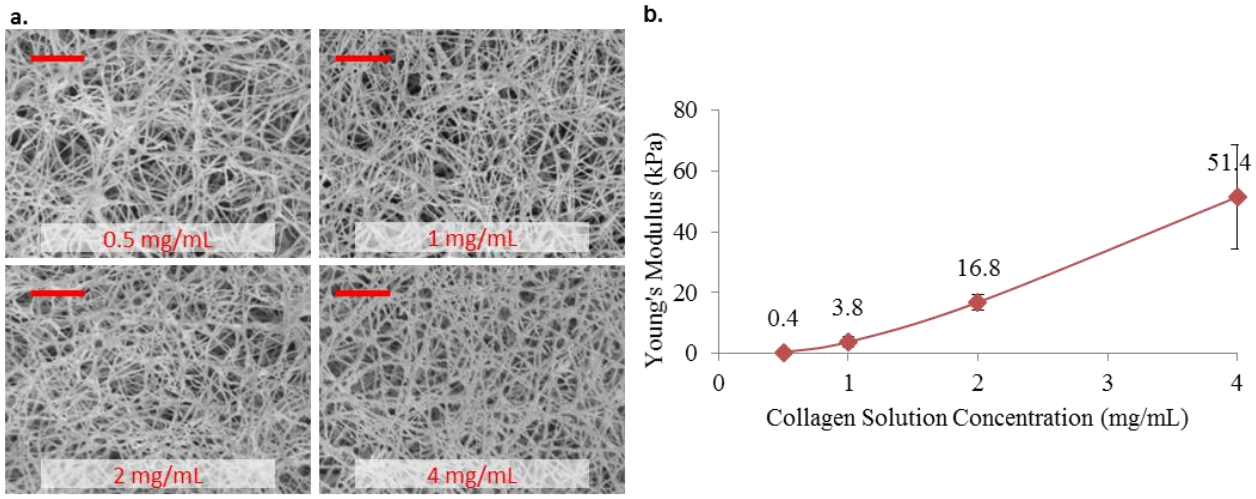

Figure 27. Collagen gel characterization. Collagen solutions up to 4.0 mg/mL could be handled on our DμF devices. (a) SEM images of hanging drop gels formed from 0.5, 1.0, 2.0, and 4.0 mg/mL collagen solutions. Each image was acquired at 10,000x magnification (Scale bar = 2 μm). (b) Young's moduli measurements of collagen gels formed on the DμF platform as determined by AFM. Error bars correspond to the standard deviation from at least 10 separate measurements.

Extended (>24 h) spheroid culture assays require the ability to perform medium exchange. To determine if medium could be effectively exchanged from a collagen hydrogel, a standard solution of dyed collagen was used to form hanging drops. The change in the concentration of the dye in the collagen gel after successive liquid exchange cycles, as described in the Materials and Methods, was measured by UV-vis absorption. Figure 28 depicts the degree of medium exchange achieved after multiple exchange cycles. The data show that two exchange cycles result in the exchange of >50% of the liquid in a hanging-drop gel, which is sufficient for performing cell spheroid culture [176, 177]. According to the medium

exchange protocol used in this work, and assuming an initial hanging drop volume of five dispensed drops, the liquid in the well dilutes at a theoretical rate of $C = C_0(2/3)^n$, where C = the concentration of dye in the hanging drop, C_0 = the initial concentration of dye in the hanging drop, and n = the number of exchange cycles. The measured concentrations after each exchange cycle agree closely with the predicted values, demonstrating the ability to precisely control the composition of the hanging drop.

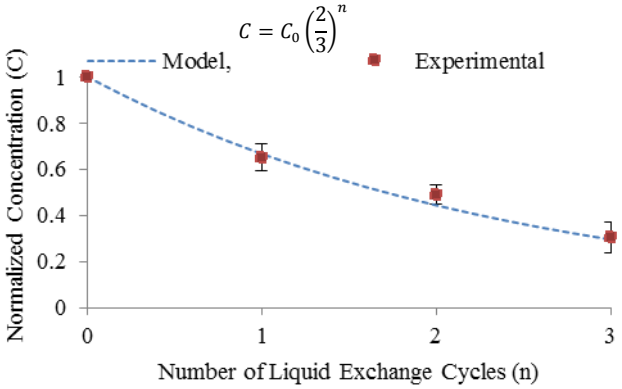

Figure 28. Liquid exchange from hanging collagen gel drops. The normalized concentration of dye in a drop of 1 mg/mL collagen after successive liquid exchange cycles. The dashed curve indicates the theoretical dilution rate based on the medium exchange sequence used in this work. Error bars correspond to the standard deviation from at least three separate samples.

To demonstrate the ability to assay spheroids with migration modulating agents, bone morphogenic protein 2 (BMP-2), a growth factor known to stimulate migration in a variety of cell types [178], and prostaglandin E2 (PGE2), which is known to inhibit fibroblast migration [179], were added to the spheroids to induce and inhibit migration, respectively. Untreated spheroids, which were encapsulated

in collagen without any exposure to exogenous migration modulating agents were used as a control.

Figure 29 compares the degree of migration for BMP-2-treated, PGE2-treated, and untreated fibroblast spheroids in collagen. Consistent with both 2D and 3D migration assays reported in literature, fibroblast spheroids encapsulated within collagen hanging drops on the DμF device exhibited cell invasion within 24 h [152]. Confocal imaging of fluorescently labeled actin filaments clearly shows the invasion of cells from the periphery of the spheroid into the surrounding gel. As expected, the addition of BMP-2 to the gel stimulated enhanced migration of cells from the spheroid while PGE2-treated spheroids exhibited reduced migration compared to the untreated controls. Spheroids exposed to 100 ng/mL BMP-2 showed an average ~85% increase in invasion compared to spheroids maintained in standard growth medium while PGE2 treated spheroids exhibited a ~33% decrease in invasion compared to untreated controls. The data illustrate that PGE2-treated spheroids exhibit migration out to ~50 μm from the spheroid perimeter after 24 h, compared to ~170 μm for untreated and BMP-2-treated spheroids (Figure 5c). Compared to the untreated controls, the BMP-2-treated spheroids, exhibit greater overall fluorescence at each radial distance, indicating a greater number of cells migrating from the spheroid.

Consistent with literature, we also observed that fibroblast migration varied with gel stiffness [79, 95, 180]. In this work, fibroblast migration increased with increasing collagen gel concentration. On average, the 4 mg/mL collagen gels exhibited a 46% increase in total migration, while the 0.5 mg/mL gels exhibited an average 40% decrease in migration compared to the 1 mg/mL gels.

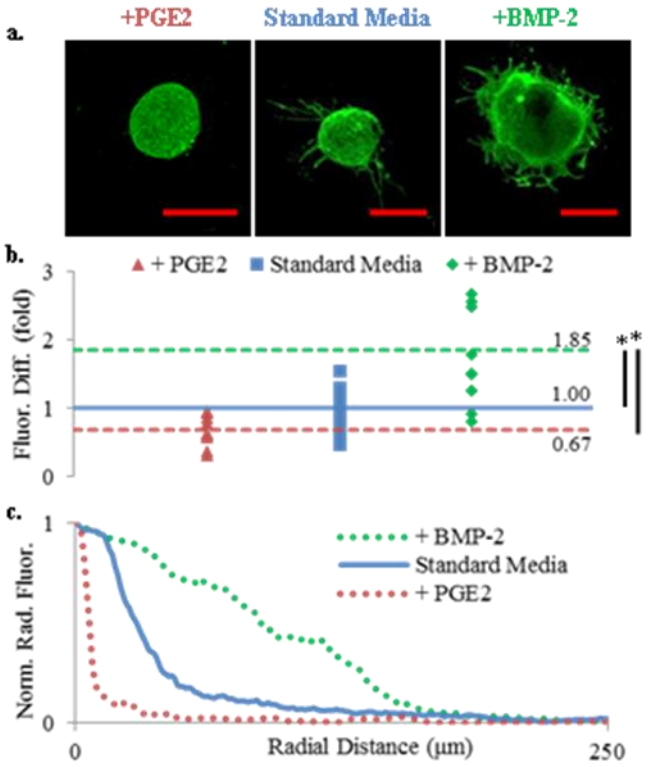

Figure 29. 24 h migration assays. (a) Representative images of actin stain spheroids encapsulated within collagen gels and exposed to either standard medium or medium supplemented with either PGE2 or BMP-2. Scale bars = 300 μm. (b) A comparison of the total fluorescence measured outside of the spheroid perimeter for untreated, PGE2-treated, and BMP-2-treated spheroids (N = 8 for each condition). The data have been normalized to the average value of the untreated controls, which was set = 1. The dashed lines indicate the average change in migration compared to the untreated controls (solid line). The * indicates values that differ at the 99% CI as determined by a Student's t-test. (c) The average radial fluorescence distribution of untreated, PGE2-treated, and BMP-2-treated spheroids (data normalized to max fluorescence).

Viability staining indicated that encapsulating the fibroblast spheroids in collagen does not decrease cell viability. The gel-encapsulated fibroblast spheroids exhibited viability >90% after 96 h in culture (48 h in solution and 48 h in collagen), which is comparable to spheroids cultured in suspension for the same duration [181].

To demonstrate the ability to model a physiologically relevant cell invasion process, we used the DμF platform to explore tumor-stromal communication in vitro. Paracrine secretions from tumors are known to induce an activated phenotype in adjacent fibroblasts, characterized by the production of α-smooth muscle actin and enhanced invasiveness [182, 183]. To mimic paracrine signaling in the tumor microenvironment, secretions from human colon carcinoma spheroids cultured in hanging drops were delivered to fibroblast spheroids immediately prior to encapsulation in collagen. A comparison of the migration from paracrine-stimulated and non-stimulated fibroblast spheroids is shown in Figure 30.

The results, shown in Figure 30, reveal enhanced migration for paracrine-stimulated fibroblast spheroids, supporting evidence that paracrine signaling from a spheroid microenvironment induces fibroblast activation in the tumor microenvironment [155, 184, 185]. The HT-29 treated spheroids exhibited a >130% increase in actin fluorescence outside of the spheroid perimeter compared to untreated controls. On average, cells from HT-29 treated spheroids exhibited migration out to ~270 μm from the spheroid perimeter compared to ~90 μm for untreated spheroids. Another interesting observation from these experiments is the evidence of multiple modes of fibroblast migration occurring simultaneously. In three dimensions, cells can exhibit different migration mechanisms depending on a

variety of factors including matrix stiffness, density, and orientation, as well as the activity of matrix proteases [180, 186, 187]. The HT-29-treated spheroids in Figure 30 exhibit characteristics of: (a) mesenchymal-type migration, characterized by cellular polarization and the formation of invadopodia; (b) amoeboid-type migration, characterized by individual, non-adherent cells that have migrated outside of the spheroid perimeter, and (c) collective-type cell migration, characterized by migration of multicellular streams or aggregates from individual spheroids. Non-treated spheroids also appear to exhibit multiple modes of migration, however, migration was lower overall compared to the HT-29 stimulated spheroids.

Intra-experiment variability is likely associated with variation in liquid handling operations including drop dispensing volume and medium exchange efficiency [181]. This variability may result in changes to the cell concentration and spheroid size, collagen gel concentration, and chemical concentration. Data should also only be compared in an intra-experiment manner, as opposed to an inter-experiment manner. The spheroids in the 48 h migration study had longer time to compact which could alter invasive capacity. Different collagen sources, noted in the Materials and Reagents section, were used for the 24 h and 48 h experiments. Biomolecular gels are known to exhibit lot-to-lot variability, particularly from different manufacturers.

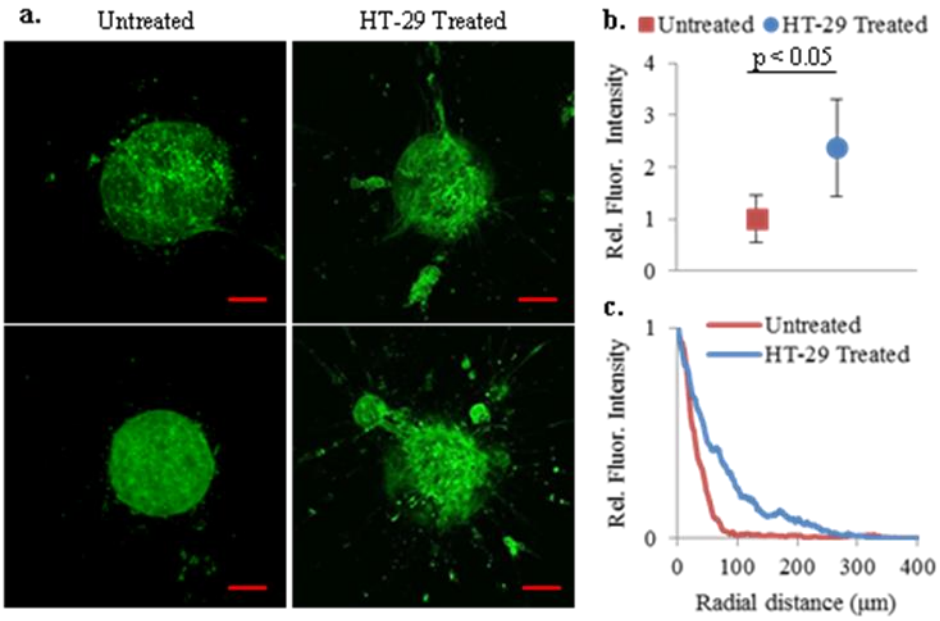

Figure 30. Comparison of HT-29 secretion-stimulated and untreated fibroblast spheroids. (a) Representative images of actin-stained, collagen-encapsulated fibroblast spheroids. Red bars correspond to 100 μm. (b) The average total fluorescence intensity of stained actin outside of the spheroid perimeter for both untreated and HT-29 treated spheroids. Data normalized to the fluorescence intensity of the untreated spheroids. (N = 7 spheroids for each condition) (c) Average radial distribution of the fluorescence intensity of stained actin outside of the spheroid perimeter. Data normalized to fluorescence intensity value at the spheroid perimeter. (N = 7 spheroids for each condition).

4.5 Discussion

This work builds upon the cell culture and assaying capabilities established for the DμF platform. Previous works have developed the ability to culture cells in

adherent monolayers, encapsulate cell suspensions within hydrogels, and culture cell spheroids in suspension on a DμF device [167, 181, 188]. While cell spheroids in a hanging drop suspension provide excellent in vitro tissue models, the addition of an extracellular scaffold allows for cell-ECM signaling, which is paramount to tissue homeostasis and morphogenesis. By enabling the encapsulation of three-dimensional spheroids in an extracellular matrix, this platform allows the modeling of processes that are highly dependent on cell-ECM interactions, such as the epithelial-mesenchymal transition, which plays a key role in important physiological processes such as embryogenesis, wound-healing, and tumor progression, and which cannot be modeled effectively using cell monolayers or encapsulated cell suspensions. Additionally, the methods described here can be extended to any type of spheroid-forming cell type and thermoresponsive sol-gel formulation. While not explored in this work, other gelation techniques, such as photopolymerization, could also be employed to encapsulate cell spheroids.

The DμF platform described here provides various advantages over existing spheroid-based invasion assays. Primarily, we have shown that DμF can effectively automate all of the liquid handling steps necessary for spheroid culture and encapsulation in collagen. Advanced DμF systems, such as the DropBot system or commercially developed systems that have integrated droplet volume metering, temperature control, and hundreds of addressable electrodes would enable fully automated, 'walk-away,' operation and medium-throughput (dozens of wells per chip) assay capabilities [189-191]. These systems can also have integrated sample treatment and analytical capabilities such as localized heating, magnetic bead separation, electrochemical detection, fluorescence microscopy, and absorption

spectroscopy, providing a level of in situ analysis that is difficult or impossible to achieve using robotic liquid handling systems. Such a platform would enable more sophisticated yet user-friendly assay capabilities than is possible with current spheroid-based invasion assays.

The DμF platform described here does have certain limitations. The primary limitation of DμF is the relatively lower throughput compared to robotic liquid handling systems. Migration assays using well insert membranes, for example, are compatible with robotic liquid handling equipment, which can process up to 96 wells simultaneously. Unlike robotic liquid handling, DμF liquid handling occurs on the same plane as the wells, which limits the well density on the chip. Thus, in the case of cell-based assays, the DμF platform is best suited for research environments in which medium-throughput sample processing is sufficient. Another limitation of the platform described here is the incompatibility with certain multi-component gel type systems that form physical crosslinks upon mixing (i.e. alginate). If the gelation kinetics of a multi-component system are faster than the mixing kinetics on the DμF device, then the addition of one component to the other results in the formation of a gel barrier at the interface of the drops or a gel with inhomogeneous crosslinking density throughout the drops. Despite these limitations, the automation, flexible liquid handling, and in situ analytical capabilities of the DμF platform make it a powerful tool for cell-based assays and screens.

4.6 CONCLUSIONS

We have developed protocols for the encapsulation of cell spheroids in hanging-drops of collagen gel using DμF. The encapsulation of spheroids within a three-dimensional, ECM scaffold allows for the creation of a tissue microenvironment that mimics tissues in vivo. With the ability to automate spheroid formation, gel encapsulation, and the addition of exogenous agents to spheroids, the DμF platform described here would reduce the tedium associated with manual 3D invasion assays and provide an alternative to robotic liquid handling instruments for assay automation. Making three-dimensional cell-based invasion assays easier to perform and more accessible to life sciences researchers could ultimately lead to new insights into tissue homeostasis and morphogenesis, as well as the development of novel treatments and therapies for a variety of injuries and diseases.

4.7 ACKNOWLEDGEMENTS

The authors thank Prof. Heather Maynard (UCLA) for providing access to cell culture facilities and equipment. Confocal laser scanning microscopy was performed at the CNSI Advanced Light Microscopy/Spectroscopy Shared Resource Facility (ALMS-SRF) at UCLA, supported with funding from NIH-NCRR shared resources grant (CJX1-443835-WS-29646) and NSF Major Research Instrumentation grant (CHE-0722519). The authors also acknowledge Dr. Matthew Schibler (UCLA ALMS-SRF) for assistance with confocal microscopy.

5 DIGITAL MICROFLUIDIC SYSTEM WITH VERTICAL FUNCTIONALITY

5.1 ABSTRACT

Digital (droplet) microfluidics (DμF) is a powerful platform for automated lab-on-a-chip procedures, ranging from quantitative bioassays such as RT-qPCR to complete mammalian cell culturing. The simple MEMS processing protocols typically employed to fabricate DμF devices limit their functionality to two dimensions, and hence constrain the applications for which these devices can be used. This paper describes the integration of vertical functionality into a DμF platform by stacking two planar digital microfluidic devices, altering the electrode fabrication process, and incorporating channels for reversibly translating droplets between layers. Vertical droplet movement was modeled to advance the device design, and three applications that were previously unachievable using a conventional format are demonstrated: (a) solutions of calcium dichloride and sodium alginate were vertically mixed to produce a hydrogel with a radially symmetric gradient in crosslink density; (2) a calcium alginate hydrogel was formed within the through-well to create a particle sieve for filtering suspensions passed from one layer to the next, and (3) a cell spheroid formed using an on-chip hanging-drop was retrieved for use in downstream processing. The general capability of vertically delivering droplets between multiple stacked levels represents a processing innovation that increases DμF functionality and has many potential applications.

5.2 INTRODUCTION

Digital (droplet) microfluidics (DμF) allows the dispensing, splitting, mixing, and translation of nanoliter to microliter-sized droplets of liquid on a 2D array of electrodes [9, 25]. By applying a voltage across dielectric-coated electrodes, a combination of electrostatic and dielectrophoretic (DEP) forces enables these basic liquid handling steps [9, 160]. As the benefits and processing capabilities of the DμF platform have grown, the range of lab-on-a-chip applications in chemistry, biology and medicine has expanded [162]. Notable benefits include reduced reaction times and reagent consumption on the microscale [192, 193], the lack of pumps or valves [17], reconfigurability [14], and automation [194].

DμF devices are fabricated with a planar array of electrodes for actuating the droplets. The fabrication process typically involves patterning conductive electrodes using standard photolithography techniques. Thin films of dielectric materials and hydrophobic coatings are also deposited to prevent electrolysis and establish non-wetting conditions. Discrete liquid droplets are created or inserted between the two plates that incorporate dielectric-coated driving electrodes and a ground electrode (Figure 31). To move the droplets, an electric potential is applied to electrodes adjacent to the target liquid droplet. The resulting electromechanical force drives droplet translation through a combination of electrowetting and dielectrophoretic mechanisms, depending on the liquid [14, 15, 24]. The electrode shape and position dictate where droplets can be moved and the types of operations that can be performed [16]. In this format droplets can only be moved laterally, which limits the potential applications.

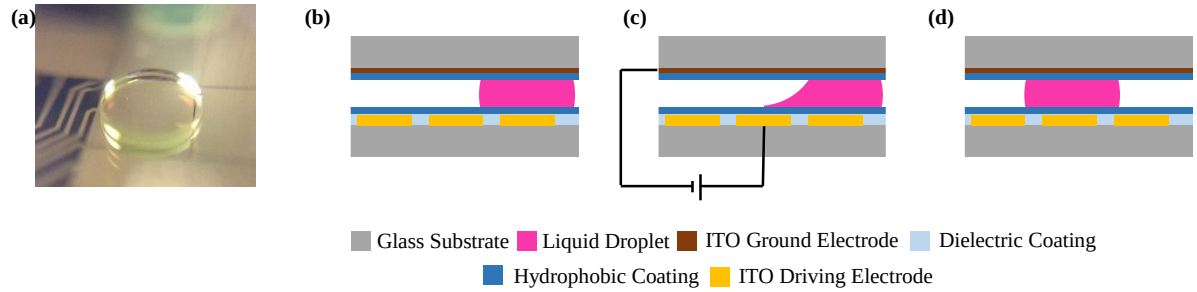

Figure 31. Image and schematic of a two-plate DμF device. (a) Oblique image of a 1-μL droplet sandwiched between a gold driving electrode and a transparent top plate. (b) Side schematic of a droplet in a standard DμF configuration with layers indicated by color. (c) By applying a voltage across adjacent electrodes, electrowetting and dielectrophoretic forces drive droplet translation and (d) position the droplet over the actuated electrode.

To improve the functionality to DμF systems, several innovative device designs have been developed to interface the planar droplet system with the external environment or circumvent the two-dimension constraint. Abdelgawad et al. developed a method to transfer a liquid droplet from a DμF configuration into a channel-based microfluidic system [195]. Their design makes it possible to combine the higher throughput characteristic of channel-based systems with the reconfigurability of DμF. Wang and Jones extended this work and accomplished the reverse: establishing the conditions for reversibly transitioning between closed and open DμF configurations [196]. A design by Ren et al. used an external syringe pump to introduce discrete droplets into a DμF system, obviating the need to manually replenish reservoirs [197]. Bhargava et al. created a modular design for

assembling 3D channel-based microfluidic systems that enables vertical channel assembly [198]. The use of novel substrate materials has enabled fabrication of flexible DμF devices [199]; in this work, the droplets were still been restricted to lateral movement in the device. To date, there are no DμF designs that permit vertical movement between planes or layers in the device.

A major application of DμF is as a platform for biological assays and cell manipulation [18, 40, 41, 43, 48, 50, 160, 200-207]. Technological advances that have enabled these applications have included improvements to automated proteomics [164, 194, 202], complete mammalian cell culture on-chip [163], and cell spheroid development [181]. Spatiotemporal control of tissue-engineered scaffolds has emerged as a critical tool for controlling cell behavior and directing cell fate [76, 85, 86, 88, 208, 209], so it is not surprising that hydrogels have also recently been incorporated into DμF devices [164, 200, 202, 203, 210]. The mechanical properties of hydrogels, such as their elastic modulus and toughness, have been shown to correlate with cell behaviors such as extracellular matrix protein production, cell adhesion, migration, and stem cell differentiation [85, 86, 88, 110, 208, 209]. Other physical properties of a hydrogel scaffold, such as porosity and crosslink density similarly effect cellular behavior [85, 86, 99, 110]. And temporal cues, such as the timing of growth factor delivery and mechanical stress induction, play important roles in directing stem cell differentiation [85, 86, 88, 208, 209, 211]. With the aim of creating biomimetic microenvironments, researchers have shown that using hydrogels that have tailored crosslink density gradients for cell encapsulation better mimics the complex extracellular matrix and tissue gradients that exist naturally [85, 86]. Thus controlling the spatiotemporal

cell microenvironment during directed cell culture is of vital importance [76, 85, 86, 88, 208, 209]. For DμF to become better suited for tissue engineering applications that utilize hydrogels, good control over crosslink gradient profiles is necessary [212].

Aijian et al. recently demonstrated the use of wells created in DμF devices for 3D cell culture experiments [181]. Cell suspensions were translated to the wells to form hanging drop cultures for cell spheroid creation. The DμF device was relocated to an incubator after droplet manipulation, and after 24 to 48 h, the cells naturally aggregated into spheroids that were later used as tumor models in a drug screening assay. While this platform offers a new tool for 3D tissue development for automated drug screening, the difficulty in manually retrieving the spheroid limits downstream processing capabilities. The ability to retrieve these spheroid samples would enable further experimentation on them, including hydrogel encapsulation or electric field stimulation.

In the first section below, we introduce the fabrication protocols for introducing vertical functionality and demonstrate the capability. Next, a theoretical framework for droplet translation between stacked layers is presented and used to establish design parameters for DμF devices with vertical functionality. Finally, three illustrative applications are presented that demonstrate some the new opportunities and areas of research that are enabled by this innovation in DμF.

5.3 EXPERIMENTAL SECTION

5.3.1 Experimental Design and Configuration

The electrodes were fabricated using transparent indium-tin oxide (ITO) so that droplets could be easily viewed through multiple stacked layers. The driving electrodes were 2 mm × 2 mm in size and a gap height of approximately 120 μm was used between each layer. The experiments were performed by stacking three plates, as shown in Figure 32a. These plates are referred to as the bottom, middle, and top. The bottom and middle plates contain driving electrodes and are used to translate discrete droplets of liquid during experiments. The top plate is stacked on top of the middle plate and contains no driving electrodes; it is coated with an electrically conductive ITO layer to act as a ground electrode and also with a hydrophobic Teflon-AF® layer. When describing the experiments, the gap between the bottom plate and middle plate will be referred to as the bottom layer, while the gap between the middle plate and the top plate will be referred to as the top layer.

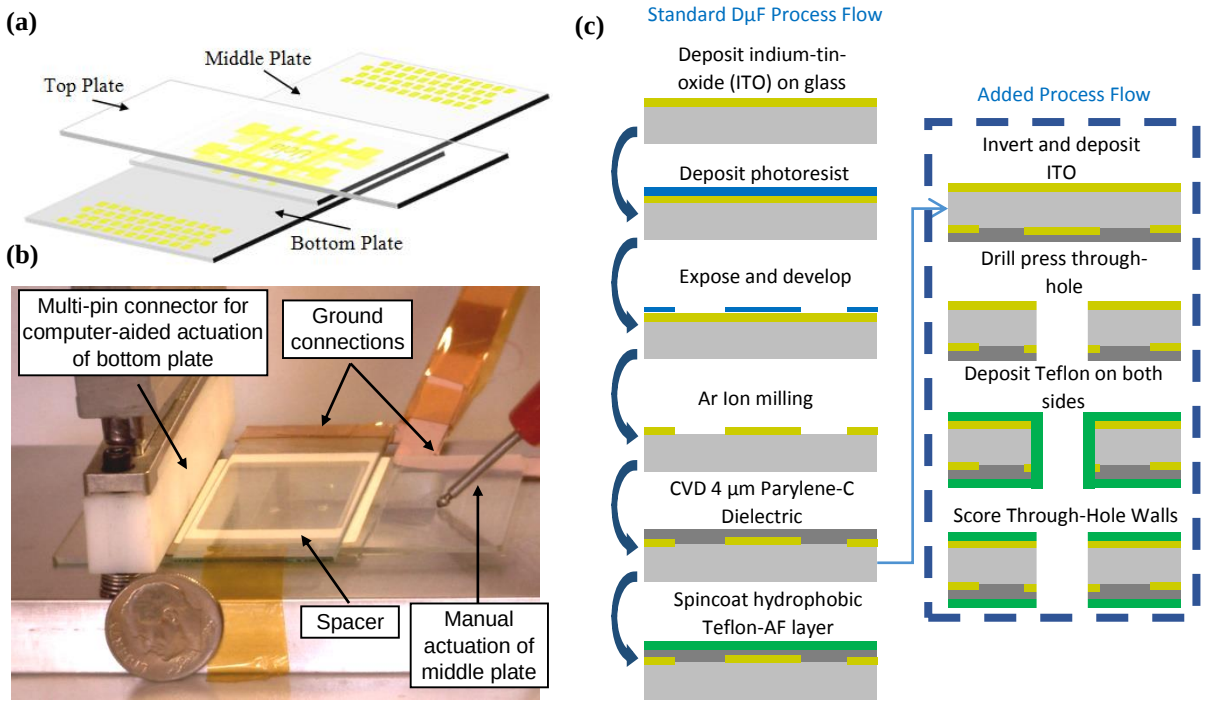

Figure 32. Vertically stacked architecture and fabrication workflow. (a) Oblique schematic of the stacked design, identifying the bottom, middle, and top plates, and (b) actual experiment showing full setup. (c) Cross-section schematic showing the typical two-plate fabrication process with the additional steps required for the middle plate.

The bottom plate's contact pads were brought in contact with a multi-pin connector attached to a laptop computer running LabView software for bottom plate electrode actuation. The middle plate was actuated by manually touching contact pads with metal probes to actuate middle plate electrodes. Ground wires were attached to the ITO coatings on both the top plate and the underside of the middle plate. A spacer was placed between each layer with an approximate thickness of

120 μm (Figure 32b). To translate the droplet, a voltage of approximately 110 V_{PP} at 17 kHz was applied.

5.3.2 Bottom DμF Plate and Top Plate Fabrication

The bottom plate was fabricated in the California NanoSystems Institute (CNSI) Integrated System Nanofabrication Cleanroom (ISNC) at UCLA. The substrate consisted of a 7.5-cm long × 5-cm wide x 1-mm thick piece of soda-lime glass. For patterning of the driving electrodes, the substrate was sputter-coated with 100 nm of indium-tin oxide (ITO) using an Ulvac JSP 8000. The ITO was coated with AZ5214 photoresist (spin-coated, 3000 rpm for 60 s), soft-baked on a hot plate (110 °C for 60 s), and exposed to 170 mJ of UV light under a patterned mask using a Karl Suss MA6 contact aligner (soft contact). The plate was developed using diluted AZ400K Developer (5:1 DI water to developer) for 60 s and rinsed clean with DI water. The exposed ITO was subjected to a 13.5-min argon ion milling process using an Oxford 80 Plus RIE (50 mTorr, 300 V RF bias, 400 V DC bias, 40 sccm Ar flow rate) to remove the unwanted ITO. The plate was then sonicated in methanol for several minutes to remove the remaining photoresist, following by a rinse in DI water. The contact pads were covered with Kapton tape and a dielectric layer consisting of 3.4 μm of Parylene-C was deposited via chemical vapor deposition (Specialty Coating Systems PDS 2010). Finally, a thin Teflon-AF film was spin coated (2000 rpm for 60 s) and post-baked on a hot plate (110 °C for 5 min and 180 °C for 15 min) on top of the Parylene-C to provide a hydrophobic outer surface.

The top plate, an ITO-coated glass slide, was coated with Teflon-AF.

5.3.3 Middle DμF Plate Fabrication

The middle plate was fabricated by the same protocol as was used for the bottom plate, with the following exceptions, highlighted in Figure 32c. A 100-nm layer of ITO was sputter-coated onto the reverse side of plate as well as the top. One surface of the substrate was patterned with actuating electrodes using the previously described methods, while the other surface was left as a continuous ITO layer. Prior to Parylene-C deposition, 1.1-mm diameter holes were drilled through the plate at the center of various electrodes. After Parylene-C deposition, Teflon-AF was deposited onto both sides of the plate using the same protocol as mentioned previously. The drilled holes were mechanically scored to remove the hydrophobic Teflon-AF coatings on the inside walls of the holes.

5.3.4 DμF Experiments

5.3.4.1 Vertical Functionality

A ~3-μL droplet of deionized (DI) water with 0.05% (w/v) Pluronics™ and methylene blue dye was dispensed within the top plane. The droplet was surrounded by 10-cst silicone oil to enhance mobility and facilitate droplet insertion into the through-hole channel.

5.3.4.2 Calcium Alginate Hydrogel Particle Sieve

A calcium alginate hydrogel was created within a channel by delivering a 1.5-μL droplet of alginic acid solution into the 1.1-mm diameter channel; this was followed by a droplet of 100 mM $CaCl_2$ to gel the solution in situ. For the sieving experiments, a droplet of DI water was mixed with 1 to 2-μm diameter sulfonated

polystyrene beads functionalized with carboxyl groups (Bang's Laboratories, Product #PC04N) and dispensed onto the top layer. A 2-μL droplet of the suspension was delivered to the gelled channel and pulled through to the bottom layer by actuating the bottom layer electrodes directly underneath the channel.

5.3.4.3 Calcium Alginate Hydrogel Fabrication and Characterization

Calcium alginate hydrogels were fabricated by merging a 2-μL droplet of calcium dichloride (100 mM and 1 M) with a 2-μL droplet of 1.2 wt% alginic acid in deionized water. The gelation process commenced immediately upon contact between the two droplets and was allowed to continue for 15 min. The calcium alginate hydrogels were characterized primarily by scanning electron microcopy (SEM) and atomic force microscopy (AFM). SEM was used to view the pore structure that resulted from mixing solutions of alginic acid and calcium dichloride either horizontally or vertically. After gelation, the samples were removed from the device to prepare them for SEM imaging. The fully hydrated gel samples were first frozen by immersion in liquid nitrogen and cut in half with a razor blade along the axis of diffusion. The thawed samples then underwent a stepwise dehydration in methanol by soaking them first in 100% DI water, followed by 10 min each in 25, 50, 75, 90, and 100% methanol solutions. The dehydrated samples were then supercritically dried to render a dry, sponge-like gel [118]. This step was necessary because allowing the gel to dry through evaporation caused collapse of the gel structure via capillary forces. The dried samples were sputter-coated for 90 s to deposit approximately 10-15 nm gold-palladium, and viewed using a JOEL JSM-6700F FE-SEM.

To analyze physical properties of the calcium alginate gels formed on-chip, AFM was performed on hydrated samples immersed in DI water using a Veeco Dimension Icon Scanning Probe Microscope. The Young's modulus was determined by probing the hydrated gel and calculating the stiffness based on cantilever deflection [116]. Bruker DNP-D probes were used in an aqueous environment. The spring constant of the probes were first calibrated by measuring the thermal noise and fitting the response of a simple harmonic oscillator in fluid. The sample stiffness was measured by fitting probe deflection curves according to the Sneddon model and eliminating close range sample-probe interactions [115, 116].

5.4 Results and Discussion

5.4.1 Vertical Functionality

In this section, we describe the process for moving a droplet from one layer of the device to another and the underlying principles. In the proof-of-principle experiment, shown in Figure *33* and Video S1 (Supplemental Information), droplets were brought into the channel from the top layer through standard DμF electrode actuation. Scoring the channel walls rendered them hydrophilic and helped the water droplet pass through. Immersing the water droplet in silicone oil helped reduce the surface tension of the liquid and effectively reduce the surface roughness of the channel walls, which enhanced droplet mobility. Electric potentials were then applied to the bottom layer electrodes to pull the water droplet away from the hole in the bottom plate. Typically some liquid was left behind at the channel's hydrophilic walls. If the walls were pre-coated with the silicone oil, the

droplet could be separated from the walls more readily without leaving any liquid behind.

The capillary length λ_c is defined by Equation 24; it is roughly 2 mm for water in air and 250 μm for water in oil.

$$\lambda_c = \sqrt{\frac{\gamma}{\rho g}} \qquad \text{Equation 24}$$

Below the capillary length scale, surface forces dominate over gravity [14]. When aqueous droplets come into the vicinity of the hydrophilic channel walls and are drawn near them, the radius of curvature will change at the contact line and will result in a pressure differential. To satisfy equilibrium conditions, the droplet will be forced through the hole. The contact angle is described by Young's equation [9, 14].

$$cos\theta = \frac{\gamma_{sv} + \gamma_{sl}}{\gamma_{lv}} \qquad \text{Equation 25}$$

The sequence shown in Figure *33* could be reversed. Droplets in the bottom layer were moved under the hole where they joined with any residual water adhering the hydrophilic walls of the channel. The middle plate electrodes were actuated to pull water back up through the channel to the top layer. Droplets were then pulled off from the channel onto the top layer, leaving some residual water on the channel walls.

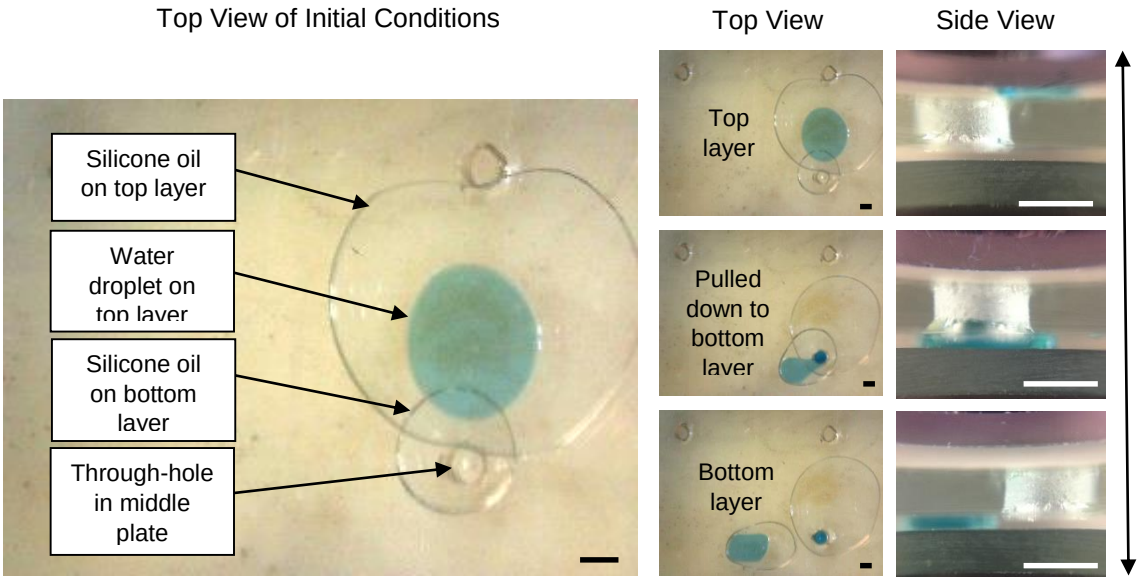

Figure 33. Images showing vertical droplet functionality. The initial conditions (left) and experimental verification (right) of reversible vertical functionality on a DμF platform using a through-hole to act as the conduit between the vertically stacked layers. Scale bar = 1 mm.

Water droplets could be moved reversibly between the bottom and top layers several times without loss in functionality. Droplets in the bottom and top layers could also be actuated simultaneously. Automating the actuation of droplets on both levels enables lab-on-a-chip procedures with significant versatility and throughput, as the layers can be stacked and access provided between each layer. This eliminates the limitation on system size imposed by standard photolithography fabrication methods.

5.4.2 Characterization of Droplet Forces and Design Parameters

In earlier work by Lee et al., a horizontal capillary on a DμF platform was created and characterized [38]. Because vertical functionality is new to the DμF platform, we proceeded to estimate the force required to insert droplets into a channel between the layers, as this will dictate device design parameters such as the channel radius, gap height, and electrode dimensions needed for insertion. Droplets of water have a characteristic capillary length, λ, of around 2 mm, according to Equation 24. The dimensions of typical DμF devices, including the ones used in these experiments, are below the capillary length, so gravitational forces were ignored in the following derivation.

The modeling of droplet insertion was done for four scenarios, which will be referred to as the initial, trapped, suspended, and final phases (Figure 34). After positioning the droplet above or below a channel, the droplet will assume one of these static conditions. In which scenario the droplet comes to rest will depend on factors such as the Laplace pressure differential and the frictional forces present. These static conditions necessary to transition a droplet from one scenario to the next were considered most important for establishing the design parameters. In this first-order analysis, we did not consider the dynamics of droplet insertion.

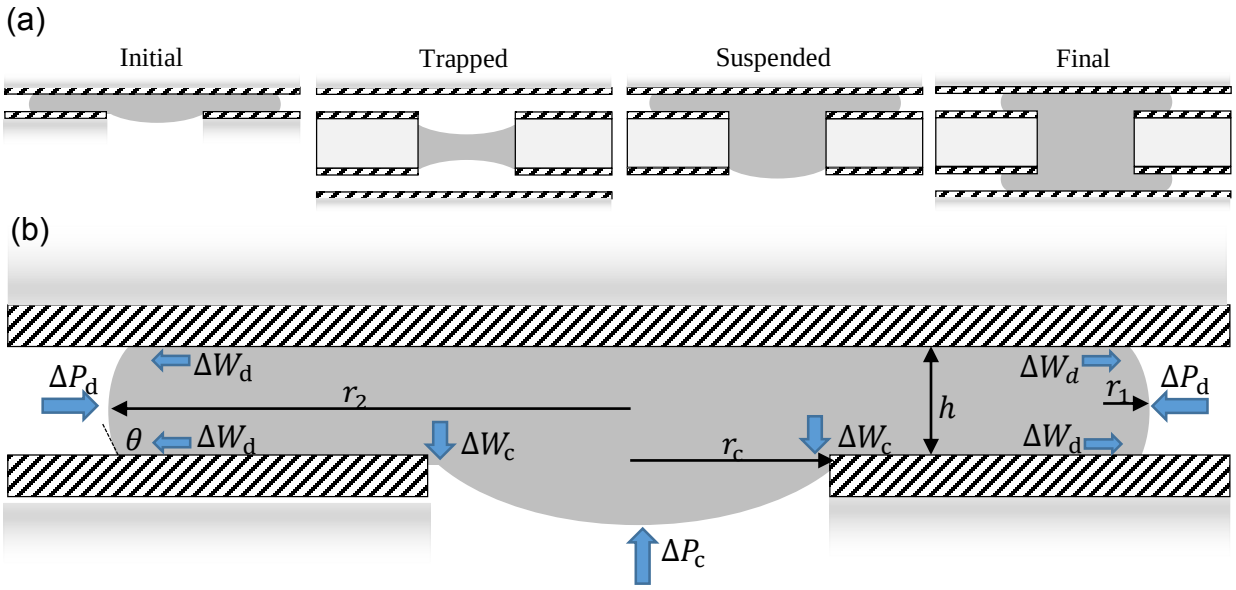

Figure 34. (a) Side schematic of the initial, trapped, suspended, and final scenarios showing the droplet-channel interactions. The hatched areas indicate the hydrophobic top coatings, the light grey areas represent the hydrophilic glass substrate, and the dark grey area represents the water droplet. (b) A free body diagram highlights the equilibrium forces using wide, blue arrows.

During the initial phase, the droplet is assumed to have been positioned over the channel via electrowetting forces. Once the applied voltage is removed, the droplet returns to the non-wetting state and rests above the channel. In this initial state, the droplet is subjected to both a Laplace pressure differential and static friction forces. The Laplace pressure differential, ΔP, is defined below (Equation 26).

$$\Delta P = \gamma_{LV}\left(\frac{1}{r_1}+\frac{1}{r_2}\right) \qquad \text{Equation 26}$$

The Laplace pressure at the surface of the sandwiched droplet is different to that of the droplet at the channel opening because of differences in geometry relating to the radius of curvature. The radius of curvature of the sandwiched droplet is defined by Equation 27 and Equation 28, where r_1 and r_2 are the principle radii of curvature, *h* is the gap height between the parallel plates, θ is the contact angle, and *V* is the droplet volume.

$$r_1 = \frac{-h}{2\cos\theta} \qquad \text{Equation 27}$$

$$r_2 = \sqrt{\frac{V}{\pi h}} \qquad \text{Equation 28}$$

The radius of curvature at the channel opening, $r_c = r_1 = r_2$, resembles a spherical cap and reduces to the capillary pressure, p_c, defined as Equation 29.

$$p_c = \frac{2\gamma_{LV}\cos\theta}{r_c} \qquad \text{Equation 29}$$

When these two pressures differ, a net driving force acts on the surface, s, which strives to equilibrate the system (Equation 30).

$$F = (P_r - P_a) \cdot s \qquad \text{Equation 30}$$

The frictional forces were calculated as the work of adhesion associated with changing the contact angle of water on Teflon-AF® from a sessile drop position to its receding contact angle of approximately 105º. Liquid droplets flowing through a capillary tube will experience resistive forces that arise from contact angle hysteresis, contact line friction, and viscous shear forces from the wall and the surrounding medium [213]. The correct mechanisms and modeling for these drag forces in both static and dynamic conditions are not fully understood or agreed upon [14]. The following analysis incorporates only the contact angle hysteresis effect, for two reasons. First, the droplet modeling was assumed to be from a static position above the open channel. In this scenario, the droplet has been positioned over the channel via electrode actuation, and as the droplet comes to rest, the velocity, and therefore the dynamic viscosity, becomes zero. Second, empirical data quantifying the viscous drag forces have been found to be from one to several orders of magnitude smaller than both the contact angle hysteresis effect and the driving capillary forces during actuation [213]. Once the capillary forces are large enough to drive the droplet into the channel, and the velocity is greater than zero, the droplet immediately comes in contact with the hydrophilic glass walls and generates a capillary force far greater than the viscous drag forces that arise during the dynamic episode of droplet insertion. The contact angle hysteresis, however, is manifested as resistance to droplet movement from a static position and must be included in the modeling. The resistive force arising from contact angle hysteresis can be thought of as a shear frictional force given by the integral of the change in work of adhesion ΔW, at the interface [214].

Equation 31 shows how the work of adhesion is related to the three surface tensions, which are directly related to the energy associated with changing the interfacial contact areas [215].

$$W = \gamma_{SV} + \gamma_{LV} - \gamma_{SL} \quad \text{Equation 31}$$

The change in work of adhesion can be expressed in terms of the receding and advancing contact angles for the static friction case [214, 215]. Substituting Equation 25 into Equation 31 yields the resistive force per length derived from the work of adhesion (Equation 32).

$$\Delta W = \gamma_{LV} \Delta |cos\, \theta| \quad \text{Equation 32}$$

The normal force of the Laplace pressure at the droplet edge of the top layer is thus resisted by a work of adhesion that acts at both the top and bottom interfaces of the droplet. By multiplying the equation above by a factor of 2 to account for each plate, and by normalizing the force by the surface area to obtain the normal force acting in the opposite direction of the Laplace pressure, the three primary forces can be combined to form the expression below that describes the equilibrium condition for droplet insertion, F_i, Equation 33).

$$F_i(V, h, r_c, \theta) = 0 = (\Delta P_d - \Delta P_c) + (\Delta W_c - \Delta W_d) \quad \text{Equation 33}$$

The electrode size (width *w* and length *l*) and gap height *h* dictate the minimum droplet volume that can be actuated [19, 216]. By solving Equation 10 for r_c, one can see how these device dimensions also determine the minimum channel radius that will permit droplet insertion for a given droplet volume (Equation 34). This equation can be used to predict whether a droplet positioned over a channel will remain in the initial scenario or pass into the channel.

$$r_c = \frac{2h(\cos\theta_o - 2\Delta|\cos\theta_{oA}|)}{\frac{h}{\sqrt{\frac{lw}{h}}} - 2\cos\theta_o - 2\Delta|\cos\theta_{oR}|} \qquad \text{Equation 34}$$

If the Laplace pressure is large enough to overcome the capillary pressure exerted upwards by the hydrophobic layer and the frictional forces that arise from the contact angle hysteresis effect, the droplet will move downwards to reduce the Laplace pressure differential. As the droplet moves downward, it will quickly pass the narrow thickness of the hydrophobic layer and come into contact with the hydrophilic glass walls (the contact angle for soda lime glass θ_G was measured with a contact angle goniometer to be ~ 5°). When the droplet touches the hydrophilic walls, the change in surface tension causes a substantial change in contact angle to a near complete wetting condition, and the relatively large capillary force drives the droplet downward through the channel. If the volume of the droplet is less than the volume of the channel, the droplet could become trapped.

Even if the droplet volume is greater than the channel volume, it could become suspended rather than pulling through to the bottom plate. Rendering the

channel walls hydrophilic is of paramount importance for ensuring complete droplet passage. When channels with hydrophobic walls were tested, we found that droplets would not spontaneously pull through. This behavior can be modeled by using Equation *33*, and considering the forces present at the droplet edges that tend to drive the droplet into the channel along with the forces acting in the channel that oppose this motion. In the absence of hydrophilic channel walls, droplet insertion is dictated by a competition between the droplet geometry above and below the channel. As the pressure differential overcomes the initial pressure required to move the droplet into the channel, the volume and surface area of the droplet above the channel decreases. This leads to a decrease in the driving force, and the droplet quickly comes to rest as the forces equilibrate. Solving Equation 10 shows that for a droplet volume < 0.65 μL and a channel diameter of 1.1 mm, the capillary forces exceed the insertion forces (Figure 35). Indeed, our experiments showed that with these volumes and dimensions, vertical functionality could only be obtained with hydrophilic walls. It would theoretically possible to achieve vertical functionality by adding several droplets to the channel to increase the driving Laplace pressure differential, but this strategy would be inefficient.

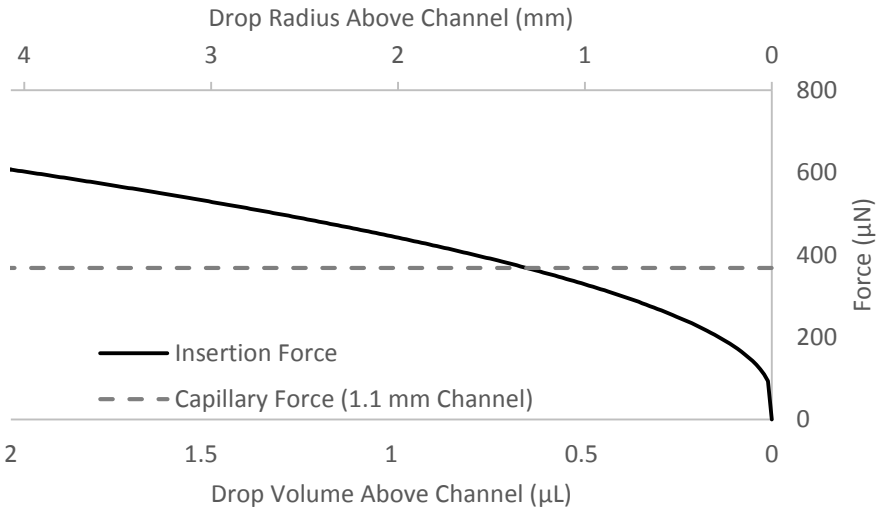

Figure 35. The droplet size (volume and radius) vs. the driving insertion force and the capillary force that resists droplet insertion. The insertion force is largely dependent on droplet size, while the capillary force remains relatively constant. The competing forces demonstrate the difficulty of moving a droplet through a channel with hydrophobic walls. The resistive capillary forces exceed the insertion forces a droplet volume of 0.65 µL. A larger droplet will move into the channel, but the insertion force will gradually decrease as the volume of the droplet above the channel decreases. The plot was prepared using our experimental conditions: a 1.1-mm diameter channel, a 1-mm thick middle plate, and a 120-µm gap height.

Once the droplet is pulled further down, the droplet comes into contact with the edges of the hydrophobic layer on the bottom side of the middle plate. This results in a capillary force that opposes downward motion. The strong capillary forces that derive from the hydrophilic glass walls also act to restrain the liquid from moving into the bottom layer. To model the suspended and final scenarios and

determine the pressures needed to allow the droplet to overcome these capillary forces, we used a similar approach to that used for droplet insertion. The final phase requires modifying Equation *33* to incorporate the strong capillary force imposed by the hydrophilic glass wall p_{cG} into Equation 35.

$$F_i(V, h, r_c, \theta) = 0 = (\Delta P_d - \Delta P_{c1} - \Delta P_{c2}) + (\Delta W_c - \Delta W_d) \qquad \text{Equation 35}$$

Once the droplet is injected into the bottom layer by overcoming these forces, the droplet enters the final phase. In the final phase the droplet is in contact with the bottom plate. Applying a voltage to electrodes on the bottom layer in contact with the droplet can then result in the generation of electrowetting forces that pull the droplet into the bottom layer.

Plotting Equation 33 and Equation 35 yields Figure 36, a series of correlations between critical device geometries and the pressures generated. Figure 36a is useful as a guide for DμF electrode design relating the electrode size to the minimum channel radius necessary to achieve vertical functionality with a single droplet to enter either the initial phase or the final phase. For a given electrode dimension, Equation *34* dictates the minimum channel radius required to obtain the necessary pressure differential to drive the droplet into the channel. It is important to note that the addition of multiple droplets is a practical method for increasing the pressure differential to a magnitude capable of driving droplet insertion. If droplet insertion does not routinely enter the final phase, a more efficient design may make use of proper dimensioning given by Equation *34*.

It is interesting to note that the surface tension does not appear in Equation *34*; however, the contact angle is directly related to the Laplace pressure and the work of adhesion through Equation *33* and Equation *35*. Immersing the water droplet in oil increases the contact angle [217] and reduces contact angle hysteresis, which makes it possible to insert droplets into channels with a smaller radius and makes vertical functionality easier to achieve (Figure 36b).

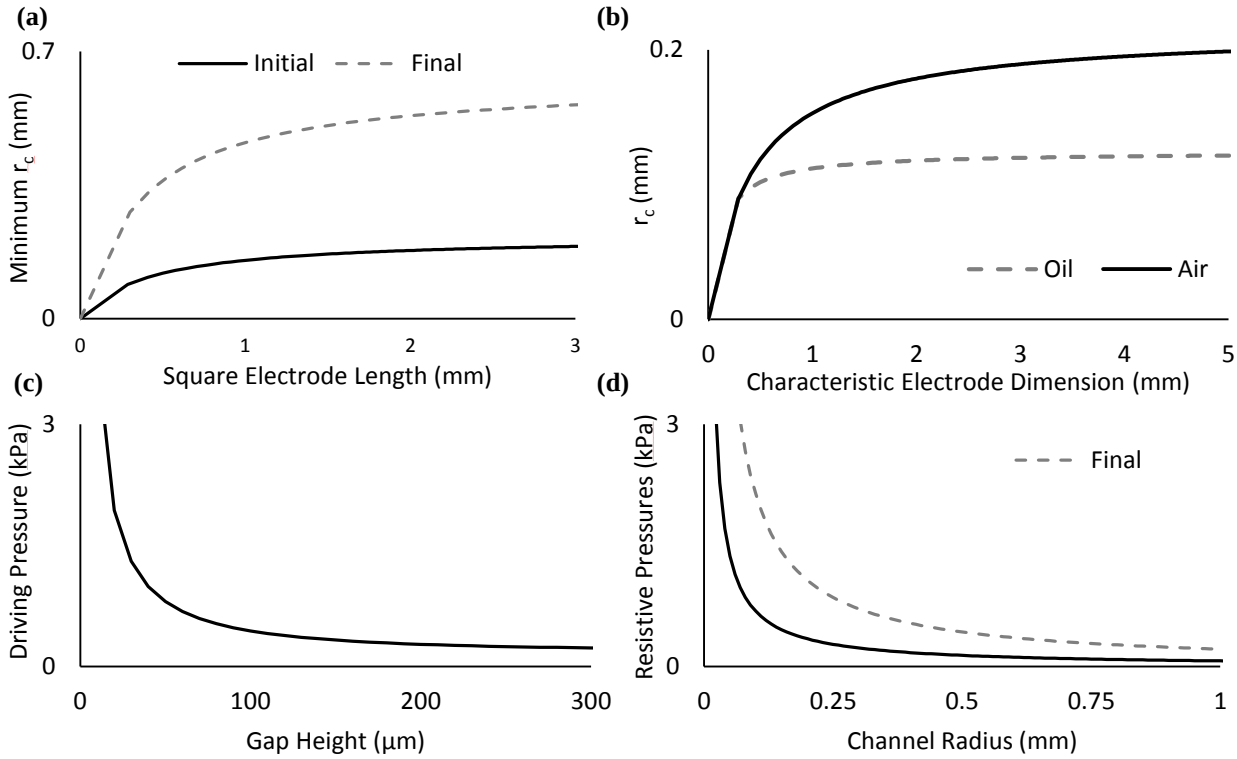

Figure 36. Correlations between the device geometry and characteristics related to vertical droplet functionality derived from Equation *33* and Equation *35*. (a) The minimum channel radius required for droplet the droplet to overcome the initial phase and the final phase as a function of square electrode size; (b) the minimum channel radius required for the droplet to overcome the initial scenario when immersed in either oil or air as a function of square electrode size; (c) the driving pressure for a droplet at equilibrium initial conditions as a function of gap height; and (d) the resistive pressure for a droplet at equilibrium conditions in the initial and final phases as a function of channel radius.

The gap height plays a large role in the Laplace pressure via Equation *26*: it decreases as the gap height increases. Therefore, the relationship between the gap

height and the channel radius plays a significant role in whether vertical functionality can be achieved, and should be a consideration in device design (Figure 36c). Experiments testing larger and smaller gap heights corroborated these findings, with larger gap heights making droplet insertion more difficult and a smaller gap height making droplet insertion easier. In much the same way, the resistive capillary pressure decreases with increasing channel radius (Figure 36d), and Figure 36c-d highlight that the driving pressure for water becomes greater than the resistive pressure for all gap heights at a channel radius of around 1 mm.
If the driving force for droplet insertion is greater than the minimum initial threshold but less than the final force required for injection into the bottom layer, vertical functionality can only be achieved if the height of the spherical cap protruding through the channel is large enough to allow the liquid to contact the opposing electrode to enable actuation. The height of the spherical cap is related to the channel radius by Equation 36.

$$h = \frac{-r_c}{cos\theta_{oA}} - \sqrt{\left(\frac{-r_c}{cos\,\theta_{oA}}\right)^2 - r_c^2} \qquad \text{Equation 36}$$

Solving for the height of the spherical cap as a function of the volume requires solving a cubic equation and is not trivial. Therefore, the most straightforward tool for checking this design parameter involves first solving for the minimum channel radius via Equation *34*. Upon choosing a channel radius greater than this minimum, one can check the height of the maximum spherical cap via

Equation 36. If this height is greater than the gap height, one may achieve vertical functionality prior to the final burst-through phase conditions.

5.5 APPLICATIONS

5.5.1 Sample-in-Sample Delivery with Spatiotemporal Control

Vertical functionality enables droplet delivery through the through-hole channel to a specific region of a sample positioned in the layer below. Diffusion assays are one type of application that could benefit from this functionality. These assays typically require the ability to control the location and timing of reagent delivery [218]: for example, to control cell-cell communication and phenotypic responses in cellular co-culture systems [219, 220].

To demonstrate the ability to deliver specific reagents to an internal location within a much larger sample positioned in the bottom layer, DI water droplets containing colored dyes were delivered to a reservoir of DI water from the top to the bottom layer. A large volume of DI water was dispensed on the bottom layer to emulate a homogenous liquid sample analogous to a single cell or co-culture system. Through-holes fabricated within different electrodes were used to insert discrete droplets of dyed water into a continuous water sample in the bottom layer at varying time points (Figure 37). Droplets with blue dye were first positioned on the top layer (Figure 37a). Droplet translation via DμF actuation was performed on each droplet (Figure 37a-c) to deliver them to distinct channels at specific time points. One important observation is that this mode of droplet delivery makes it possible to achieve a radially symmetric diffusion profile within the bottom layer

sample. This capability provides a new and straightforward method for producing chemical gradient profiles. An important application would be to create novel hydrogel crosslink gradient profiles for tissue engineering studies.

To demonstrate the ability to automate the simultaneous delivery of two different samples to separate channels, a droplet with blue dye and a droplet with red dye were moved at the same time (Figure 37d-e). A second droplet with blue dye was subsequently delivered to the channel containing the red dye (Figure 37f), where the liquids spontaneously mixed.

Taken together, these experiments show that it is possible to use vertical functionality to access the internal regions of a sample, delivering and mixing reagents there with spatiotemporal control not previously achievable on a DμF device.

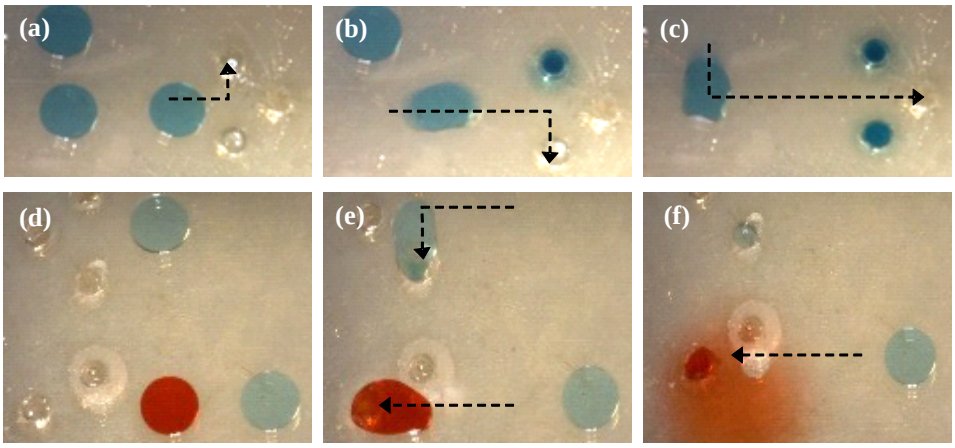

Figure 37. Spatial and temporal control of droplet delivery from the top to the bottom layer. (a) Blue droplets positioned on top layer prior to translation and insertion into the bottom layer containing bulk water. (a-c) Blue droplets are translated via DμF actuation and inserted into the channels where they mix with the continuous water sample in the bottom layer. (d) Blue and red droplets positioned on top layer prior to translation and insertion. (e) Automated actuation was used to translate a red and blue droplet simultaneously into separate channels to mix with the continuous water sample in the bottom layer. (f) A second blue droplet was delivered to same channel as the red droplet.

5.5.2 Calcium Alginate Hydrogel Crosslink Gradient

As noted in the Introduction, gradient hydrogels have diverse applications in cell and tissue culture. Using hydrogels that have radially symmetric crosslink-density profiles is one way to control cellular response times or migration patterns. To make alginate hydrogels, aqueous solutions of calcium dichloride and alginic acid are combined and gelation commences immediately. The crosslink density depends on the relative concentrations of the two species and their rates of diffusion. Using

conventional planar DμF devices, samples can only be mixed by merging droplets horizontally (side-by-side). Combining horizontally adjacent calcium and alginate droplets would result in a crosslink density gradient across the droplet; it would not be possible to create a radially symmetric liquid gradient or hydrogel this way.

We evaluated the feasibility of utilizing vertical functionality to fabricate radially symmetric hydrogel gradients on a DμF device. The idea was to deliver a droplet of $CaCl_2$ solution into a channel containing an alginate solution droplet centered below. The expectation was that once the $CaCl_2$ solution made contact with the alginate solution through the channel, calcium ions would diffuse into the alginate solution, initiate the gelation process, and diffuse outwardly to form a radially symmetric hydrogel. Vertical mixing was achieved by dispensing a 2-μL droplet of 1.2 wt% alginate solution onto the bottom layer, and dispensing a 2-μL droplet of 100 mM $CaCl_2$ solution onto the top layer (Figure *38*b, bottom). The droplets contained methylene blue dye to make them easier to image, and both solutions were immersed in silicone oil to enhance mobility. The alginate solution in the bottom layer was first centered underneath the hole by actuating electrodes in the bottom plate. The $CaCl_2$ solution on the top layer was translated to the top of the hole where it was spontaneously pulled in via capillary forces. The solution began mixing immediately upon contact and diffusing into the more viscous alginate sample below. To compare this result with what would be achieved with a conventional 2D DμF device, droplets having the same composition were actuated and merged horizontally within a single layer (Figure *38*a, top). At least 15 min was allotted after mixing to allow for gelation to complete prior to further manipulation.

To visualize the hydrogel structure, the gels were gently removed from the device to a glass slide. A 1-μL droplet of (approx. 10 mg/mL) methylene blue dye was placed at the center of the hydrogel. After approximately 5 min, the hydrogel was removed from the dye solution and photographed. Figure *38*b shows that the hydrogel formed by merging droplets side-by-side had a horizontal gradient in color intensity, while the hydrogel formed using vertical droplet integration had a more radially symmetric color gradient (Figure *38*b).

Scanning electron microscopy (SEM) was used to image the internal hydrogel structure and to validate the qualitative observations of the blue dye imaging assay. The top row of Figure *38*c shows an increase in pore size from left to right across the gel sample, consistent with the visual assay (Figure *38*b top) The pore size is largest furthest away from the site of mixing because the calcium ion concentration is lowest there (limited diffusion). The sample preparation protocol alters the hydrogel structure; for example, methanol dehydration decreases swelling. The internal hydrogel structure, therefore, is more useful for qualitative comparisons than quantitative analysis.

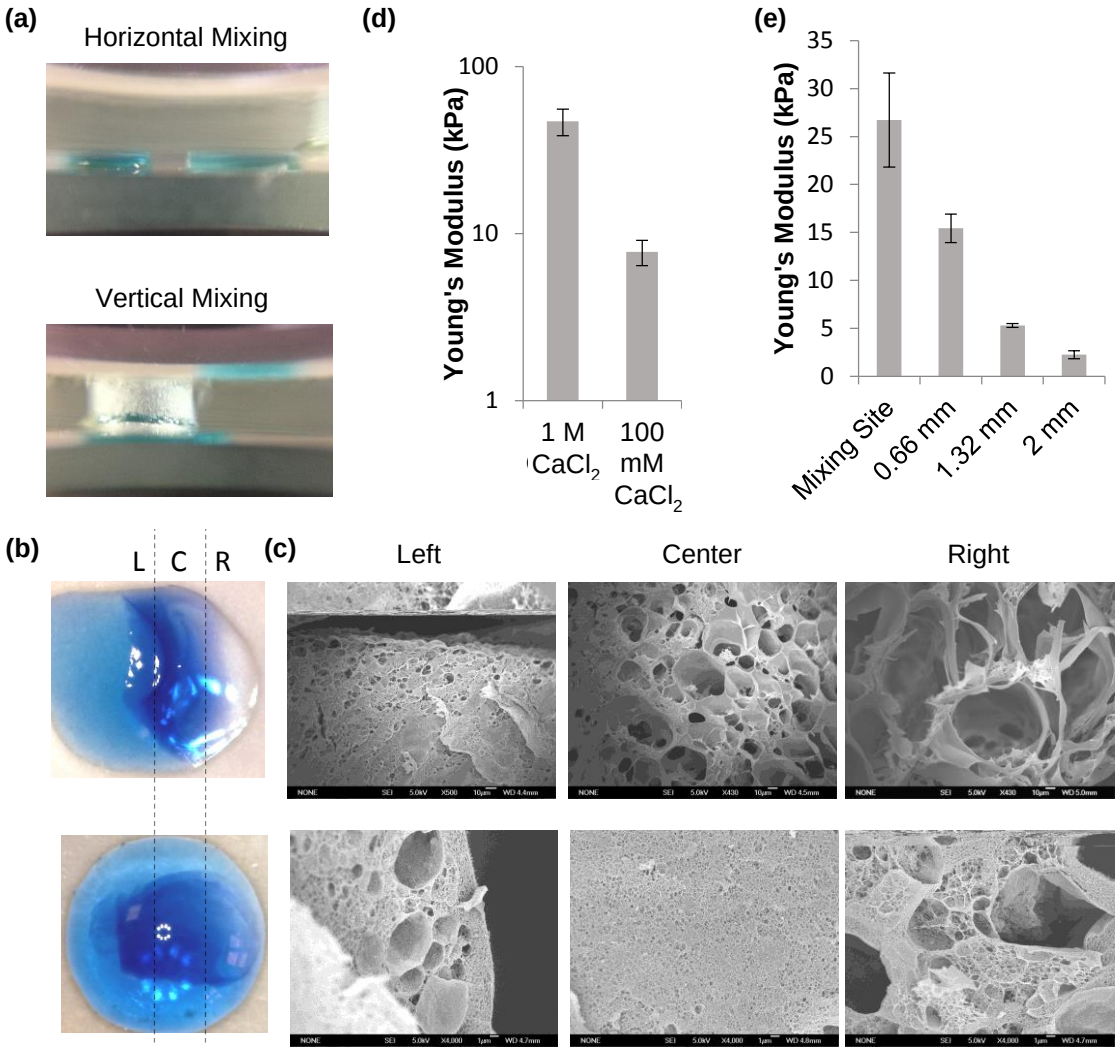

Figure 38. Calcium alginate hydrogel formed by vertical and horizontal mixing. (a) Side view of calcium alginate mixing methods; (b) top down views of methylene blue-dyed hydrogels formed by horizontal mixing (top) and vertical mixing (bottom); (c) SEM images from three sites across the horizontally-mixed gel (top row) and vertically-mixed gel (bottom row); (d) Young's modulus of vertically-mixed gels made with two different $CaCl_2$ concentrations; (e) Young's modulus vs. distance from the mixing site. The error bars correspond to standard error with $n \geq 10$.

The bottom row of Figure *38*c shows the SEM images of the gel formed using vertical mixing. The images show a much lower crosslink density on the left and right compared with the center, the locus of initial mixing. The crosslink density gradient appears qualitatively to be radially symmetric and is consistent with what was observed via the visual assay.

A gradient in crosslink density will result in a stiffness gradient. One way to measure the stiffness of a hydrogel is to use AFM and calculate the Young's modulus. We used this method to compare the stiffness gradients of hydrogels prepared by horizontal and vertical mixing (Figure *38*d). First, gels were made using either 1 M or 100 mM $CaCl_2$; their stiffness was characterized by AFM and the results compared with literature values to validate the method [100, 113, 221]. After establishing both the accuracy and precision, we used AFM to characterize the stiffness across each gel, determining the Young's modulus at the mixing site and 1/3, 2/3, and all the way across the gel for the horizontally mixed samples, and at similar distances for the vertically mixed samples. Figure *38*e shows that for both types of gels, the stiffness decreased significantly with increasing distance from the initial site of mixing. The gradients in gel stiffness are qualitatively consistent with the gradient in crosslink density shown in the SEM images.

These experiments demonstrate that radial gradients in hydrogel crosslink density can be generated using vertical functionality on a DμF device. This method for fabricating gradient hydrogels can be applied to on-chip tissue engineering applications and other hydrogel-based assays. For example, cells are encapsulated within hydrogels for cell migration assays that are used to probe phenomena such as wound healing and cancer progression. It should be possible to control both the

porosity and stiffness gradients of the hydrogels and determine how cell migration and other behaviors depend on these physical characteristics. In turn, this may facilitate development of improved tissue models, leading to greater understanding of the role of gradients in tissue development and transformation. Hydrogels with radial crosslink density profiles could also prove useful in lab-on-a-chip drug screening assays.

5.5.3 Embryoid Body (EB) Sample Retrieval

In general, the long-term culture of EBs requires the ability to create hanging drops that promote spheroid development, and to exchange media to add growth factors so that the culture can be maintained for extended periods of time. Recently, Aijian and Garrell [181] demonstrated cell spheroid formation and growth in hanging droplets using a DμF platform. A challenge that was identified with the device design was that it was not easy to retrieve and relocate the spheroids, once formed, without dismantling the device. Actuating the electrode near the hanging drop would pull away some of the liquid from the well while leaving the spheroid in place in a small amount of residual liquid. While this is a good feature for medium exchange, it renders the sample immobile.

An example where it may desirable to relocate or retrieve a spheroid is the culture of EBs for cardiomyogenesis and certain cardiomyogenic assays. The ability to impart electric fields to actuate and sense cellular characteristics, for example, requires the sample to be positioned near electrodes [120, 222, 223]. We hypothesized that using a second plane below the hanging drop would provide a path for a delivering a new droplet to the hanging drop that could be used to

retrieve the EB. We designed an experiment to retrieve an embryonic stem cell EB, formed as described in [224], from a well by delivering a droplet of media to the hanging drop via the bottom layer. We found that the EB fell into the droplet on the bottom layer when the two droplets came into contact. The droplet on the bottom plane containing the EB was then actuated and moved away from the channel and back in between the parallel plate electrodes, as shown in Figure *39* and Video S2 in the Supplemental Information.

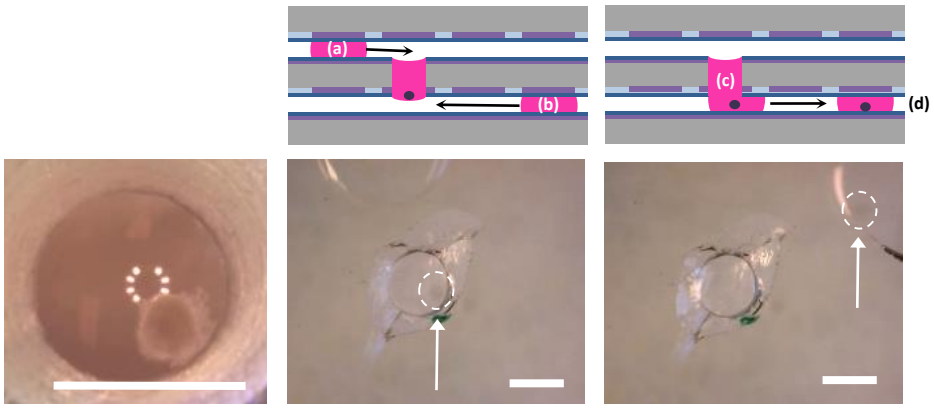

Figure 39. An EB (left image) inside of an on-chip well, and the protocol used for media replacement and sample retrieval. A side-schematic showing the protocol for EB growth and media replenishment for long-term culture via the top plane (a), and spheroid retrieval (b-c) and sensing (d) via the bottom plane. The images below the schematic highlight an EB inside of the well (dotted circle). A droplet is moved to the well from the bottom plate (center image). After the droplets merge, the EB falls to the bottom layer, and the droplet can be actuated away with the EB sample inside (right image). Scale bar = 1 mm.

This experiment shows that it is possible to use the top plane to deliver a cell suspension, exchange media, and deliver growth factors in order to culture EBs, and to use the bottom plane to retrieve the sample at a later time. Subsequent processing can then be performed, such as exposing the EB to electric fields for directing differentiation or impedance sensing, or delivering the EB to an adhesion pad for monolayer growth and monitoring.

5.5.4 Particle Sieving

As a final application, we used vertical functionality to create a hydrogel within a channel that could act as a particle sieve. This application was motivated by bead-based immunoassays. These assays are promising because of their selectivity and specificity, but they require easy and effective ways for sorting, trapping, and filtering microparticles [218]. Recently, Chen et al. showed that hydrogel posts could be fabricated on a device to mechanically filter particles [225]. Droplets were brought into contact with either side of the posts; particles in the droplets could be sieved based on the hydrogel post spacing. The primary limitation to this approach is the micro-post fabrication. The posts must be fabricated before performing any assays, they cannot be altered in situ, and the filtering capabilities are constrained by the difficulty in achieving fine spacing of the posts. Additionally, the fixed post length constrains the droplet size. Larger droplet volumes may allow particles to flow around the posts if the posts don’t extend far enough to each side, whereas our design requires the entire droplet to pass through the channel regardless of volume.

For our proof-of-principle experiment, a calcium alginate hydrogel was fabricated within a channel and a polystyrene bead contained droplet was pulled through it as it passed from the top layer to the bottom layer. The water was able to pass through the gel and form a new discrete droplet on the bottom layer that did not contain any of the polystyrene beads. As shown in Figure *40*, the beads were effectively sieved by the gel and remained on the top layer (Video S3 in Supplemental Information). This experiment was repeated using 10-μm sized polystyrene beads that were closer to cells in size. Again, a droplet was successfully sieved through the gel onto the bottom layer.

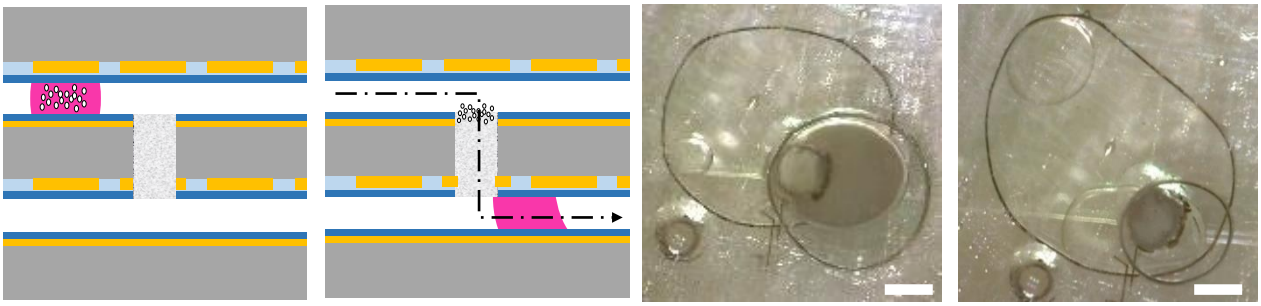

Figure 40. Schematic and experimental images showing a droplet of DI water containing 1-2-μm diameter polystyrene beads being pulled down from the top layer through a hydrogel sieve to the bottom layer. The side schematic (left) depicts a droplet containing the polystyrene beads on the top layer next to a channel with a calcium alginate hydrogel spanning its length. The droplet is pulled through to the bottom layer leaving the beads behind, effectively sieved by the calcium alginate hydrogel. The top-down images (right) show the experimental equivalent of these steps. The darker droplet contains the polystyrene beads. Once the droplet is pulled through to the bottom layer, the droplet is clear again after the beads are sieved by the calcium alginate hydrogel in the channel. Scale bar = 1 mm.

This technique for hydrogel-based particle sieving pulls the entire sample through the channel and into the bottom layer. This effectively filters out all particles that are larger than the gel pore size. The hydrogel crosslink density and porosity can be tailored to different sizes based on gelation conditions and component concentrations providing an easy way to tailor particle-sieving characteristics in situ. Conveniently, calcium alginate can be gelled and de-gelled through the delivery of a monovalent cation solution, such as sodium chloride. This

property would enable sieves to be created and eliminated as needed during a multi-step protocol. It also enables recovery of the trapped particles for downstream processing or analysis.

5.6 Conclusions

We have described the incorporation of through holes on a multi-layer planar DμF device as a means to introduce vertical functionality, specifically, the electric field-induced actuation of discrete liquid droplets between the layers in addition to the conventional movement within each layer. Three functional applications were demonstrated. First, sample-in-sample droplet delivery was performed with spatiotemporal control, and was used to produce a calcium alginate hydrogel having a radially symmetric crosslink gradient. Second, a method for producing cell spheroids on-chip was enhanced by demonstrating a means for retrieving the sample for downstream processing. Finally, an on-chip hydrogel sieve was fabricated that enabled complete particle removal.

Since the initial development of DμF, its uses and capabilities have expanded considerably and are quite diverse, despite the limitation of actuating droplets within a single two-dimensional plane. Incorporating vertical functionality can enable many useful and interesting applications of DμF platforms, including studies of surface interactions, membrane dynamics, bioseparations, and drug delivery. Further enhancements for specific applications are possible. These could include tailoring the channel geometry and surface chemistry, as well as optimizing the channel size, electrode geometry, and actuation voltage for specific processes and

for liquids other than water. Importantly, this approach described here is not limited to two layers; multi-layer stacks and interesting electrode designs could facilitate more complex 3D manipulations. Stacking multiple layers could also significantly increase the potential size of DμF platforms that are generally subject to the constraints of standard photolithography fabrication methods.

5.7 ACKNOWLEDGMENTS

The authors would like to thank Andrew Aijian for help with our digital microfluidic platform operation, the UCLA California NanoSystems Institute (CNSI) for access and assistance with the Integrated Systems and Nanofabrication Cleanroom (ISNC), and UCLA Prof. Atsushi Nakano and his lab for access to cellular embryoid bodies.

6 LAB-ON-A-CHIP PLATFORM FOR CULTURING AND ASSAYING CARDIOMYOCYTE TISSUE DERIVED FROM HUMAN EMBRYONIC STEM CELLS

6.1 ABSTRACT

Automated 3D tissue culture platforms that incorporate non-invasive assay capabilities have the potential to advance basic research on cardiomyogenesis and to support non-invasive assays of cardiotoxicity. A novel digital (droplet) microfluidic (DμF) system has been developed to enable automated stem cell culture for cardiomyogenesis. Aliquots of stem cell suspensions are delivered to on-chip wells to create hanging drops in which compact embryoid bodies (EBs) form after two days. The device materials support long-term culture (> two weeks) in an incubator, during which time differentiation of the EBs into beating cardiomyocyte clusters can be observed. The feasibility of performing drug assays in situ was demonstrated by delivering to discrete EBs chronotropic and inotropic agents that elicit changes to beating behaviors. The stacked, vertical architecture of the device enables EB sample retrieval and downstream processing. The EBs can be positioned so that electric potentials can be applied and the resulting changes in the capacitance and impedance monitored. Beating parameters such as heterogeneity and amplitude can thereby be observed. This in vitro culture platform is not limited to cardiomyogenesis. It supports differentiation of stem cells into a broad range of 3D tissue samples, the delivery of chemical and/or electrical stimulation to them, and non-invasive assays of phenotypic behavior.

6.2 INTRODUCTION

Cardiomyogenesis via embryonic stem cell (ESC) differentiation is now achievable in the laboratory. Although the process for differentiating stem cells into functional, mature cardiac tissue is still not fully understood [61, 68], applications that employ the in vitro culture and testing of cardiomyocytes have been expanding. Systems have been developed that permit the high-throughput culture of ESC-derived cardiomyocytes [226], or that can dynamically sense beating activity [227], bioimpedance [120, 228], or metabolic activity [229]. These systems are being used to study pharmacokinetics of therapeutics, cardiomyocyte maturation, and the feasibility of implantable tissue engineered constructs [68]. The existing platforms have shortcomings or constraints, however, that limit their applicability [6]. For example, many of these systems cannot act as a culture platform, so samples must be transferred to these standalone systems. These additional steps can be laborious and introduce the potential for errors. These platforms are also largely designed for 2D culture systems, which can fail to encompass in vivo behavior that 3D systems can better mimic. Digital microfluidic (DμF) systems may be able to overcome these limitations by streamlining and automating the liquid handling steps to culture and assay 3D cardiomyocyte tissue.

High-throughput systems increase the scale of assays while reducing costs, and process automation can improve accuracy, precision, and repeatability [230]. Among currently available automated culture platforms for research in cellomics, and particularly cardiomyogenesis, few miniaturized systems enable long-term stem cell culture with integrated sensing capability [212]. One of the most common

approaches to culturing and differentiating ESCs is through the formation of EBs [231]. EBs are spherical clusters of ESCs that have adhered together during the culture process. The first approach taken towards creating ESC-derived EBs was by culturing ESCs on petri dishes altered to have non-adherent conditions [232]. After a few day in culture, the ESCs naturally coalesced and adhered into EBs. A major drawback of this method was the inability to create homogenous, uniformly-sized EBs. Uniform EB development became more important as size-dependency emerged as a factor in fate specification. The hanging drop method was developed and has become a widely used method for forming EBs. Small volumes of a cell suspension are pipetted onto a petri dish as individual droplets. The petri dish is then inverted so that the droplets hang below, letting gravity bring the cells together over time so that they naturally adhere to each other and form EBs (Figure 41).

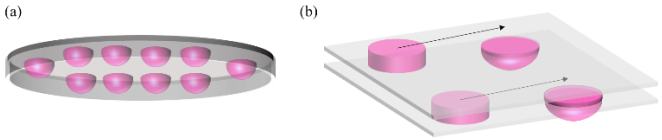

Figure 41. Schematics for creating hanging drops. (a) A conventional hanging drop schematic showing droplets of cell suspension pipetted onto a substrate such as a petri dish or cover slip. (b) A digital microfluidic schematic for creating hanging droplets by actuating droplets towards a well in the bottom plate.

With known volumes and cell densities, the hanging drop method can produce EBs with a much tighter size distribution, but the method is labor intensive

and prone to variability [233]. Also, the hanging drops must be detached after a few days as the media becomes depleted of nutrients, preventing the method from being used in experiments designed to study long term, suspension-based conditions. Other methods have been explored to automate and standardize EB development. Stirring bioreactors have found success in creating large-scale quantities of EBs with a relatively uniform size [234]. Microwell platforms are another automated, high throughput technique for creating uniformly-sized EBs [232, 235]. Channel-based microfluidic devices have been designed to create microwell-like devices [236], and have been cleverly designed to incorporate methods for in situ monitoring [237]. Automated 96-well plate systems that are often paired with specially designed plates that facilitate hanging drop formation can also achieve impressive scale [94]. Despite the ability to create large-scale quantities of EBs using these methods, a major drawback is the inability to access individual EBs, retrieve them, or alter culture protocols in real time.

Methods for monitoring the electrophysiology of 3D cardiomyocyte tissue lack breadth because the majority of techniques are designed for 2D cultures. Characterizing the electrophysiology of cardiomyocytes is important for diagnosing and understanding heart physiology and developing new therapeutics [126, 127]; particularly for preventing and treating arrhythmias [129]. Many electrophysiological recordings are performed using the patch-clamp method. It is invasive and limited to recording the action potentials of single cells [125], and so cannot be used to monitor whole tissue behavior. A common method for monitoring and quantifying 3D cardiomyocyte tissue is through video analysis [122, 138]. Visual assessment can be challenging because the tissue sample itself can obscure

specific regions of interest [238]. And while EBs have been plated onto microelectrode arrays [121], it would also be difficult or impossible to monitor field effects derived from the internal regions of a 3D tissue sample with this type of platform. Impedance sensors have been developed for monitoring cardiomyocytes with a planar microelectrode array, in which a 2D cell monolayer is attached to the surface [120, 239]. A disadvantage is that 2D monolayers are not as good as 3D cultures in mimicking the behaviors of real tissues. For example, cell-cell communication that exists in 3D EBs has been shown to stimulate early cardiomyogenesis [240]. It would therefore be advantageous to develop a cell culture platform that can be used to perform non-invasive functional assays on 3D, non-adherent cell cultures.

In this paper, we describe innovations in DμF to support long-term stem cell culture for cardiomyogenesis. DμF systems use applied electric fields to take advantage of electrowetting and dielectrophoretic forces [15, 30]. These phenomena make it possible manipulate liquid droplets in the range of picoliters to microliters [19]. DμF lab-on-a-chip process functions may include dispensing, splitting, mixing, and translating [16]. The conditions for applying DμF to long term cell culture conditions will be discussed, as well as some characterization of droplet actuation within a cell culture environment. A new DμF device design that permits vertical functionality using stacked layers was used to show the feasibility of EB sample retrieval and downstream processing. We also show that hESCs can be cultured and differentiated into cardiomyocytes, as evidenced by the onset of beating. Chronotropic stimulation of beating EBs was performed to demonstrate the ability to perform phenotypic drug screening. Impedance sensing was

demonstrated as a new method for monitoring 3D EB maturation and inotropic stimulation non-invasively on a DμF platform.

6.3 METHODS

6.3.1 Device Fabrication and Operation

Bottom DμF plate fabrication was conducted in the California NanoSystems Institute (CNSI) Integrated System Nanofabrication Cleanroom (ISNC) at UCLA. The substrate consisted of a 7.5 cm long x 5 cm wide x 1 mm thick piece of soda-lime glass. For patterning of the driving electrodes, the substrate was sputter-coated with 100 nm of indium-tin oxide (ITO) using an Ulvac JSP 8000. The ITO was coated with AZ5214 photoresist (spin-coated, 3000 rpm for 60 s), soft-baked on a hot plate (110 °C for 60 s), and exposed to 170mj of UV light under a patterned mask using a Karl Suss MA6 contact aligner (soft contact). The plate was developed using diluted AZ400K Developer (5:1 DI water to Developer) for 60 s and rinsed clean with DI water. The exposed ITO was subjected to a 17 min argon ion milling process using an Oxford 80 Plus RIE (50 mTorr, 300V RF bias, 400V DC bias, 40 sccm Ar flow rate) to remove the unwanted ITO. The plate was then sonicated in methanol for several min to remove the remaining photoresist, following by a rinse in DI water. The contact pads were covered using 2-mil thick Kapton tape, and a dielectric layer consisting of 3.4-μm Parylene-C was deposited via chemical vapor deposition (Specialty Coating Systems PDS 2010). Finally, a thin Teflon-AF film was spin coated (2000 rpm for 60 s) and post-baked on a hot plate (110 °C for 5 min and 180 °C for 15 min) on top of the Parylene-C to provide a

hydrophobic outer surface. The top plate, an ITO-coated glass-, was coated with Teflon-AF as well.

Middle DμF plate fabrication followed the same protocols as the bottom DμF plate with the following exceptions: a 100 nm layer of ITO was sputter-coated onto the reverse side of plate in addition to the top side. One surface of the substrate was patterned with actuating electrodes using the previously described methods while the other surface was left as a continuous ITO layer. Prior to Parylene-C deposition, 1.1-mm diameter holes were drilled through the plate at the center of various electrodes; after Parylene-C deposition, Teflon-AF was coated onto both sides of the plate using the same protocol as mentioned previously (Fig 3). Prior to droplet manipulation, the drilled holes were mechanically scored to remove the hydrophobic coatings on the inside walls of the holes. Two-μm SiO_2 layers were deposited using an ULVAC j-sputter machine, and a 2-μm Si_xN_y layers were deposited by sputtering silicon under nitrogen flow.

The DropBot system developed by Fobel et al. [192] was used for DμF device actuation. Long wire cable assemblies were purchased (Digi-Key, USA) to enable the device to be positioned inside of an incubator while the rest of the DropBot equipment and signal amplifier remained on the bench top beside the incubator. This prevented as many electronic components as possible from experiencing unnecessarily high levels of humidity that could result in electronic malfunction or corrosion. The μDrop software developed for use with the DropBot system enabled the developed automated protocols and feedback measurements.

6.3.2 Evaporation Tests

The droplet evaporation tests were performed by placing a 1-µL droplet of DI water on a DµF device between two Teflon coated slides with a gap height of 120 µm. The droplet volume was calculated geometrically based on time-lapse image analysis performed using ImageJ software. The droplet was allowed to evaporate on the bench top, in an un-equilibrated incubator, and an incubator that had equilibrated overnight. A humidifier and thermometer verified the bench top test to be approximately 22 °C and roughly 40 %RH. The un-equilibrated incubator test was performed by first leaving the door open for 30 s to allow the humidity to dissipate to a value close to atmospheric conditions (~36.5 °C and ~38 %RH). To assess equilibrium conditions, a droplet left overnight in the incubator was re-recorded the following day over the same duration.

6.3.3 Droplet Velocity Measurements

The feedback measurements developed by Fobel et al. [192] for the DropBot system and the µDrop software enabled the velocity testing performed in this work. Droplets were actuated across adjacent electrodes using an 80 V field at 20 kHz. The instantaneous velocity was recorded as the droplet moved between electrodes. The device was placed in an incubator that had been open for enough time to allow the humidity to reach atmospheric conditions. The temperature quickly equilibrated at 37 °C, but the humidity equilibrated slowly. This allowed a programmed sequence to be performed as the humidity levels slowly rose. The velocity measurements were recorded until maximum humidity was reached in the incubator. The device was then removed from the incubator and re-tested at

atmospheric conditions to ensure the device was not permanently altered by the incubating conditions.

6.3.4 Cell Culture

Cell suspensions of either HT-29 human colorectal adenocarcinoma cells or BJ human foreskin fibroblasts (ATCC® CRL-2522™) were used to form cell spheroids to demonstrate EB formation. To prepare the cell suspensions, cryopreserved cell stocks were thawed and seeded in polystyrene dishes in growth medium (DMEM, 4 mM L-glutamine, 10% FBS, 1% P/S solution). Cells were grown to ~80% confluency, trypsinized, and re-suspended in growth medium with 0.04% Pluronic® F-68 to enhance droplet movement at ~1e6 cells/mL for culture on the device. Prior to use, the devices were sterilized by rinsing them with a 70% aqueous ethanol solution and gently drying with compressed air.

To initiate hanging drop spheroid culture, the method developed by Aijian and Garrell [181] was employed. Briefly, droplets of cell suspension were dispensed from on-chip reservoirs and delivered to the location of a well, where they were pulled into the well spontaneously via capillary forces. Approximately 5 dispensed droplets of ~1 µL each were used to form a hanging drop.

Human embryonic stem cell (hESC) EBs were created at Prof. Atsushi Nakano's lab at UCLA (Department of Molecular, Cell & Developmental Biology, UCLA, personal communication [8/13/2014 – 8/1/2015]) by culturing hESC suspensions on non-adherent tissue culture plates for two days, where the cells naturally aggregated into EBs. These 2-day-old EBs were then manually transferred to DµF device wells and remain as hanging drops. Differentiation and downstream

processing continued from this point and was deemed equivalent to the 2-day EB formation demonstrated with other cell lines. The stock culture medium and differentiation protocol was also developed at Prof. Atsushi Nakano's lab at UCLA. Cell culture medium was replaced after 3 days in culture with proprietary growth medium using the following sequence developed by Aijian [181]: (1) deliver a drop of fresh medium to the hanging drop; (2) mix the liquid in the drop by repeatedly pulling out and releasing a liquid finger from the well; (3) extract two drops of liquid from the hanging drop; (4) deliver another drop of fresh medium to the hanging drop. This method was determined to replace a sufficient amount of media through repetitive dilution. At day seven, the process was repeated with a new growth medium. Spontaneous beating began between days 6 and 7, and some longer-term studies were continued by replacing the medium at day 10 with medium containing no chemical additives.

The culture medium in the hanging drops was also exchanged with collagen at day 9 in small set of samples and the cells were allowed to culture overnight within the gelled collagen matrix. Beating was observable in these samples after 24 h, indicating no immediate adverse effects to viability or lineage.

6.3.5 Live/Dead Assays

Live/Dead assays (Life Technologies) were performed according to the manufacturer's specifications. Confocal microscopy (Leica, SP2 MP-FLIM) was used to obtain a three-dimensional z-stack image (manufacturer's protocol, http://www.zmbh.uni-heidelberg.de/Central_Services/Imaging_Facility/info/How%20to%20SP2.pdf) of

the fluorescence with excitation and emission wavelengths of calein (494/517 nm) and ethidium homodimer-1 (528/617). ImageJ software was used to obtain percent viability estimates by summing the fluorescence intensity of both green and red filters.

6.3.6 Drug Assays and Video Recordings

Spontaneous beating was observed in EBs after 7 days in culture. After the confirmation of beating, phenotypic drug assays of chronotropic stimulation were performed. EBs were video recorded (~25 fps under 100-200x microscopy) to observe the intrinsic beating behavior of each EB before chemical stimulation. Media containing chemical stimulants were then delivered to the EBs and allowed to culture for a minimum of 5 min in the incubator. The EBs were again video recorded to observe any changes to the beating behavior. The goal was to use agents with known chronotropic and inotropic effects to hESC-derived cardiomyocytes to verify the validity of the assay protocols. The stimulants used included 5 mM epinephrine, 5 μM epinephrine, 5 mM caffeine, 5 μM caffeine, and medium containing no chemicals as a control. Videos of beating behavior were recorded and subsequently analyzed for beating frequency and rhythm. Timing between major contractions were measured 3 times and averaged for each EB.

6.3.7 Impedance Assays and Inotropic Stimulation

Impedance spectroscopy was performed using the DropBot feedback system and the μDrop software [241]. The EBs were positioned between electrodes after EB retrieval. EB retrieval was accomplished using a vertically stacked DμF

architecture. A droplet of media was delivered to the hanging drop via a bottom layer, the EB fell to the bottom layer after the droplets merged, and a droplet was dispensed from the well on the bottom layer containing the EB. Impedance spectroscopy was performed using an 80 V signal at 15 kHz. Using a standard lumped circuit analysis [14], the voltage penetrating the sample was calculated to be approximately 1 mV. AC fields at frequencies of less than ~5 Hz can induce field-evoked activity and pacing, fields between 100-1000 Hz can induce conduction block, and fields at frequencies at ~10 kHz and greater show no effect on cardiomyocyte beating behavior or cell viability [134]. The field was delivered to the EB in bulk media and held for several seconds. The capacitance and impedance were continuously monitored, and changes to the electric field derived from spontaneous cardiomyocyte contractions were recorded. The capacitance and impedance of cell culture media containing no cells, humid air, and a dead EB (previously beating EB left in air until it was no longer beating) were recorded as negative controls. A droplet containing 250 μM epinephrine was also delivered to a beating EB to create a ~50 μM concentrated solution around the EB, and the impedance was again monitored to detect any changes in the recorded response.

6.4 Results and Discussion

6.4.1 Device Stability in the Incubator

Before culturing and differentiating cardiomyocytes, it was necessary to establish that the DμF devices were stable and functional in the incubator environment. Operating a DμF system within the confines of a sterile, heated, and

humidified environment would mitigate contamination, temperature shock, sample disruption, and evaporation while minimizing operator intervention and handling. Device materials were tested for operability and longevity within an incubated environment. Parylene-C is a commonly used dielectric layer material because it has favorable dielectric properties, and is relatively inexpensive and easy to fabricate. While these properties have made Parylene-C the dielectric layer of choice for DμF devices, this material did not perform well inside the incubator. Immediately after placing the system inside the incubator, the device was used to dispense two droplets of media (Figure 42a). After 24 h of incubation, the device was used to dispense a new droplet of media. Immediately upon applying the electric field, dielectric breakdown occurred. This is likely due to the relatively poor wet adhesion characteristics of Parylene films to most metals [242].

Silicon dioxide (SiO_2) has been previously used as a dielectric layer in DμF devices, but has not been investigated for long-term stability in an incubator. SiO_2 has better wet adhesion characteristics with metals and possesses a Young's modulus and thermal expansion coefficient that is a closer match to ITO and soda lime lass than Parylene. We found that that devices with SiO_2 as the dielectric could be used within an incubated environment without failure caused by delamination. These devices were tested for over two weeks, and could continue to be operated within the incubator at standard cell culture conditions of 37 °C, 5% CO_2, and 95% relative humidity. Note that contamination of surfaces during clean room fabrication could promote SiO_2 delamination, so care should be taken during processing (Figure 42b). Silicon nitride was also tested for delamination and showed positive results similar to SiO_2 for longevity.

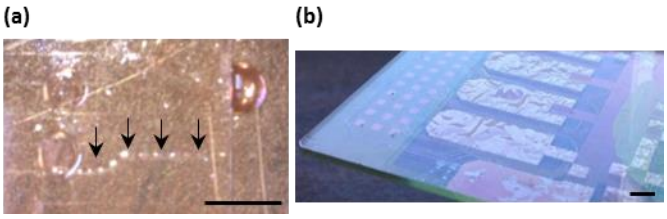

Figure 42. Images of DμF devices evaluated for functionality and integrity following incubation at 37 °C, 5% CO_2, and 95% for 24 h. (a) Delamination of Parylene-C inside of an incubator after 24 h; this delamination resulted in device failure. (b) Device with contamination on the electrode substrate prior to SiO_2 deposition showed evidence of SiO_2 delamination after incubation. Scale bar = 2 mm.

Differentiating hESCs first requires the formation of EBs. They could be formed on the DμF device by delivering aliquots of cell suspensions to the wells to form hanging drops. Because of biosafety laboratory restrictions for handling hESCs, we used human cell lines as a proxy for hESCs to demonstrate the feasibility of forming the spheroids in situ. The cell suspensions are dispensed and translated to the wells via DμF actuation forces [181, 243]. The suspensions form stable hanging drops, and after 24 h the cells aggregate into spheroids that maintain viability near 100%. This same protocol was performed with human fibroblasts, mouse embryonic stem cells, and human colon cancer cells. Figure 43 shows Live/Dead assays of a fibroblast spheroid and a human colon cancer spheroid that display a 3D morphology and over 95% green fluorescence. These cell suspensions were very similar in the time needed to form spheroids and the viability of the resulting spheroids. We infer that hESCs will behave in a comparable way.

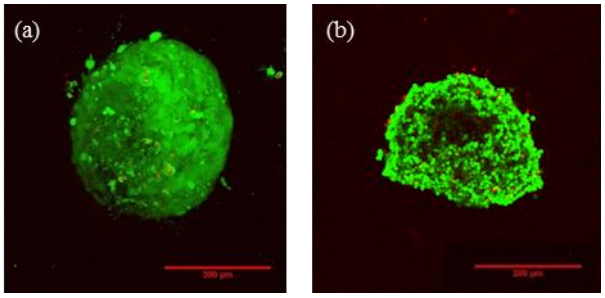

Figure 43. A Live/Dead assay of spheroids created from (a) human fibroblasts and (b) human HT29 colon cancer cells after 48 h of seeding into a hanging drop created on a DμF platform. The 3D morphology is evidence of a well-developed agglomerate, and the ratio of green to red fluorescence indicated >95% viability. Scale bar = 200 μm.

6.4.2 Long-Term Culture

The differentiation of hESCs into cardiomyocytes requires the ability to maintain the cells for at least 7 days to observe spontaneous beating. In previous cell culture studies using DμF platforms, the droplet handling operations were performed on the bench top; only once the DμF liquid manipulation steps had been completed was the culture plate was disconnected and relocated to an incubator [163, 181, 223, 244]. Removing the DμF device from the incubator and exposing it to atmospheric conditions can result in condensation, which may coalesce and disrupt hanging droplets and may also create fog on the camera lens that can impair visualization. By placing the camera and the device inside of the incubator throughout the cell culturing experiment, the entire closed system can be at equilibrium and prevent condensation from developing. Additionally, the behavior of

cardiomyocytes is highly temperature-sensitive. For example, beating cardiomyocytes will gradually become arrhythmic, and eventually stop beating after 5 – 10 min at room temperature. This process is reversible, and contraction can reinitiate when the cardiomyocytes are warmed up within a reasonable time. It is therefore beneficial to manipulate and assay cardiomyocyte behavior at a stable temperature.

Working with EBs in an incubator eliminated condensation and the need to periodically move the device, but the high surface-to-volume ratio of droplets in DμF means that evaporation is also concern [17]. In fact, evaporation is a primary limitation in the development of miniaturized commercial systems for cell-based assays [6]. Experiments were performed to monitor evaporation under three conditions: a bench top environment, in an incubator reaching equilibrium, and an incubator at equilibrium. Figure 44a shows the amount of droplet evaporation over time in an incubated, semi-incubated, and non-incubated environment. The droplet left on the bench top is presumed to reach steady-state equilibrium relatively quickly [245] and evaporated at a nearly linear rate. After an hour, the droplet on a device outside of the incubator decreased in volume by roughly 50%. Even after a quick, fifteen min session outside of an incubator, the droplet volume decreased ~20%, causing concentration changes that could confound study results. A drug assay could also be negatively affected by concentration changes. For example, caffeine elicits a positive inotropic effect at low concentrations and a negative inotropic effect at high concentrations [138].

An unequilibrated incubator (e.g., after opening and closing) also could cause significant evaporation as maximum saturation is being restored. Opening the

incubator door for roughly 30 s – a condition that was common when delicately handling cell-chips containing hanging drops – caused only a small temperature drop – from 37 to ~36.5 °C , but the humidity to drop from 95 to ~38 %RH. The temperature was restored to 37 °C in roughly 10 min, but the relative humidity did not reach the maximum saturation level for nearly 3 h. A 5-µL droplet lost approximately 60% of its volume after being placed within an unequilibrated incubator. By letting the system equilibrate before dispensing and delivering droplets, the media and reagent concentrations can be maintained as prescribed. As can be seen in Figure 44, we found no significant evaporation when droplets were maintained within the high-humidified environment of the incubator during experimentation. Droplets maintained a pinkish hue throughout two-day cultures, indicating the media was still fresh and at the proper pH.

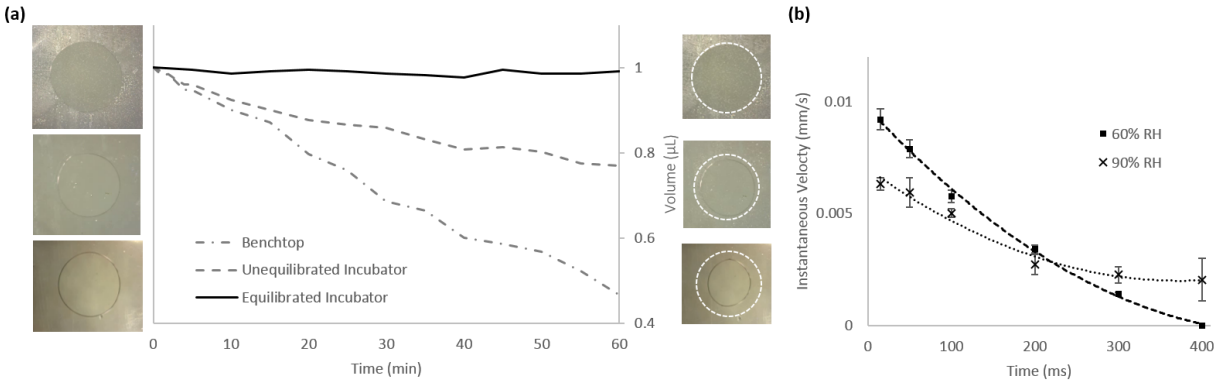

Figure 44. Droplet volume vs. time for droplets on a DµF device in an incubator, in an unequilibrated incubator, and on the bench top, and droplet velocity recorded from inside the incubator. (a) Evaporation of 1 µL droplet in a standard DµF configuration over 1 h on a bench top, after immediately put into an un-equilibrated incubator, and in an incubator at equilibrium. (b) Instantaneous velocity of DI water moving to an adjacent electrode actuated at 80 V and 20 kHz from within an incubator, highlighting that as the temperature and humidity rise the droplet velocity decreases. The error bars correspond to the standard error with n=6.

6.4.3 Characterizing Droplet Velocity

Automating DµF sequences requires attention to the timing and duration of electrode actuation, so the velocity of DµF actuated droplets in an incubator was measured. Instantaneous droplet velocity measurements were acquired at 60, 70, 80, 90, and 95 % RH as the incubator slowly reached equilibrium conditions. Figure 44b shows that droplet velocity decreased with an increase in humidity. The decrease in droplet velocity can likely be attributed to a decrease in the electrowetting actuation force. This can be understood by considering the roles of

surface tension and the Laplace pressure in droplet actuation. The surface tension force acting on an actuated droplet can be described by Equation 37, and is proportional to the surface tension between the liquid and surrounding fluid environment, γ_{LF} [14].

$$F(V) = \gamma_{LF} \cos\theta_a(V) \quad \text{Equation 37}$$

Because the surface tension of the water-air interface decreases as the humidity and/or temperature increase [246], the surface tension force acting on the altered contact angle, $\cos\theta_a(V)$, will decrease commensurately.

Another way to think about the change in the actuation force is by considering how the force derives from the Laplace pressure differential at the liquid-air interface (Equation 38) [14].

$$F(V) = (P_r - P_a(V)) \cdot h \quad \text{Equation 38}$$

The change in Laplace pressure is a function of both the surface tension between the liquid and the air, as well as the change in contact angle (Equation 39) [24].

$$\Delta P = \frac{\gamma_{LF}}{d}(\cos\theta_a - \cos\theta_o) \quad \text{Equation 39}$$

The decrease in the liquid-air interfacial surface tension again lowers the Laplace pressure differential. The static contact angle, θ_o, decreases as the

temperature rises and the humidity are increased [247]. The wetted contact angle, θ_a, also decreases in a humid environment according to Equation 40 below [14, 35].

$$cos\,\theta_a = cos\,\theta_o + E_W = cos\,\theta_o + \frac{C_H V^2}{2\gamma_{LF}} \qquad \text{Equation 40}$$

The electrical energy of the solid-liquid interface, shown as the voltage squared multiplied by the Helmholtz capacitance per unit area of the solid-liquid interface, C_H, will remain relatively constant because this term does not depend on changes in the ambient medium. The electrowetting number, E_W, will change as a result of the decrease in surface tension. This increase in the electrowetting number is of a much smaller magnitude than the change in the static contact angle; while calculated estimates put a change to the wetted contact angle at roughly 3-4%, the change in the static contact angle due to increases in temperature and humidity to incubator-like conditions can be on the order of 20-30% [247]. Therefore, $cos\,\theta_o$ drives the change in the contact angle between wetted and non-wetted conditions, $\Delta\theta$ is reduced, and the decrease in the driving force resulting from a decrease in the Laplace pressure differential results from both a drop in the liquid-air interfacial tension and a reduced change in the contact angle during actuation.

In addition to altering the driving force on droplets in a humidified environment, a decrease in the static contact angle typically results in a stronger impeding force to droplet translation. Chatterjee et al. [15] showed that the lower contact angle of water on certain surfaces results in a higher threshold voltage

needed to initiate movement. This impeding force can be thought of as a static friction force derived by the work of adhesion between surfaces that makes droplet translation more difficult [214].

6.4.4 Chronotropic Stimulation

To show that this lab-on-a-chip system can be used not only as a long-term culture platform but also to support drug screening assays, the cultured cardiomyocyte EBs were treated with different chronotropic agents known to elicit changes in their beating frequency. After first obtaining a video recording of the baseline beating behavior, these agents were delivered to wells in the incubator, each containing an EB, and allowed to culture for 5-10 min before being removed from the incubator and imaged again to assess changes in the beating frequency or rhythmicity. The initial range of EB beating frequencies (24 – 39 b.p.m.) fell within the range of previously reported beating rates (17 – 85 b.p.m.) of newly formed EBs [248]. Both epinephrine [5 μM and 5 mM] and caffeine [5 μM and 5 mM] in culture media were easily translated via DμF actuation. Figure 45 shows that epinephrine increased the beating rate (positive chronotropy) at both low and high concentrations. Caffeine triggered an increase in the beating rate (positive chronotropy) at low concentrations and decreased the beating rate (negative chronotropy) at high concentrations. These observations are consistent with the literature for both epinephrine [249] and caffeine [250-252]. Similar small doses of epinephrine have produced positive increases of over 200% in cardiomyocyte monolayers [248]. Very high doses of epinephrine, however, are associated with the onset of arrhythmias and can invoke a switch from positive to negative cardiac

output after ~10 min of stimulation [253]. Similar to our observations, doses of 5 – 10 mM of caffeine produced a negative chronotropic effect up to ~50% in [250]. Stimulant-free culture media showed no significant change in the beating frequency.

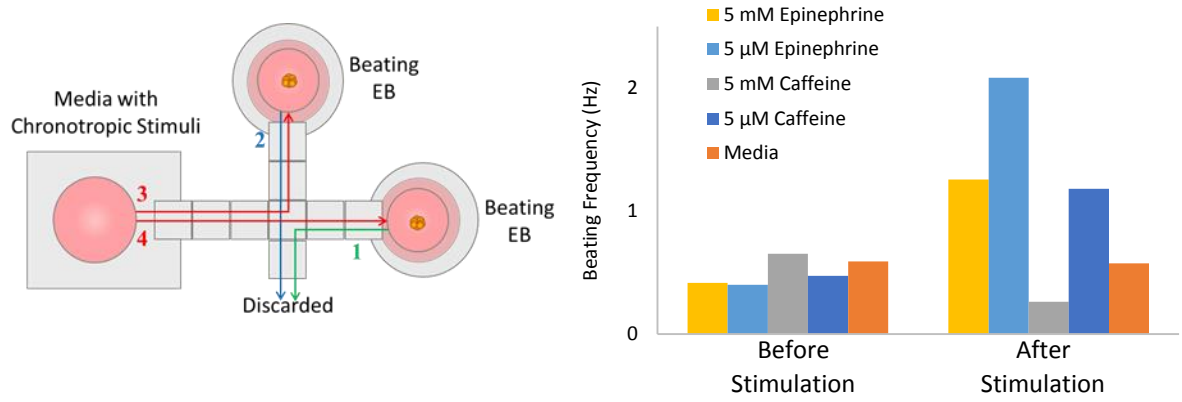

Figure 45. Chronotropic drug screening assay protocol and the change in the beating frequency measured after chemical stimulation. (a) Schematic showing the process for replacing the suspension media with fresh media containing different chronotropic stimulants. (b) Video analysis of the beating EBs after 5 min of incubation showed positive and negative chronotropic effects that were consistent with their known effects. The delivery of standard media with no chemical additives showed no change to beating frequency or rhythm.

6.4.5 EB Retrieval

To relocate the EB to a position on the DµF device where it could interact with the application of an electric field, it was necessary to be able to retrieve the sample from the hanging drop. A vertically stacked DµF architecture was used to retrieve the EB samples. Bender and Garrell previously developed vertical

functionality for the DμF platform (as described in the previous Chapter). This method enabled the retrieval of the EB by delivering a droplet of media to the hanging drop from a lower layer of electrodes. Vertical functionality was necessary because DμF actuation from the top layer could not retrieve the sample from the hanging drop once the volume became minimal; the hydrophilic sidewalls of the well create capillary forces too strong to pull the droplet away. By creating a vertical, parallel stack of devices, it is straightforward to bring a droplet of culture media to the hanging drop to form a bridge between the two layers. The EB then falls to the bottom layer due to gravity, and by actuating and dispensing the bottom layer droplet away from the well; the EB could be retrieved for downstream processing.

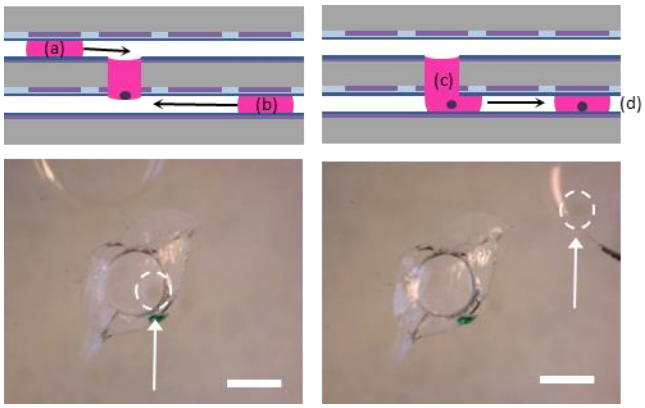

Figure 46. A schematic (top) shows how vertically stacked DμF design enables the formation, maintenance, and retrieval of EBs: (a) delivery of droplets from the top layer seed hanging drops and replace media; (b) delivery of droplets from the bottom layer can retrieve the EB sample, by (c) forming a liquid bridge upon mixing where the EB falls downward, and (d) dispensing a droplet on the bottom layer with the EB inside. The bottom images show the delivery of a droplet to a hanging drop containing an encircled EB (bottom left) from the bottom layer, and the dispensing of a droplet containing the EB after retrieval from the hanging drop (bottom right). Scale bar = 1 mm.

6.4.6 Impedance Spectroscopy of 3D Cardiomyocyte Tissue

Impedance spectroscopy using a DμF device could streamline assay analysis and reduce the need for external tools such as microscopes. Impedance spectroscopy could also non-invasively collect a rich data set of cardiomyocyte beating behavior for observing tissue maturation and drug screening assays. Impedance spectroscopy was performed on a DμF device after retrieving the EB and relocating it between parallel electrodes. The same electrodes used to drive

droplet translation were used for bioimpedance sensing. An AC field of 80 V at 15 kHz was applied to the EB and the surrounding media while the capacitance and impedance were continuously measured using μDrop software.

Figure 47 shows the impedance and capacitance measurements of 8-day old and 8-week old EBs. The measurements showed spikes characteristic of beating cardiomyocytes. The impedance data from 8-day old, newly beating EBs contrasts with 8-week old, large growth EBs in expected ways. Newly differentiated EBs have a smaller percentage of beating cells that tend to be localized to a single area, and they tend to beat with a wider field potential, slower frequency, and with less force [131, 132]. The impedance and capacitance measurements, as well as the video recordings, displayed this behavior (Figure 47a-b). The field changes were broadly spaced, and correspond to the relatively slow beating rate associated with early phase cardiomyogenesis [61]. The average peak-to-peak beating spacing was approximately 1.95 s ± 0.5. EB maturation typically begins with the onset of a small cluster of pacemaker cells [125]. These cells have leaky ion channels that slowly change the ion current during depolarization [126]. These newly differentiated EBs contained a smaller number of beating cells with 1 beating foci among the population examined (n=8).

The maturation and development of atrial and ventricular-like cardiomyocytes with rapid depolarizations was present in the 8-week old EBs [125, 254]. As shown in Figure 47c and d, 8-week old EBs produced larger and sharper spikes. The heterogeneity of maturing EBs can explain much of the phenomena present in the spectra. As an EB matures, cells differentiate into non-contractile and contractile cells of multiple cardiac lineages, and they often contain multiple beating

foci with a more complex, erratic behavior [60, 67, 125]. This was evidenced by the occurrence of smaller, intermittent spikes that are likely produced by the presence of multiple beating foci and chaotic, arrhythmic depolarizations caused by intermittent changes in the ion flux [255]. Although the 8-day old EB peaks have some differences and imperfect rhythmicity, they appear to have a greater degree of homogeneity among peak profiles compared to the more mature EBs. The capacitance and impedance of a "dead" EB that was previously beating but left outside of an incubator for an extended period of time, humidified air from within an incubator, and cell-less growth medium were monitored as negative controls and showed no measurable change over time (Figure 47e-f).

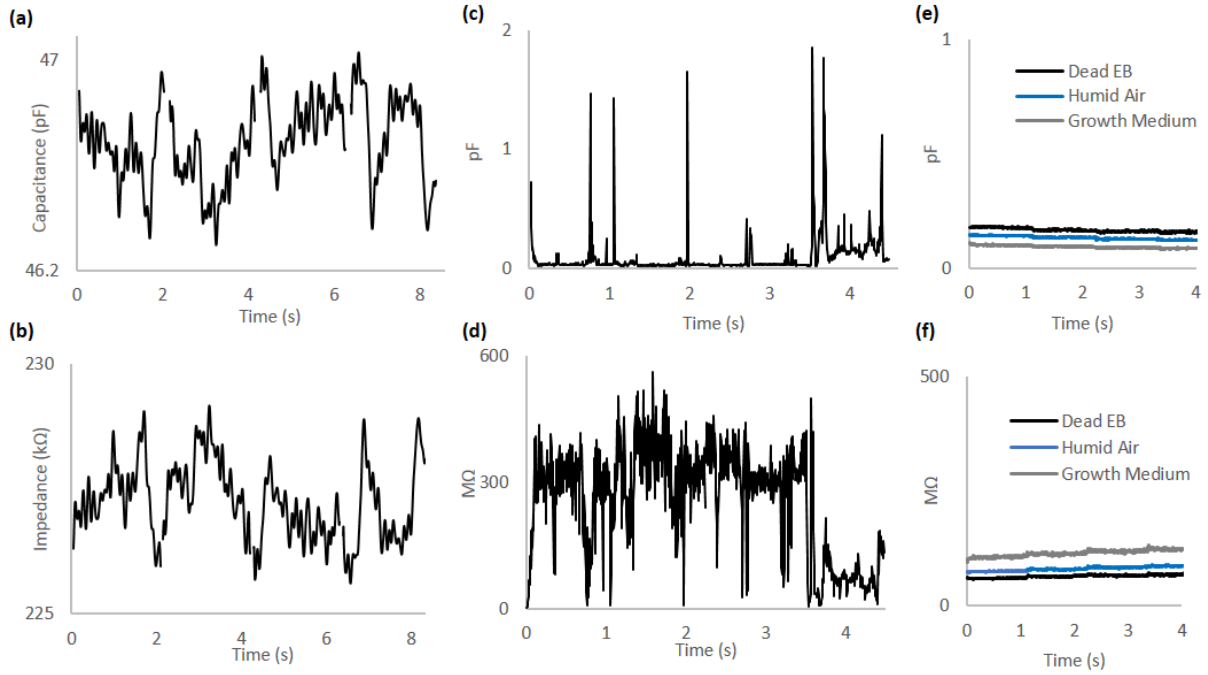

Figure 47. Impedance sensing performed on 3D cardiomyocyte tissue by applying an AC field of 80 V at 15 kHz around the sample and monitoring changes in impedance and capacitance caused by beating. (a) Capacitance and (b) impedance measurements of an 8-day old beating cardiomyocyte EB possess slow, small, and broad peaks. (c) Capacitance and (d) impedance measurements of a more mature, 8-week old beating cardiomyocyte EB contain larger, sharper peaks with a more heterogeneous rhythmicity. Plots (a) and (b) were smoothed using a 19-point weighted triangular smoothing operation to reduce noise to better highlight the peaks. (e) Capacitance and (f) impedance measurements of a "dead" EB, humid air, and growth medium were monitored as negative controls.

As was shown in early work by Cole and Curtis [256], the field impedance of a giant squid axon decreased rapidly during action potential spikes. Understanding

this behavior can be conceptualized by modeling the EB and sensor configuration as an electrical circuit. This method was originally pioneered for excitable cells by Hodgkin and Huxley [257] but has been used by recent researchers when understanding experiments such as single-cell impedance [258] or cell proliferation [223]. These lumped circuit models represent the cell culture media as a resistor and capacitor in parallel. This lumped circuit element is then placed in series with the tissue sample. Each cell within the tissue sample can then be broken down into further circuit elements. For example, the cell's membrane, consisting of a lipid bilayer, is modeled as a capacitor. This is placed in parallel with a resistor to model the cell's cytoplasm. While some models become very detailed by further modeling organelles [259] or gap junctions [260], the Hodgkin-Huxley model would suggest using variable resistors for voltage-gated ion channels. To model the voltage-gated ion channels of the cardiomyocyte, the Luo-Rudy model [255] would suggest using one each for the sodium, calcium, and potassium ion channels. This method of modeling individual ion channels can be useful when understanding the change in impedance during cardiomyocyte contraction. When a cardiomyocyte spontaneously contracts, it does so due to the opening and closing of gated ion channels in the cell membrane that cause ion flux and efflux. The main contributors to myocardial impedance are the extracellular and intracellular resistance, the gap junction conductance, and the cell membrane capacitance [261]. Ion mobility through the cardiac tissue is momentarily enhanced by the opening of voltage-gated ion channels [262], and the contraction of cells alters current flow. Finally, each cell's lumped circuit model can be placed in parallel with N number of cells to model the entire system. Other methods exist, such as modeling the complex impedance of

the system by way of Maxwell's mixture equation [258, 263]. Ultimately, the best model may depend on the specific type of experimentation and analysis pursued. However, the lumped circuit model provides a relatively simple analog for conceptually understanding the dynamic impedance changes seen during tissue excitation.

Viewing 3D tissue development using this method can be helpful because cardiomyocyte maturation is still poorly understood [60, 67]. EBs themselves, although widely used for differentiating pluripotent stem cells, have been characterized little due in part to the difficulty of studying phenomena within these complex 3D structures [60]. Impedance spectroscopy data provides a holistic view of the 3D tissue behavior, and may provide a new method for observing aspects of this complex behavior that can be difficult to observe using other methods. For example, an important observation from the impedance and capacitance measurements in the 8-week old samples (Figure 47c-d) is that the EBs exhibit erratic and heterogeneous behavior. The reason for this heterogeneity lies in the complex cell and tissue structures that develop in an EB over time. EBs differentiate into cells from all three germ layers [68, 264]. Other researchers have observed that EBs possess a variety of cell types with random patterns [105]. Early work by He et al. [125] observed that hESCs differentiate into multiple types of cardiac myocytes that display action potentials similar to nodal, atrial, and ventricular-like myocytes. Other work by Maltsev et al. [265] also revealed similar patterns in the cardiomyogenic differentiation of EBs. Maltsev's work showed that in newly differentiated EBs, the action potentials are homogenously similar to pacemaker cells; however, as the EBs further develop over time the development of atrial and

ventricular-like action potentials emerge with much more rapid upstroke velocities and a more heterogeneous mixture [264, 265]. This matches similar work showing that maturation leads to a more rapid current flux in older cardiomyocytes [266], and EBs containing multiple types of cardiomyocytes along with non-contractile tissue produces non-homogenous conduction [267]. Irregular beating rhythmicity and multiple foci are often present in later stages of EB cardiomyogenesis [264]. Multiple beating foci were observed in the current work (Supplemental Video), and sample-to-sample heterogeneity was significant. Using interferometry, Arshi et al. [224] monitored the erratic contractile properties of cardiomyogenic EBs after plating onto a monolayer of neonatal cardiomyocytes. Here, the beating profiles align well with the impedance assay performed on-chip. However, the method of mechanical interferometry used still requires integration with optical microscopes and high speed cameras [268] and may still not capture the 3D behavior of EBs due to focal plane constraints.

6.4.7 Inotropic Stimulation

The magnitude of the current change is related to the force of contractility of the EB due to the concentration of mobile ions in flux [135]. The amplitude of the peaks can therefore be monitored and correlated to the strength of contractility. For example, the amplitude of capacitance spikes changes after the delivery of epinephrine, can indicate inotropic stimulation [249]. Eight-week old EBs were subjected to inotropic stimulation by exposing the EB to a 50-μM-epinephrine environment. A field was applied around the EB in solution, and the capacitance and impedance were measured over time. The largest consecutive five peaks were

assessed before and after stimulation to compared changes in the peak amplitude. Figure 48 shows that the peak amplitude increased significantly for the tallest peaks in each spectrum (500 ± 28%). These observations were compared against contractility measurements performed by Chang et al. [141] They measured the cantilever deflection of an AFM probe after the delivery of epinephrine to beating cardiomyocytes. They observed an increase in deflection of 253 ± 39% after the delivery of 10-μM epinephrine. The chronotropic effects of epinephrine were more difficult to discern due to the inherit heterogeneity of EB beating profiles [60, 125]. Better spectra analysis may help categorize beat profiles to better identify frequency between similar beats. While future experiments may broaden the precision of these types of measurements, these initial experiments demonstrate the breadth of opportunities available to this platform.

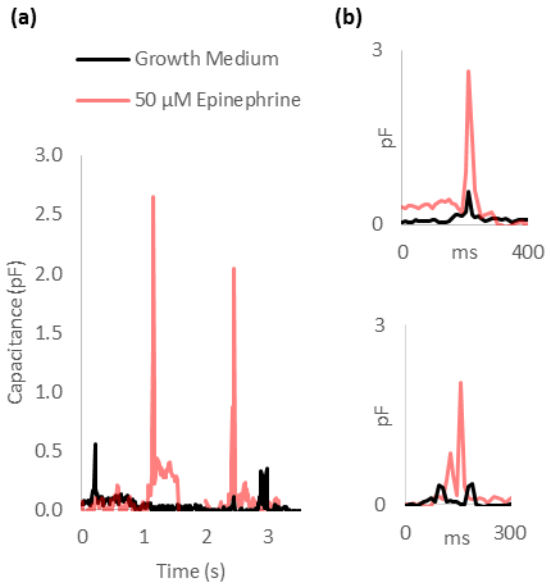

Figure 48. Positive inotropic stimulation of EB-derived cardiomyocytes was performed by delivering epinephrine and monitoring the magnitude change in the EB droplet capacitance. (a) Exposing the cardiomyocyte tissue to 50 µM epinephrine led to a ~5x increase in beating amplitude as measured by the change in the field capacitance. (b) Isolating and aligning individual beats allowed the comparison of similarly shaped peaks to measure changes in the capacitance.

6.5 Conclusions

A DµF lab-on-a-chip platform was designed for long-term cell culture, human embryonic stem cell differentiation into cardiomyocytes, and phenotypic analysis. The device was modified to enable stable, long-term actuation in an incubated environment. Success was achieved by re-evaluating the dielectric materials used in fabricating the device. The stability and functionality of the device in the elevated temperature and humidity environment were confirmed through direct

testing, assessment of droplet evaporation rates and droplet velocities. Hanging drops were formed on-chip to culture and differentiate hESC-derived EBs into cardiomyocytes. A stacked DμF design permitting vertical functionality was used for EB retrieval using DμF actuation. After EB retrieval, impedance sensing allowed the analysis of beating rhythmicity and peak shape. This ability to use impedance sensing on whole cardiomyocyte tissue enables the examination of 3D cardiomyocyte tissue maturation.

A benefit of using DμF as a stem cell niche lies in its versatility. DμF enables the culture of 3D and 2D monolayers [163] and certain hydrogels can be gelled in situ to enable the automated fabrication of more complex tissue structures. While our work demonstrates the ability to form hanging drops from cell suspension, and earlier work has demonstrated complete mammalian cell culture on-chip [163], the more complex protocols required for hESC harvesting were performed in a traditional cell culture environment. Future experiments may integrate hESC-culturing steps into the DμF for a more streamlined workflow. Another limitation of this design was the heterogeneity of beating EBs led to difficulty in analyzing some traits traditionally monitored for in vitro testing.

Recent work has sought to characterize the ratio of these phenotypes present in EBs [254] while other efforts have sought to direct their differentiation produce a more homogenous EB of a specific lineage [269]. These efforts are pursued because 3D tissue structures often recapitulate in vivo conditions and behaviors better than their 2D counterparts [67], and EBs can provide a more sophisticated tissue model [105, 267]. Furthermore, studying individual components of complex systems does not afford the same insight as understanding the entire system as a

whole [270]. In practice, cardiomyocytes from EBs are usually dissociated to isolate homogenous regions. Beating cardiomyocytes are then monitored either one cell at a time via methods such as the patch-clamp method [130], through point electrodes that measure a small tissue location [131, 271], or as a homogenously beating 2D monolayer [120]. Dissociating and re-seeding cell clusters can lead to more homogenous samples, but this process loses 3D growth patterns and information regarding maturation. Furthermore, a monolayer's substrate material has been shown to effect beating characteristics such as the number of activation sites, beating frequency and variability, ectopic heterogeneity, and development of reentrant arrhythmias [272]. Therefore, understanding the complex, heterogeneous structure of 3D EBs for cardiac tissue engineering and drug screening purposes will require more holistic systems to help characterize behavior of the entire structure and take a more systems biology approach [273, 274].

This lab-on-a-chip system brings the DμF platform closer to an automated 3D stem cell culture niche capable of long-term differentiation and assays. This tool can be further developed into a sophisticated drug-screening platform performing automated, parallel processing. Future work may entail the addition of more sensing capabilities and a higher multiplexing of differentiation protocols towards body-on-a-chip assaying models. Other work may take advantage of applied electrical fields themselves to direct differentiation.

6.6 ACKNOWLEDGMENTS

The authors would like to thank and acknowledge Haruko Nakano and the Atsushi Nakano lab in the Department of Molecular, Cell, and Developmental

Biology, UCLA College of Life Sciences, for providing human ESC derived EBs, differentiation media, and assistance with ESC culture. The authors would also like to acknowledge Ryan Fobel, Christian Fobel, and the Aaron Wheeler lab in the Department of Chemistry at the University of Toronto for extensive assistance with the DropBot system (http://microfluidics.utoronto.ca/dropbot/) and the μDrop software platform.

7 DIGITAL MICROFLUIDIC PLATFORM WITH INTEGRATED PIEZOELECTRIC/PYROELECTRIC SENSING

7.1 ABSTRACT

Digital microfluidics (DμF) is a miniaturized, lab-on-a-chip system that can manipulate liquid droplets through the application of electric fields. Some recent applications for DμF include cell culture and assay development. As more cell culture and assay protocols are streamlined into the DμF platform, more methods for biosensing will increase the array of on-chip procedures available and improve the amount of data that can be extracted. A PZT-based piezoelectric material was integrated with the digital microfluidic platform to add a new method for on-chip sensing of the heat produced from chemical reactions and the mechanical forces generated by beating cardiomyocytes. In one method of integration, the piezoelectric sensor was placed beneath a through-hole wherein droplets could pass through and reach the sensor. In another mode of integration, the substrate material was replaced with the piezoelectric material and electrodes were photolithographically patterned for on-chip sensing. The pyroelectric effect inherent in this piezoelectric material was exploited for on-chip temperature sensing of HCl dilution and ITO etching. The feasibility of detecting the mechanical forces generated from an adherent layer of beating cardiomyocytes was demonstrated by measuring the voltage changes generated through piezoelectric strain. Future researchers may use piezoelectric materials and similar device configurations for sensitive detection of chemical and biochemical processes for applications in

chemical processing and sample preparation, fundamental cell research, or drug screening.

7.2 INTRODUCTION

Lab-on-a-chip technologies aim to miniaturizize full-scale laboratory procedures to reduce reagent consumption, reduce costs, minimize human-related errors and tedium, and eventually automate procedures traditionally performed manually [10]. Integrating more capabilities has transferred more complex laboratory protocols from the benchtop to the lab-on-a-chip environment; ultimately bringing us closer to "walk-away" systems.

Digital microfluidics (DμF) is a lab-on-a-chip platform that has grown in sophistication over the last few decades. In DμF, the application of electric fields enables the manipulation (dispensing, translating, splitting, merging, etc.) of pico- to microliter sized droplets of liquid across an array of electrodes [25]. This platform has found myriad applications in such fields as analytical chemistry and biomedical engineering [162]. Advantages of DμF include reduced reagent volumes, faster reaction times, automation, and customization [14, 160, 193]. Complex assaying can be performed on-chip using tools such as magnetic beads or employing dielectrophoretic (DEP) forces for cell sorting [18].

Visual assays can be very effective when coupled with DμF platforms. Fluorescence microscopy has been used to characterize biological activity such as cell viability and protein production [275]. Imaging typically requires incorporating fluorescent labels, however, and the chemical modification process or the labels

themselves may alter cell behavior. Imaging methods that require may sample fixation inherently prevent further analysis of living systems. Mass spectrometry techniques can be very powerful for analyzing samples processed on DμF platforms, but cells are destroyed before or during the analysis. Recently, electrical measurements have been incorporated into DμF platforms to quantify cell behaviors non-invasively. Shih et al. used electrical impedance measurements to monitor cell proliferation, applying the method to a two-dimensional monolayer of fibroblasts on a small hydrophilic patch located on a DμF electrode[223]. As cells proliferated, the exposed electrode area shrank, altering the impedance measured between the ground and actuating electrodes. Sadeghi et al. also used impedance as a feedback mechanism for measuring chemical reactions [276]. Nelson et al. used conductive wires to act as both a resistive heater and a resistive temperature sensor [277]. The integration of these measurement techniques has increased the sensing power of DμF platforms; however, DμF still lacks the capability to measure the mechanical forces generated by cells. This is of interest for studying cardiomyocyte maturation and drug screening chronotropic or inotropic agents. An array of microposts is one MEMS-based technique for measuring forces in cells adhered to the tops of micromachined pillars [278]. As the cells contract, the micro-posts bend. The amount of bending can be correlated to cell forces based on the pillars' geometry and material properties. Zhao and Zhang adapted this design for measuring forces associated with cardiomyocyte contractility [139]. It is difficult to extract information on cell behavior from micropost arrays due to complexities associated with the micropost geometry, viscoelasticitiy, and their surface properties [140]. Atomic force microscopy (AFM) has also been used to characterize cardiomyocyte

contractile forces [141], but AFM requires complex equipment and is difficult to integrate into cell culture systems or downstream processing. As the field of cellomics expands, it has become evident that better non-invasive sensing modalities capable of real-time monitoring on a scalable platform are needed to accelerate advances in the field [212].

Piezoelectric transducers that can harvest energy from contracting cardiomyocytes have recently been developed [143, 144]. Piezoelectricity is the phenomenological coupling of mechanical and electrical properties. In piezoelectric materials, the polarization of the material along a given axis, $\mathrm{P_i}$, changes linearly with an applied stress, σ_i, in accordance with its piezoelectric coefficient, $\mathrm{d_{ij}}$, (Equation 41) [145, 146].

$$P_i = d_{ij}\sigma_i \qquad \text{Equation 41}$$

Pyroelectricity is the phenomenological coupling of thermal and electrical properties, and is a property that often accompanies piezoelectricity [146]. In pyroelectric materials, a temperature change will expand or contract the atomic crystal structure. This distortion of the crystal structure repositions internal charge and creates a net polarization [279]. The pyroelectric coefficient, p, is related to the change in net polarization, dP, with respect to the change in temperature, dT, (Equation *42*).

$$p = \frac{dP}{dT} \qquad \text{Equation 42}$$

Energy harvesting designs exploit this inherent property to turn cardiomyocyte contractility into a useable voltage. These systems are elegant in their simplicity, but these MEMS-based systems for measuring cellular forces would benefit from integration with an automated cell culture microenvironment [140]. Thus, liquid handling platforms such as DμF that are capable of automated cell culture may benefit from integrating piezoelectric sensors. We hypothesize that integrating materials with piezoelectric and pyroelectric properties could make it possible to detect heat changes and cardiomyocyte contractile forces on a DμF platform. Presented here are preliminary results demonstrating the feasibility of measuring the heat produced from chemical reactions and the contractility of adhered cardiomyocytes using a PZT-based piezoelectric sensor.

7.3 EXPERIMENTAL

7.3.1 Materials & Device Fabrication

APC850, a high d_{33} piezoelectric coefficient, lead, zirconium, titanium (PZT)-based ceramic, was purchased from APC International, Ltd. (Cat. #70-1000). This proprietary class of soft piezoelectric ceramics offered through APC International, Ltd. was chosen because they exhibit high piezoelectric coefficients, large electromechanical coupling factors, and are generally better suited for sensing applications than their class of hard piezoelectric ceramics generally reserved for high power generation. These samples possessed thin films of silver on each

surface that were left from the poling process. The piezoelectric coefficient was verified against the manufacturer's values using an AFM to perform piezoresponse force microscopy (PFM). The probe was pressed against the material and a bias sweep was applied to the tip. The change in probe deflection was monitored, and the rate of change between deflection (pm) and field bias (V) was calculated to approximate the d_{33} (pm/V) [280]. The d_{33} measurements obtained using PFM agreed with the manufacturer's specification of 400 (10^{-12} m/V).

The DμF devices were fabricated according to previously described protocols at UCLA's California NanoSystems Institute (CNSI) Integrated System Nanofabrication Cleanroom (ISNC) [194]. To fabricate electrodes onto the PZT substrate, a 100 nm layer of chromium, followed by a 1000 nm layer of gold was deposited using CHA evaporation. A photomask was printed on a transparency film (FineLine Imaging) and used to photolithographically pattern an electrode design by wet etching the Cr/Au layer. The interdigitated electrode pattern was based on a previously published electrode optimization study (Figure 49) [281]. Equal widths and spacings of 100 μm or 50 μm were used to measure possible differences in their sensitivity. The sensitivity of interdigitated electrodes will begin to decrease if the widths and spacings become too small, but the number of rings was chosen to closely match the size of the driving electrodes for droplet manipulation (~1 mm).

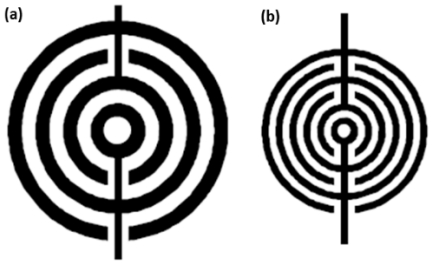

Figure 49. Interdigitated electrode designs tested, using electrode widths and spacing of (a) 100 μm and (b) 50 μm.

7.3.2 Configurations

PZT was used as a sensor in two configurations. First, a ~4 mm x 5 mm x 1 mm PZT material was positioned below a 1.1 mm diameter through-hole drilled through a DμF top plate (Figure 50a). Wires were connected to the conductive silver surfaces of on each side of the PZT sensor and monitored using a voltmeter. Second, the DμF top plate glass substrate was replaced entirely with a 25 mm x 25 mm x 1 mm PZT sample (Figure 50b). The silver surfaces on the PZT samples were removed using 320, 1000, and 2000 grit sandpaper, followed by a final polishing with 0.3 μm aluminum oxide powder. Then sample then underwent our typical processing protocols for top plate fabrication. Briefly, 110 nm of indium tin oxide (ITO) was deposited on one side of the sample followed by the deposition of a thin, hydrophobic top coat of Cytop®. The piezoelectric coefficient was measured again using PFM to ensure that the piezoelectric coefficient was not altered by the heating process. Finally, this second configuration was modified by photolithographically patterning the interdigitated gold electrodes (Figure 49) onto the reverse side of the substrate.

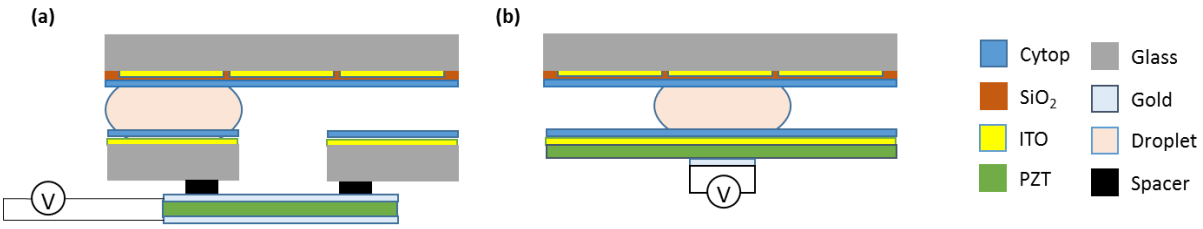

Figure 50. Two DμF device configurations were tested to investigate different ways of integrating piezoelectric sensing materials into a DμF system. (a) PZT sensor integration using a small PZT sample with continuous electrodes on opposing faces placed below a through-hole that permits droplets to pass through to the PZT surface. (b) PZT material was used to replace the glass substrate under the ground electrode; interdigitated sensing electrodes were patterned on the reverse side of the substrate. The dimensions are not to scale; the square driving electrode widths were 2 mm and the gap height was ~120 μm.

7.3.3 DμF Actuation

DμF actuation was performed using a DropBot system designed by Fobel et al. [192]. Droplets were translated by applying an AC field of ~90 V at 15 kHz. Droplets that were translated on the device to the through-hole were spontaneously pulled in via capillary forces.

7.3.4 Chemical Reactions

Four chemical reactions were performed on-chip. First, 37% hydrochloric acid (HCl) was diluted with DI water using the first sensor configuration (Figure 50a). Both solutions contained ~10 mg/mL methylene blue dye to improve visibility.

Droplets roughly 1 μL in volume were dispensed from on-chip reservoirs. A droplet of HCl was delivered to the through-hole and allowed to pass through to the PZT sensor surface. A droplet of DI water was then brought to the same through-hole and allowed to mix with the HCl droplet. The heat of dilution was recorded by monitoring the voltage change during this process using a nanovoltmeter. After the voltage returned to baseline, mixing was presumed to be complete. A droplet was dispensed from the mixed solution away from the through-out and discarded. A second droplet of DI water was then dispensed and brought to the same solution for a second dilution. Again, the voltage was measured during the diffusive mixing process.

In the second experiment, a droplet of 37% HCl was brought to a through-hole and allowed to pass through to the underlying PZT sensor. This sensor had continuous layers of silver on both sides and was similarly arranged for measuring the voltage. On one side facing the through-hole, a continuous, 110 nm layer of ITO had been deposited over the silver. The droplet of HCl began etching the ITO layer immediately upon contact, and the voltage was measured until the reaction was complete.

Third, a droplet of 37% HCl was diluted with DI water using the first PZT sensor configuration (Figure 50b). Instead of having continuous silver electrode sensors, however, the interdigitated electrode sensor was patterned on the PZT material and positioned directly below the through-hole. A droplet of HCl was delivered to the through-hole and allowed to pass through to the PZT sensor surface. A droplet of DI water was then brought to the same through-hole and

allowed to mix with the HCl droplet. The heat of dilution was recorded by monitoring the voltage change during this process using a nanovoltmeter.

Fourth, a droplet of 37% HCl was diluted with DI water using the second PZT sensor configuration (Figure 50b). A ~1 μL droplet of HCl and a ~1 μL droplet of DI water were translated and mixed horizontally within the 2D plane of DμF operation. They mixed directly above the interdigitated electrode positioned on the reverse side of the PZT. The electrodes were connected to a nanovoltmeter, and changes to the voltage were measure during mixing.

7.3.5 Cell Culture

Human embryonic stem cell embryoid bodies (EBs) were graciously provided by Atsushi Nakano's lab at UCLA (Department of Molecular, Cell, and Developmental Biology, UCLA College of Life Sciences). Two-week old EBs had been differentiated into functional cardiomyocytes as verified by visualizing the onset of spontaneous beating. The EBs were transferred to a DμF and pipetted onto a reservoir. The EB was dispensed and translated to a 1.1-mm diameter well drilled into the PZT substrate located above the patterned sensing electrodes on the reverse side. The depth of the well was approximately 250-300 μm, measured using profilometry. The PZT substrate was moved to a cell culture incubator and allowed to culture for 3 days at 37 ^{0}C, 5% CO_2, and 95% relative humidity.

7.4 Results and Discussion

7.4.1 Pyroelectric sensing

Pyroelectric sensing was performed on a DμF device by integrating a PZT-based material using different configurations. The heat generated by diluting 37% HCl with DI water was monitored by measuring the voltage generated by the PZT sensor (Figure 51). A ~1 μL droplet of HCl was first delivered to the through-hole where it was pulled in via capillary forces and brought in contact with the PZT sensor below. Upon coming in contact with the PZT sensor, a small but detectable voltage spike was produced. A droplet of DI water was then dispensed from a reservoir using DμF actuation and translated to the HCl solution for mixing. The voltage rapidly rose by approximately 60 mV upon mixing. The voltage gradually declined back to baseline over the course of around 10 s. A second droplet of DI water was then dispensed and mixed with the remaining solution to dilute the sample a second time. Again, the voltage quickly rose, but by an expectedly smaller amount of approximately 26 mV. The second rise was presumably smaller due to the lesser extent of dilution that would occur during serial mixing steps.

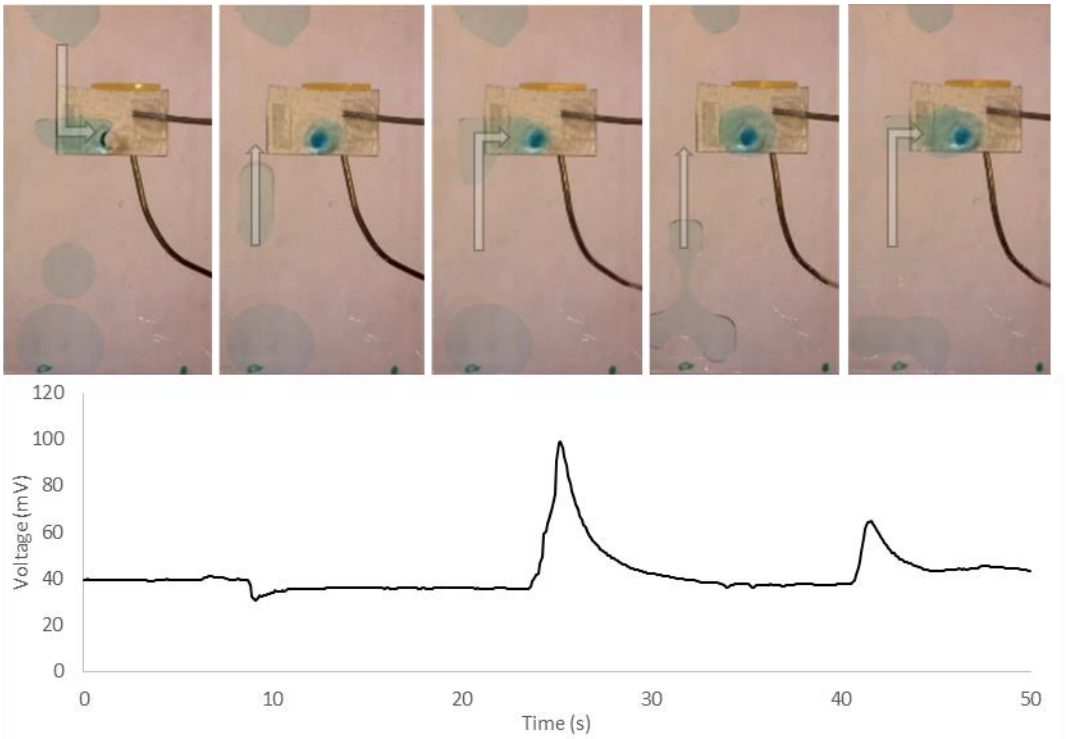

Figure 51. The heat of dilution created by mixing droplets of 37% HCl and DI water was monitored by measuring the voltage created using a piezoelectric PZT-based sensor. The top row of images show the sequential steps of droplets delivered to the through-hole and mixed while in contact with the PZT sensor below. The voltage reading below shows the change monitored during mixing.

The exothermic heat of dilution experiment was repeated using an interdigitated electrode design placed directly beneath the through-hole (Figure 52a). The droplets were mixed directly on top of the interdigitated electrodes. A detectable voltage change was again produced upon droplet mixing. The two interdigitated electrode designs (Figure 49) produced similar voltage profiles (Figure 52b).

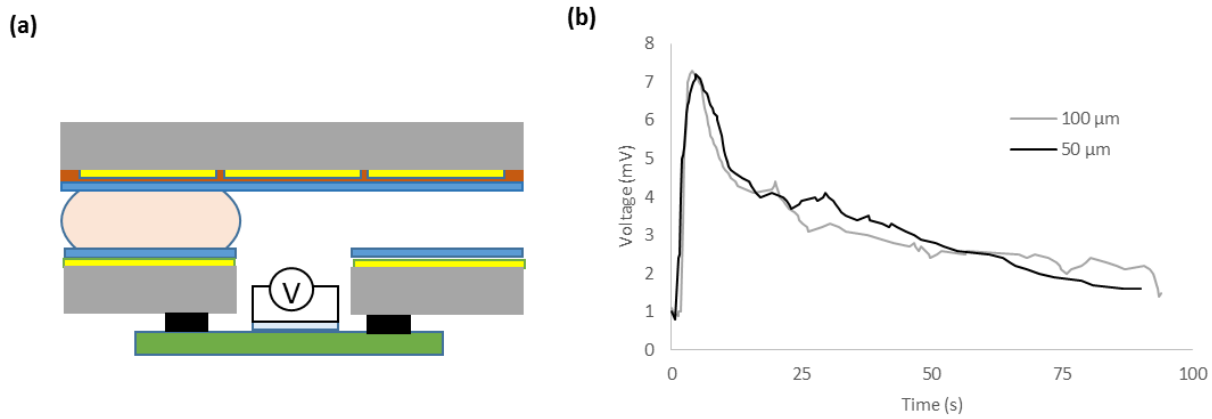

Figure 52. An interdigitated electrode design was used to compare methods for monitoring the voltage due to the heat of dilution generated from mixing 37% HCl with DI water. (a) A side schematic shows the change in electrode configuration. (b) The heat of dilution of 37 % HCl and DI water mixed directly on the gold electrodes showed a rapid spike in voltage of around 7 mV that slowly returned to baseline in around 100 s. The interdigitated electrodes with 50 µm and 100 µm widths and spacings produced similar voltage changes.

To monitor a chemical reaction in real time, a droplet of 37% HCl was delivered to an exposed area of ITO. HCl catalyzes the dissolution of ITO through a chemical reaction immediately upon contact with sputtered ITO [282]. This was evidence by the sharp spike in the voltage upon contact between the HCl droplet and the exposed ITO surface.

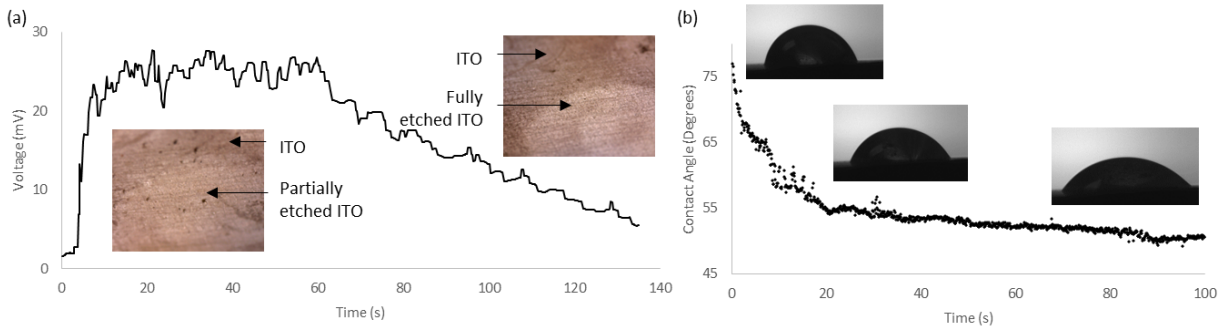

Figure 53. The etching process of ITO with 37% HCl was monitored by measuring the voltage change across the piezoelectric sensor. (a) Upon contact of 37% HCl with an ITO thin film, the voltage rapidly spiked indicating the onset of an exothermic chemical reaction; the voltage remained elevated before returning to baseline. (b) The droplet spread and the contact angle rapidly decreased until it attained the equilibrium contact angle of aqueous HCl on PZT.

The voltage generated by the chemical reaction between a droplet of 37% HCl on top of a thin film of ITO is most likely explained by a momentarily sustained surface reaction and the dynamics of droplet spreading over time. The rapid spike upon initial contact results from the initiation of the chemical reaction between ITO and HCl. The reaction generates a temperature gradient that in turn generates a voltage via the pyroelectric effect of the underlying PZT substrate. The reaction reaches a steady-state equilibrium as the entire ITO film is etched away. The heat rapidly dissipates into the surrounding environment while new ITO is continually exposed and etched by the HCl, maintaining a temperature gradient. As the ITO film is etched, the droplet comes into contact with the underlying metal electrode and spreads out (decreased contact angle). The reaction slows as the HCl droplet

can no longer access the ITO film, and the temperature of the PZT substrate equilibrates as the reaction stops.

7.4.2 PZT Substrate Configuration

Although placing a piezoelectric sensor under a through-hole can be effective and efficient for certain applications, simplifying the system by replacing one of the traditional glass substrate materials with a piezoelectric material could reduce system complexity by reducing the number of components. The top plate fabricated using the PZT substrate performed equally well at allowing facile droplet translation.

The heat of dilution experiment was repeated by horizontally mixing a droplet of 37% HCl with DI water. The mixing was performed at the location directly opposite the interdigitated electrode on the reverse side of the PZT substrate (Figure 50b). The heat generated was effectively monitored by measuring the voltage changes. The different interdigitated electrode widths did not produce markedly different profiles (Figure 54).

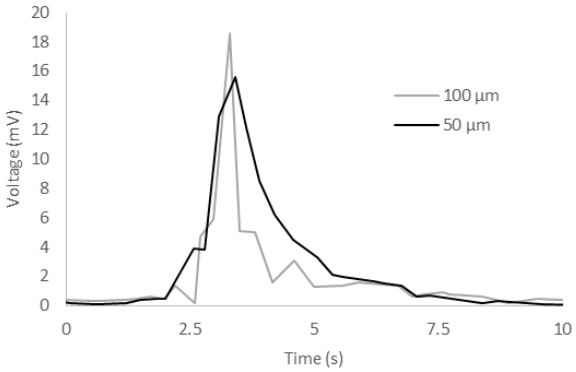

Figure 54. The heat produced from mixing 37% HCl with DI water was monitored by measuring the voltage change generated in the piezoelectric substrate via interdigitated electrodes located on the reverse side of the substrate. A voltage change of roughly 16 mV was produced with and a rapid decline back to baseline in around 5 s. Both the 100 µm and 50 µm interdigitated electrode designs showed comparable voltage changes.

7.4.3 Piezoelectricity

Recently, the Garrell lab at UCLA developed a method for forming hanging drop cell cultures [181], culturing and differentiating embryoid bodies of human embryonic stem cells into functional cardiomyocytes, and retrieving the embryoid bodies using vertical functionality. We have built upon this work to develop an on-chip method for measuring cardiomyocyte contractility behavior using piezoelectricity. After delivering an EB containing 2-week-old differentiated cardiomyocytes to the PZT well (Figure 55a), the EB was allowed to settle and incubate for 72 h to adhere to the hydrophilic surface. After adhering to the surface, the cardiomyocytes pull on the substrate surface as they spontaneously

contract (Figure 55b). This stress imparted by the contracting cardiomyocytes produces a strain in the piezoelectric surface and a detectable voltage change (Figure 55c). The voltage signal produced periodic perturbations with spacing similar to the beating behavior captured through video recordings of around 0.25 – 0.5 Hz. The system was monitored using only air, only the wires, and cell culture media without any cells as controls to determine the level of noise.

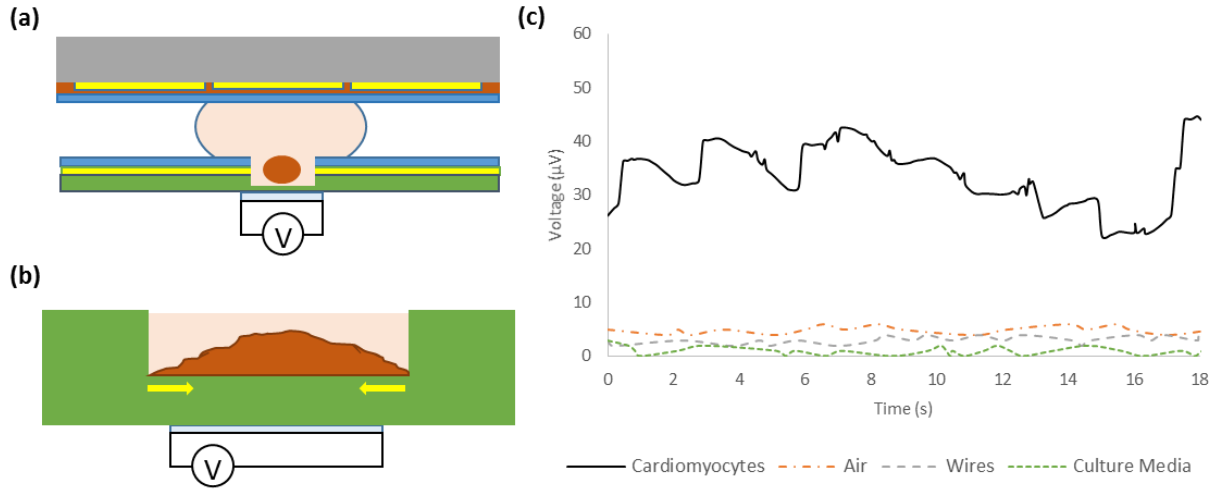

Figure 55. Embryoid body-derived cardiomyocytes were cultured in wells drilled into the PZT substrate to measure the piezoelectric voltage change created from spontaneous beating. (a) Schematic showing a droplet of culture medium containing an embryoid body consisting of 2-week-old differentiated cardiomyocytes was delivered to a drilled well opposite the electrode. (b) A magnified representation of the well shows that after 72 h in incubation the cells adhered to the surface of the PZT substrate inside the well and produce a shear force during spontaneous contraction. (c) The voltage response was monitored over time, showing characteristic repetitive peaks that emerge above the noise.

The well creates a thin region between the cell adhesion site and the interdigitated sensing electrodes. The larger strain resulting from this thinned region produces a larger voltage during contraction. The voltage changes show irregular and ill-defined peaks (Figure 55c). Variability in peak profiles existed between the 5 samples tested (data not shown). Each profile produced periodic voltage changes that were similarly above the system noise. The peak shapes between samples, however, also varied in the amplitude of the voltage change and the rate of change of voltage spikes. The variability could arise from several factors related to the device materials and fabrication. For example, the substrate material properties can have an effect on the beating periodicity, variability, ectopic heterogeneity, and arrhythmia development in adhered cardiomyocyte monolayers [272]. The wells were fabricated using a drill press that resulted in a relatively rough surface profile as measured using profilometry. The angle variations associated with a rough surface profile likely cause irregularities in the output voltage because the piezoelectric coefficient is highly orientation-based and the magnitude of transduction depends on both the crystal orientation and the poling direction [279]. Therefore, the strains induced by contracting cardiomyocytes were likely produced in inexact alignment that resulted in varying degrees of signal output and signal loss. In addition, 3D cardiomyocyte EBs possess inherent heterogeneity [224, 264, 265]. The voltage reading also depends upon electrode, wire, and voltmeter properties [281], and inefficiency and charge loss are inherent piezoelectric materials properties [279]. Future work in this area may make use of better cell attachment methods, cell separation technologies, or substrate surface modifications for improved signal generation and quantification.

7.5 CONCLUSIONS

Piezoelectricity and pyroelectricity have been integrated into a DμF platform for on-chip sensing applications. The two configuration tested include a sensor placed beneath a through-hole, and the replacement of a glass substrate with a piezoelectric substrate. The piezoelectric sensor could effectively monitor the heat of dilution of 37% HCl and the etching of an ITO thin film in real-time on-chip via the pyroelectric effect. Additionally, piezoelectricity may prove to be a sensing method for observing on-chip cardiomyocyte contractility. This technique may be used for fundamental studies in cell contractility force or pharmaceutical screening. It is difficult to quantify and analyze the data due to the variability in the voltage changes within a single sample and between samples, but improvements to substrate preparation and electrode design may provide a sensitive platform for measuring biochemical and mechanical phenomena using DμF.

In addition to sensing applications, future applications may include the use of piezoelectric materials for actuation. For example, the ability to impart minute strains on stem cells or immature cardiomyocytes may introduce new on-chip methods for directed differentiation or beat pacing. One barrier to adoption may be the cost of high piezoelectric coefficient materials like PZT and PMN-PT. To create a more economical solutions that could drive commercial adoption of these sensing capabilities, less expensive choices may be considered. For example, poly-vinylidene fluoride (PVDF), a known piezoelectric polymer [283], be easily spin-coated onto a device and becomes optically transparent when crystallized into the piezoelectric α phase. While the piezoelectric and pyroelectric coefficients of PVDF

are considerably smaller than materials like PZT, proper electrode and DμF design may make this material suitable for certain applications.

7.6 Acknowledgments

The authors would like to acknowledge the Nakano lab at UCLA for providing human embryonic stem cell-derived cardiomyocyte embryoid bodies. The authors would like to acknowledge the California NanoSystems Institute (CNSI)'s Integrated Systems and Nanofabrication Cleanroom (ISNC) for cleanroom equipment used in the fabrication of devices used in these experiments. Finally, the authors would like to acknowledge the Wheeler lab at the University of Toronto for providing materials, training, and assistance with their DropBot platform and μDrop software package.

8 FUTURE DIRECTIONS

8.1 ABSTRACT

This chapter provides future researchers with relevant topics to pursue to further improve the sophistication of DμF-based tissue culture systems. The role that the DμF platform may play with regards to more complex tissue culture systems is presented to suggest its potential to become a body-on-a-chip platform for personalized drug screening. The ability for the DμF platform to impart electric fields suggests at least two relevant research topics: the use of electric fields to direct cardiomyogenic behavior; and the use of dielectrophoretic forces to stretch cells for characterization and directed differentiation.

8.2 TISSUE CULTURE, AND TOWARDS A BODY-ON-A-CHIP PLATFORM

This work has demonstrated the first use of a DμF platform for the long-term culture of human embryonic stem cells and integration with in situ assays. Clearly DμF systems could be used to support the differentiation of other cell lines, as demonstrated through the adipogenesis of mouse mesenchymal stem cells in Appendix B. Replacing embryonic stem cells with induced pluripotent stem cells (iPSC) could further direct DμF research into personalized drug screening and towards a so-called body-on-a-chip platform.

The technical innovations and proof-of-principle establish the potential for using DμF as an alternative platform for tissue engineering. The ability to culture

individually addressable culture sites on a DμF platform in parallel suggests the possibility of a body-on-a-chip system, whereby an individual's iPSC's are dispensed and cultured on-chip into each of their major organ systems simultaneously. A therapeutic could then be dispensed and delivered to each system simultaneously and its effects analyzed in situ. This approach has the potential to yield more accurate information on an individual's drug response compared to current methods [284].

Testing drugs in 2D cell culture systems produce untrustworthy results due to unnatural cell states, animal models have obvious physiological differences, and even human diversity produces varying levels of therapeutic success and patient-specific side-effects. The ability to reduce drug development time and better predict patient-specific outcomes renders DμF with iPSCs a tantalizing combination. Heart, liver, kidney, brain, and lung-on-a-chip platforms have been developed and are improving in sophistication [284]. The innovations of this dissertation will help researchers investigate these opportunities using DμF systems.

8.3 Electric Field Stimulation for Directed Cardiomyogenesis

Stimulation via electric fields and current can impact cardiomyocyte-directed differentiation [83, 285]; but the extent to which these stimuli effect cardiomyogenesis is not fully understood. The ability to impart electric fields presents an opportunity for DμF as a future tool for investigating electric field stimulation for directed cardiomyogenesis. By considering electrode array and dielectric coating designs, a system could be developed that would allow the

application of either AC or DC fields. These applied stimuli could vary in amplitude, frequency, or duration to investigate future cell and tissue effects. A major advantage this DμF platform could have over other research tools is the ability to impart electric fields while simultaneously delivering chemical or biochemical agents. This ability to multiplex external stimuli on an automated culture platform could greatly simplify and streamline studies in tissue maturation. Furthermore, modulation of the electric field, coupled with a cleverly designed array of electrodes, could permit constant electric field impedance sensing while intermittently imparting electric field stimulations.

Another fuse of applied electric fields could be for investigation drug interactions both before, during, and after a cardiac conduction block [133, 134]. The ability to impart AC fields naturally lends itself to these types of studies. There is a dearth of high-frequency AC field investigations, but research suggests these may be important tools for understanding future developments of more effective defibrillators and therapeutics.

8.4 DIELECTROPHORETIC (DEP) CELL STRETCHING

Stretching cells using DEP forces is a relatively new technique that will be presented and discussed with regards to integration with DμF and stem cell niche development. The use of DEP forces for characterizing biomechanical cell properties is introduced, followed by a review of the theories regarding the underlying physical mechanisms that drive this phenomena. Several applications for DEP cell stretching

from the literature are reviewed, followed by opportunities for future DEP-related research using DμF.

There are a multitude of diagnostic systems for various diseases and cancers that vary in their complexity, detection capabilities, cost, and accessibility [286, 287]. Early detection can improve patient outcomes, and reducing the cost of diagnostics can promote their use, particularly in developing countries [287]. An interesting approach has been to utilize cellular biomechanics as a tool for assessing a cell's phenotypic state [288, 289]. Understanding cellular biomechanics and biophysics has become an important tool for elucidating the qualitative and quantitative behavior of biological cells from the differentiation capability of stem cells [289, 290] to elucidating disease pathways and cancer development [288, 289, 291]. Many techniques have been used to study the biomechanics of cells, such atomic force microscopy [292], scanning ion conductance microscopy [293], magnetic twisting cytometry [294], sheared cell monolayers [137], micropipette aspiration [295], optical tweezers [289, 296], microplate rheometer [297], optical stretcher [298], hydrodynamic stretching [299], and bulge generation method [300]. Although these methods can be used to probe the biomechanics of single cells, they typically produce a variations in values among tests [288, 301]. Many of these tests are also destructive and prevent downstream processing [302]. For example, some methods require the conjugation of magnetic beads, which could alter cell behavior associated with surface proteins.

The ability to deform biological cells in a microfluidic environment using dielectrophoresis (DEP) is an emerging technique that is being used to study and quantify electrical and mechanical cellular properties that may offer a new approach

for more accurate and consistent measurements [205]. DEP has found wide use and applications across scientific and engineering fields involving biological cells. DEP forces have been used to manipulate biological cells through translation, orientation, rotation, and deformation [45]. Only recently has DEP induced cell deformation been used to quantify cell deformation for cell line characterization and downstream processing. Measured cell mechanical properties include the elastic [300, 301] and shear moduli [41], Poisson ratio [41], relaxed elastic [41, 302] and shear moduli [41], and viscosity [41]. Simulations have been performed with electrodeformation in conjunction with varying cell electrical properties, including conductivity and membrane relative permittivity, to better understand electro-mechanical properties [303].

DEP-induced cell deformation within a microfluidic regime offers several advantages for mechanical assessment: it eliminates the need for moving parts or micro-beads; it minimizes the contact between cells and device structures; it can be performed using an instrument that is easy to develop using well established micro-fabrication techniques that are cheap and offer low energy demands; it offers the ability for integration with other microfluidic DEP manipulation techniques such as aligning, sorting, and positioning; and it develops a platform for automated and non-destructive high throughput operations [41, 302].

Biological cells are often modeled as conductively neutral, dielectric particles that become polarized in the presence of an applied AC electric field. Biological cells may be modeled as layered spherical shells. This approach converts a layered spherical particle with multiple complex permittivities to a homogenous sphere with an effective relative complex permittivity as shown below [34] (Figure 56, similar to

Fig. 2.3 in Jones [34]). The complex effective relative permittivity described in Equation 14 describes how this equivalent homogenous sphere relates to the layered dielectric shell model.

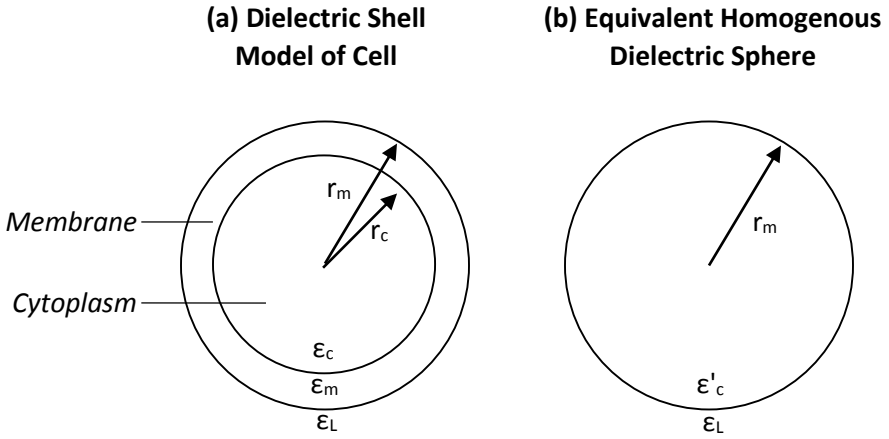

Figure 56. Cell modeling schematics. (a) The spherically symmetric layered cell model, and (b) a homogenous sphere.

Single cell compression tests using modified atomic force microscopy (AFM) tips have identified a force-displacement relationship expressed by Equation 43 [304].

$$F_{DEP} = F_{cytoskeleton} + F_{membrane} \qquad \text{Equation 43}$$

By substituting equations for the DEP force (Equation 43) and equations derived from the elastic theory of membranes and Hertzian contact mechanics [304], the force-displacement relationship can be estimated by Equation 44.

$$2\pi r_m^3 \varepsilon_L Re\left(\underline{K}\right)\nabla E_L^2 = \frac{\sqrt{2}E_c}{3(1-\nu_c^2)} r_c \varepsilon_s^{\frac{3}{2}} + \frac{E_m}{1-\nu_m} h r_m \varepsilon_s^3 \qquad \text{Equation 44}$$

where, ε_s, is the cell strain, h, is the membrane thickness, r_m, is the membrane radius, E_c, is the cytoplasm elastic modulus, E_m, is the membrane elastic modulus, ν_c, is the cytoplasm Poisson ratio, and, ν_m, is the membrane Poisson ratio. The DEP force was plotted as a function of strain to estimate the amount of cell deformation imposed with initial conditions of a 100 V signal at 3.7 MHz with mesenchymal stem cells (h of 5 nm [33], E_m of 1.5 GPa [33], E_c of 1.9 kPa [33], ν_m of 0.5 [304], ν_c of 0 [304], r_c of 7 μm [41]) in cell culture medium (σ_L of 0.048 S/m [33], ε_L of 78 [33, 34]) (Figure 57). This creates a ~26 nN positive DEP force on the cell that produces a strain of ~0.35. These results are on an order of magnitude similar to the results found for Chinese hamster ovary cells and U937 human promonocytes [41].

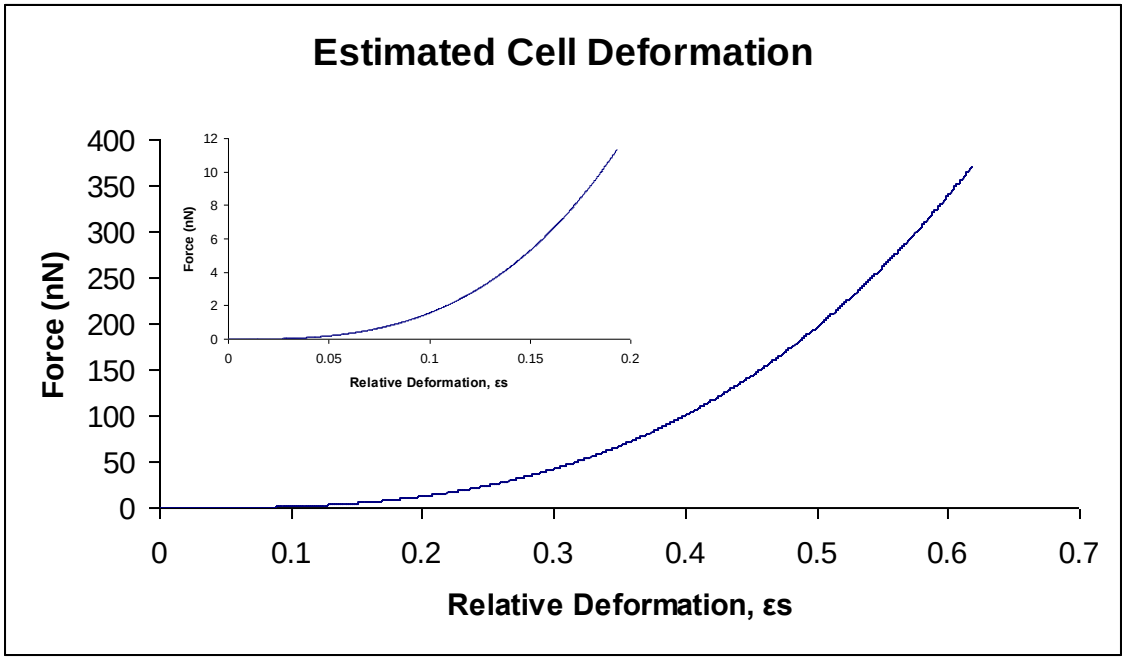

Figure 57. The relative deformation as a function of force from Equation 44. In-set magnifies the small deformation regime.

The Clausius-Mossotti function depends on the polarizability of the cell membrane and cytoplasm, which may possess different kinetics, and exemplifies the profound effect frequency can have on DEP behavior. The magnitude and sign of the DEP force depends on the electric field gradient, the field frequency, and the relationship between the cell and medium permittivities. In typical microfluidic configurations, the magnitude of the DEP force is on the scale of piconewtons to micronewtons [40]. Positive DEP (pDEP) forces attract particles toward an electric field intensity maxima and occur when $Re(K) > 0$, and negative DEP (nDEP) forces repel particles away from electric field intensity maxima and occur when $Re(K) < 0$ (Figure 58a) [34]. The shape of cell deformation also has been shown to be a

function of frequency and the ratio of the intracellular to extracellular conductivities (Figure 58b) [204, 305].

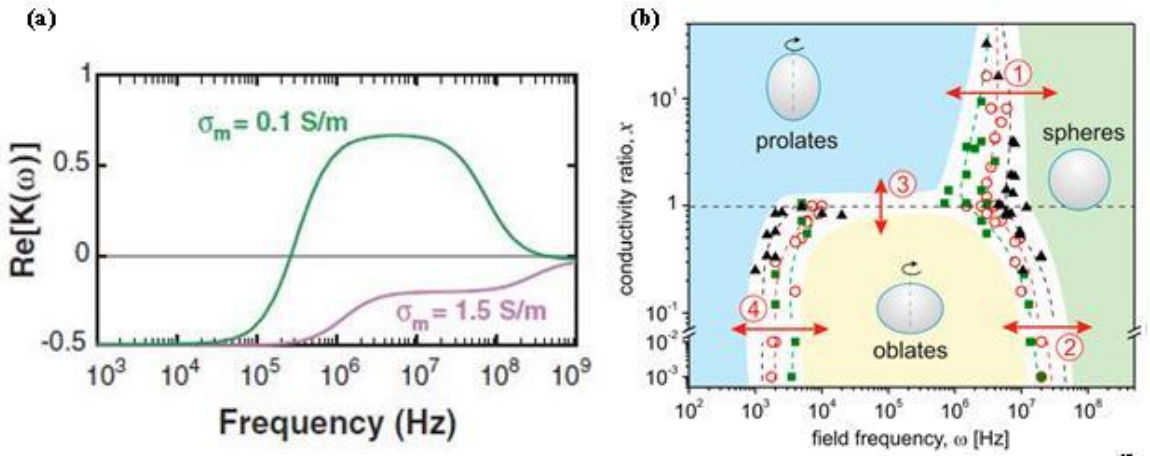

Figure 58. Modeling of the cell response to electric fields of varying frequencies. (a) The sign of the Clausius-Mossotti function, dependent on cell and medium conductivities, will dictate the direction of the DEP force (reprinted from [45]). (b) The lipid vesicle deformation dependence on the intracellular to extracellular conductivity ratio and the field frequency also exhibited by cells subjected to DEP forces in a microfluidic environment (reprinted from [305]).

8.4.1 Proposed Mechanisms of DEP-Induced Cell Deformation

The mechanisms involved with DEP induced cell deformation are debatable and not yet fully understood. Some numerical approaches, such as a study performed by Li et al. [206] models cell deformation in a nonuniform AC electric field through the use of a Maxwell stress tensor model. Here, a membrane force accounts for the bending rigidity, while the DEP force is calculated across the membrane as a function of the electric field intensity. An erythrocyte cell was

computationally modeled while flowing down a microfluidic channel lined with electrodes (Figure 59). The nonuniform field gradient is strongest on the cell near the electrode and causes a negative, inward DEP force at a relatively low frequency of 2π kHz and a positive, outward DEP force at a relatively high frequency of 2πGHz. The change from nDEP to pDEP force occurs at the crossover frequency of around 2π MHz and is dependent on the relative permittivities of the cell and suspension medium. However, models such as these are not broad enough to account for such experimentally observed phenomena such as dependence on cell and media conductivity ratios as well as unusual transient shapes like cylinders seen in cells other than erythrocytes.

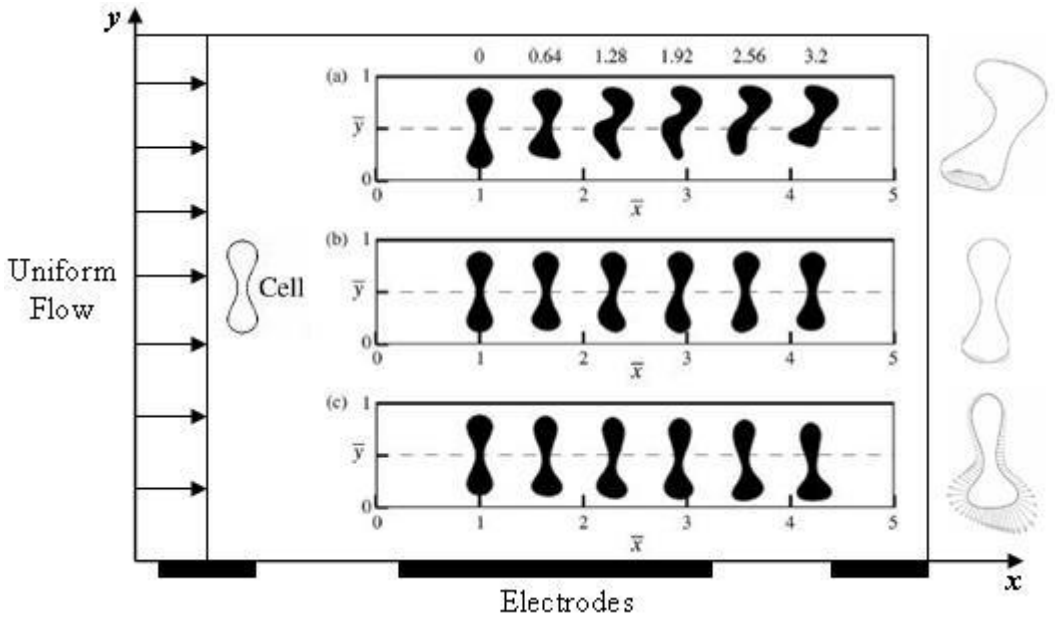

Figure 59. Modified figure from Li et al. [206] that depicts erythrocyte deformation in a microfluidic channel subjected to AC electric fields at (a) 2π kHz, (b) 2π MHz, and (c) 2π GHz. Images on the right depict the inward, negative DEP forces at relatively low frequencies (a), nearly neutral DEP forces at the crossover frequency (b), and the outward, positive DEP forces at relatively high frequencies (c).

Vlahovska et al. [204] used a different approach, modeling analytically the transient vesicle deformation employs a force balance approach to numerically evaluate the electric, hydrodynamic, bending, and tension forces exerted on the membrane. By rigorously accounting for electric, hydrodynamic, bending, and tension forces, this force balance model can account for deformation magnitude and behavior better than previous theories that are based on energy minimization approaches. This approach accurately describes experimentally observed cell deformation phenomena such as the frequency and conductivity ratio dependencies

based on a model incorporating electrohydrodynamic flows within the cellular cytoplasm (Figure 60).

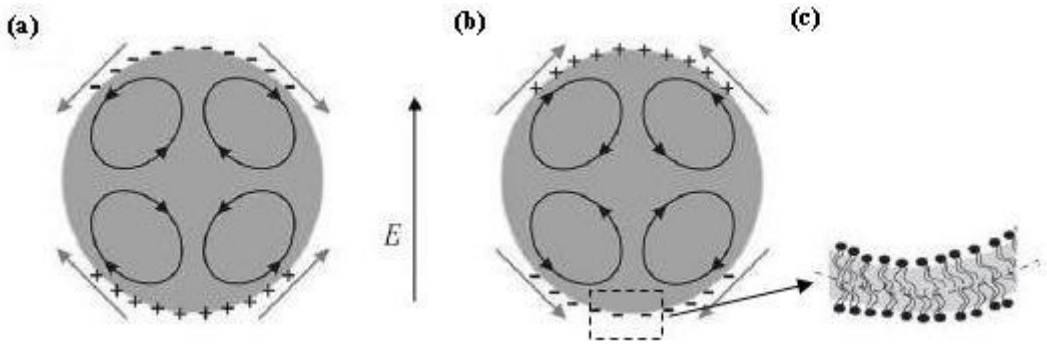

Figure 60. Modified image from Vlahovska et al. [204] that depicts (a) the intracellular electrohydrodynamic flows that produce oblate ellipsoids when the internal conductivity is lower than the surrounding medium, (b) prolate ellipsoids when the internal conductivity is higher than the surrounding medium, and (c) tension in the lipid bilayer.

8.4.2 Applications

Emerging applications for DEP-induced cell deformation demonstrate the opportunities this technique may provide for cell line characterization, diagnostics, and fundamental cell research. After introducing research into these applications, lab-on-a-chip platforms that integrate DEP-induced cell deformation are reviewed. These application may be well suited for integration with DμF-based lab-on-a-chip platforms. DEP-induced cell deformation may also be useful as a tool for directing stem cell differentiation, particularly with respect to cardiomyogenesis.

The intracellular stress induced through mechanical strain provides important signals for cellular functions such as remodeling, healing, homeostasis, migration, proliferation, gene expression, protein synthesis, and differentiation [78, 208]. Better understanding the roles of cellular mechanics and mechanobiology has led to improving implant design, clinical evaluations, and tissue engineering applications [306]. Cells of various lineages or phenotypic states possess different mechanical properties that arise from different cell structures, such as varying membrane rigidity or cytoskeleton composition [302]. Different cell lines also possess different mechanobiology, and respond differently to mechanical stimuli by altering gene expression and protein synthesis. One way DEP-induced cell deformation has been used to exploit this phenomenon advantageously was by measuring cellular mechanical properties and differentiating between cell lines based on the magnitude of the DEP-induced strain [41, 302].

8.4.2.1 Cell Line Characterization

Characterizing cell lines can be an important processing step in many assays, and the application of DEP forces to measure cell deformation is a new approach that is non-invasive and easily integrated with streamlined culture and assay platforms. Cell lines differ in cytoskeletal composition and therefore have different mechanical properties [41, 208, 302]. For cell identification purposes, it may be useful to measure mechanical properties and distinguish between distinct cell lines. MacQueen et al. [41] estimated cellular mechanical properties, including the Young's Modulus and the Poisson ratio, and demonstrated the ability to distinguish between Chinese hamster ovary (CHO) cells and U937 human promonocytes

through DEP-induced deformation. Ti/Pt electrodes with thicknesses of 10/70 nm were deposited through electron beam evaporation and sputtering atop glass slides. A 550 nm hydrogenated silicon nitride dielectric later was deposited over the electrodes to prevent electrolysis (Figure 61).

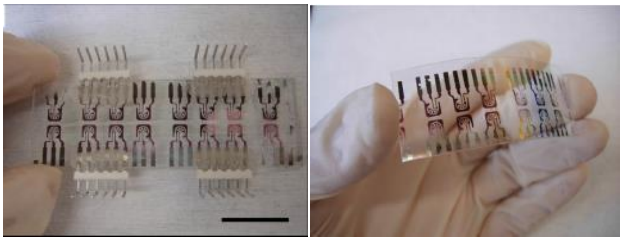

Figure 61. Microfluidic device fabricated on a glass slide that enables DEP-induced deformation for cell-line characterization through Young's Modulus calculations. The same pattern was fabricated on a flexible polymer (reprinted from [41]).

A low conductivity medium was used with an electric field generated at 5 MHz and 2 V for cell trapping and 10 V for stretching. An optical microscope was used to observe and quantify the degree of cellular deformation and calculate the strain. These experiments demonstrate the use of biomechanical characterization and the potential for integration with other microfluidic processes. MacQueen et al. also demonstrated their device could be fabricated on a flexible polymer substrate, paving the way for additional insights and potential applications.

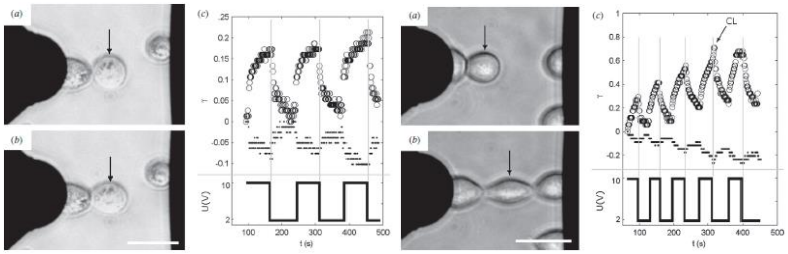

Figure 62. DEP induced cell deformation used to measure viscoelastic mechanical behavior and distinguish between CHO cells (left) and U937 cells (right) through DEP-induced deformation (reprinted from [41]).

A study by Chen et al. [303] used dielectrophoretic cell deformation to measure the Young's modulus of SiHa and ME180 cells (Figure 63). Here, SiHa and ME180 cells were suspended in an isotonic sucrose solution with low conductivity to permit pDEP manipulation. A microdevice with patterned electrodes was developed where single cells were positioned using a robotic manipulator and viewed while applying a voltage in a step-wise manner at frequencies of 500 kHz, 1 MHz, and 5 MHz. A numerical analysis employing the Maxwell stress tensor model was performed, and varying electrical properties were analyzed to simulate the electrodynamic forces generated on the cell. The experimental Young's modulus obtained was comparable to that of micropipette aspiration measurements and thus helps to validate the use of DEP-induced cell deformation for measuring mechanical properties.

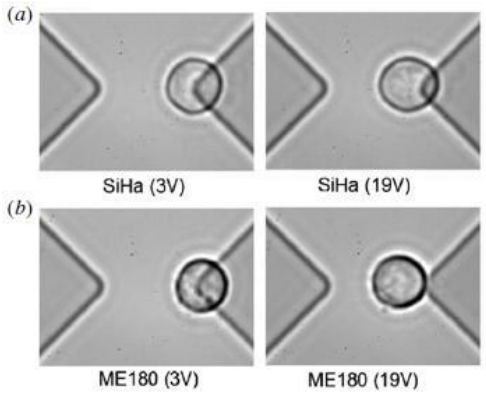

Figure 63. Image from Chen et al. [303] showing DEP-induced cell deformation for accurate characterization of the Young's modulus for SiHa and ME180 cells.

8.4.2.2 Cell Behavior and Diagnostics

The biomechanics of cells play an important role in many cellular behaviors, and studying the physics of live cells in different environments can elucidate fundamental understanding of intracellular functions and disease pathways [307]. Guido et al. [308] used DEP to stretch live cells to measure the effect of medium consumption on cell elasticity. A microchip was designed using ITO electrodes spaced 20 μm apart on top of a glass slide encased in a silicone trough (Figure 64). Experiments used culture medium concoctions of various pH and nutrient levels to study its effect on HL-60 cell elasticity during DEP-induced deformation. The results found that nutrient depletion increases the degree of cell strain, and presents a model that exemplifies the ability to observe a living cell's dynamic response to chemical variations using dielectrophoretic deformation.

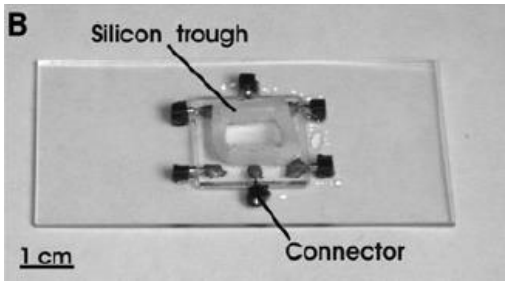

Figure 64. A microfluidic device designed to measure a living cell's elasticity using DEP-induced deformation while varying the chemical environment (reprinted from [308]).

As with different cells lines, cancer cells also possess a different elastic modulus due in part to differences in the cytoskeletal composition. A study by Guido et al. [302] used an electrode patterned microfluidic device to unambiguously distinguish between cancerous human breast adenocarcinoma cells (MCF-7) and noncancerous human nontumorigenic epithelial cells (MCF-10A) in an aqueous suspension (Figure 65). This study also monitored the dynamic mechanical behavior of live cells receiving cytoskeletal toxins to observe real time cytoskeletal behavior. This study exemplifies the ability to identify cell lines based on DEP-induced mechanical behavior, and as a previous study by Engelhardt et al. [205] also showed one may subsequently study dynamic mechanical effects of biochemical agents all within a microfluidic environment. By being used in conjunction with already established microfluidic DEP technology for cell trapping [41] and sorting [40], these studies highlight the potential for automated, parallel processing with high throughput capabilities in areas such as diagnostics and drug development.

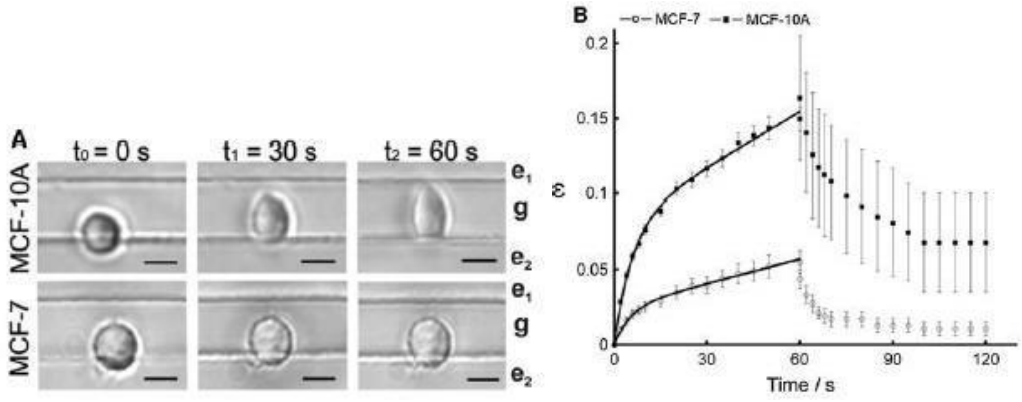

Figure 65. Images from Guido et al. [302] that depict (a) DEP-induced cell deformation in a noncancerous (MCF-10A) and cancerous (MCF-7) cell line that can be distinctively distinguished by (b) measuring differences between the strain vs. time.

The elastic and viscoelastic cell properties are critical factors for mediating cell behaviors and can respond to the progression of disease states by cytoskeletal rearrangement [289, 291]. One example of this involves the single cell mechanics of red blood cells (RBC) infected with P. falciparum, known to cause malaria [289]. The deformability of the RBCs increases throughout the progressive disease states and can potentially provide a means for diagnostics. Doh et al. [309] designed a single-cell microchamber array capable of deforming RBCs in large populations (Figure 66). The chamber was fabricated using a 10 μm thick SU8 layer coated with 120 nm of indium tin oxide (ITO) and 20/100 nm thick Cr/Au layers atop a pyrex glass wafer. These metallic electrodes were used to apply an AC voltage varying from 0 – 8 V at 20 MHz. RBC populations from normal donors and donors with hereditary spherocytosis were deformed using dielectrophoretic forces after the

cells were fluorescently labeled. The RBC deformation was greater in the RBC population from donors with spherocytosis, and the degree of the deformation was consistent with the well-established deformation characterization method of ektacytometry. Doh et al. thus demonstrate an array chamber capable of labeling and analyzing large, single cell populations of RBCs for cellular characteristics and hematologic disorders.

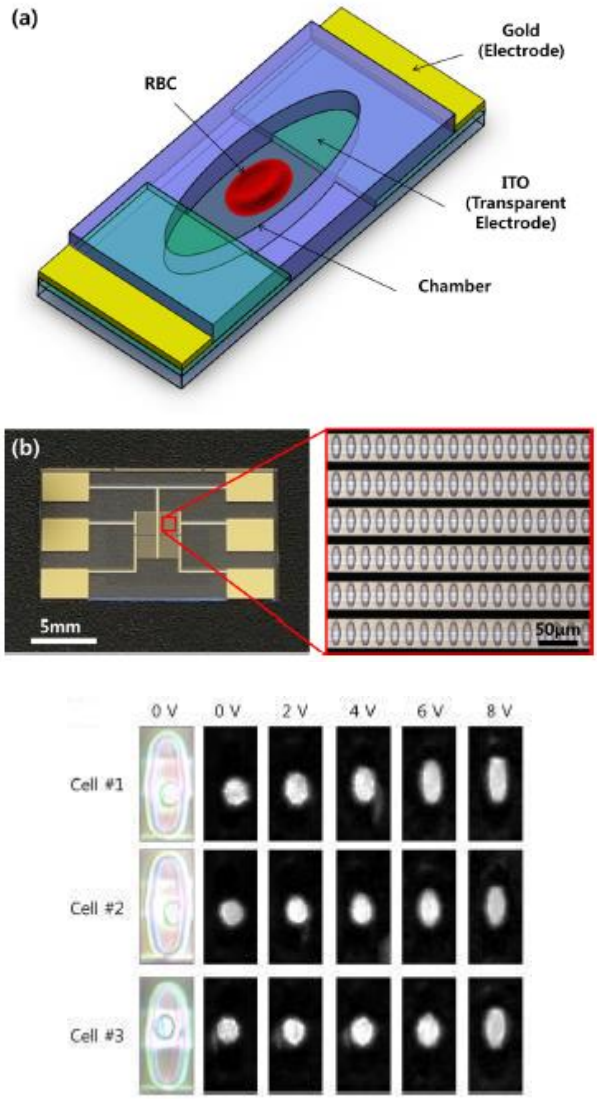

Figure 66. Images from Doh et al. [309] that show a microfluidic device design that allows high throughput diagnostic screening of diseased erythrocytes based on DEP-induced cell deformation.

8.4.2.3 Lab-on-a-Chip Integration

Integration of DEP-induced cell deformation into other microfluidic and lab-on-a-chip devices will enable parallel sample preparation and manipulation at the

micron scale. DEP offers an approach for cell line characterization through deformation measurements that can be performed without adverse effects to cell function or viability. This nondestructive testing allows later downstream processing. These systems also offer advantages such as low power consumption and relatively inexpensive fabrication processes.

Guido et al. [310] developed a microfluidic system that integrates with a dielectrophoretic cell stretcher capable of cell line characterization. The dielectrophoretic stretcher consisted of 250-μm wide ITO electrodes spaced 20 μm apart atop a glass slide. This device was integrated into a 15 mm long PDMS microfluidic channel equipped with a syringe pump (Figure 67).

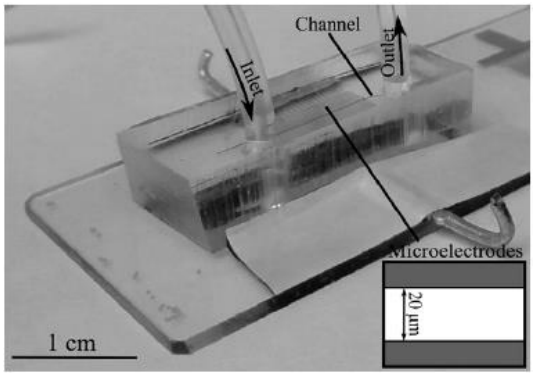

Figure 67. A dielectrophoretic cell stretching device integrated into a PDMS microfluidic chamber demonstrates the combination of DEP-induced cell deformation for cell characterization and parallel microfluidic manipulation for lab-on-a-chip processing (reprinted from [310]).

Two cell lines were tested for cell line characterization using a dielectrophoretic cell stretcher: the MCF-10A non-tumorigenic epithelial cell line,

and MCF-7 cells from human adenocarcinoma tissue. The cells were stretched using an electric field generated at 6 Vrms and at a frequency of 15 MHz. The non-cancerous MCF-10A cells stretched to a considerably larger strain value than the cancerous MCF-7 cells, and taking note of the cell size and dielectric properties led to conclusive distinction between cell lines based on strain. The microfluidic system integration first permitted a syringe pump to introduce single cells near the ITO electrodes. The syringe pump was then turned off, and the electrodes were turned on at 2 Vrms, 15 MHz to position the cells via pDEP. Then the voltage was increased to 6 Vrms to stretch the cell and identify its lineage using optical microscopy. Finally the syringe pump was re-activated to move cell towards the outlet channel and introduce a new cell. This integration establishes the feasibility for incorporating non-destructive DEP-induced cell deformation for cell line characterization into a microfluidic system with multiple processing steps.

8.4.3 Future Directions for Research

DEP forces have been shown to impart stresses and strains that can deform mammalian cells [41, 204-206]. Techniques for DEP induced cell deformation may provide a means for further quantification of cellular mechanical properties and a better qualitative description of intracellular structure and dynamic cytoskeletal rearrangement during disease progression. DEP is progressing as a powerful tool for furthering our understanding of biomechanics and mechanobiology. Future practical uses may involve the exploitation of varying cellular mechanical properties for identification that can provide a quick and easy nondestructive method for cell characterization. Studies have shown the difference in DEP deformation response

between cancerous and noncancerous cell lines and may provide for an early diagnostic screening platform. The incorporation of currently established droplet and channel microfluidic technology provides a platform for high throughput, large scale operations. Multiple step-wise processes are a likely next step, combining emerging deformation-related characterization methods with already established cell sorting procedures for downstream processing. A platform capable of monitoring live cell deformation while administering chemical agents may find use for diagnostic purposes, studies in mechanobiological pathways, and in drug development.

DEP forces have not yet been used to deform stem cells as a way of directly imparting intracellular stresses and strains to direct fate specification. The ability to utilize DEP forces to deform cells in a precise and quantifiable way will help to correlate the amount of deformation to specific cellular behaviors, such as differentiation [208, 209, 290]. Mechanical stresses are known to promote stem cell lineage specification [208, 209, 290], but the link between the magnitude and frequency of stimuli with the resultant behavior is still an inexact science [208]. DμF technology offers a tool to impart precise strains on the nanometer scale to precise locations based on electrode design.

8.5 Economizing Piezoelectric Sensing

Using piezo- and pyroelectricity as a method for in situ sensing opens up a wide array of options and potential applications. In addition to adding new sensing modalities, the ability to actuate samples is also available. Applying an electric field

to either generate heat or induce a strain may find other applications in stem cell differentiation or biochemical reactions.

A practical drawback to this method of on-chip sensing and actuation is the high cost of PZT and other similar piezoelectric substrate materials. This cost may be prohibitively high for many applications, and thus prevent its commercial adoption. Therefore, it may be worthwhile to investigate other piezoelectric materials that can be substituted. One piezoelectric material that is relatively inexpensive and easily fabricated is poly(vinylidene fluoride) (PVDF). PVDF is an electroactive polymer that could be an interesting alternative material, because, in addition to lower costs, exhibits excellent processibility, mechanical and chemical resistance, and low impedance [283]. Although PVDF has a piezoelectric coefficient that is an order of magnitude smaller than PZT, and two orders of magnitude smaller than PMN-PT, it may still be an economical alternative for non-sensitive sensing applications.

For PVDF to be used in a DμF device, it must be able to be processed in a way that is consistent with the other device materials. One property that is of a practical necessity is transparency. In order to investigate the optical transparency PVDF, thin films were spin-coated onto glass substrates and solidified at room temperature, 30 °C, and 90 °C. Figure 68 shows that the PVDF film became more transparent at higher solidification temperatures.

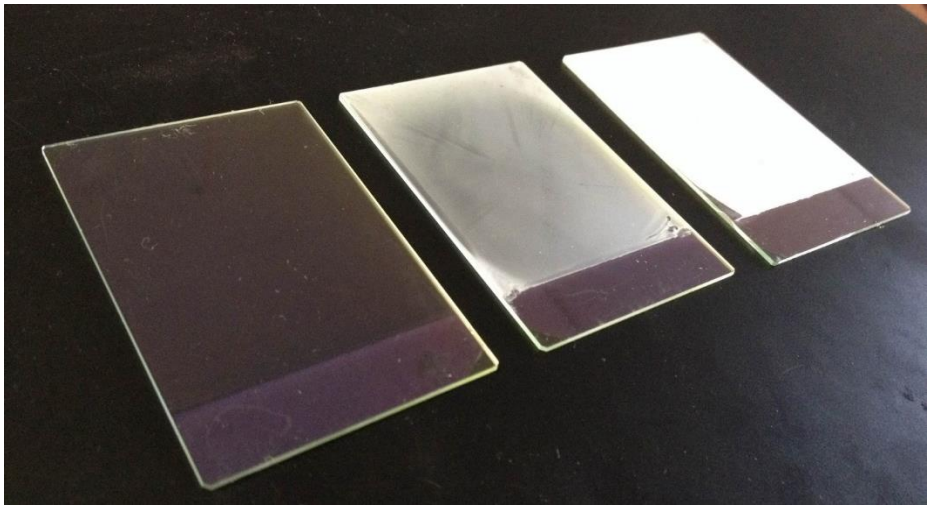

Figure 68. 2-inch x 3-inch glass slides with thin films of solidified PVDF. The optically transparent slide (left) was solidified at 90 °C, the middle plate was solidified at 30 °C, and the opaque slide (right) was solidified at room temperature.

PVDF does not crystallize into a highly piezoelectric crystal orientation. Several attempts to promote crystallization into the piezoelectric alpha phase include the addition of impurities into the solvent, mechanical loading, electric-field poling, and heat treatments. Because heat treatments must be used for the addition of the hydrophobic top coatings, thin films heat treated at 30 °C, and 90 °C were subjected to FT-IR to investigate the resultant crystal structure. Figure 69 shows that the thin films crystallizes into the low piezoelectric β phase at low temperatures and the high piezoelectric α phase at high temperatures.

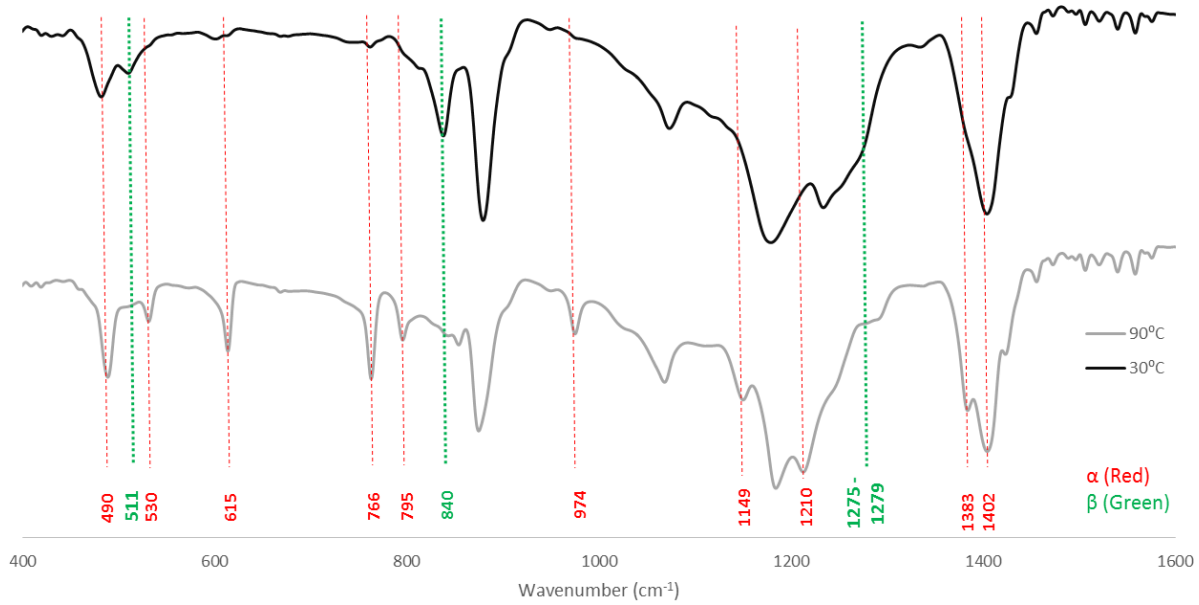

Figure 69. FT-IR spectra of PVDF thin films annealed at 30 and 90 °C, showing the transition from the B phase to the piezoelectric α phase at 90 °C.

9 CONCLUSIONS

The innovations presented herein add new functionality, characterization, and tissue culture methods to the field of DμF. Vertical functionality was developed by stacking multiple DμF planes and creating a fabrication protocol that enables droplets to transfer between layers. Three applications that were previously unachievable were demonstrated using this architecture: a hydrogel was fabricated with a radially symmetric crosslink gradient; a hydrogel-based particle sieve was designed; and a 3D embryoid body tissue sample was retrieved for downstream processing. Collagen was used to encapsulate 3D cell spheroids to develop an automated invasion assay. A stem cell microenvironment was established for culturing human embryonic stem cell and differentiating them into functional cardiomyocytes. This platform was used to demonstrate the feasibility of chronotropic and inotropic drug assays, and a novel impedance sensing modality was presented to monitor the field changes that occur in beating, 3D cardiomyocyte tissue. The impedance assay used on a DμF device allows a rich set of data collection regarding the heterogeneous beating behavior of maturing embryoid bodies. Finally, PZT-based piezoelectric materials were integrated with the DμF platform to measure exothermic chemical reactions via the pyroelectric effect and cardiomyocyte contractile behavior via the piezoelectric effect.

Together, these technological improvements will promote the integration of DμF with various tissue engineering applications and enable new lab-on-a-chip procedures. These innovations will improve the tools and understanding for future DμF researchers, and they may also help drive the drug development and tissue

engineering communities towards DμF platforms for streamlined assay protocols, reduced costs, and reduced error and variability.

Stem cell culture, regenerative medicine, and tissue engineering have all made tremendous strides over the past few decades. Significant effort will be needed to reach their full potential. Progress must be made in numerous fields including biology, materials science, chemistry, and engineering. Better understanding of stem cell maturation and differentiation, tissue development, scaffold design, and better drug screening models are just a few of the areas that will need continued improvement. Engineering the conditions and methods necessary for DμF-based tissue engineering has helped bring DμF into the tissue engineer's toolbox to help society reach these goals.

10 APPENDIX A

10.1 CELL SPHEROID DEVELOPMENT WITHIN MICROLITER-SIZED DROPLETS VIA NON-ADHERENT CONDITIONS

10.1.1 Abstract

Cell spheroids are 3D cell clusters that self-assemble in conditions where cells self-adhere to enhance survival. Spheroids are used as 3D tumor models for drug testing. Spheroids that form from pluripotent stem cells are called embryoid bodies, and are used in basic research on stem cell differentiation. Digital microfluidic (DμF) platforms have many features that make them potentially useful for spheroid culture. For example, hydrophobic surfaces are typically used to facilitate droplet movement. Cells do not readily adhere to these materials and non-adherent conditions promote embryoid body formation. In this preliminary study, we tested three common hydrophobic surfaces: Teflon-AF®, Parylene-C, and SU-8 photoresist to determine how readily cell spheroids could be formed and their viability. Mouse mesenchymal stem cell (MSC) suspensions, with and without the addition of 0.05% F-68 Pluronics, were tested on each surface in a 37 °C, 5% CO_2, and 95% RH incubated environment. MSC suspensions produced cell spheroids with an average diameter of ~600 – 800 μm on all three surfaces. The spheroids remained viability for up to 4 days, and Pluronics (a surfactant used to assist droplet movement) did not appear to have any adverse effects on spheroid viability.

10.1.2 Introduction

Cell spheroids are used as research tools for drug discovery because 3D cell cultures recapitulate the native environment better than 2D cell cultures [176, 311]. Once cell spheroids reach a diameter of ~300 μm, cell necrosis occurs at the core because of the long diffusion path nutrients must traverse from the outer surface of the spheroid [176, 311]. Spheroids of this size resemble avascular tumors and are used for drug screening research for cancer. The ability to culture 3D cell spheroids on a DμF platform could enable automated drug screening and other lab-on-a-chip assays.

Pluronics is an organic solution of a polyethylene oxide (PEO) - polypropylene oxide (PPO) copolymer that helps prevent biofouling on DμF device surfaces [312]. Pluronics prevents biofouling by causing the proteins to interact with the hydrophilic regions of PEO and PEG while the hydrophobic ends of these molecules interact with the hydrophobic surface (Figure 70).

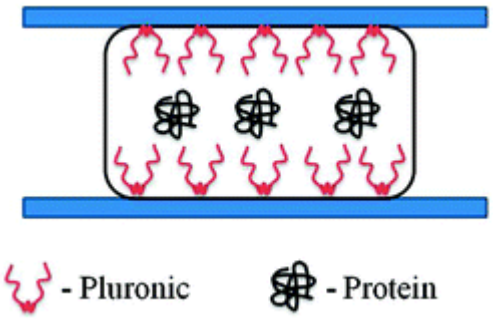

Figure 70. Schematic of interaction between Pluronics, a hydrophobic surface, and serum proteins from a cell medium showing the prevention of biofouling (adapted from [312]).

Certain cells will self-assemble into spheroids when no adherent surface exists. These cells agglomerate to enhance cell survival [311]. This chapter presents research on the tendency for cells to form spheroids on hydrophobic surfaces typical for DμF devices and the role of Pluronics on cell viability.

10.1.3 Materials and Methods

10.1.3.1 Substrate Preparation

Thin films of Parylene-C, Teflon-AF, and SU-8 negative photoresist were deposited on 7.5 cm x 2.5 cm glass microscope slides at UCLA's California NanoSystems Institute (CNSI) Integrated Systems Nanofabrication Cleanroom (ISNC). Briefly, eight slides were coated with a ~1-μm thick layer of Parylene-C using chemical vapor deposition (CVD), eight slides were coated with ~1 μm thick layer of Teflon-AF by spin coating and post-baking, and eight slides were coated with ~1 μm-thick layer of SU-8 by spin coating, developing, and baking.

10.1.3.2 Cell Culture and Medium Preparation

Mouse mesenchymal stem cells (MSC) were cultured via adherent conditions until ~70-80% confluency was reached. The cells were then trypsinized and reseeded in Dulbecco's modified eagle's medium supplemented with 10% bovine growth serum and 1% penicillin streptomycin at a density of 1.84×10^6 cells/mL. A 0.05% F-68 Pluronics solution and a 0.02% F-68 Pluronics solution were used as well.

10.1.3.3 Experimental Procedure

Microscope slides coated with Parylene-C, Teflon-AF, and SU-8 were prepared and stored in an incubator at 37 °C, 5% CO_2, and 95% humidity during the length of the experiment. Eight 30-µL droplets of MSC suspension were placed on each slide. Four droplets of cell suspension were placed directly on each slide, and four droplets of the cell/Pluronics suspension were placed directly on each slide (Figure 71). These cell suspensions did not have differences in appearance. One slide of each surface treatment was removed every 24 h for 7 consecutive days and analyzed for cell morphology by optical microscopy and cell viability by a Live/Dead assay described below. Medium exchange was performed on the remaining droplets each day by removing approximately 15 µL of spent medium from each droplet using a capillary tube and adding 15 µL of fresh medium back into each droplet.

Figure 71. Example slide (Teflon-coated) showing eight droplets: four contain media with Pluronics, and four contain media without Pluronics.

10.1.3.4 Cell Viability Assessment

Cell staining was performed using a Live/Dead® viability stain (Invitrogen catalog L#3224) according to the manufacturer's specification. Green fluorescent

calcein-AM is used to indicate intracellular esterase activity and red-fluorescent ethidium homodimer-1 is used to indicate loss of plasma membrane integrity. The staining procedure was performed by first removing ~10 – 20 µL of medium from each droplet using capillary tubes. Then 15 µL of staining solution was added to each droplet of interest and allowed to incubate for 10 min at 37 °C, 5% CO_2, 95% humidity, and darkness. Capillary tubes were again used to remove ~10 – 20 µL of stained medium and 15 µL of fresh medium was added back to each droplet. Medium exchange was repeated a second time before viewing under fluorescent microscopy. Cell viability and morphology were viewed using an inverted Zeiss fluorescent microscope and AxioVision software.

10.1.4 Results and Discussion

The MSCs began to agglomerate into spheroids on top of both Teflon-AF and Parylene-C after 24 h (Figure 72). Some cells adhered to each surface when the suspensions did not contain Pluronics. The droplets of suspension changed color from the pinkish medium color to a dull yellowish color after each day in incubation, indicating a pH change and nutrient depletion. Some evaporation was evident after each day. Viability staining after 24 h showed >95% viability for all sample types tested.

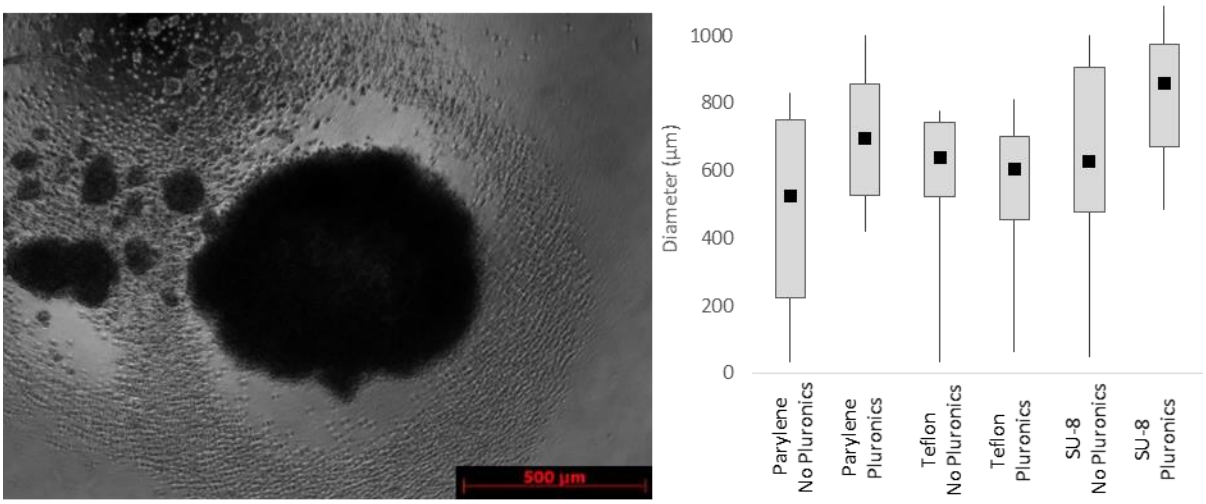

Figure 72. An optical microscope image (left) shows a MSC spheroid that developed after 24 h in a suspension without Pluronics on a Parylene-C thin film. The size of the MSC spheroids that formed was highly variable (~30 – 1080 µm diameter). A box-and-whiskers plot (right) shows the distribution of spheroid diameters for the different experimental conditions tested and shows no correlation between spheroid diameter and condition.

The spheroids ranged in size from under 30 to more than 1000 µm in diameter. Each droplet typically contained one large spheroid with an average diameter of ~600 – 900 µm. Several smaller spheroids with diameters less than ~300 µm were also commonly found alongside the larger spheroid. Figure 72 shows that no correlation existed between the spheroid size and the surface type or the presence of Pluronics. We did not perform longitudinal studies to monitor the change in spheroid size over time; other reports indicate that spheroids shrink over

time due to compacting of the cells. Figure 73 shows that our cell spheroids remained viable for up to 4 days in culture across all surface conditions.

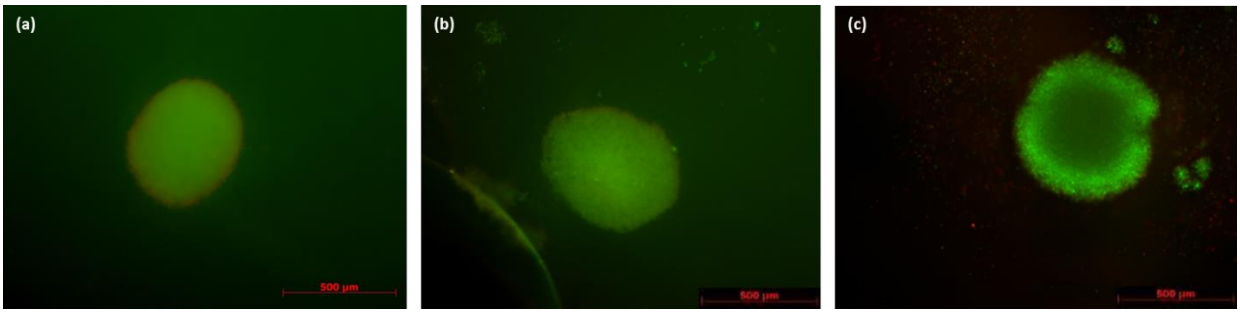

Figure 73. Live (green)/Dead (red) assay of MSC viability and spheroid morphology. (a) Spheroid on Parylene-C; (b) Spheroid on SU-8; and (c) Spheroid on Teflon-AF after 4 days in culture. Scale bar = 500 μm.

Droplets of cell suspension with and without Pluronics were placed onto the surface of a polystyrene Petri dish and were examined for morphology and cell viability after day 2 and day 5. Figure 74 show that the cells adhered to the substrate surface in close proximity to each other at the middle of the droplets but did not compact in a spheroid. Cell viability showed >95% living cells in both cell suspensions at day 2 and day 5.

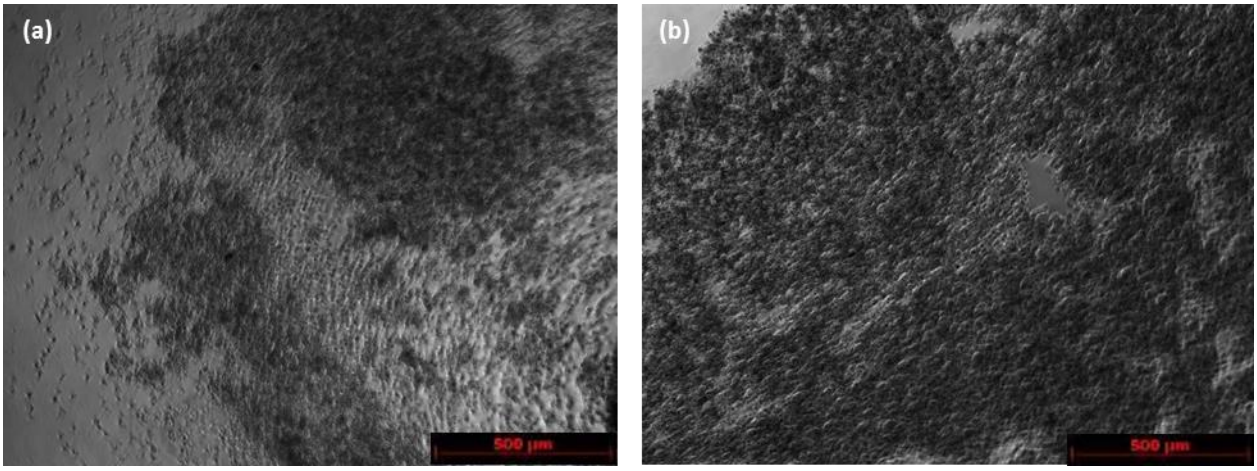

Figure 74. MSCs adhered to the surface of the polystyrene Petri dish; (a) without Pluronics after day 2 and (b) with Pluronics after day 5 contained no spheroids.

Visually assessing the degree of spreading of the sessile droplets indicated that Parylene-C was the only surface to significantly decrease in hydrophobicity throughout the lifetime of the experiment. This increase in wetting could be due to serum protein adsorption on the Parylene surface over time. Another possibility for an increase in wetting is due to an alteration in the Parylene-C surface chemistry. Spheroid formation was correlated with surface hydrophobicity. MSCs formed spheroids on each of the hydrophobic surfaces tested, but they failed to form spheroids on a hydrophilic Petri dish. Spheroid diameter was highly variable and showed no correlation to the type of surface or media composition. MSCs typically adhere to a surface for proper growth and survival. Because these cells could not attach to the slide surface they began to attach to each other to enhance their tendency for survival [311]. Cell suspensions containing Pluronics did not exhibit significant differences from the suspensions without Pluronics with regard to spheroid size, morphology, growth rate, or viability.

10.1.5 Conclusions

Three hydrophobic thin films - Teflon-AF, Parylene-C, and SU-8 photoresist - produced spheroids of mouse MSC after 1 day of incubation when stored in an incubated environment of 37 °C, 5% CO_2, and 95% humidity. Cell surface adhesion was absent, and spheroids remained viable for up to 4 days in culture. No observable differences were noted between the MSC suspensions with and without Pluronics in terms of spheroid growth, size, morphology, or cell viability. MSC droplets placed on a hydrophilic Petri dish show similar viability, but the cells did not form compact spheroids after several days in culture. Hydrophobic surface conditions appear to encourage spheroid development in the presence and absence of Pluronics surfactant. Furthermore, Pluronics was shown to have no adverse effect on cell viability.

11 APPENDIX B

11.1 DIGITAL MICROFLUIDIC PLATFORM AS A STEM CELL NICHE

11.2 ABSTRACT

A stem cell niche is a microenvironment where the fate of stem cells can be regulated. These environments may be designed to maintain stem cell viability and plasticity, while other environments may be designed to direct fate specification. Digital microfluidics (DμF) is a platform for manipulating small volumes of liquid through the application of electric fields, and may provide a tool for automating the development of stem cell microenvironments. The feasibility of using DμF to create a stem cell niche microenvironment was performed by encapsulating mouse mesenchymal stem cells within a calcium alginate hydrogel and delivering adipogenic growth factors on-chip. Live/Dead assays were performed to determine the viability of stem cell suspensions after DμF manipulation and calcium alginate encapsulation. Nile Red staining was used to observe adipogenesis by examining lipid vesicle formation.

11.2.1 Introduction

Digital (droplet) microfluidic (DμF) technology uses the application of electric fields to dispense, mix, split, and translate picoliter to microliter sized droplets of liquid on a 2D array of electrodes [25]. By applying a voltage across dielectric coated electrodes, a combination of electrostatic and dielectrophoretic (DEP) forces enable these lab-on-a-chip procedures [9, 160]. DμF devices offer the advantages

of being programmable and automatable, easily and inexpensively produced using well established microfabrication techniques, and low reagent and input power requirements. DμF has grown as a platform for biological assays and as a tool for cell manipulation [18, 40, 50, 160, 200-203]. DEP forces have been used to measure electric, dielectric, and mechanical cell properties [48, 201]. DEP forces have also been employed for innovative cell sorting procedures [18, 40, 43, 48, 50]. Mammalian cell culture has recently been demonstrated on a DμF device [163], and hydrogels are beginning to be investigated for use in DμF technology [200, 202, 203].

DμF may provide a novel approach towards developing a stem cell niche microenvironment with precise control over environmental stimuli such as the spatiotemporal delivery of biochemicals and the application of electric fields. A study by Eyedelnant et al. recently demonstrated the on-chip culture of embryonic stem cells [313]. This feat was performed by seeding stem cells onto a 2D hydrophilic patch created over particular electrodes. This design, however, was limited to 2D cultures. It has been shown that 3D cell cultures mimic the in vivo characteristics of cell behavior more accurately than their 2D counterparts [58, 59, 284]. Physical and chemical gradients exist in vivo on both the macroscopic and microscopic levels, giving rise to cues that dictate behaviors such as cell-cell communication, migration, proliferation, aggregation, and differentiation. These gradients and cues are determined in part by external stimuli and the extracellular matrix. Hydrogels are used as extracellular matrix mimics and exhibit highly tunable properties with regards to stiffness, porosity, chemical diffusivity, and cell attachment [85]. Alginate-based hydrogels are used in tissue engineering as

scaffolds for cell encapsulation because they are easy to fabricate with tunable properties [99-101]. Alginate is an acidic linear polysaccharide consisting of α-L-guluronic acid (G) and β-D-mannuronic acid (M) [99, 102]. These residues are arranged as either G-block or M-block block copolymers, or as a mixed sequence of MG-blocks [102]. Divalent cations, such as Ca^{2+}, join guluronic acid residues of adjacent chains to form an "egg-box" gel structure [99]. Alginate hydrogels are biocompatible [99, 103], and their sponge-like structure of large, interconnecting pores promotes cell growth and rearrangement [103]. Alginate gels also provide a convenient method for encapsulating cells within a 3D environment and evoke a more natural tissue and cellular response to stimuli compared to similar 2D culture systems [85, 87]. The diffusive properties of alginate hydrogels are tunable [101, 107], and they can control the delivery of growth factors to cells with a diffusion-regulated response [82, 88].

A DμF system was used to encapsulate mouse mesenchymal stem cells (MMSC) within a calcium-alginate hydrogel, deliver medium supplemented with growth factors, and maintain viability to promote adipogenic differentiation within a 3D microenvironment.

11.2.2 Methods, Results, and Discussion

DμF fabrication was similar to previously described protocols[314] and was conducted in the California NanoSystems Institute (CNSI) Integrated System Nanofabrication Cleanroom (ISNC) at UCLA. Briefly, 1100 Å of indium tin oxide (ITO) was deposited onto glass substrates by metal sputter deposition and patterned into electrodes via photolithography. The dielectric layer consisted of

Parylene-C (Specialty Coating Systems, ~2 μm) and was applied via vapor deposition. A fluoropolymer coating was then applied by spin coating Teflon-AF® onto the substrates at 2000 rpm for 60 s and post-baking on a hot plate at 110°C for 5 min and 180°C for 15 min. The top plate, an ITO-coated glass slide, was coated with Teflon-AF® as well. Through holes were then drilled using a drill press through selected electrodes.

MMSC were harvested via standard cell culture protocols. The MMSC suspension consisted of Leibovitz CO_2-free medium supplemented with 7.5% FBS, 1% PS, and 0.02% Pluronics to assist droplet translation. A 3-μL-droplet of the MMSC was encased in silicone oil to enhance droplet translation and mitigate evaporation. An applied AC field of 100 V at 18 kHz was used to translate the MMSC droplet towards a 3-μL droplet of 1% alginate in media and was allowed to mix. A 3-μL droplet of 50 mM $CaCl_2$ in media was then mixed with the alginic acid solution containing MMSCs in order to initiate gelation (Figure 75).

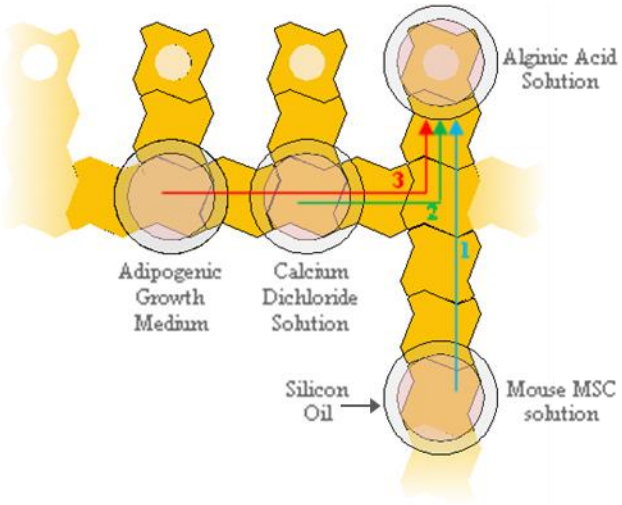

Figure 75. Protocol for on-chip MMSC encapsulation and delivery of growth medium. The alginic acid solution was delivered to an electrode underneath a through hole. (1) A suspension containing MMSC was mixed with the aliginic acid solution. (2) A calcium chloride solution was mixed with the alginic acid solution to encapsulate the MMSC in a calcium alginate hydrogel. (3) Media supplemented with adipogenic growth factors was delivered to the hydrogel.

The calcium alginate hydrogel formed instantly upon mixing of the calcium chloride solution with the alginic acid solution, encasing the MMSCs inside. Scanning electron microscopy ensured the integrity of cells after the encapsulation process. The cells showed a spherical morphology with little adhesion to the hydrogel (Figure 76). A Live/Dead staining assay was performed to ensure that the electric field induced translation and hydrogel encapsulation process did not affect viability. The staining revealed >95% viability after encapsulation and droplet translation, suggesting a benign gelation process (Figure 76).

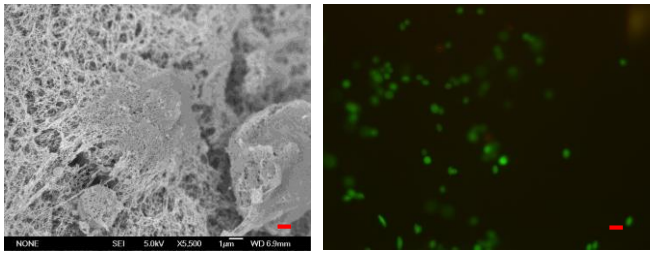

Figure 76. SEM image and Live/Dead assay of calcium alginate encapsulation of MMSCs. (Left) Scanning electron microscope image of MMSCs encapsulated within the calcium alginate hydrogel structure shows immobilized cells with little adhesion; (Right) Live/Dead staining of encapsulated stem cells indicates >95% viability. Scale bar is 1 μm on the left image and ~20 μm on the right image.

After the MMSCs were immobilized within the calcium alginate hydrogel, a 3-μL droplet of Leibovitz medium supplemented with 7.5% FBS, 1% PS, 0.02% Pluronics, 10 μM of dexamethasome, and 100 nM of insulin was mixed with the hydrogel. The system was incubated at 37°C and 95% humidity for 5 days. To verify adipogenesis, the cell-laden hydrogel was stained using Nile Red to highlight lipid vesicle formation. Abundant lipid vesicle formation was present in the growth factor supplemented solutions imaged via confocol microscopy (Figure 77).

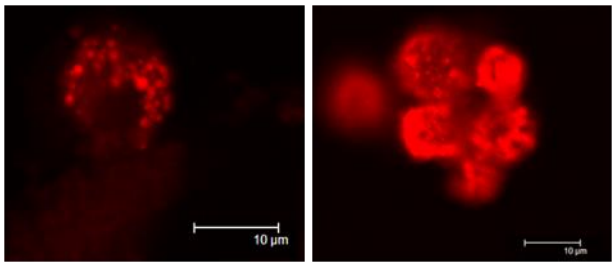

Figure 77. Nile Red fluorescence staining of calcium alginate encapsulated MMSCs after 5 days with growth factor supplemented medium expressed an abundance of lipid vesicles in singular (left) and clustered (right) cells.

11.2.3 Conclusions

A stem cell niche microenvironment was formed on a DμF platform by encapsulating MMSC in a calcium alginate hydrogel. Immobilizing stem cells within hydrogels on a DμF platform provides unique opportunities for automated control of sophisticated tissue engineering microenvironments. The ability to control hydrogel crosslink density profiles, spatiotemporal chemical delivery, and electric field generation may provide unique opportunities for innovative stem cell maturation studies using DμF. Future work may investigate optimizing stem cell niche development for differentiation into other cell lines.

12 REFERENCES

1. Dariush Mozaffarian, e.a., *Heart Disease and Stroke Statistics—2015 Update.* Circulation, 2015. **131**: p. e29-e322.

2. Vunjak-Novakovic, G., et al., *Challenges in Cardiac Tissue Engineering.* Tissue Eng, 2010. **16**(2): p. 169-187.

3. Schuster, D., C. Laggner, and T. Langer, *Why Drugs Fail - A Study on Side Effects in New Chemical Entities.* Current Pharmaceutical Design, 2005. **11**(27): p. 3545-3559.

4. DiMasi, J.A., H.G. Grabowski, and R.W. Hansen, *Innovation in the Pharmaceutical Industry: New Estimates of R&D Costs*. 2015, Tufts Center for the Study of Drug Development.

5. DiMasi, J., R. Hansen, and H. Grabowski, *The price of innovation: new estimates of drug development costs.* Journal of Health Economics, 2003. **22**(2): p. 151-185.

6. Nagavarapu, U., *Cell-based Assays: Technologies and Global Markets*. 2014, BCC Research: Wellesley, MA. p. 199.

7. Andersson, H. and A.v.d. Berg, *Microfabrication and microfluidics for tissue engineering: state of the art and future opportunities.* Lab on a Chip, 2004. **4**(2): p. 98-103.

8. Nguyen, N.-T., et al., *Design, fabrication and characterization of drug delivery systems based on lab-on-a-chip technology.* Advanced Drug Delivery Reviews, 2013. **65**(11–12): p. 1403-1419.

9. Mugele, F. and J.-C. Baret, *Electrowetting: from basics to applications.* Journal of Physics: Condensed Matter, 2005. **17**(28): p. R705-R775.

10. Whitesides, G.M., *The origins and the future of microfluidics.* Nature, 2006. **442**(7101): p. 368-373.

11. Teh, S.-Y., et al., *Droplet microfluidics.* Lab on a Chip, 2008. **8**(2): p. 198-220.

12. Blow, N., *PCR's next frontier.* Nature Methods, 2007. **4**: p. 869-875.

13. Edd, J.F., et al., *Controlled encapsulation of single-cells into monodisperse picolitre drops.* Lab on a Chip, 2008. **8**(8): p. 1262-1264.

14. Nelson, W.C. and C.-J. Kim, *Droplet Actuation by Electrowetting-on-Dielectric (EWOD): A Review.* Journal of Adhesion Science and Technology, 2012. **26**(12-17): p. 1747-1771.

15. Chatterjee, D., H. Shepherd, and R.L. Garrell, *Electromechanical model for actuating liquids in a two-plate droplet microfluidic device.* Lab on a Chip, 2009. **9**(9): p. 1219-1229.

16. Zeng, J. and T. Korsmeyer, *Principles of droplet electrohydrodynamics for lab-on-a-chip.* Lab on a Chip, 2004. **4**: p. 265-277.

17. Sukhatme, S. and A. Agarwal, *Digital Microfluidics: Techniques, Their Applications and Advantages.* Journal of Bioengineering and Biomedical Science, 2012. **S8**(001).

18. Fan, S.-K., et al., *Cross-scale electric manipulations of cells and droplets by frequency-modulated dielectrophoresis and electrowetting.* Lab Chip, 2008. **8**: p. 1325-1331.

19. Nelson, W.C. and C.-J. Kim, *Monolithic Fabrication of EWOD Chips for Picoliter Droplets.* Journal of Microelectromechanical Systems, 2011. **20**(6): p. 1419-1427.

20. Lippmann, M.G., *Relation entre les phénomènes électriques et capillaires.* Annales de chimie et de physique, 1875. **5**(494): p. 912-914.

21. Dahms, H., *Electrocapillary Measurements at the Interface Insulator-Electrolytic Solution.* Journal of the Electrochemical Society, 1969. **116**(11): p. 1532-1534.

22. Colgate, E. and H. Matsumoto, *An investigation of electrowetting-based microactuation.* Journal of Vacuum Science and Technology A, 1990. **8**(4): p. 3625-3633.

23. Berge, B., *E'lectrocapillarité et mouillage de films isolants par l'eau'.* Hebd. Seances Acad. Sci, Ser. B, 1993. **317**: p. 157-163.

24. Chatterjee, D., et al., *Droplet-based microfluidics with nonaqueous solvents and solutions.* Lab on a Chip, 2005. **6**(2): p. 199-206.

25. Cho, S.K., H. Moon, and K. Chang-Jin, *Creating, transporting, cutting, and merging liquid droplets by electrowetting-based actuation for digital microfluidic circuits.* Journal of Microelectromechanical Systems, 2003. **12**(1): p. 70-80.

26. Zhao, Y.-P. and Y. Wang, *Fundamentals and Applications of Electrowetting: A Critical Review.* Reviews of Adhesions and Adhesives, 2013. **1**(1): p. 114-174.

27. Ali, H.A.A., H.A. Mohamed, and M. Abdelgawad, *Repulsion-based model for contact angle saturation in electrowetting.* Biomicrofluidics, 2015. **9**: p. 014115.

28. Blake, T.D., *The physics of moving wetting lines.* Journal of Colloid and Interface Science, 2006. **299**(1): p. 1-13.

29. Shikhmurzaev, Y.D., *Some dry facts abut dynamic wetting.* The European Physical Journal Special Topics, 2011. **197**: p. 47-60.

30. Mugele, F. and J. Buehrle, *Equilibrium drop surface profiles in electric fields.* Journal of Physics: Condensed Matter, 2007. **19**: p. 1-20.

31. Kang, K.H., *How Electrostatic Fields Change Contact Angle in Electrowetting.* Langmuir, 2002. **18**: p. 10318-10322.

32. Jones, T.B., *More about the electromechanics of electrowetting.* Mechanics Research Communication, 2009. **36**: p. 2-9.

33. Shih-Kang Fan, P.-W.H., Tsu-Te Wang and Yu-Hao Peng, *Cross-scale electric manipulations of cells and droplets by frequency-modulated dielectrophoresis and electrowetting.* Lab on a Chip, 2008. **8**: p. 1325-1331.

34. Jones, T.B., *Electromechanics of Particles*. 1995, New York: Cambridge University Press.

35. Jones, T.B., *On the Relationship of Dielectrophoresis and Electrowetting.* Langmuir, 2002. **18**: p. 4437-4443.

36. Jones, T.B., et al., *Frequency-Based Relationship of Electrowetting and Dielectrophoretic Liquid Microactuation.* Langmuir, 2003. **19**: p. 7646-7651.

37. Wang, K.-L., T.B. Jones, and A. Raisanen, *DEP actuated nanoliter droplet dispensing using feedback control.* Lab on a Chip, 2009. **9**(7): p. 901-909.

38. Lee, J., et al., *Electrowetting and electrowetting-on-dielectric for microscale liquid handling.* Sensors and Actuators, A, 2002. **95**(1): p. 259-268.

39. Young, P.M. and K. Mohseni, *Calculation of DEP and EWOD Forces for Application in Digital Microfluidics.* J Fluids Eng, 2008. **130**(081603): p. 1-9.

40. Huang, Y., et al., *Introducing Dielectrophoresis as a New Force Field for Field-Flow Fractionation.* Biophys J, 1997. **73**: p. 1118-1129.

41. MacQueen, L.A., M.D. Buschmann, and M.R. Wertheimer, *Mechanical properties of mammalian cells in suspension measured by electro-deformation.* J Micromech Microeng, 2010. **20**(065007): p. 1-11.

42. Alazzam, A., et al., *Analytical formulation of electric field and dielectrophoretic force for moving dielectrophoresis using Fourier series.* Microfluid Nanofluid, 2010. **9**: p. 1115-1124.

43. Gupta, S., et al., *On-Chip Dielectrophoretic Coassembly of Live Cells and Particles into Responsive Biomaterials.* Langmuir, 2009. **26**(5): p. 3441-3452.

44. Mahaworasilpa, T.K., H.G.L. Coster, and E.P. George, *Forces on biological cells due to applied alternating (AC) electric fields. I. Dielectrophoresis.* Biochim Biophys Acta, 1994. **1193**: p. 118-126.

45. Voldman, J., *Electrical Forces for Microscale Cell Manipulation.* Annu Rev Biomed Eng, 2006. **8**: p. 425-454.

46. Nerguizian, V., et al., *Analytical solutions and validation of electric field and dielectrophoretic force in a bio-microfluidic channel.* Electrophoresis, 2012. **33**: p. 426-435.

47. Clague, D.S. and E.K. Wheeler, *Dielectrophoretic manipulation of macromolecules: The electric field.* Phys Rev E, 2001. **64**(026605): p. 1-8.

48. Pethig, R., *Review Article—Dielectrophoresis: Status of the theory, technology, and applications.* Biomicrofluidics, 2010. **4**: p. 4-35.

49. Pethig, R., et al., *Dielectrophoresis: A Review of Applications for Stem Cell Research.* J Biomed Biotech, 2010. **2010**: p. 1-7.

50. Huang, Y., et al., *Differences in the AC electrodynamics of viable and non-viable yeast cells determined through combined dielectrophoresis and electrorotation studies.* Phys Med Bio, 1992. **37**(7): p. 1499-1517.

51. Chiang, M., S.-Y. Chen, and S.-K. Fan. *Construting Heterogeneous Microcomponents on an Electro-Microfluidic Platform*. in *9th International Meeting on Electrowetting and Related Micro/Electrofluidic Science and Technology*. 2014. Cincinnati, OH.

52. Chiang, M.-Y., et al., *Microengineered Heterogeneous Substrates for Cell Culture by Electro-Microfluidics*, in *18th International Conference on Miniaturized Systems for Chemistry and Life Sciences*. 2014: San Antonio, TX.

53. Betz, J.F., et al., *Optically clear alginate hydrogels for spatially controlled cell entrapment and culture at microfluidic electrode surfaces.* Lab on a Chip, 2013. **13**(10): p. 1854-1858.

54. Puttaswamy, S.V., et al., *Enhanced cell viability and cell adhesion using low conductivity medium for negative dielectrophoretic cell patterning.* Biotechnol J, 2010. **5**(10): p. 1005-1015.

55. Burdick, J.A. and G. Vunjak-Novakovic, *Engineered Microenvironments for Controlled Stem Cell Differentiation.* Tissue Engineering Part A, 2009. **15**(2): p. 205-219.

56. Mitra, S.K., D.A. Hanson, and D.D. Schlaepfer, *Focal adhesion kinase: in command and control of cell motility.* Nat Rev Mol Cell Biol, 2005. **6**(1): p. 56-68.

57. Ghafar-Zadeh, E., J.R. Waldeisen, and L.P. Lee, *Engineered approaches to the stem cell microenvironment for cardiac tissue regeneration.* Lab Chip, 2011. **11**: p. 3031-3048.

58. Baker, B.M. and C.S. Chen, *Deconstructing the third dimension: how 3D culture microenvironments alter cellular cues.* Journal of Cell Science, 2012. **125**(13): p. 3015-3024.

59. Biomatrix, D. *5 Reasons Cancer Researchers Adopt 3D Cell Culture*. in *http://3dbiomatrix.com/*. 2013.

60. Negro, A. and M. Boehm, *Cardiomyocyte maturation: It takes a village to raise a kid.* Journal of Molecular and Cellular Cardiology, 2014. **74**: p. 193-195.

61. Robertson, C., D.D. Tran, and S.C. George, *Concise Review: Maturation Phases of Human Pluriopotent Stem Cell-Derived Cardiomyocytes.* Stem Cells, 2013. **31**(5): p. 829-837.

62. Ertl, P., et al., *Lab-on-a-chip technologies for stem cell analysis.* Trends in Biotechnology, 2014. **32**(5): p. 245-253.

63. Takahashi, K., et al., *Induction of Pluripotent Stem Cells from Adult Human Fibroblasts by Defined Factors.* Cell, 2007. **131**(5): p. 861-872.

64. Campbell, C.J.V., et al., *The human stem cell hierarchy is defined by a functional dependence on Mcl-1 for self-renewal capacity.* Blood Journal, 2010. **116**(9): p. 1433-1442.

65. Beltrami, A.P., et al., *Adult cardiac stem cells are multipotent and support myocardial regeneration.* Cell, 2003. **114**(6): p. 763-776.

66. Bollini, S., N. Smart, and P.R. Riley, *Resident cardiac progenitor cells: At the heart of regeneration.* Journal of Molecular and Cellular Cardiology, 2011. **50**(2): p. 296-303.

67. Rajala, K., M. Pekkanen-Mattila, and K. Aalto-Setala, *Cardiac Differentiation of Pluripotent Stem Cells.* Stem Cells International, 2011. **2011**: p. 12.

68. Vidarsson, H., J. Hyllner, and P. Sartipy, *Differentiation of Human Embryonic Stem Cells to Cardiomyocytes for In Vitro and In Vivo Applications.* Stem Cell Rev and Rep, 2010. **6**: p. 108-120.

69. Assmus, B., et al., *Clinical outcome 2 years after intracoronary administration of bone marrow-derived progenitor cells in acute myocardial infarction.* Circulation: Heart Failure, 2010. **3**(1): p. 89-96.

70. Molkentin, J.D. and S.R. Houser, *Are Resident c-Kit+ Cardiac Stem Cells Really All That Are Needed to Mend a Broken Heart?* Circulation Research, 2013. **113**: p. 1037-1039.

71. Hirt, M.N., A. Hansen, and T. Eschenhagen, *Cardiac Tissue Engineering State of the Art.* Circulation Research, 2014. **114**: p. 354-367.

72. Urbanek, K., et al., *Myocardial regeneration by activation of multipotent cardiac stem cells in ischemic heart failure.* Proceedings of the National Academy of Sciences of the United States of America, 2005. **102**(24): p. 8692-8697.

73. Genead, R., et al., *Islet-1 Cells Are Cardiac Progenitors Present During the Entire Lifespan: From the Embryonic Stage to Adulthood.* Stem Cells and Development, 2010. **19**(10): p. 1601-1615.

74. Keller, G., *Embryonic stem cell differentiation: emergence of a new era in biology and medicine.* Genes and Development, 2005. **19**: p. 1129-1155.

75. C, F., et al., *Resident cardiac stem cells.* Current Pharmaceutical Design, 2011. **17**(30): p. 3252-3257.

76. Johnson, P.C., et al., *Strategic Directions in Tissue Engineering.* Tissue Eng, 2007. **13**(12): p. 2827-2837.

77. Mummery, C.L., et al., *Differentiation of Human Embryonic Stem Cells and Induced Pluripotent Stem Cells to Cardiomyocytes A Methods Overview.* Circulation Research, 2012. **111**: p. 344-358.

78. Discher, D.E., D.J. Mooney, and P.W. Zandstra, *Growth Factors, Matrices, and Forces Combine and Control Stem Cells.* Science, 2009. **324**: p. 1673-1677.

79. Miron-Mendoza, M., J. Seemann, and F. Grinnell, *The differential regulation of cell motile activity through matrix stiffness and porosity in three dimensional collagen matrices.* Biomaterials, 2010. **31**(25): p. 6425-35.

80. Geuss, L.R. and L.J. Suggs, *Making cardiomyocytes: How mechanical stimulation can influence differentiation of pluripotent stem cells.* Biotechnology Progress, 2013. **29**(5): p. 1089-1096.

81. Kihara, T., J. Ito, and J. Miyake, *Measurement of Biomolecular Diffusion in Extracellular Matrix Condensed by Fibroblasts Using Fluorescence Correlation Spectroscopy.* PLoS ONE, 2013. **8**(11): p. e82382.

82. Leddy, H.A., S.E. Christensen, and F. Guilak, *Microscale Diffusion Properties of the Cartilage Pericellular Matrix Measured Using 3D Scanning Microphotolysis.* J Biomech Eng, 2008. **130**(6): p. 1-20.

83. Cui, H. and L. Tang, *Stem Cell Lineage Commitment by Electrical Fields and the Potential Application in Drug Discovery.* Current Drug Metabolism, 2012. **14**(3): p. 272-278.

84. Kim, D.-H., et al., *Guided Three-Dimensional Growth of Functional Cardiomyocytes on Polyethylene Glycol Nanostructures.* Langmuir, 2006. **22**(12): p. 5419-5426.

85. Geckil, H., et al., *Engineering hydrogels as extracellular matrix mimics.* Nanomedicine-UK, 2010. **5**(3): p. 469-484.

86. Sant, S., et al., *Biomimetic Gradient Hydrogels For Tissue Engineering.* Can J Chem Eng, 2010. **88**(6): p. 899-911.

87. Slaughter, B.V., et al., *Hydrogels in Regenerative Medicine.* Adv Mater, 2009. **21**: p. 3307-3329.

88. Lee, K., E.A. Silva, and D.J. Mooney, *Growth factor delivery-based tissue engineering: general approaches and a review or recent developments.* J R Soc Interface, 2011. **8**: p. 153-170.

89. Huh, D., et al., *Microengineered physiological biomimicry: Organs-on-Chips.* Lab Chip, 2012. **12**: p. 2156-2164.

90. Amsden, B., *Solute Diffusion within Hydrogels. Mechanisms and Models.* Macromolecules, 1998. **31**: p. 8382-8395.

91. Li, Z. and J. Guan, *Hydrogels for Cardiac Tissue Engineering.* Polymers, 2011. **3**: p. 740-761.

92. Gelse, K., E. Pöschl, and T. Aigner, *Collagens--structure, function, and biosynthesis.* Advanced Drug Delivery Reviews, 2003. **55**(12): p. 1531-1546.

93. Jawerth, L.M., et al., *A Blind Spot in Confocal Reflection Microscopy: The Dependence of Fiber Brightness on Fiber Orientation in Imaging Biopolymer Networks.* Biophysical Journal, 2010. **98**(3): p. L1-L3.

94. Guzman, A., M.J. Ziperstein, and L.J. Kaufman, *The effect of fibrillar matrix architecture on tumor cell invasion of physically challenging environments.* Biomaterials, 2014. **35**(25): p. 6954-6963.

95. Helary, C., et al., *Fibroblast populated dense collagen matrices: cell migration, cell density and metalloproteinases expression.* Biomaterials, 2005. **26**(13): p. 1533-43.

96. Goodsell, D.S. *Molecule of the Month: Collagen*. RCSB PDB Molecule of the Month, 2000.

97. Pryse, K.M., et al., *Incremental Mechanics of Collagen Gels: New Experiments and a New Viscoelastic Model.* Annals of Biomedical Engineering, 2003. **31**(10): p. 1287-1296.

98. Roeder, B.A., et al., *Tensile Mechanical Properties of Three-Dimensional Type I Collagen Extracellular Matrices with Varied Microstructure.* Journal of Biomechanical Engineering, 2002. **124**(2): p. 214-222.

99. Wan, L.Q., et al., *Calcium Concentration Effects on the Mechanical and Biochemical Properties of Chondrocyte-Alginate Constructs.* Cell Mol Bioeng, 2008. **1**(1): p. 93-102.

100. Kong, H.J., E. Wong, and D.J. Mooney, *Independent Control of Rigidity and Toughness of Polymeric Hydrogels.* Macromolecules, 2003. **36**: p. 4582-4588.

101. Amsden, B. and N. Turner, *Diffusion Characteristics of Calcium Alginate Gels.* Biotechnol Bioeng, 1999. **65**(5): p. 605-610.

102. Kurachi, M., T. Nakashima, and C. Miyajima, *Comparison of the activities of various alginates to induce TNF-α secretion in RAW264.7 cells.* J Infect Chemother, 2005. **11**: p. 199-203.

103. Glicklis, R., et al., *Hepatocyte Behavior Within Three-Dimensional Porous Alginate Scaffolds.* Biotech Bioeng, 2000. **67**(3): p. 344-353.

104. Li, X., et al., *Culture of Neural Stem Cells in Calcium Alginate Beads.* Biotechnol Prog, 2006. **22**: p. 1683-1689.

105. Trounson, A., J. Morser, and S.I. Nishikawa, *Human Embryonic Stem Cell Derivation and Directed Differentiation*

The Promises and Challenges of Regenerative Medicine. 2005, Springer Berlin Heidelberg. p. 27-44.

106. Davidovich-Pinhas, M. and H. Bianco-Peled, *A quantitative analysis of alginate swelling.* Carbohydrate Polymers, 2010. **79**: p. 1020-1027.

107. Blandino, A., M. Macı´as, and D. Cantero, *Glucose oxidase release from calcium alginate gel capsules.* Enzyme Microb Tech, 2000. **27**: p. 319-324.

108. Amsden, B., *Modeling solute diffusion in aqueous polymer solutions.* Polymer, 2002. **43**: p. 1623-1630.

109. Martinsen, A., I. Storro, and G. Skjak-Braek, *Alginate as Immobilization Material: III. Diffusional Properties.* Biotech Bioeng, 1992. **39**: p. 186-194.

110. Rowley, J.A. and D.J. Mooney, *Alginate type and RGD density control myoblast phenotype.* J Biomed Mat Res, 2002. **60**: p. 217-223.

111. Rowley, J.A., G. Madlambayan, and D.J. Mooney, *Alginate hydrogels as synthetic extracellular matrix materials.* Biomaterials, 1999. **20**: p. 45-53.

112. Yu, J., et al., *The use of human mesenchymal stem cells encapsulated in RGD modified alginate microspheres in the repair of myocardial infarction in the rat.* Biomaterials, 2010. **31**: p. 7012-7020.

113. Candiello, J., et al., *Early differentiation patterning of mouse embryonic stem cells in response to variations in alginate substrate stiffness.* J Biol Eng, 2013. **7**(1): p. 9.

114. Ahearne, M., *Introduction to cell-hydrogel mechanosensing.* Interface Focus, 2014. **4**(2): p. 20130038.

115. Heuberger, M., G. Dietler, and L. Schlapbach, *Elastic deformations of tip and sample during atomic force microscope measurements.* Journal of Vacuum Science and Technology B, 1996. **14**(2): p. 1250-1254.

116. Zhu, Y., et al., *Determination of mechanical properties of soft tissue scaffolds by atomic force microscopy nanoindentation.* Journal of Biomechanics, 2011. **44**(13): p. 2356-2361.

117. Kim, Y., et al., *Characterization of cellular elastic modulus using structure based double layer model.* Medical & Biological Engineering & Computing, 2011. **49**(4): p. 453-462.

118. Yin, C., et al., *High density of immobilized galactose ligand enhances hepatocyte attachment and function.* Journal of Biomedical Materials Research, 2003. **67A**(4): p. 1093-1104.

119. Pluemsab, W., et al., *Cyclodextrin-linked alginate beads as supporting materials for Sphingomonas cloacae, a nonylphenol degrading bacteria.* Bioresource Technology, 2007. **98**(11): p. 2076-2081.

120. Peters, M.F., et al., *Evalulation of Cellular Impedance Measures of Cardiomyocyte Cultures for Drug Screening Applications.* ASSAY and Drug Development Technologies, 2012. **10**(6): p. 525-532.

121. Dolnikov, K., et al., *Functional properties of human embryonic stem cell-derived cardiomyocytes.* Annals of the New York Academy of Sciences, 2005. **1047**: p. 66-75.

122. Lundy, S.D., et al., *Structural and Functional Maturation of Cardiomyocytes Derived from Human Pluripotent Stem Cells.* Stem Cells and Development, 2013. **22**(14): p. 1991-2002.

123. Gherghiceanu, M., et al., *Cardiomyocytes derived from human embryonic and induced pluripotent stem cells: comparative ultrastructure.* Journal of Cellular and Molecular Medicine, 2011. **15**(11): p. 2539-2551.

124. Fang, Y., *Label-Free Biosensors for Cell Biology.* International Journal of Electrochemistry, 2011. **2011**: p. 16.

125. He, J.-Q., et al., *Human Embryonic Stem Cells Develop Into Multiple Types of Cardiac Myocytes: Action Potential Characterization.* Circulation Research, 2003. **93**(1): p. 32-39.

126. Baruscotti, M., A. Bucchi, and D. DiFrancesco, *Physiology and pharmacology of the cardiac pacemaker ("funny") current.* Pharmacology & Therapeutics, 2005. **107**(1): p. 59-79.

127. Nerbonne, J.M. and R.S. Kass, *Molecular Physiology of Cardiac Repolarization.* Physiological Reviews, 2005. **85**(4): p. 1205-1253.

128. Nattel, S., et al., *Arrhythmogenic Ion-Channel Remodeling in the Heart: Heart Failure, Myocardial Infarction, and Atrial Fibrillation.* Physiological Reviews, 2007. **87**(2): p. 425-456.

129. Yaniv, Y., K. Tsutsui, and E.G. Lakatta, *Potential effects of intrinsic heart pacemaker cell mechanisms on dysrhythmic cardiac action potential firing.* Frontiers in Physiology, 2015. **6**(47): p. 1-8.

130. Liem, L.K., et al., *The Patch Clamp Technique.* Neurosurgery, 1995. **36**(2): p. 382-392.

131. Hescheler, J., et al., *Determination of electrical properties of ES cell-derived cardiomyocytes using MEAs.* Journal of Electrocardiology, 2004. **37, Supplement**(0): p. 110-116.

132. Banach, K., et al., *Development of electrical activity in cardiac myocyte aggregates derived from mouse embryonic stem cells*. Vol. 284. 2003. H2114-H2123.

133. Dura, B., G.T.A. Kovacs, and L. Giovangrandi, *Spatiotemporally Controlled Cardiac Conduction Block Using High-Frequency Electrical Stimulation.* PLoS ONE, 2012. **7**(4): p. e36217.

134. Tandri, H., et al., *Reversible Cardiac Conduction Block and Defibrillation with High-Frequency Electric Field.* Science Translational Medicine, 2011. **3**(102): p. 102ra96.

135. Bers, D.M., *Cardiac excitation-contraction coupling.* Nature, 2002. **415**(6868): p. 198-205.

136. Ikonnikov, G. and D. Yelle. *McMaster Pathophysiology Review*. Physiology of Cardiac Conduction and Contractility 2015 [cited 2015; Available from: http://www.pathophys.org/physiology-of-cardiac-conduction-and-contractility/.

137. Brown, T.D., *Techniques for mechanical stimulation of cells in vitro: a review.* J Biomech, 2000. **33**(1): p. 3-14.

138. Hossain, M.M., et al., *Non-invasive characterization of mouse embryonic stem cell derived cardiomyocytes based on the intensity variation in digital beating video.* Analyst, 2010. **135**(7): p. 1624-1630.

139. Zhao, Y. and X. Zhang, *Adaptation of myofibrils to a microstructured polymeric substrate.* Sensors and Actuators A, 2007. **136**(2): p. 491-495.

140. Zheng, X.Y.R. and X. Zhang, *Microsystems for cellular force measurement: a review.* Journal of Micromechanics and Microengineering, 2011. **21**(5): p. 13.

141. Chang, W.-T., et al., *Characterization of the Mechanodynamic Response of Cardiomyocytes with Atomic Force Microscopy.* Analytical Chemistry, 2013. **85**(3): p. 1395-1400.

142. Rodriguez, M.L., et al., *Measuring the Contractile Forces of Human Induced Pluripotent Stem Cell-Derived Cardiomyocytes With Arrays of Microposts.* Journal of Biomechanical Engineering, 2014. **136**(5): p. 051005-051005.

143. Choi, E., et al., *MEMS-based power generation system using contractile force generated by self-organized cardiomyocytes.* Sensors and Actuators, B, 2010. **151**: p. 291-296.

144. Liu, X., et al. *Energy Harvesting Using Uniaxially Aligned Cardiomyocytes*. in *MEMS 2014*. 2014. San Fransico, CA, USA.

145. Trolier-McKinstry, S. and P. Muralt, *Thin Film Piezoelectrics for MEMS.* Journal of Electroceramics, 2004. **12**(1-2): p. 7-17.

146. Kasap, S.O., *Principles of Electronic Materials and Devices*. Third Edition ed. 2006, New York, NY: McGraw-Hill.

147. Hulkower, K.I. and R.L. Herber, *Cell Migration and Invasion Assays as Tools for Drug Discovery.* Pharmaceutics, 2011. **3**(1): p. 107-124.

148. Becchetti, A. and A. Arcangeli, *Integrins and Ion Channels in Cell Migration: Implications for Neuronal Development, Wound Healing and Metastatic Spread*, in *Integrins and Ion Channels*, A. Becchetti and A. Arcangeli, Editors. 2010, Springer New York. p. 107-123.

149. Ahearne, M., *Introduction to cell-hydrogel mechanosensing.* Interface Focus, 2014. **4**(2): p. 1-12.

150. Polacheck, W., I. Zervantonakis, and R. Kamm, *Tumor cell migration in complex microenvironments.* Cellular and Molecular Life Sciences, 2013. **70**(8): p. 1335-1356.

151. Sackmann, E.K., A.L. Fulton, and D.J. Beebe, *The present and future role of microfluidics in biomedical research.* Nature, 2014. **507**(7491): p. 181-189.

152. Kramer, N., et al., *In vitro cell migration and invasion assays.* Reviews in Mutation Research, 2013. **752**(1): p. 10-24.

153. Riahi, R., et al., *Advances in Wound-Healing Assays for Probing Collective Cell Migration.* Journal of Laboratory Automation, 2012. **17**(1): p. 59-65.

154. Pampaloni, F., E. Reynaud, and E. Stelzer, *The third dimension bridges the gap between cell culture and live tissue.* Nat Rev Mol Cell Biol, 2007. **8**: p. 839 - 845.

155. Ungefroren, H., et al., *Interaction of tumor cells with the microenvironment.* Cell Communication and Signaling, 2011. **9**(1): p. 18.

156. Zimmermann, M., C. Box, and S. Eccles, *Two-Dimensional vs. Three-Dimensional In Vitro Tumor Migration and Invasion Assays*, in *Target Identification and Validation in Drug Discovery*, J. Moll and R. Colombo, Editors. 2013, Humana Press. p. 227-252.

157. Petrie, R.J., H. Koo, and K.M. Yamada, *Generation of compartmentalized pressure by a nuclear piston governs cell motility in a 3D matrix.* Science, 2014. **345**(6200): p. 1062-1065.

158. Naber, H.P.H., et al., *Spheroid assay to measure TGF-β-induced invasion.* Journal of Visualized Experiments, 2011. **16**(57): p. e3337.

159. Aijian, A.P. and R.L. Garrell, *Digital Microfluidics for Automated Hanging Drop Cell Spheroid Culture.* Journal of Laboratory Automation, 2014.

160. Choi, K., et al., *Digital Microfluidics.* Annual Review of Analytical Chemistry, 2012. **5**: p. 413-440.

161. Fair, R. *Digital Microfluidics*. Digital Microfluidics 2010 [cited 2012; Available from: http://microfluidics.ee.duke.edu/.

162. Jebrail, M.J., M.S. Bartschb, and K.D. Patel, *Digital microfluidics: a versatile tool for applications in chemistry, biology and medicine.* Lab on a Chip, 2012. **12**(14): p. 2452-2463.

163. Barbulovic-Nad, I., S.H. Auab, and A.R. Wheeler, *A microfluidic platform for complete mammalian cell culture.* Lab on a Chip, 2010. **10**(12): p. 1536-1542.

164. Fiddes, L.K., et al., *Hydrogel discs for digital microfluidics.* Biomicrofluidics, 2012. **6**(1): p. 014112–014112-11.

165. Bender, B.F., A.P. Aijian, and R.L. Garrell. *Digital Microfluidic Platform with Vertical Functionality*. in *Society for Laboratory Automation and Screening 3rd Annual International Conference*. 2014. San Diego, CA.

166. Eydelnant, I.A., B. Betty Li, and A.R. Wheeler, *Microgels on-demand.* Nat Commun, 2014. **5**.

167. Au, S.H., et al., *Hepatic organoids for microfluidic drug screening.* Lab on a Chip, 2014. **14**(17): p. 3290-3299.

168. Aijian, A.P. and R.L. Garrell. *Automated Hanging Drop Cell Spheroid Culture Using Digital Microfluidics*. in *Society for Laboratory Automation and Screening 3rd Annual International Conference*. 2014. San Diego, CA.

169. Madar, S., I. Goldstein, and V. Rotter, *'Cancer associated fibroblasts' – more than meets the eye.* Trends in Molecular Medicine, 2013. **19**(8): p. 447-453.

170. Kharaishvili, G., et al., *The role of cancer-associated fibroblasts, solid stress and other microenvironmental factors in tumor progression and therapy resistance.* Cancer Cell International, 2014. **14**(1): p. 41.

171. Blacher, S., et al., *Cell Invasion in the Spheroid Sprouting Assay: A Spatial Organisation Analysis Adaptable to Cell Behaviour.* PLoS ONE, 2014. **9**(5): p. e97019.

172. Arwert, E.N., E. Hoste, and F.M. Watt, *Epithelial stem cells, wound healing and cancer.* Nat Rev Cancer, 2012. **12**(3): p. 170-180.

173. Ozerdem, B. and A. Tozeren, *Physical Response of Collagen Gels to Tensile Strain.* Journal of Biomechanical Engineering, 1995. **117**(4): p. 397-401.

174. Lopez-Garcia, M.D., D.J. Beebe, and W.C. Crone, *Young's modulus of collagen at slow displacement rates.* Biomed Mater Eng, 2010. **20**(6): p. 361-9.

175. Levental, I., P.C. Georges, and P.A. Janmey, *Soft biological materials and their impact on cell function.* Soft Matter, 2007. **3**(3): p. 299-306.

176. Friedrich, J., et al., *Spheroid-based drug screen: considerations and practical approach.* Nature Protocols, 2009. **4**(3): p. 309-324.

177. *Cell Culture Media Exchange*, in *HDP1384 Perfecta3D® 384-Well Hanging Drop Plates Protocol*. 2012, 3D Biomatrix Inc.

178. Inai, K., et al., *BMP-2 induces cell migration and periostin expression during atrioventricular valvulogenesis.* Developmental Biology, 2008. **315**(2): p. 383-396.

179. Rieder, F., et al., *Prostaglandin E2 inhibits migration of colonic lamina propria fibroblasts.* Inflammatory Bowel Diseases, 2010. **16**(9): p. 1505-1513.

180. Friedl, P. and K. Wolf, *Plasticity of cell migration: a multiscale tuning model.* The Journal of Cell Biology, 2010. **188**(1): p. 11-19.

181. Aijian, A.P. and R.L. Garrell, *Digital Microfluidics for Hanging Drop Cell Spheroid Culture.* Journal of Laboratory Automation, 2014. **20**(3): p. 283-295.

182. Wels, J., et al., *Migratory neighbors and distant invaders: tumor-associated niche cells.* Genes & Development, 2008. **22**(5): p. 559-574.

183. Hawinkels, L.J.A.C., et al., *Interaction with colon cancer cells hyperactivates TGF-[beta] signaling in cancer-associated fibroblasts.* Oncogene, 2014. **33**(1): p. 97-107.

184. Martinez-Outschoorn, U.E., et al., *Tumor cells induce the cancer associated fibroblast phenotype via caveolin-1 degradation: implications for breast cancer and DCIS therapy with autophagy inhibitors.* Cell Cycle, 2010. **9**(12): p. 2423-33.

185. Tyan, S.-W., et al., *Breast Cancer Cells Induce Cancer-Associated Fibroblasts to Secrete Hepatocyte Growth Factor to Enhance Breast Tumorigenesis.* PLoS ONE, 2011. **6**(1): p. e15313.

186. Petrie, R.J. and K.M. Yamada, *At the leading edge of three-dimensional cell migration.* J Cell Sci, 2012. **125**(Pt 24): p. 5917-26.

187. Friedl, P., et al., *New dimensions in cell migration.* Nat Rev Mol Cell Biol, 2012. **13**(11): p. 743-747.

188. Barbulovic-Nad, I., S.H. Au, and A.R. Wheeler, *A microfluidic platform for complete mammalian cell culture.* Lab on a Chip, 2010. **10**(12): p. 1536-1542.

189. Fobel, R., C. Fobel, and A.R. Wheeler, *DropBot: An open-source digital microfluidic control system with precise control of electrostatic driving force and instantaneous drop velocity measurement.* Applied Physics Letters, 2013. **102**(193513): p. 1-5.

190. Sista, R., et al., *Development of a digital microfluidic platform for point of care testing.* Lab on a Chip, 2008. **8**(12): p. 2091-2104.

191. Ng, A.H.C., et al., *Digital Microfluidic Magnetic Separation for Particle-Based Immunoassays.* Analytical Chemistry, 2012. **84**(20): p. 8805-8812.

192. Fobel, R., C. Fobel, and A.R. Wheeler, *DropBot: An open-source digital microfluidic control system with precise control of electrostatic driving force and instantaneous drop velocity measurement.* Applied Physics Letters, 2013. **102**: p. 193513.

193. Paik, P., V.K. Pamula, and R.B. Fair, *Rapid droplet mixers for digital microfluidic systems.* Lab on a Chip, 2003. **3**(4): p. 253-259.

194. Aijian, A.P., D. Chatterjee, and R.L. Garrell, *Fluorinated liquid-enabled protein handling and surfactant-aided crystallization for fully in situ digital microfluidic MALDI-MS analysis.* Lab Chip, 2012. **12**: p. 2552-2559.

195. Abdelgawad, M., M. Watson, and A. Wheeler, *Hybrid microfluidics: a digital-to-channel interface for in-line sample processing and chemical separations.* Lab Chip, 2009. **9**(8): p. 1046-51.

196. Wang, W. and T.B. Jones, *Moving droplets between closed and open microfluidic systems.* Lab on a Chip, 2015.

197. Ren, H., R.B. Fair, and M.G. Pollack, *Automated on-chip droplet dispensing with volume control by electro-wetting actuation and capacitance metering.* Sensors and Actuators. B: Chemical, 2004. **98**: p. 319-327.

198. Bhargava, K.C., B. Thompson, and N. Malmstadt, *Discrete elements for 3D microfluidics.* Proceedings of the National Academy of Sciences, 2014. **111**(42): p. 15013–15018.

199. Yang, H., et al. *3D Droplet Transportations by EWOD Actuations on Flexible Polymer Films*. in *ASME International Mechanical Engineering Congress and Exposition*. 2005. Orlando, FL, USA.

200. George, S.M. and H. Moon, *Three Dimensional Tissue Based Digital Microfluidic Screening Platform*, in *Int C Mini Sys Chem Life Sci*. 2011: Seattle, Washington, USA. p. 1545-1547.

201. Ay, C., et al., *Evaluation of the Correlation between Focal Adhesion Kinase Phosphorylation and Cell Adhesion Force Using "DEP" Technology.* Sensors, 2012. **12**: p. 5951-5965.

202. Luk, V.N., et al., *Digital microfluidic hydrogel microreactors for proteomics.* Proteomics, 2012. **12**: p. 1310-1318.

203. Chiang, M.-Y. and S.-K. Fan, *Electric Manipulations of Hydrogel on a Digital Microfluidic Platform*, in *NEMS 2012*. 2012: Kyoto, Japan. p. 407-410.

204. Vlahovska, P.M., et al., *Electrohydrodynamic Model of Vesicle Deformation in Alternating Electric Fields.* Biophys J, 2009. **96**: p. 4789-4803.

205. Engelhardt, H. and E. Sackmann, *On the Measurement of Shear Elastic Moduli and Viscosities of Erythrocyte Plasma Membranes by Transient Deformation in High Frequency Electric Fields.* Biophys J, 1988. **54**: p. 495-508.

206. Li, H., T. Ye, and K.Y. Lam, *Qualitative and quantitative analysis of dynamic deformation of a cell in nonuniform alternating electric field.* J Appl Phys, 2011. **110**(104701): p. 1-6.

207. Cho, S.K. and H. Moon, *Electrowetting on Dielectric (EWOD): New Tool for Bio/Micro Fluids Handling.* Biochip Journal, 2008. **2**(2): p. 79-96.

208. Wang, J.H.-C. and B.P. Thampatty, *Mechanobiology of Adult and Stem Cells.* Int Rev Cell Mol Bio, 2008. **271**: p. 301-334.

209. Sheehy, S.P., A. Grosberg, and K.K. Parker, *The contribution of cellular mechanotransduction to cardiomyocyte form and function.* Biomech Model Mechanobiol, 2012([Epub ahead of print]).

210. George, S.M. and H. Moon, *Digital microfluidic three-dimensional cell culture and chemical screening platform using alginate hydrogels.* Biomicrofluidics, 2015. **9**: p. 024116.

211. Cao, L., et al., *Promoting angiogenesis via manipulation of VEGF responsiveness with notch signaling.* Biomaterials, 2009. **30**: p. 4085-4093.

212. Primiceri, E., et al., *Cell chips as new tools for cell biology - results, perspectives and opportunities.* Lab on a Chip, 2013. **13**(19): p. 3789-3802.

213. Schertzer, M.J., et al., *An Empirically Validated Analytical Model of Droplet Dynamics in Electrowetting on Dielectric Devices.* Langmuir, 2010. **26**(24): p. 19230-19238.

214. Tenan, M.A., S. Hackwood, and G. Beni, *Friction in capillary systems.* Journal of Applied Physics, 1982. **53**(10): p. 6687-6692.

215. Adamson, A.W. and A.P. Gast, *Physical Chemistry of Surfaces*. 6th ed. 1997, Canada: John Wiley & Sons.

216. Gong, J. and C.J. Kim, *All-electronic droplet generation on-chip with real-time feedback control for EWOD digital microfluidics.* Lab Chip, 2008. **8**: p. 898-906.

217. Brassard, D., et al., *Water-oil core-shell droplets for electrowetting-based digital microfluidic devices.* Lab on a Chip, 2008. **8**: p. 1342-1349.

218. Woolley, C.F. and M.A. Hayes, *Recent Developments in Emerging Microimmunoassays.* Bioanalysis, 2013. **5**(2): p. 245-264.

219. Song, K., et al., *Investigation of the Effective Action Distance Between Hematopoietic Stem/Progenitor Cells and Human Adipose-Derived Stem Cells During Their In Vitro Co-culture.* Appl Biochem Biotech, 2011. **165**(3-4): p. 776-784.

220. Frank, T. and S. Tay, *Automated co-culture system for spatiotemporal analysis of cell-to-cell communication.* Lab on a Chip, 2015.

221. Banerjee, A., et al., *The Influence of Hydrogel Modulus on the Proliferation and Differentiation of Encapsulated Neural Stem Cells.* Biomaterials, 2009. **30**(27): p. 4695-4699.

222. Dean, D.A., et al., *Electrical Impedance Spectroscopy Study of Biological Tissues.* Journal of Electrostatics, 2009. **66**(3-4): p. 165-177.

223. Shih, S.C.C., et al., *Digital microfluidics with impedance sensing for integrated cell culture and analysis.* Biosensors and Bioelectronics, 2013. **42**: p. 314-320.

224. Arshi, A., et al., *Rigid microenvironments promote cardiac differentiation of mouse and human embryonic stem cells.* Sci Technol Adv Mater, 2013. **14**(2): p. 8.

225. Chen, S., et al. *Electrowetting-driven chemical synthesis and radioisotope purification of positron emission tomography (PET) radiotracers*. in *9th International Meeting on Electrowetting and Related Micro/Electrofluidic Science and Technology*. 2014. Cincinnati, OH.

226. Willems, E., P.J. Bushway, and M. Mercola, *Natural and Synthetic Regulators of Embryonic Stem Cell Cardiogenesis.* Pediatric Cardiology, 2009. **30**(5): p. 635-642.

227. You, J., et al., *Cardiomyocyte sensor responsive to changes in physical and chemical environments.* Journal of Biomechanics, 2014. **47**(2): p. 400-409.

228. Abassi, Y.A., et al., *Dynamic monitoring of beating periodicity of stem cell-derived cardiomyocytes as a predictive tool for preclinical safety assessment.* British Journal of Pharmacology, 2011. **165**(5): p. 1424-1441.

229. Xu, J., *Nanocalorimetric Sensor for Ultra-Low Volume Biological Measurements and Calibration by Chemical Method*, in *Physics*. 2007, Vanderbilt University: Nashville, TN. p. 132.

230. Mayr, L.M. and D. Bojanic, *Novel trends in high-throughput screening.* Current Opinion in Pharmacology, 2009. **9**(5): p. 580-588.

231. Haponen, M., *Optimization of Cardiomyocyte Differentiation of Human Pluripotent Stem Cells*, in *Laboratory Sciences*. 2010, Tampere University of Applied Sciences: Tampere. p. 50.

232. Pettinato, G., X. Wen, and N. Zhang, *Formation of Well-defined Embryoid Bodies from Dissociated Human Induced Pluripotent Stem Cells using Microfabricated Cell-repellent Microwell Arrays.* Scientific Reports, 2014. **4**(7402): p. 1-11.

233. Frey, O., et al., *Reconfigurable microfluidic hanging drop network for multi-tissue interaction and analysis.* Nat Commun, 2014. **5**.

234. Trettner, S., A. Seeliger, and N.I.z. Nieden, *Embryoid Body Formation: Recent Advances in Automated Bioreactor Technology*, in *Embryonic Stem Cell Therapy for Osteo-Degenerative Diseases*, N.I.z. Nieden, Editor. 2011, Humana Press: Riverside, CA. p. 135-150.

235. Spelke, D.P., et al., *Methods for Embryoid Body Formation: The Microwell Approach*, in *Embryonic Stem Cell Therapy for Osteo-Degenerative Diseases*, N.I.z. Nieden, Editor. 2011, Humana Press: Riverside, CA. p. 151-162.

236. Torisawa, Y.-s., et al., *Efficient formation of uniform-sized embryoid bodies using a compartmentalized microchannel device.* Lab on a Chip, 2007. **7**(6): p. 770-776.

237. Frey, O., Y. Schmid, and A. Hierlemann. *Monitoring of 3D multi-cellular spheroids in hanging drop networks thrugh in-situ impedance spectroscopy*. in *The 18th International Conference on Miniaturized Systems for Chemistry and Life Sciences*. 2014. San Antonio, TX, USA.

238. Burton, B.M., et al., *Uncertainty Visualization in Forward and Inverse Cardiac Models.* Computational Cardiology, 2010. **40**: p. 57-60.

239. Hua, N., et al., *Comparison between ECIS and LAPS for establishing a cardiomyocyte-based biosensor.* Sensors and Actuators B: Chemical, 2013. **185**: p. 238-244.

240. Tran, T.H., et al., *Wnt3a-Induced Mesoderm Formation and Cardiomyogenesis in Human Embryonic Stem Cells.* STEM CELLS, 2009. **27**(8): p. 1869-1878.

241. Fobel, R. and C. Fobel. *DropBot Website*. 3/10/2015]; Available from: http://microfluidics.utoronto.ca/dropbot/.

242. Seymour, J.P., et al., *The insulation performance of reactive parylene films in implantable electronic devices.* Biomaterials, 2009. **310**(31): p. 6158-6167.

243. Bender, B.F., A.P. Aijian, and R.L. Garrell. *Digital Microfluidic Platform for Cell Spheroid-Based Migration/Invasion Assays*. in *18th International Conference on Miniaturized Systems for Chemistry and Life Sciences*. 2014. San Antonio, TX.

244. Srigunapalan, S., et al., *A digital microfluidic platform for primary cell culture and analysis.* Lab on a Chip, 2012. **12**(2): p. 369-375.

245. Ahmadi, A., M.D. Buat, and M. Hoorfar, *Microdroplet evaporation in closed digital microfluidic biochips.* Journal of Micromechanics and Microengineering, 2013. **23**(13): p. 1-8.

246. Perez-Diaz, J.L., M.A. Alvarez-Valenzuela, and J.C. Garcia-Prada, *The effect of the partial pressure of water vapor on the surface tension of the liquid water-air interface.* Journal of Colloid and Interface Science, 2012. **1**(381): p. 180-182.

247. Perez-Diaz, J.L., et al. *On the Influence of Relative Humidity on the Contact Angle of a Water Droplet on a Silicon Wafer*. in *Proceedings of the ASME 2013 International Mechanical Engineering Congress and Exposition IMECE2013*. 2013. San Diego, CA.

248. Brito-Martins, M., S.E. Harding, and N.N. Ali, *β(1)- and β(2)-adrenoceptor responses in cardiomyocytes derived from human embryonic stem cells: comparison with failing and non-failing adult human heart.* British Journal of Pharmacology, 2008. **153**(4): p. 751-759.

249. Tashjian, A.H. and E.J. Armstrong, *Principles of Pharmacology: The Pathophysiologic Basis of Drug Therapy*. 2011: Lippincott Williams & Wilkins. 1008.

250. Satoh, H., *Positive and negative chronotropic effects of caffeine in spontaneously beating rabbit sino-atrial node cells.* General Pharmacology, 1993. **24**(5): p. 1223-30.

251. Satoh, H., *Caffeine depression of spontaneous activity in rabbit sino-atrial node cells.* General Pharmacology, 1993. **24**(3): p. 555-63.

252. Neco, P., et al., *Paradoxical Effect of Increased Diastolic Ca(2+) Release and Decreased Sinoatrial Node Activity in a Mouse Model of Catecholaminergic Polymorphic Ventricular Tachycardia.* Circulation, 2012. **126**(4): p. 392-401.

253. Paur, H., et al., *High Levels of Circulating Epinephrine Trigger Apical Cardiodepression in a β2-Adrenergic Receptor/Gi–Dependent Manner: A New Model of Takotsubo Cardiomyopathy.* Circulation, 2012. **126**(6): p. 697-706.

254. Gorospe, G., et al., *Automated Grouping of Action Potentials of Human Embryonic Stem Cell-Derived Cardiomyocytes.* IEEE TRANSACTIONS ON BIOMEDICAL ENGINEERING, 2014. **61**(9): p. 2389-2395.

255. Luo, C.-h. and Y. Rudy, *A Model of the Ventricular Cardiac Action Potential. Depolarization, repolarization, and their interaction.* Circulation Research, 1991. **68**(6): p. 1501-1526.

256. Cole, K.S. and H.J. Curtis, *Electric Impedance of the Squid Giant Axon During Activity.* Journal of General Physiology, 1939. **22**(5): p. 649-670.

257. Hodgkin, A.L. and A.F. Huxley, *A quantitative description of membrane current and its application to conduction and excitation in nerve.* Journal of Physiology, 1952. **117**(4): p. 500-544.

258. Morgan, H., et al., *Single cell dielectric spectroscopy.* Journal of Physics D: Applied Physics, 2007. **40**(1): p. 61.

259. Bauchot, A.D., F.R. Harker, and W.M. Arnold, *The use of electrical impedance spectroscopy to assess the physiological condition of kiwifruit.* Postharvest Biology and Technology, 2000. **18**(1): p. 9-18.

260. Gersing, E., *Impedance spectroscopy on living tissue for determination of the state of organs.* Bioelectrochemistry and Bioenergetics, 1998. **45**(2): p. 145-149.

261. Cinca, J., et al., *Changes in Myocardial Electrical Impedance Induced by Coronary Artery Occlusion in Pigs With and Without Preconditioning.* Circulation, 1997. **96**: p. 3079-3086.

262. Fry, C.H., et al., *Cytoplasm Resistivity of Mammalian Atrial Myocardium Determined by Dielectrophoresis and Impedance Methods.* Biophysical Journal, 2012. **103**(11): p. 2287-2294.

263. Sun, T. and H. Morgan, *Single-cell microfluidic impedance cytometry: a review.* Microfluidics and Nanofluidics, 2010. **8**(4): p. 423-443.

264. Kenneth R. Boheler, J.C., David Tweedie, Huang-Tian Yang, Sergey V. Anisimov, Anna M. Wobus, *Differentiation of Pluripotent Embryonic Stem Cells Into Cardiomyocytes.* Circulation Research, 2002. **91**: p. 189-201.

265. Maltsev, V.A., et al., *Embryonic stem cells differentiate in vitro into cardiomyocytes representing sinusnodal, atrial and ventricular cell types.* Mechanisms of Development, 1993. **44**(1): p. 41-50.

266. Guo, W., et al., *Changes in action potentials and ion currents in long-term cultured neonatal rat ventricular cells.* American Journal of Physiology, 1996. **271**(1): p. C93-102.

267. Schild, L., et al., *Rapid pacing of embryoid bodies impairs mitochondrial ATP synthesis by a calcium-dependent mechanism—A model of in vitro differentiated cardiomyocytes to study molecular effects of tachycardia.* Biochimica et Biophysica Acta (BBA) - Molecular Basis of Disease, 2006. **1762**(6): p. 608-615.

268. Reed, J., et al., *Mechanical Interferometry of Nanoscale Motion and Local Mechanical Properties of Living Zebrafish Embryos.* ACS Nano, 2009. **3**(8): p. 2090-2094.

269. Ionta, V., et al., *SHOX2 Overexpression Favors Differentiation of Embryonic Stem Cells into Cardiac Pacemaker Cells, Improving Biological Pacing Ability.* Stem Cell Reports, 2015. **4**: p. 129-142.

270. Seely, A.J. and P.T. Macklem, *Complex systems and the technology of variability analysis.* Critical Care, 2004. **8**: p. R367-R384.

271. Natarajan, A., et al., *Patterned cardiomyocytes on microelectrode arrays as a functional, high information content drug screening platform.* Biomaterials, 2011. **32**(18): p. 4267-4274.

272. Boudreau-Béland, J., et al., *Spatiotemporal Stability of Neonatal Rat Cardiomyocyte Monolayers Spontaneous Activity Is Dependent on the Culture Substrate.* PloS 2015. **10**(6): p. e0127977.

273. Young, D.A., J.A. DeQuach, and K.L. Christman, *Human Cardiomyogenesis and the Need for Systems Biology Analysis.* Wiley Interdisciplinary Reviews: Systems Biology and Medicine, 2011. **3**(6): p. 666-680.

274. Yaniv, Y., et al., *Synchronization of sinoatrial node pacemaker cell clocks and its autonomic modulation impart complexity to heart beating intervals.* Heart Rhythm, 2014. **11**(7): p. 1210-1219.

275. Barbulovic-Nad, I., et al., *Digital microfluidics for cell-based assays.* Lab on a Chip, 2008. **8**: p. 519-526.

276. Sadeghi, S., et al., *On Chip Droplet Characterization: A Practical, High-Sensitivity Measurement of Droplet Impedance in Digital Microfluidics.* Analytical Chemistry, 2012. **84**(4): p. 1915-1923.

277. Nelson, W.C., et al., *An EWOD Digital Microfluidic Chip with Integrated Localized Temperature Control for Multiplex Proteomics Sample Processing*, in *Proc. IEEE Int. Conf. MEMS*. 2009: Sorrento, Italy. p. 280-283.

278. Polacheck, W.J., et al., *Microfluidic platforms for mechanobiology.* Lab on a Chip, 2013. **13**(12): p. 2252-2267.

279. Barsoum, M.W., *Fundamentals of Ceramics*. 2003, New York, NY: Taylor & Francis Group.

280. Soergel, E., *Piezoresponse force microscopy (PFM).* Journal of Physics D: Applied Physics, 2011. **44**: p. 464003.

281. Bowen, C.R., et al., *Optimisation of interdigitated electrodes for piezoelectric actuators and active fibre composites.* Journal of Electroceramics, 2006. **16**(4): p. 263-269.

282. Choi, J.-H., et al., *Acid-catalyzed kinetics of indium tin oxide etching.* Thin Solid Films, 2014. **565**(0): p. 179-185.

283. Cardoso, V.F., et al., *Micro and nanofilms of poly-vinylidene fluoride with controlled thickness, morphology and electroactive crystalline phase for sensor and actuator applications.* Smart Materials and Structures, 2011. **20**: p. 087002.

284. Williamson, A., et al., *The future of the patient-specific Body-on-a-chip.* Lab on a Chip, 2013. **13**(18): p. 3471-3480.

285. Serena, E., et al., *Electrical stimulation of human embryonic stem cells: cardiac differentiation and the generation of reactive oxygen species.* Experimental Cell Research, 2009. **315**(20): p. 3611-3619.

286. Ma, S., C.C. Funk, and N.D. Price, *Systems approaches to molecular cancer diagnostics.* Discov Med, 2010. **10**(55): p. 531-542.

287. Peeling, R.W., P.G. Smith, and P.M.M. Bossuyt, *A guide for diagnostic evaluations.* Nat Rev Microbiol, 2006. **4**(9): p. S2-6.

288. Suresh, S., *Biomechanics and biophysics of cancer cells.* Acta Biomater, 2007. **3**: p. 413-438.

289. Suresh, S., et al., *Connections between single-cell biomechanics and human disease states: gastrointestinal cancer and malaria.* Acta Biomater, 2005. **1**: p. 15-30.

290. González-Cruza, R.D., V.C. Fonsecaa, and E.M. Darling, *Cellular mechanical properties reflect the differentiation potential of adipose-derived mesenchymal stem cells.* PNAS, 2011. **Early Edition**: p. 1-7.

291. Buehler, M.J. and Y.C. Yung, *Deformation and failure of protein materials in physiologically extreme conditions and disease.* Nature Materials, 2009. **8**: p. 175-188.

292. González-Cruz, R., V. Fonseca, and E. Darling, *Cellular mechanical properties reflect the differentiation potential of adipose-derived mesenchymal stem cells.* Proceeding of the National Academy of Sciences, 2012. **109**(24): p. E1523-9.

293. Suresh, S., et al., *Connections between single-cell biomechanics and human disease states: gastrointestinal cancer and malaria.* Acta Biomaterialia, 2005. **1**(1): p. 15-30.

294. Suresh, S., *Biomechanics and biophysics of cancer cells.* Acta Biomaterialia, 2007. **3**(4): p. 413-438.

295. Zhou, E.H., et al., *A power-law rheology-based finite element model for single cell deformation.* Biomechanics and Modeling in Mechanobiology, 2012. **11**(7): p. 1075-1084.

296. Tan, Y.H., et al., *Probing the mechanobiological properties of human embryonic stem cells in cardiac differentiation by optical tweezers.* Journal of Biomechanics, 2012. **45**(1): p. 123-128.

297. Desprat, N., A. Guiroy, and A. Asnacios, *Microplates-based rheometer for a single living cell.* Review of Scientific Instruments, 2006. **77**(5): p. 9.

298. Sraj, I., et al., *Erythrocyte deformation in high-throughput optical stretchers.* Physical Review E, 2012. **85**(4): p. 9.

299. Gossett, D.R., et al., *Hydrodynamic stretching of single cells for large population mechanical phenotyping.* Proceeding of the National Academy of Sciences, 2012. **109**(20): p. 7630-7635.

300. Kim, Y.C., S.J. Park, and J.K. Park, *Biomechanical analysis of cancerous and normal cells based on bulge generation in a microfluidic device.* Analyst, 2008. **133**(10): p. 1432-1439.

301. Pellegrino, M., et al., *Measuring the elastic properties of living cells through the analysis of current-displacement curves in scanning ion conductance*

microscopy. Pflugers Archiv-European Journal of Physiology, 2012. **464**(3): p. 307-316.

302. Guido, I., M.S. Jaeger, and C. Duschl, *Dielectrophoretic stretching of cells allows for characterization of their mechanical properties.* Eur Biophys J, 2011. **40**: p. 281-288.

303. Chen, J., et al., *Electrodeformation for single cell mechanical characterization.* J Micromech Microeng, 2011. **21**(054012): p. 1-11.

304. Lulevich, V., et al., *Single cell mechanics of keratinocyte cells.* Ultramicroscopy, 2010. **110**: p. 1435-1442.

305. Aranda, S., et al., *Morphological Transitions of Vesicles Induced by Alternating Electric Fields.* Biophys J, 2008. **95**: p. L19-L21.

306. Garc´ıa-Aznar, J.e.M., et al., *Mechanobiological Models for Bone Tissue. Applications to Implant Design*, in *Biomechanics of Hard Tissues: Modeling, Testing, and Materials*, D.A. Öchsner and W. Ahmed, Editors. 2010, Wiley-VCH Verlag GmbH & Co. p. 123-143.

307. Ingber, D.E., *Mechanobiology and diseases of mechanotransduction.* Ann Med, 2003. **35**(8): p. 564-77.

308. Guido, I., M.S. Jaeger, and C. Duschl, *Influence of medium consumption on cell elasticity.* Cytotechnology, 2010. **62**(3): p. 257-263.

309. Doh, I., et al., *Deformation measurement of individual cells in large populations using a single-cell microchamber array chip.* Appl Phys Lett, 2012. **100**(17): p. 173702-1737023.

310. Guido, I., et al., *Microfluidic system for cell mechanics analysis through dielectrophoresis.* Microelec Eng, 2012. **97**: p. 379-382.

311. Bates, R.C., N.S. Edwards, and J.D. Yates, *Spheroids and cell survival.* Critical Reviews in Oncology/Hematology, 2000. **36**(2-3): p. 61-74.

312. Au, S.H., P. Kumar, and A.R. Wheeler, *A New Angle on Pluronic Additives: Advancing Droplets and Understanding in Digital Microfluidics.* Langmuir, 2011. **27**(13): p. 8586-8594.

313. Eydelnant, I.A., et al. *UPSIDE-DOWN" DIGITAL MICROFLUIDIC BASED EMBRYONIC STEM CELL CULTURE*. in *15th International Conference on Miniaturized Systems for Chemistry and Life Sciences*. 2011. Seattle, Washington, USA.

314. Nelsona, W.C., et al., *Incubated protein reduction and digestion on an EWOD digital microfluidic chip for MALDI-MS.* Anal Chem, 2010. **82**(23): p. 9932-9937.